University of Southampton

Faculty of Engineering and Physical Sciences
School of Chemistry

Parahydrogen-Induced Polarization in Microfluidic Devices

by

Sylwia Joanna Ostrowska-Barker

ORCiD: 0000-0001-7867-5938

A thesis for the degree of
Doctor of Philosophy

March 2023

University of Southampton

Abstract

Faculty of Engineering and Physical Sciences
School of Chemistry

Doctor of Philosophy

Parahydrogen-Induced Polarization in Microfluidic Devices

by Sylwia Joanna Ostrowska-Barker

Microfluidic lab-on-a-chip (LoC) systems hold great potential for the study of live microscopic cultures of cells, tissue samples, and small organisms. This is because the LoC microenvironment can be engineered to precisely simulate the physiological or pathological state of an organism in a highly controlled, repeatable manner. High-resolution Nuclear Magnetic Resonance (NMR) spectroscopy is an ideal tool to follow chemical and biochemical processes in LoC due to its non-invasive nature, chemical specificity and the ability to quantify metabolites, yet it is rarely used in combination with LoC due to its low sensitivity. Integration of hyperpolarization methods such as parahydrogen induced polarization (PHIP) enables NMR signals to be enhanced by several orders of magnitude. This would enable quantitative studies of a wider range of metabolites in such volume limited systems by NMR.

This thesis presents the advances made to improve the efficiency of PHIP in LoC and to generalise the approach to ^{13}C - hyperpolarization, a nucleus of choice for biological applications. This is achieved by developing a spatially-resolved kinetic finite element model of a PHIP reaction in LoC. The model is then used to design an optimised micro-reactor that integrates the formation, sample transport, RF excitation and observation of ^{13}C-hyperpolarized metabolites onto one compact device at the microscale.

Contents

List of Figures

List of Tables

Declaration of Authorship

I declare that this thesis and the work presented in it is my own and has been generated by me as the result of my own original research.

I confirm that:

1. This work was done wholly or mainly while in candidature for a research degree at this University;
2. Where any part of this thesis has previously been submitted for a degree or any other qualification at this University or any other institution, this has been clearly stated;
3. Where I have consulted the published work of others, this is always clearly attributed;
4. Where I have quoted from the work of others, the source is always given. With the exception of such quotations, this thesis is entirely my own work;
5. I have acknowledged all main sources of help;
6. Where the thesis is based on work done by myself jointly with others, I have made clear exactly what was done by others and what I have contributed myself;
7. Parts of this work have been published as: [2], [3]

Signed:.. Date:..................

Acknowledgements

I would like to start by thanking my supervisor, Marcel Utz who has been a constant source of support and encouragement throughout my PhD, especially during the COVID-19 pandemic. Marcel taught me the principles of scientific research and communication, which I will carry with me for the rest of my scientific career.

I am very grateful to Giuseppe Pileio for introducing me to the subject of NMR and inspiring me to pursue a PhD. I would like to thank my colleagues: Christian Bengs, Laurynas Dagys, Evie Rogers, William Hale, James Eills, Malcolm Levitt, Barbara Ripka, Manvendra Sharma, Bishnubrata Patra, Ciara Nelder, Jake Keely, Aabidah Rana, Marek Plata, James Whipham, Mohamed Sabba, Weidong Gong, Harry Collins, Thomas Robertson, Topaz Cartlidge, Maria Concistre, Karel Kouřil, Hana Kouřilová, Beno Meier, George Bacanu, Murari Soundararajan, Ilya Kuprov, Urvashi Heramun, and Sebastiaan Van Dyck; who helped me with various aspects of the work presented in this thesis. To my dear friends Kerry Maltby, Evie Rogers, Melli Darrington, Laura Sutcliffe, Anita Dudź and James Pearce who were always available when I needed a break and made amazing food to lift my spirits, you helped me tremendously.

Z całego serca dziękuję mojej mamie, Alinie Ostrowskiej, siostrze Kamili oraz siostrzenicy Wiktorii za miłość, opiekę i porady przez te wszystkie lata.

Thank you to my husband, Timothy Barker, the list is too long to single out everything that you have done to support me throughout these years. I am very thankful for having you in my life.

To my family

Abbreviations

ALTADENA	Adiabatic Longitudinal Transport After Dissociation Endengers Net Alignment
CE	Capillary Electrophoresis
CIDNP	Chemically Induced Dynamic Nuclear Polarization
cLOD	Concentration Limit of Detection
CRP	C-reactive Protein
CW-S2M	Continuous Wave Singlet-to-Magnetisation
dDNP	Dissolution Dynamic Nuclear Polarization
DMSO	Dimethyl Sulfoxide
DNA	Deoxyribonucleic Acid
DNP	Dynamic Nuclear Polarization
DSS	Sodium Trimethylsilylpropanesulfonate
ECM	Extracellular Matrix
ELISA	Enzyme-Linked Immunosorbent Assay
emf	Electromotive Force
FEM	Finite Element Method
FID	Free Induction Decay
FT	Fourier Transform
HPLC	High-Performance Liquid Chromatography
IgG	Immunoglobulin G
IPA	Propan-2-ol
LoC	Lab-on-a-Chip
MAS-DNP	Magic Angle Spinning Dynamic Nuclear Polarization
MRI	Magnetic Resonance Imaging

nLOD	Mass Limit of Detection
NMR	Nuclear Magnetic Resonance
$o-H_2$	Orthohydrogen Gas
OoC	Organ-on-a-Chip
$p-H_2$	Parahydrogen Gas
PASADENA	Parahydrogen and Synthesis Allow Dramatically Enhanced Nuclear Alignment
PC	Polycarbonate
PCR	Polymerase Chain Reaction
PDMS	Poly(Dimethyl Siloxane)
PHIP	Parahydrogen Induced Polarization
PID	ProportionalIntegralDerivative
PMMA	Poly(Methyl Metacrylate)
ppm	Parts Per Million
PS	Polysytene
PTFE	Polytetrafluoroethylene
RF	Radio Frequency
SABRE	Signal Amplification by Reversible Exchange
SAH-PHIP	Side-Arm Hydrogenation ParaHydorgen Induced Polarization
SEOP	Spin-Exchange Optical Pumping
SNR	Singal-to-Noise Ratio
S2hM	Singlet-to-Heteronuclear Magnetisation
S2M	Singlet-to-Magnetisation
TEMPO	2,2,6,6-Tetramethylpiperidin-1-yl)oxyl
TLP	Trnasmission Line Probe
UV-light	Ultraviolet Light
μPAD	Microfluidic Paper-Based Analytical Device
μTAS	Micro Total Analysis Sytem
2D	Two Dimensional
3D	Three Dimensional

Chapter 1

Introduction

The manipulation and analysis of small volumes of fluids, typically in the pL to μL range, lies at the heart of microfluidic technology [4, 5]. Fluids are controlled through the careful design of networks of microchannels, pumps, valves, and reservoirs that enable complex chemical and biochemical processes to be performed in a miniaturised platform; generally referred to as a "Lab-on-a-Chip" (LoC) or a micro-total analysis system (μTAS) [6–11]. Miniaturisation brings many advantages such as reduced reagent consumption and waste, increased surface-to-volume ratio, rapid prototyping, parallelisation, and precise control of the physical and chemical properties of fluids [12]. As a result, microfluidics finds applications across many disciplines but perhaps the most important is its use in the culture of biological systems. Apart from simply substituting Petri dishes and flasks used in conventional cultures with more compact and cost-effective alternatives, microfluidic technology enables precise control over the environment in a repeatable manner. This is a vital advantage in biological research, where manipulation of the local or systemic environment is necessary to study cellular processes and functions as well as their response to external stimuli such as drugs [13], therapeutic targets [14–16], toxins [17, 18], oxygen or nutrient supply [19, 20].

High-resolution Nuclear Magnetic Resonance (NMR) spectroscopy is an ideal technique to follow chemical reactions and monitor biological systems in LoC due to its non-invasive nature, chemical specificity and the ability to quantify metabolites, yet it is rarely used in combination with LoC due to its low sensitivity [21].

Hyperpolarization methods such as Parahydrogen-Induced Polarization (PHIP) make it possible to enhance NMR signals by up to 5 orders of magnitude [22, 23]. PHIP utilises *para*hydrogen ($\mathrm{p-H_2}$), a spin isomer of hydrogen, as a polarization source. The nuclear spin order is transferred to a target molecule via a chemical reaction of $\mathrm{p-H_2}$ with an unsaturated molecule in the presence of an organometallic catalyst. The chemical reaction is followed by spin manipulations to transfer the parahydrogen-derived spin order to a desired nucleus, as well as purification steps to remove unwanted compounds [24]. LoC devices can be used to implement some or all of these processes, thus offering the possibility of integrating the production, purification, and application of hyperpolarized species to a biological system at the microscale. Mass sensitives of the order of pmol/s for ^{1}H were reported using such systems [1]. However, for practical applications, microfluidic devices need to be optimised to improve the yield of the reaction. This requires a quantitative understanding of the interplay between the reaction chemistry, the flow properties of the device, the spin order transfer as well as the relaxation properties. Another objective is to be able to transfer the polarization to other nuclei such as ^{13}C. Observation of ^{13}C is preferred for biological applications due to the longer longitudinal relaxation times than ^{1}H, larger chemical shift dispersion, and reduced overlap with background signals [25].

This thesis describes the advances made to enable the formation, sample transport, radio frequency excitation, and observation of ^{13}C-hyperpolarized metabolites on a single, compact platform at the μL scale. Chapter 2 provides the background theory for the four concepts discussed in this thesis: microfluidics, NMR, hyperpolarization and finite element simulations. This is followed by the Materials and Methods in Chapter 3. Then, in Chapter 4, the development of a spatially-resolved kinetic model of a PHIP reaction is described. The model enables quantitative prediction of the uptake of hydrogen into the device, the concentration of PHIP hyperpolarized products, and identification of the rate limiting factors. Findings from the finite element model are used to inform the design of an optimised micro-reactor presented in Chapter 5. Additionally, the temperature dependence of the PHIP reaction is studied. The work presented in this thesis also highlights LoC as an excellent platform for the investigation of complex physical phenomena as operation under continuous flow allows a steady-state between the rate of reaction and relaxation to be established. Since the fresh solution is continually provided to the detection chamber, samples do not need to be replaced between experiments. Therefore systematic studies can be performed in a highly controlled and repeatable manner. This is demonstrated in Chapter 6, which describes a systematic study of the methods that combat singlet-triplet mixing, a phenomenon which can substantially hinder the achievable polarization. The most favourable conditions for the polarization transfer at the microscale are also discussed here. Lastly, the aforementioned mentioned optimizations in polarization transfer methods and micro-reactors enable carbon-hyperpolarized metabolites to be observed at the microscale. In the last chapter, the conclusions are presented.

Chapter 2

Background

This chapter lays the foundations for the four core concepts discussed in this thesis: microfluidics, NMR, hyperpolarization and finite element simulations.

2.1 Microfluidic Lab-on-a-Chip Technology

Microfluidic technology enables the precise control and manipulation of small volumes (10^{-6} to 10^{-18} litres) of fluids [4, 5]. Fluids are controlled through the careful design of networks of microchannels, pumps, valves, and reservoirs that enable complex biochemical processes to be performed and analysed in a single, compact, miniaturized platform; generally referred to as a "Lab-on-a-Chip" (LoC) [26, 14, 27–32, 12]. In this section, the key concepts in microfluidics are discussed, starting with the examination of physics at the microscale to explain the behaviour of fluids in LoC. Then, materials commonly employed in device manufacturing and subsequent applications are discussed. The section concludes by reviewing detection methods frequently integrated with microfluidics.

2.1.1 Physics of Microfluidics

2.1.1.1 Flow Pattern

The key to precise control of microfluidic devices lies in the flow pattern that is obtained. Generally, the flow pattern is determined by the Reynolds number (Re), which describes the ratio between the inertial and viscous forces [33]:

$$Re = \frac{\text{inertial forces}}{\text{viscous forces}} = \frac{\rho u L}{\eta}, \tag{2.1}$$

where ρ is the density of the fluid, u is the fluid velocity, L is the dimension of the system (the diameter or channel depth) and η is the dynamic viscosity. When Re is low i.e. $Re < 1500$ the flow regime is laminar [34]. The flow profile is smooth and the flow lines are parallel to each other, as illustrated in Fig. 2.1 a which shows the confluence of two channels joined by a Y-junction. In the laminar flow regime and low flow rates, the two liquids stay in contact with a flat boundary along which diffusion leads to a partial mass interchange between the two streams, but the process is slow and inefficient. In contrast when the Re is high ($Re > 4000$) as illustrated in Fig. 2.1 b, the flow regime is turbulent. Such a regime is dominated by the inertial forces leading to unexpected movements and chaotic, convective mixing between fluid streams. In between ($1500 < Re < 4000$), there is a transition region where the flow profile is laminar near the edges of the channel and more turbulent in the centre [35].

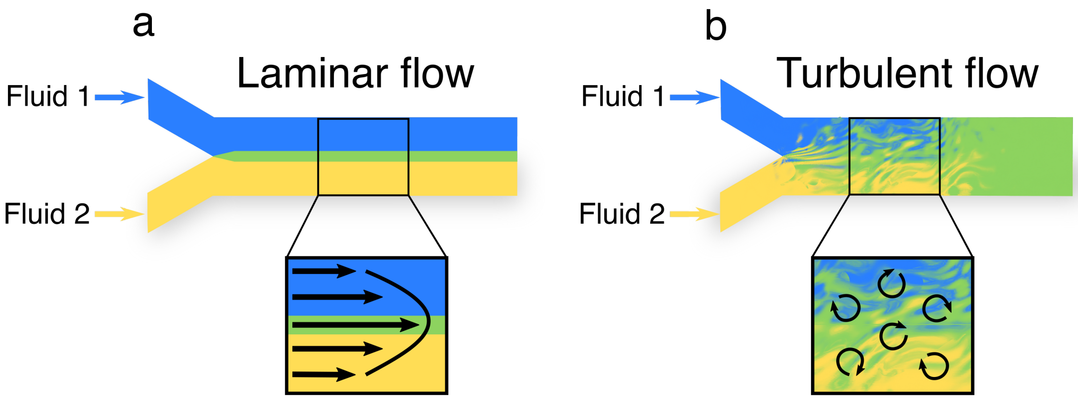

FIGURE 2.1: An illustration of the flow regimes governed by the Reynolds number. The image was adapted from [12]

Fluid	**Temperature** / °C	**Density** / g cm^3	**Viscosity** / 10^{-2} g cm^{-1} s^{-1}
Water	0	0.999	1.787
Water	20	0.998	1.002
Ethanol	0	0.806	1.773
Ethanol	20	0.791	1.200
Acetone	25	0.784*	0.316
Blood	37	1.060**	4.0
Olive oil	20	0.92	84
FC-43	25	1.860***	4.7

Table 2.1: A comparison of the densities and viscosities of common fluids. Values were taken from [36].$*$ Value taken from [37]. $**$ Value taken from [38]. *** Value taken from [39].

While turbulent flow is common at the macroscale, laminar flow is prevalent in microfluidics. A typical microfluidic channel has a diameter of $L = 100\,\mu m$ and assuming that water ($\rho = 0.998\,\mathrm{g\,cm^3},\ \eta = 0.01\,\mathrm{g\,cm^{-1}\,s^{-1}}$ at 20°C) flows through the system at a velocity of $u = 1\,\mathrm{cm\,s^{-1}}$ this yields Reynolds number of $Re \approx 1$; therefore, the fluid follows the laminar flow regime [36]. In order to reach a turbulent flow regime with $Re = 4000$, water would need to be pumped at a velocity of $u = 40$ m s^{-1}. Table 2.1 lists the densities and viscosities of other common fluids. If an oil, such as FC-43, flows through a microfluidic device, the pumping rate would have to be even higher to induce turbulence since the fluid is more viscous than water.

The laminar flow regime is well understood and thus highly predictable. As a result, the internal environment of a LoC can be precisely engineered. For instance, Komen *et al.* [19] developed a microfluidic device capable of delivering physiological concentration profiles of an anti-cancer drug to a cell culture while simultaneously measuring its efficacy on-chip. Their chip comprised a cell culture chamber and a drug-dosing channel separated by a porous membrane. The drug was delivered using an external pump. The study demonstrated that applying an *in-vivo* like, dynamic dose of the drug results in a significantly higher cell growth inhibition compared with conventional methods, where the maximum dose of the drug is applied to the cell culture.

Another advantage of the laminar flow regime is the lack of convective mixing, leading to highly predictable kinetics. This allows for mathematical models to be created at relatively low expense, providing microfluidics with an indispensable tool for optimization, simulation and modelling of LoC processes without the expense of the laboratory time. In the above mentioned study, Komen *et al.* used numerical simulation to estimate the exposure of HTC116 (colon carcinoma) cells to an anticancer drug in their microdevice [19]. Microfluidic simulations are discussed in more detail in Section 1.4.

2.1.1.2 Mass Transport

The mass transport of a fluid is described by the Péclet number (Pe) [40]:

$$Pe = \frac{uL}{D}, \tag{2.2}$$

where D is the diffusion coefficient. Similarly to the flow pattern, the mass transport is dictated by the dimensions of the system. In systems where the Péclet number is less than 1, transport is dominated by diffusion but, if the number is above 1, mixing is negligible. As mentioned above, a typical channel diameter and flow velocity in microfluidic devices is $L = 100\ \mu m$ and $u = 1$ cm s^{-1}, respectively. If water is flowed in the device ($D = 1 * 10^{-9}$ m^2 s^{-1}) this yields $Pe = 1000$. As a consequence, the mass transport in microfluidic devices is slow, leading to very predictable kinetics [8].

2.1.1.3 Surface Tension

Another important feature in microfluidic systems is the large surface-to-volume ratio. This is defined by the Bond (B_o) number that defines the ratio between the gravity force to the surface tension force [41]:

$$B_o = \frac{\Delta\rho g L^2}{\sigma}, \tag{2.3}$$

where σ is the surface tension, g is the gravitational acceleration, and $\Delta\rho$ is the difference in density between two immiscible fluids (gas-liquid, liquid-liquid). Assuming a typical value of the channel dimension in the microfluidic device of $L = 100\,\mu m$, density of oil and water mixture as $\rho_w = 999\,kg/m^3$ and $\rho_o = 920\,kg/m^3$, the surface tension $\sigma = 0.5\,N/m$, and $g = 9.8\,m/s^2$ the Bond number, $B_o = 0.0015 \ll 1$. Therefore, at the microscale, the gravitational force becomes insignificant and thus surface tension is the strongest and dominant force. This phenomenon is widely exploited in droplet microfluidics [42].

2.1.1.4 Capillary Forces

Due to the small channel dimension, gravitational forces are dominated by the capillary forces, which means that the fluid will flow without assistance or opposition of other forces [36].

2.1.1.5 Heat Transfer

The heat transfer is very efficient in microfluidic devices due to the high surface-to-volume ratio. This ensures an even heat distribution throughout the device and avoids the formation of local hot spots. In conventional macroscale reactors, exothermic reactions have to be performed at suboptimal conditions due to the potential hazards caused by thermal runaways. In contrast, microfluidic devices can maintain an isothermal condition throughout the device, significantly reducing the risk [43].

Polymerase chain reaction (PCR) tests require precise control over the sample temperature. During a PCR test, a DNA sample is amplified in three stages: denaturation, annealing and extension, during which the sample needs to be maintained at 90 – 97 °C, 50 – 60 °C and ~72 °C, respectively [44]. Easley *et al.* [45] demonstrated a microfluidic genetic analysis system that generates a genetic profile from a crude blood sample. The microdevice comprised three functional domains: nucleic acid purification, amplification of target sequence by PCR and amplicon separation. Lastly, the sample was detected by microchip electrophoresis. Apart from reducing the volume of the sample required to perform the test to only 4 μL, this microfluidic implementation also reduced the time required to run the test to <30 minutes, which is a dramatic improvement over conventional culturing methods that have a turnaround time of 24 - 48 hours.

2.1.1.6 Mixing time

The mixing time (t_m) can be defined as the square of the diffusion distance (x) divided by the molecular diffusivity (D) [46]:

$$t_m = \frac{x^2}{D}. \tag{2.4}$$

Therefore, it is evident that a smaller channel dimension results in faster mixing. This revelation has governed the development of micromixers where the stream is split into several lamelle to reduce the diffusion distance. Such micromixers include Y- and T-shaped micromixers [47–50], and split- and recombine micromixers [51, 52].

2.1.2 Materials and Applications

The first Lab-on-a-Chip platform was reported by Terry *et al.* in 1979 who demonstrated that sample injection, separation and detection for gas chromatography can be performed on a single 5 cm silicon wafer [53]. In this study, the device was made of silicon using photolithography and chemical etching and it included a sample injection valve and a 1.5 m long separator column. A thermal conductivity detector was clamped at the tip of the capillary. This resulted in a gas chromatograph capable of separating simple gas mixtures in seconds and enabled size reduction by 3 orders of magnitude compared with conventional lab equipment. Volumes as small as 1 nL could be injected into the capillary, greatly lowering the reagent consumption. Additionally, since the cross-sectional area of the separator column was reduced, which resulted in increased performance. Following this invention in the 1980s, technological advances were made to manufacture microvalves [6–8] and micropumps [9, 10, 8] for precise fluid manipulation at the small scale. 3D printing also emerged as a cost effective approach to fabricate bespoke parts, replacing costly and specialist equipment. However, this technique was not popularised until later date [54].

In 1990 Manz *et al.* reported a 5 × 5 mm chip manufactured from silicon wafers that contained a $6\,\mu\mathrm{m} \times 2\,\mu\mathrm{m} \times 15\,\mathrm{cm}$ open-tubular column and a detector which connected to an external HPLC pump and valves. This enabled high pressure liquid chromatography to be performed with a sample detection volume of 1.2 pL and a total volume of 1.5 nL [55]. Another major advance brought about by microfluidics was the development of capillary electrophoresis (CE) that performed DNA sequencing 3 times faster and provided better resolution than slab gel electrophoresis, which was the standard technology at the time [56]. At the same time, the concept of a "miniaturized Total Analysis System" (μTAS) that would encompass all functionality required for analysis i.e. sample injection, preparation, transport, chemical reaction, separation and detection was coined by Manz *et al.* [11]. In this seminal paper, it was recognized that microfluidic instrumentation offers the potential for automation, parallelization and improvement in the performance of analytical devices going beyond simply reducing their size.

Increasing demand for portable analysis tools with high sensitivity and resolution for molecular analysis, biodefence, and molecular biology drove innovation in mirofluidics [5]. The primary chip material used in the early years of microfluidics was silicon, which is costly, brittle and opaque to visible and ultraviolet light. Therefore, the most commonly used optical detection methods could not be integrated. An additional disadvantage of silicon chips is that the bonding procedure requires clean room facilities and significant expertise [57].

Glass is an alternative material for chip manufacture as it is transparent thus optical biosensors can be incorporated. Development in photolithography allowed fabrication of CE arrays on a single glass chip to further speed up the sequencing procedures while maintaining very economic use of reagents [58–60]. However, glass is also brittle, requires clean-room facilities and complex bonding protocols to manufacture the devices. Additionally, increasing demand for complexity of the devices required incorporation of valves and pumps within the chip design, which is easier when utilising flexible organic materials such as elastomers, plastics or paper. These materials offer the advantage of simpler and faster manufacturing procedures, easy surface modification and biocompatibility; therefore lowering the barrier to entry for microfluidic research.

Elastomers are weakly cross-linked polymers that can be deformed under application of force and will return to their original shape when these forces are removed. Whitesides and co-workers introduced polydimethylsiloxane (PDMS) as an alternative material for chip manufacture in 1995 [61] and to date it is one of the most widely used materials for chip fabrication in research [62, 63]. The vast popularity of the material is due to the straightforward fabrication process that employs soft lithography, which does not require clean room facilities. A device is manufactured by pouring a mixture of the polymer and a curing base into a master mould. The release from the mould is a simple process and devices with channel dimensions below 1 μm can be obtained [8]. Obtaining the master mould is the main hurdle as these are made from silicon wafers using conventional photolithography techniques. However, techniques to manufacture master moulds from cheaper thermoplastics such as poly(methyl methacrylate) (PMMA) and polycarbonate (PC) have been introduced. PDMS is biocompatible with most cell lines and permeable to gas and vapour therefore, unlike glass or silicon, it can support long term biological culture [64]. It is optically transparent, can be bonded to itself or other materials, and its durability is on par with glass and silicon [62, 63]. The inherent flexibility of the material allows a large number of pumps and valves (as many as 1 million per square centimeter) to be incorporated, which enables automated, high-throughput screening [65]. As a result, PDMS devices have been used in biological assays [63], genomics [66], chemical reactions [8], and biochemical detection [67]. Perhaps the most important application of PDMS is its use in biological cell culture. Apart from simply substituting Petri dishes and flasks used in conventional cell cultures with a more compact and cost-effective alternative, microfluidic technology allows the precise control over a cell culture environment in a repeatable manner. This is a vital advantage in biological research, where manipulation of the local or systemic environments is necessary to study cellular processes and functions. This was demonstrated by Luni *et al.* [68] who showed a 50-fold increase in the efficiency of reprogramming human somatic cells to induced pluripotent stem cells using microfluidic devices due to the improved spatio-temporal control at the microscale.

Operating at a a smaller volume also allows the use of fewer cells down to single cells analysis [69]. On the other end of the scale, Organ-on-a-Chip (OoC) devices can be used to mimic the *in vivo* environment of an organ. A carefully designed channel network is used for perfusion which simulates vascularity [70]. OoCs allow regulation of the concentration gradients, shear force, cell patterning, tissue boundaries and tissue-organ interactions. Huh *et al.* [71] reported a device capable of mimicking the structure and functionality of a human lung. The lung-on-a-chip was made of two channels separated by a 10μm PDMS membrane. One channel was lined with extracellular matrix (ECM) and alveolar epithelial cells and the second channel contained human pulmonary microvascular endothelial cells. The channels were filled with air and culture medium respectively, to mimic the lung environment. To simulate the characteristic movement of lungs, the device was connected to a vacuum. Application of the vacuum led to contraction of PDMS and when it was released, the chip returned to its original shape thus mimicking lung contraction and expansion. This device was used to replicate the immune response by introducing inflammatory mediators into the culture medium. Such models are extremely valuable for rapid drug screening. Si *et al.* [13] used lung-on-a-chip technology to examine antimalariar drugs as inhibitors of SARS-CoV-2 infection. The team identified amodiaquine as a robust inhibitor of the infection. Other organs such as liver [72, 73], kidney [74], heart [75], skin[76], gut [77–80] and brain [81] have been used for disease modelling, drug screening, toxicity testing, to study pathophysiology, and other medical applications. OoC platforms can be modular allowing multiple OoCs to be combined with the aim to create Human-on-a-Chip as shown in Fig. 2.2, which can be used to imitate the normal or a pathological state of human physiology [82, 83].

Although it has many advantages, PDMS comes with some major disadvantages. Its hydrophobic nature leads to adsorption of hydrophobic molecules [8]. Another issue is its incompatibility with most organic solvents, resulting in swelling and even

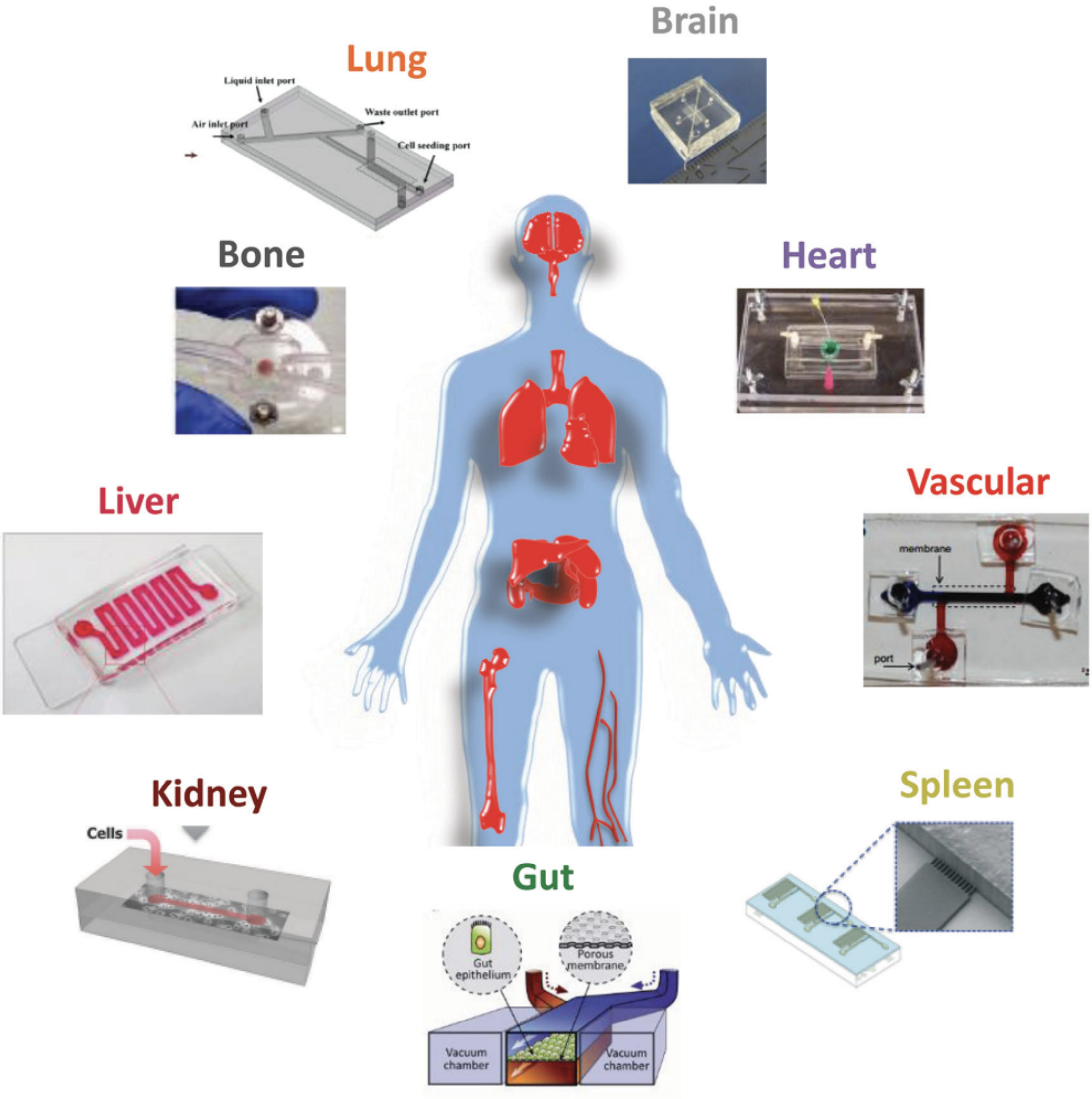

Figure 2.2: Human-on-a-Chip: Integrating multiple Organ-on-a-Chip systems to replicate the normal or pathological state of human physiology. Image taken from Ref. [70].

adsorption of some molecules [62]. PDMS is expensive to produce on a mass-scale which hinders its commercial applications.

Owing to better chemical resistance, gas-impermeability and greater rigidity compared to PDMS, plastics such as PMMA, PC, polystyrene (PS), Teflon, and polytetrafluoroethylene (PTFE) are commonly used for microfluidic applications [62] and are also preferred for mass-scale production [84]. Initially, plastics were disfavoured as thermo-processing procedures were required for device fabrication. However, development of priecise milling and laser cutting technologies enabled rapid prototyping from PMMA [85, 86] and PTFE [87], and allowed efficient manufacturing of sophisticated devices. For instance, Cho and co-workers [88] reported a microfluidic disk capable of performing enzyme-linked immunosorbent assay (ELISA) from 200 μL of crude samples such as blood or saliva in 20 minutes. The device contained six reaction chambers interlinked with fluidic channels and laser irradiated ferrowax microvalves, which are open and closed using laser irradiation. Sample chambers were filled with three different types of ELISA beads modified for: (i) cardiovascular disease biomarkers, (ii) the positive control, and (iii) unknown samples. The crude sample injected into the device was firstly separated by centrifugation and the plasma was mixed with immunoreagents before transferring to the reaction chambers. Once the binding reaction was complete, the beads were washed with a buffer solution to remove residues and the substrate solution was injected into the reaction chambers. The presence of a biomarker was detected by absorbance measurement using a photodiode and a light-emitting diode. The performance of this assay was comparable with conventional ELISA assays [88]. Other ELISA based assays in microfluidic devices allow detection of infectious diseases such as HIV and syphilis using as little as 1 μL of blood [89, 64].

Chemical synthesis in LoC devices remains a challenge as most common organic solvents are not compatible with plastics however, material such are PTFE or glass can be utilised when this is an issue [90].

Another material commonly used in microfludics is hydrogel. It is composed of water-insoluble, cross-linked polymers that can retain a large volume of water. Some hydrogels can shrink or swell in response to stimuli such as pH, light, magnetic or electric field [91]. They are biocompatible, porous and can be used as structural support for a cell culture within a secured environment in the form of a 3D ECM [92]. Shim *et al.* [93] reported a gut-on-a-chip platform where collagen was used a scaffold for human colon carcinoma cell line (Caco-2) and introduced fluidic shear to mimic absorption in human intestines. In their study, the 3D cell culture was compared with a standard 2D monolayer cell culture. The morphology of cells in OoC was found to be prismatic, which resembles gut morphology, while the monolayer culture was flat.

Additionally, the metabolic activity of 3D cell culture was enhanced compared with the 2D cell culture.

Manufactured from cellulose fibers, paper microfluidic devices are a highly porous and hydrophilic [94, 95]. Paper-based microfluidic analytical devices (μPADs) are functionalised by introducing hydrophobic barriers which guide the sample towards detection zones containing a desired receptor [96]. The hydrophilic nature and high porosity of paper increases passive transport of liquids and its white colour makes it particularly suited for colorimetric assays [62]. μPAD has been used to measure markers of liver function from a sample of blood taken from a finger-prick test. The device was used for sample preparation, where red blood cells were filtered out and the resulting plasma distributed to three detection zones for a colorimetric assay. The results were digitised using a mobile device, and subsequently incinerated for an easy disposal [97, 98]. This work demonstrated that comprehensive assays can be run on a paper-based device and produce semi-quantitative results which can feed into clinical decision making. Vasantham *et al.* [99] demonstrated that a paper-based microdevice can be used to detect cardiac troponin I using an electrochemical immunoassay in $\sim$1 minute with detection limit of 0.05 ng/mL. μPADs are of particular interest for point-of-care diagnostics because they can be rapidly manufactured using a printer and even complex patterns can be easily transferred. They are easy to handle, non-toxic and biodegradable [100].

Integration of analytical techniques with LoC devices is an integral requirement as all LoC systems must provide information on samples under the investigation. One of the common ways to study biological systems at the macroscale is to remove aliquots of the culture media for analysis. Such approach is not usually possible at the microscale as the sample is volume limited. Instead, detection methods based on mechanical [101–104] and electrochemical [105–107] detection, liquid chromatography-mass spectrometry [108], as well as Raman [109, 110], fluorescent [111, 112], UV-Visible [113, 114] and NMR spectroscopy [115, 116] have been incorporated with LoC devices [21]. In the following section these common detection methods are discussed.

2.1.3 Detection Methods

Mechanical detection methods measure the changes in either the static deflection or the resonant frequency of a cantilever sensor. In both cases one side of the sensor is functionalised and once an analyte binds to the sensor the change in the surface stress or frequency shift is measured [117]. This detection is highly sensitive as attograms of analyte can be detected. The shape and size of the sensor can be easily tunable using standard photolithography methods but fabrication is complex and requires clean-room facilities. Surface functionalisation of the sensors allows label free detection however, detection usually requires relatively long wait times of ∼30 mins.

Integrating electrodes with LoC devices enables electrochemical detection where the interaction of chemical species with the electrodes is quantified. A current is passed between the electrodes and the change in conductance, resistance and/or capacitance is measured at the surface of the electrodes [117]. This method allows real-time detection, is low cost and its sensitivity falls in the mM range. Additionally, it can be easily incorporated with LoC and has low power requirements, which makes it an attractive solution. However, the detection is influenced by changes in pH, ion concentrations, has a short shelf life, and is very invasive [21].

Fluorescence spectroscopy is amongst the most common detection methods used in microfluidic devices due to its high sensitivity (∼nM), reproducibility, and biocompatibility for use *in vivo* studies. As a result, labelling protocols for proteomics and genomics studies are well established [112]. After tagging the target molecule, a typical set up requires a light source to induce fluorescence, which is achieved using a laser and a detector with a set of focusing lenses. Additionally, appropriate filters are used to reduce the background noise [118, 119]. Implementing fluorescence spectroscopy with LoC found many applications including monitoring processes such as heart- and liver-on-chip models [120], portable diagnostics [121] as well as biosensors [122]. A disadvantage of this method is that it is highly specific because distinct fluorescent tags are required. More over, fluorophores are often ruthenium based dyes that can be toxic to biological cultures [123] [21].

UV-Visible spectroscopy requires simple and low cost equipment as this technique relies on measuring absorption of specific wavelength of light induced by electronic transitions. Minimal sample preparation is required to yield a quantitative measurement and this method is frequently used to follow the progress of a reaction in LoC [124]. However, the solvent needs to be carefully chosen as to not cause an overlap with peaks resulting from the compound of interest. Overall, this method is not highly specific for different compounds and results in a significant peak overlap, which is the main limitation.

Raman spectroscopy provides information about the vibrational modes on a target molecule through observing upward or downward shifts of scattered light. This technique enables real-time detection with minimal sample preparation. Shanmukth *et al.* [125] used a variation of Raman spectroscopy namely surface-enhanced resonance Raman scattering to uniquely identify different respiratory viruses without using any labels or probes. The disadvantages of Raman spectroscopy lies in the fact that the Raman effect is weak (limit of detection 1 μM in solution [126]) and thus highly optimised equipment is required leading to high instrumentation cost. Additionally, the material used for microfluidic devices must be transparent to light.

Nuclear Magnetic Resonance (NMR) spectroscopy is an ideal tool to follow chemical and biochemical processes in microfluidic LoC devices due to its non-invasive properties and its generality and chemical specificity. NMR is quantitative and requires very little sample preparation. Despite of this NMR is rarely used with LoC due to the high instrumentation cost and limited sensitivity. The sensitivity issue can be overcome by integrating hyperpolarization methods that enable to boost the sensitivity by 5 orders of magnitude. The following section introduces the fundamentals of NMR spectroscopy to lie the foundations for understanding how the sensitivity issue can be overcome in NMR.

2.2 Microfluidic NMR

2.2.1 Fundamentals of NMR

2.2.1.1 Nuclear Spin

Spin is an intrinsic property of nuclei that can be represented by the following operators along the three Cartesian axis: $\hat{I}_z$, $\hat{I}_y$, and $\hat{I}_x$.

When an operator $\hat{A}$ acts on one of its eigenstates $|\psi\rangle$ it returns the same state multiplied by an eigenvalue as follows [127]:

$$\hat{A}\,|\psi\rangle = a\,|\psi\rangle\,, \tag{2.5}$$

where a is an eigenvalue of $|\psi\rangle$ in the operator basis of A. The number of eigenvalues depends on the nucleus in question, which is described by the nuclear spin angular momentum quantum number I. The quantum number I can possess integer $(1, 2, \dots)$ or half-integer $(\frac{1}{2}, \frac{3}{2}, \dots)$ values. The operator $\hat{I}_z$ has $(2I + 1)$ eigenstates, which may be labelled m_I that can adopt values ranging from $-I$ to $+I$ in integer steps.

A spin state is denoted as $|I, m_I\rangle$ [128] and the $\hat{I}_z$ operator acts in the following way:

$$\hat{I}_z\,|I, m_I\rangle = m_I\,|I, m_I\rangle\,, \tag{2.6}$$

The expectation value of an operator $\left\langle \hat{A} \right\rangle$ can be found using the following operation:

$$\left\langle \hat{A} \right\rangle = \langle\psi|\hat{A}|\psi\rangle = a\,\langle\psi|\psi\rangle = a, \tag{2.7}$$

thus the eigenvalue is obtained.

The commutation between two operators $\hat{A}$ and $\hat{B}$ is an important property in NMR as it dictates the rotation of spins:

$$[\hat{A}, \hat{B}] = \hat{A}\hat{B} - \hat{B}\hat{A}. \tag{2.8}$$

If the two operators commute $[\hat{A}, \hat{B}] = 0$. The three Cartesian operators obey the following cyclic commutation rules in units of the reduced Planck's constant ($\hbar$):

$$\begin{aligned} [\hat{I}_x, \hat{I}_y] &= i\hat{I}_z, \\ [\hat{I}_z, \hat{I}_x] &= i\hat{I}_y, \\ [\hat{I}_y, \hat{I}_z] &= i\hat{I}_x. \end{aligned} \tag{2.9}$$

The total square angular momentum operator, $\hat{I}^2$, can be defined as follows:

$$\hat{I}^2 = \hat{I}_x^2 + \hat{I}_y^2 + \hat{I}_z^2. \tag{2.10}$$

$\hat{I}^2$ commutes with the spin angular momentum operators in the following way:

$$\begin{aligned} [\hat{I}^2, \hat{I}_x] &= 0, \\ [\hat{I}^2, \hat{I}_y] &= 0, \\ [\hat{I}^2, \hat{I}_z] &= 0. \end{aligned} \tag{2.11}$$

The total square angular momentum operator acts according to the following:

$$\hat{I}^2 \left| I, m_I \right\rangle = I(I+1) \left| I, m_I \right\rangle. \tag{2.12}$$

The simplest spin system in NMR is the case of an isolated spin $-\ 1/2$ nucleus. When placed in a magnetic field it has two eigenstates of angular momentum along the $z-$axis also referred to as the Zeeman basis:

$$\begin{aligned} \left| \frac{1}{2}, +\frac{1}{2} \right\rangle &= \left| \alpha \right\rangle, \\ \left| \frac{1}{2}, -\frac{1}{2} \right\rangle &= \left| \beta \right\rangle. \end{aligned} \tag{2.13}$$

If the $\hat{I}_z$ operator acts on the $|\alpha\rangle$ and $|\beta\rangle$ it yields:

$$\begin{aligned}\hat{I}_z\,|\alpha\rangle &= +\frac{1}{2}\,|\alpha\rangle\,,\\ \hat{I}_z\,|\beta\rangle &= -\frac{1}{2}\,|\beta\rangle\,,\end{aligned} \tag{2.14}$$

therefore, indicating polarization of the $|\alpha\rangle$ and $|\beta\rangle$ states along the $z-$axis with an associated eigenvalue of $\pm\frac{1}{2}$.

The state $|\psi\rangle$ of a spin $-\ 1/2$ particle is not restricted to only $|\alpha\rangle$ and $|\beta\rangle$ but can be in a superposition state of these two eigenstates:

$$|\psi\rangle = c_1\,|\alpha\rangle + c_2\,|\beta\rangle\,, \tag{2.15}$$

where c_1 and c_2 are the superposition coefficients. $|\psi\rangle$ can be expressed as a column vector:

$$|\psi\rangle = \begin{pmatrix} c_1 \\ c_2 \end{pmatrix}. \tag{2.16}$$

Taking the complex conjugate of kets yields bras, which can be represented as a row vector:

$$\langle\psi| = |\psi\rangle^{\dagger} = \begin{pmatrix} c_1^* & c_2^* \end{pmatrix}. \tag{2.17}$$

The states are normalised such that $|c_1|^2 + |c_2|^2 = 1$.

Following this notation the Zeeman basis can be written as the following:

$$|\alpha\rangle = \begin{pmatrix} 1 \\ 0 \end{pmatrix} \qquad \text{and} \qquad |\beta\rangle = \begin{pmatrix} 0 \\ 1 \end{pmatrix}. \tag{2.18}$$

An important property of the basis state is that they are orthonormal giving the Kronecker delta (δ_{mn}):

$$\langle m|n\rangle = \delta_{mn} = \begin{cases} 1, & \text{if m = n,} \\ \\ 0, & \text{otherwise,} \end{cases} \tag{2.19}$$

where $\langle m|n\rangle = \delta_{mn}$ symbolises taking the dot product of $|m\rangle$ and $|n\rangle$.

A second spin (I_2) can be introduced by taking the Kronecker product of the basis states as follows:

$$\begin{aligned} |\alpha\alpha\rangle = |\alpha\rangle \otimes |\alpha\rangle = \begin{pmatrix} 1 \\ 0 \\ 0 \\ 0 \end{pmatrix} \qquad |\alpha\beta\rangle = |\alpha\rangle \otimes |\beta\rangle = \begin{pmatrix} 0 \\ 1 \\ 0 \\ 0 \end{pmatrix}, \\ |\beta\alpha\rangle = |\beta\rangle \otimes |\alpha\rangle = \begin{pmatrix} 0 \\ 0 \\ 1 \\ 0 \end{pmatrix} \qquad |\beta\beta\rangle = |\beta\rangle \otimes |\beta\rangle = \begin{pmatrix} 0 \\ 0 \\ 0 \\ 1 \end{pmatrix}. \end{aligned} \tag{2.20}$$

2.2.1.2 The Density Operator

An average NMR sample contains $\sim 10^{22}$ spins [127] therefore, it is more convenient to define a density operator which refers to an ensemble average rather than individual spins.

Considering the case of an isolated $spin - 1/2$ particle in a magnetic field, recalling Eq. 2.16 and 2.17:

$$|\psi\rangle = \begin{pmatrix} c_1 \\ c_2 \end{pmatrix} = c_1 |\alpha\rangle + c_2 |\beta\rangle ,$$

$$\langle\psi| = \begin{pmatrix} c_1^* & c_2^* \end{pmatrix} = c_1^* \langle\alpha| + c_2^* \langle\beta| .$$

The density operator ($|\psi\rangle\langle\psi|$) can be defined as [127]:

$$|\psi\rangle\langle\psi| = \begin{pmatrix} c_1 \\ c_2 \end{pmatrix} \begin{pmatrix} c_1^* & c_2^* \end{pmatrix} = \begin{pmatrix} c_1 c_1^* & c_1 c_2^* \\ c_2 c_1^* & c_2 c_2^* \end{pmatrix}. \tag{2.21}$$

The expectation value of an operator $\hat{A}$ can be extracted using the following formula:

$$\left\langle \hat{A} \right\rangle = Tr\{|\psi\rangle\langle\psi|\, \hat{A}\}. \tag{2.22}$$

The advantage of introducing the density operator is the fact that it can be used to represent an ensemble of spins. Therefore expression 2.22 can be expanded to include $\mathbb{N}$ spins by defining the average expectation value A_{obs}:

$$A_{obs} = Tr\{\mathbb{N}^{-1}(|\psi_1\rangle\langle\psi_1| + |\psi_2\rangle\langle\psi_2| + \dots)\hat{A}\}, \tag{2.23}$$

where the subscript labels individual spins of the ensemble. For brevity, an ensemble average density operator ($\hat{\rho}$) can be defined:

$$\begin{aligned} \hat{\rho} &= \mathbb{N}^{-1}(|\psi_1\rangle\langle\psi_1| + |\psi_2\rangle\langle\psi_2| + \dots) \\ &= \overline{|\psi\rangle\langle\psi|}, \end{aligned} \tag{2.24}$$

where the overline indicates an average. $\hat{\rho}$ expressed in a matrix form yields:

$$\hat{\rho} = \begin{pmatrix} \overline{c_1 c_1^*} & \overline{c_1 c_2^*} \\ \overline{c_2 c_1^*} & \overline{c_2 c_2^*} \end{pmatrix} = \begin{pmatrix} \rho_\alpha & \rho_+ \\ \rho_- & \rho_\beta \end{pmatrix}. \tag{2.25}$$

The ρ_α and ρ_β elements represent the populations of a state, while the off-diagonal elements ρ_+ and ρ_- represent the coherences between the states. The sum of populations is always equal to one, only the population difference carries a physical significance as it indicates the net longitudinal spin polarization i.e. along the external magnetic field. Coherences represent a partial alignment of spins, which results in the transverse spin magnetization i.e. net spin polarization that is perpendicular to the external field [127].

In thermal equilibrium, the population of the energy states is dictated by the Boltzmann distribution:

$$\frac{\rho_\beta}{\rho_\alpha} = e^{\frac{-\Delta E}{k_B T}}, \tag{2.26}$$

where ΔE is the difference between the two energy levels, $k_B = 1.38066 \times 10^{-23}\,\mathrm{J\,K^{-1}}$ is the Boltzmann constant, and T is the temperature. The thermal energy that is available at room temperature is is $k_B T \cong 4.1 \times 10^{-21} J$. Assuming B_0 field of 14.7 T , the difference between ρ_α and ρ_β states is $3.3 \times 10^{-25} J$. Therefore, the thermal energy is four orders of magnitude larger than the energy difference of the Zeemann eigenstates.

The nuclear spin polarization (P_I) in an ensemble of spin $-$ 1/2 nuclei is given by:

$$P_I = \frac{\rho_\alpha - \rho_\beta}{\rho_\alpha + \rho_\beta} = \tanh(\frac{\hbar \gamma B_0}{2 k_B T}), \tag{2.27}$$

where $\hbar$ is the reduced Planck's constant, B_0 is the magnetic field strength, and γ is the gyromagnetic ratio.

Analysing Eq. 2.27, it becomes clear that the sensitivity of an NMR experiment can be improved by: (i) increasing the gyromagnetic ratio, (ii) cooling the sample, or (iii) increasing the B_0. Alternatively, hyperpolarization methods can be utilised, which create a non-equilibrium magnetization state that allows the signal intensity to be increased by several orders of magnitude. These methods are discussed in detail in later chapters.

2.2.1.3 The Hamiltonian Operator

The Hamiltonian operator ($\hat{\mathcal{H}}$) is a key concept in NMR as it contains information about all interactions of a spin system. A Hamiltonian acting on an eigenstate, yields the energy level of that state:

$$\hat{\mathcal{H}} \left|\psi\right\rangle = E \left|\psi\right\rangle, \tag{2.28}$$

For convenience, it is customary to define the Hamiltonian in units of $\hbar$, commonly referred to as the natural units:

$$\hat{H} = \hbar^{-1}\hat{\mathcal{H}}. \tag{2.29}$$

Returning to the case of an isolated spin $-$ 1/2 nucleus, the eigenstates of the $\hat{I}_z$ operator are given by Eq. 2.14:

$$\hat{I}_z \left|\alpha\right\rangle = +\frac{1}{2} \left|\alpha\right\rangle \qquad \hat{I}_z \left|\beta\right\rangle = -\frac{1}{2} \left|\beta\right\rangle.$$

Thus the Hamiltonian in the Zeeman basis can be written as:

$$\hat{H} \left|\alpha\right\rangle = +\frac{1}{2}\omega_0 \left|\alpha\right\rangle \qquad \hat{H} \left|\beta\right\rangle = -\frac{1}{2}\omega_0 \left|\beta\right\rangle, \tag{2.30}$$

where ω_0 is the Larmor frequency i.e. the frequency of spin precession (rotation) around the axis of the external magnetic field, which is defined as:

$$\omega_0 = -\gamma_j B_0, \tag{2.31}$$

where γ_j is the gyromagnetic ratio of a nucleus j.

2.2.1.4 Chemical Shift

Since electrons are charged particles, when a strong magnetic field is applied, they generate a small field at the nucleus. As a result, the field experienced by the nucleus is a sum of the applied and the induced fields leading to a shift in the Larmor frequency, commonly referred to as the *chemical shift* (σ). Therefore the Larmor formula from Eq.2.31 becomes:

$$\omega = -\gamma_j B_0(1 - \sigma) \tag{2.32}$$

The magnitude of the chemical shift is dictated by the size of the induced field as well as by the orientation of the molecules with respect to the applied field. Due to the rapid molecular tumbling in liquid samples, the nuclei experience an average local field thus an average chemical shift referred to as the isotropic shift [127].

The Hamiltonian for a pair of isolated spin $-$ 1/2 nuclei, where $\omega_1 \neq \omega_2$ can be written as:

$$\hat{H} = \omega_1 \hat{I}_{1z} + \omega_2 \hat{I}_{2z}, \tag{2.33}$$

where ω_1 and ω_2 are the chemical shifts of spin $\hat{I}_{1z}$ and $\hat{I}_{2z}$, respectively.

2.2.1.5 J – Coupling

In real samples, nuclei are not isolated but interact with each other through electrons present in the chemical bonds connecting the nuclei. The interaction is referred to as the *$J-$coupling* or the *scalar coupling.* The $J-$ coupling is independent of the field and because the effect is mediated by the chemical bonds, the magnitude of $J-$ coupling falls off rapidly with the increasing number of intervening bonds. This is an important property as it provides information on the connectivity between nuclei and it is widely used in chemical structure elucidation. The Hamiltonian for a $J-$ coupled two-spin system ($\hat{I}_1$ and $\hat{I}_2$) can be expressed as:

$$\hat{H} = \omega_1 \hat{I}_1 + \omega_2 \hat{I}_2 + 2\pi J_{12} \boldsymbol{\hat{I}_1 \hat{I}_2}, \tag{2.34}$$

where J_{12} is the J-coupling constant and $\boldsymbol{\hat{I}_1 \hat{I}_2} = \hat{I}_{1x}\hat{I}_{2x} + \hat{I}_{1y}\hat{I}_{2y} + \hat{I}_{1z}\hat{I}_{2z}$. For systems where $|\omega_1 - \omega_2| \gg |2\pi J|$, Eq. 2.34 can be simplified to:

$$\hat{H} = \omega_1 \hat{I}_{1z} + \omega_2 \hat{I}_{2z} + 2\pi J_{12} \hat{I}_{1z}\hat{I}_{2z}. \tag{2.35}$$

This is referred to as the weak coupling approximation. The Hamiltonian from Eq. 2.35 in the Zeeman basis can be shown as a matrix:

$$\hat{H} = \frac{1}{2}\begin{pmatrix} \pi J + \omega_1 + \omega_2 & 0 & 0 & 0 \\ 0 & -\pi J + \omega_1 - \omega_2 & 0 & 0 \\ 0 & 0 & -\pi J - \omega_1 + \omega_2 & 0 \\ 0 & 0 & 0 & \pi J - \omega_1 - \omega_2 \end{pmatrix}. \tag{2.36}$$

2.2.1.6 Evolution of the Density Operator

The evolution of the density operator is described by the Liouville von Neumann equation:

$$\frac{\partial}{\partial t}\hat{\rho} = -i[\hat{H}, \hat{\rho}]. \tag{2.37}$$

The time-dependent solution of Eq. 2.37 is [127]:

$$\hat{\rho}(t) = \exp\left\{-i\hat{H}t\right\}\hat{\rho}(0)\exp\left\{+i\hat{H}t\right\} \tag{2.38}$$

For the simplest example of an isolated spin $-1/2$ sytem, the Hamiltonian given by: $\hat{H} = \omega\hat{I}_z$. If the density operator commutes with the Hamiltonian ($[\hat{H}, \hat{\rho}] = 0$) there's no evolution of the system. This can be shown for $\hat{\rho}(0) = \hat{I}_z$ as following:

$$\hat{\rho}(t) = \exp\left\{-i\hat{I}_z t\right\}\hat{I}_z\exp\left\{+i\hat{I}_z t\right\} = \hat{I}_z \tag{2.39}$$

However, if the density operator does not commutes with the Hamiltonian ($[\hat{H}, \hat{\rho}] \neq 0$), the outcome is different. For example if $\hat{H} = \omega\hat{I}_z$ and $\hat{\rho}(0) = \hat{I}_x$ then the density evolves as follows:

$$\hat{\rho(t)} = \exp\left\{-i\hat{I}_x t\right\}\hat{I}_z\exp\left\{+i\hat{I}_x t\right\} = \cos{(\omega t)}\hat{I}_z + \sin{(\omega t)}\hat{I}_y. \tag{2.40}$$

2.2.1.7 NMR Experiment

Upon placing a sample in a static magnetic field (B_0), the nuclear magnetic moments tend to align with the B_0 field. The nuclear magnetic moment can align with the B_0 field in $2I+1$ ways. Therefore, for a spin $-1/2$ nucleus i.e. $I=1/2$, there are two possible orientations, opposing or reinforcing the magnetic field. The overall density of the magnetic moments over the entire volume of a sample gives rise to net magnetization (M). The magnitude of the net magnetization for spin I is given by [129]:

$$M = N\frac{\gamma^2 B_0 \hbar^2 I(I+1)}{3k_B T}, \tag{2.41}$$

where N is the nuclear spin density within a sample.

To detect an NMR signal, a current (commonly referred to as a pulse) is induced through a detection coil, which creates a magnetic field (B_1) that is perpendicular to the B_0 field and rotates the magnetization vector away from its equilibrium position. The angle (θ) describes the rotation of M away from its equilibrium orientation [130]:

$$\theta = \gamma B_1 \tau, \tag{2.42}$$

where τ is the duration of the pulse. Sometime after the application of a radiofrequency pulse, which rotates the magnetization into the $xy-$ plane. The following solutions to the Bloch equations describe the components of magnetization at time t after application of a pulse $\frac{\pi}{2}_x$ [127]:

$$\begin{aligned} M_x &= M_0 \sin(\omega_0 t)\exp\{-t/T_2\}, \\ M_y &= -M_0 \cos(\omega_0 t)\exp\{-t/T_2\}, \\ M_z &= M_{z,eq} - M_{z,eq}\exp\{-t/T_1\}, \end{aligned} \tag{2.43}$$

where $M_{z,eq}$ is the magnetization at equilibrium and M_0 is the magnetization immediately after a pulse, (T_2) is the transverse relaxation rate constant, and (T_1) is the longitudinal relaxation rate constant. T_2 characterises the time it takes for the spins to dephase in the $xy-$plane, while T_1 refers to the time it takes for the magnetization to return to the equilibrium condition.

A rotating magnetic field generates an electrical field and in the presence of a conductor, an electromotive force (emf) will be generated. The larger the B_0 field, the larger the ω_0 therefore the change in $\frac{\partial \mathbf{B}}{\partial t}$ is faster thus a larger emf is generated. The consequent voltage is the NMR signal commonly referred to as the free induction decay (FID). Since the voltage is weak, it firstly gets amplified by a preamplifier, which results in a signal that oscillates at a rate that is too high to convert it into a digital form. In order to convert the 'raw' NMR signal into a digital form, a reference frequency (ω_{ref}) is subtracted from the Larmor frequency to generate a signal of a lower frequency. The resulting signal is referred to as the relative Larmor frequency (Ω_0):

$$\Omega_0 = \omega_0 - \omega_{ref}. \tag{2.44}$$

This conversion is accomplished by a quadrature receiver, which outputs two signals one with a real and the second with an imaginary component. Lastly, analogue-to-digital converter digitizes the two signals. An NMR signal for a single frequency can be expressed as:

$$s(t) \sim \exp\left\{(i\Omega_0 - \frac{1}{T_2})t\right\}. \tag{2.45}$$

Since an NMR experiment contains many signals Eq. 2.45 can be generalized:

$$s(t) = \sum_l s_l(t), \tag{2.46}$$

and

$$s_l(t) = a_l \exp\{(i\Omega_l - T_{2,l})t\}, \tag{2.47}$$

where each signal (s_l) has an amplitude (a_l), frequency (Ω_l) and a transverse relaxation rate constant ($T_{2,l}$) associated with it.

The time domain signal is converted into the frequency domain signal using a Fourier transform (FT):

$$S(\Omega) = \int_0^\infty s(t) \exp\{-i\Omega t\} dt. \tag{2.48}$$

Converting the time domain signal into the frequency domain is hugely beneficial as individual signals appear as peaks in a spectrum.

Intensity of a peak (I_i) in an NMR spectrum is directly proportional to the number of nuclei (N_i) corresponding to that peak [131]:

$$I_i = K_s N_i, \tag{2.49}$$

where K_s is the spectrometer constant, which is consistent throughout an experiment for all resonances in a spectrum. K_s can be affected by non-uniform excitation pulse, too short repetition time or broad-band decopuling [131].

The concentration of a compound A (c_a) can be calculated from a spimle ratio given that a know concentration of a reference compound (c_{ref}) is present:

$$\frac{c_a}{c_{ref}} = \frac{I_a}{I_{ref}} \frac{N_{ref}}{N_a}, \tag{2.50}$$

where I_a and I_{ref} are signal intensities of compound A and the reference, respectively. N_a and N_{ref} are the number of nuclei responsible for the signal for respective compounds.

2.2.2 Sensitivity of NMR

Sensitivity and resolution are the two metrics that determine the performance of NMR. Resolution can be defined as the minimum distance necessary to distinguish two peaks in a spectrum, while sensitivity is the minimum number of spins required to detect the signal above the noise [132]. The line widths in an NMR spectrum are very narrow with full width at half maximum being sub $-$ 1 Hz [133], which corresponds to ~4 parts per billion on a 400 MHz spectrometer. Sensitivity on the other hand, depends on the

Nucleus	**Natural abundance** / %	**Spin** I	**Gromagnetic Ratio** / MHz T^{-1}	**Magnetization** / mA m^{-1} T^{-1}
^{1}H	99.98	1/2	42.5749	29.62
^{2}H	0.015	1	6.5357	1.861
^{11}B	80.42	3/2	13.6597	15.25
^{13}C	1.108	1/2	10.7050	1.873
^{19}F	100	1/2	40.0535	26.22
^{31}P	100	1/2	17.2348	4.854

Table 2.2: A comparison of the nuclear magnetization of 1M solutions at 20°C for nuclei commonly used in NMR. Values taken from [129].

number of spins that align with the external magnetic field, recalling Eq. 2.41 [129]:

$$M = N\frac{\gamma^2 B_0 \hbar^2 I(I+1)}{3k_B T}.$$

Table 2.2 lists the nuclear magnetization of 1M solutions at 20°C and the field of 1T for a few commonly detected nuclei in NMR. ^{1}H nuclei have a large gyromagnetic ratio and over 99% natural abundance hence yield a high signal intensity. Alongside being the highest sensitivity nucleus in NMR, protons are present in most organic molecules hence nearly every metabolite can be observed by ^{1}H NMR thus it is the most prevalent nucleus used in NMR based metabolomics [134]. Other nuclei such as ^{13}C, ^{31}P, ^{19}F are frequently observed alongside protons as they provide a broader signal dispersion in an NMR spectrum hence improved resolution.

2.2.2.1 Signal to Noise Ratio

The amplitude, a, of an NMR signal after the application of a 90^o pulse is defined as:

$$a = \frac{1}{4}\frac{B_1}{i_c}\gamma^3 \hbar^2 B_0^2 \frac{n_s}{k_B T}, \tag{2.51}$$

where the factor $\frac{B_1}{i_c}$ is the coil sensitivity, and n_s is the number of spins present in the sample. The signal amplitude can be improved by using a higher magnetic field. The current state of the art NMR spectrometer operate at a field of 23.5 T, which results in a population difference of 6×10^{-6}. Such small population difference is the core of sensitivity issues of NMR.

As discussed in section 2.2.1.7, detection of an NMR signal is achieved by placing a detection coil close to a sample, which detects a voltage induced by precessing spins.

The thermal motion of electrons and ions in the solution leads to an interference that is also registered by the coil. The signal-to-noise ratio (SNR) determines if an NMR signal can be detected above the spectral noise and it depends on the efficiency of the probe used to detect the signal. The probe efficiency (η_P) can be defined as [132]:

$$\eta_P = \frac{B_1}{\sqrt{P}} = \frac{B_1}{i_c\sqrt{R}}, \tag{2.52}$$

where P is the power, R is the resistance and i_c is the current amplitude. The SNR is defined as [135, 136]:

$$SNR = \frac{k_0 \frac{B_1}{i_c} V_s \omega_0 \frac{1}{\sqrt{2}} M}{F\sqrt{4k_B T R_{noise} \Delta f}}, \tag{2.53}$$

where k_0 is a factor that accounts for the B_1 field inhomogeneity V_s is the sample volume, ω_0 is the Larmor precession frequency, F is the noise factor of the spectrometer, T is the temperature of the coil, R_{noise} is the dissipative noise of the coil, circuit and sample, and Δf is the spectral bandwidth.

Employing the principle of reciprocity for coil sensitivity, introduced by Hoult and Richards [136], it was recognised that the SNR is proportional to the coil sensitivity. Therefore, expression 2.53 can be simplified by recognising that the B_1 is within 10% of the maximum value at the centre of the coil [137]:

$$SNR = C\frac{B_1 n_s}{i_c\sqrt{R\Delta f}}. \tag{2.54}$$

For ^{1}H at 600 MHz the constant C equals 1.4×10^{-11} in SI units ($B_0 = 14.1\,\mathrm{T}$, $T = 300\,\mathrm{K}$, $\gamma = 0.2675 \times 10^9 \mathrm{rad/T\,s}$, $I = 1/2$ and $F = 1$, insignificant noise from the spectrometer was assumed). Although η_P is a good predictor of SNR, the signal-to-noise ratio ultimately depends on the electrical resistance, the coil sensitivity $\frac{B_1}{i_c}$ and the number of spins present in the detection region of the coil, termed as the filing factor α_F:

$$\alpha_F = \frac{\int B_1^2 \hat{S}(\mathbf{r}) dV}{\int B_1^2 dV}, \tag{2.55}$$

where the function $\hat{S}$ is unity in the sample area, and zero elsewhere. For a long solenoid coil with the interior space filled with sample, one finds $\alpha_F = 1/2$. Most other designs have lower filling factors.

Micro-detectors benefit from favourable scaling of the SNR since reducing the size of the detector increases the filling factor and maximises and the coil sensitivity as the detector closely adheres to the sample. This can be demonstrated by taking a helical copper coil as an example. The RF current penetrates copper to a depth of $\delta = 2.7\,\mu$m (at room temperature and 600 MHz). The field at the centre[137]:

$$\frac{B_1}{i_c} = \frac{\mu_0}{\sqrt{l^2 + d^2}}, \tag{2.56}$$

where μ_0 is the vacuum permeability , l is the height of the cylinder and d is the diameter.

The resistance can be defined as [137]:

$$R = \rho\frac{\pi d}{l\delta}, \tag{2.57}$$

where ρ is the resistivity of copper. $d/l = 1$ results in the optimal coil sensitivity thus the SNR is:

$$SNR = 0.9 \times 10^{-16}\frac{n_s}{d\sqrt{\Delta f}}. \tag{2.58}$$

Therefore, for a given number of spins, the SNR scales with $1/d$ as predicted by Hoult and Richards [136]. However, as the volume of the detector is reduced the number of spins present in the sample is reduced. This has a detrimental effect on the concentration limit of detection (cLOD) and will be discussed further in the following section.

2.2.2.2 Signal Averaging

The spectrum obtained from an NMR experiment is composed of the signal obtained from the sample as well as the thermal noise. Signals originating from the sample

(s_{NMR}) are reproducible hence can be added [127]:

$$s_{NMR}(1+2) = s_{NMR}(1) + s_{NMR}(2) = 2s_{NMR}(1). \tag{2.59}$$

On the other hand, the noise is random and proportional to the square root of the number of experiments ($\sqrt{N}$).

Signal averaging is a straightforward technique to improve the sensitivity however, an experiment needs to be carefully designed. This is because the system needs to return to its thermal equilibrium before another spectrum can be acquired therefore individual transients need to be separated by intervals that are multiples of T_1, which are often of the order of several seconds. This results in very long acquisition times, which is the main drawback of this approach.

2.2.2.3 Limit of Detection and Microdetectors

Sensitivity can be quantified in terms of the mass limit of detection (nLOD), which formally is defined as the number of spins that have to resonate per square root of bandwidth ($\sqrt{\Delta f}$) to yield a signal to noise ratio of three [132]:

$$nLOD_t = \frac{3n_s}{SNR_t\sqrt{\Delta f}}, \tag{2.60}$$

where n_s is the number of moles present in the sample, and SNR_t is the signal-to-noise ratio in the time domain. In the frequency domain the limit of detection can be expressed as:

$$nLOD_\omega = \frac{3n_s\sqrt{\Delta t}}{SNR_\omega}, \tag{2.61}$$

where Δt is the acquisition time for a single scan, and SNR_ω is the signal-to-noise ratio in the frequency domain. Since the signal quality increases as the square root of the measurement time the nLOD is measured in units of mol $\sqrt{\text{s}}$.

A conventional NMR probe is inadequate to detect micro scale samples. To enhance the sensitivity at this scale, specialised probes have been developed, where the detection region of the probe closely conforms to the sample chamber. The common coil geometries are illustrated in Fig. 2.3.

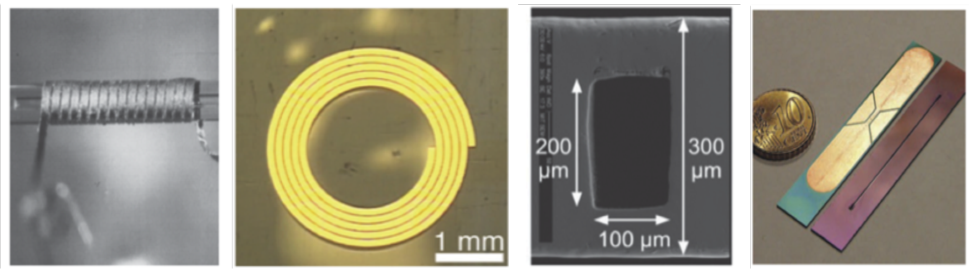

(A) Solenoid (B) Planar (C) Microslot (D) Stripline

(E) Transmission Line Probe

FIGURE 2.3: Images of different geometries of micro-detectors (a) solenoid, (b) planar, (c) microslot, (d) stripline, (e) Transmission Line Probe (TLP). Images (a) - (d) were taken from Ref. [132] and image (e) was taken from Ref [138].

As discussed in the previous section, reducing the size of the detector improves the filling factor hence increases the sensitivity. This phenomenon was the main driving force behind development of the micro-NMR. For instance, solenoid coil (a) has sample volume of 0.005 μL and reaches nLOD of 0.13 nmol $\sqrt{\text{s}}$. To compare, the sample volume of the transmission line probe (TLP) which is shown in (e) is 2.5 μL and it reaches detection limit of 1 nmol $\sqrt{\text{s}}$ [132].

Another important measure of sensitivity is the concentration concentration limit of detection (cLOD), which is defied as:

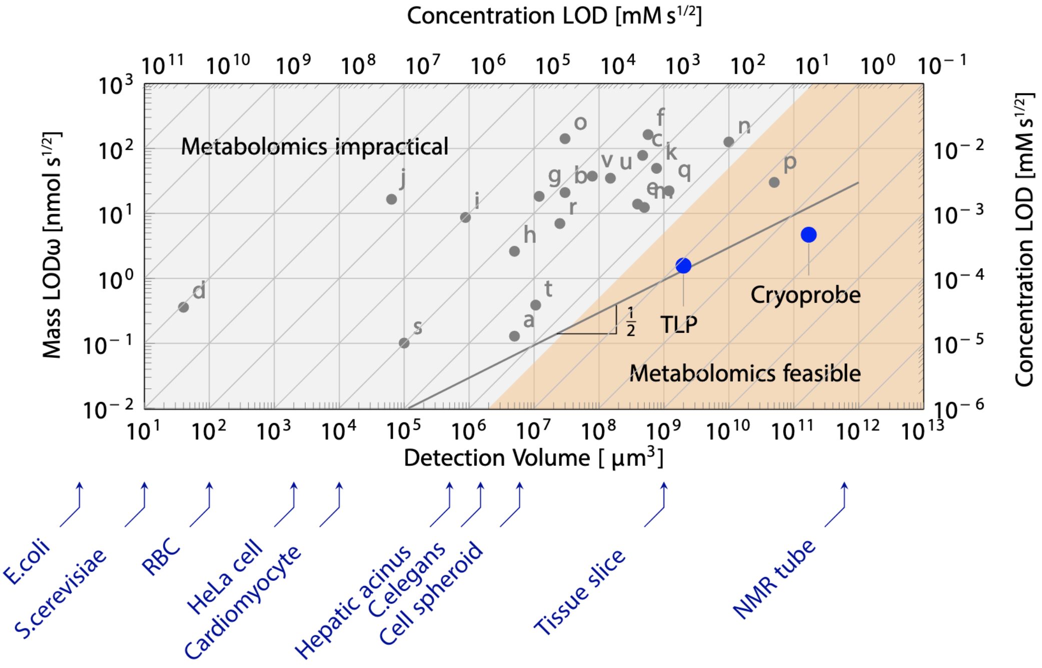

FIGURE 2.4: A plot of the interplay between the mass-limit of detection on the $y-$axis, the detection volume on the $x-$axis, and the concentration-limit of detection on the diagonal. Letters a-v correspond to different micro-detectors, technical specifications for a-t can be found in Ref. [132]; u in Ref.[139], and v in Ref.[140]. The plot was taken from Ref. [141].

$$cLOC = \frac{nLOD_\omega}{V_s} = \frac{nLOD}{\alpha_f V_c}, \tag{2.62}$$

where V_s is the sample volume, V_c is the volume occupied by the coil. Again comparing the solenoid and TLP detectors, the cLOD of the former is 50 mM $\sqrt{\mathrm{s}}$ whereas the latter reaches detection limit of 1 mM $\sqrt{\mathrm{s}}$ thus the TLP performs much better for concentration limited samples [138]. Unfortunately, cLOD scales negative with the detector volume since the smaller the volume, less of spins are present in the system.

Fig. 2.4 illustrates the interplay between the nLOD plotted on the y − axis, the detection volume on the x − axis and cLOD plotted on the diagonal. Points a − v correspond to different micro-detectors as listed in Ref. [141]. Cryoprobe marks the ^{1}H sensitivity of a state-of-the-art commercial 5mm probe with the detection volume of 170 μL. The transmission lime probe marked as TLP in Fig. 2.4 was used in this work. The TLP detector is composed of two stripline planes with a constriction in the centre as shown in Fig. 2.3 e [138]. The constriction region is the sensitive part of the detector as it concentrates the RF field. The TLP achieves 1.4 nmol $\sqrt{\mathrm{s}}$ nLOD, which is comparatively high as micro-detectors with $\mathrm{sub} - 1\,\mathrm{nmol}\,\sqrt{\mathrm{s}}$ have been reported. However, the concentration limit of detection of TLP is 1 mM $\sqrt{\mathrm{s}}$, which is a much lower detection limit compared with detectors of similar size and volume. The orange in Fig. 2.4 marked as "metabolomics feasible" denotes a range where 0.1 mM compound can be detected in 20 minutes corresponding to a cLOD of $5\,\mathrm{mM}\,\sqrt{\mathrm{s}}$. The TLP has a cLOD of 1 mM $\sqrt{\mathrm{s}}$ meaning that metabolites with a concentration higher than 0.02 mM can be detected. In physiologically relevant conditions, compounds are often in concentration far below mM region. The grey line represents the theoretical advancements in micro-detector design that would enhance the nLOD. However, it is apparent that further technological improvements will only yield marginal benefits in augmenting the sensitivity. Rather implementation of hyperpolarization techniques represents a more effective alternative to achieve a significant boost in the sensitivity of NMR.

2.3 Hyperpolarization

The sensitivity issue arises due to the low polarization levels in thermal equilibrium, recalling Eq. 2.27:

$$P_I = \tanh(\frac{\hbar\gamma B_0}{2k_B T}),$$

where P_I defines the nuclear spin polarization. For a field of 9.4 T (corresponding to a proton Larmor frequency of 400 MHz) and room temperature of 298 K, the nuclear spin polarization for proton, calculates to only 32 ppm. Meaning that only 32 out of 10^6 spins contribute to the observable signal [142].

Physiologically relevant sample concentrations lie in the μM - mM region. The goal is to utilise NMR to observe these in the relevant conditions hence concentrating samples is not a viable option. Manufacturing NMR spectrometers with higher magnetic field is an extremely challenging endeavour. Instead, hyperpolarization methods are being developed where a non-equilibrium spin magnetization is created, which allows the sensitivity of NMR to be boosted by several orders of magnitude compared to its thermal equilibrium counterpart. In the following section common hyperpolarization techniques are discussed.

2.3.1 Hyperpolarization Techniques

2.3.1.1 Optical Pumping

Spin-Exchange Optical Pumping (SEOP) is a technique used for polarization of noble gases such as ^{3}He and ^{129}Xe [143, 144]. The method uses a vapour cell containing alkali vapour (rubidium or potassium), a noble gas, and nitrogen. During the experiment, a circularly polarized pumping light is used to polarize the alkali metal vapour, which results in polarization of the electron spins. The electron polarization is then transferred to a noble gas during collisions. Nitrogen is used to reduce relaxation due to radiation trapping from alkali metal atoms [145]. This method allows near unit polarization of ^{129}Xe to be achieved [146–148] and has been an indispensable tool for lung MRI, biosensing and to study fundamental spin physics [149–151].

The first implementation of optical pumping on a microfluidic chip was reported by Jiménez-Martínez *et al.* [152]. In their work, a device made of silicon and glass was used to polarize ^{129}Xe. The device had four chambers: an inlet, an outlet, a pump and a probe chamber, all connected through a microchannel as shown in Fig. 2.5. Xenon was polarized through collisions with an optically pumped ^{87}Rb metal present in the pumping chamber. $> 0.5\%$ polarization of ^{129}Xe was achieved at flow rates of several microlitres per second. More recently, Kennedy *et al.* [153] reported an optimized microfluidic platform for generation and detection of hyperpolarized ^{129}Xe. The device proposed by Kennedy *et al.* reported ^{129}Xe polarizations of 7% and lifetimes of 6 s that allow for both *in situ* and *ex situ* detection. Unlike the device reported by Jiménez-Martínez *et al.* [152] it does not show any signs of degradation. The increase in observed ^{129}Xe polarization is due to the implementation of novel fabrication methods that did not produce by-products, which previously contributed to rapid relaxation of xenon.

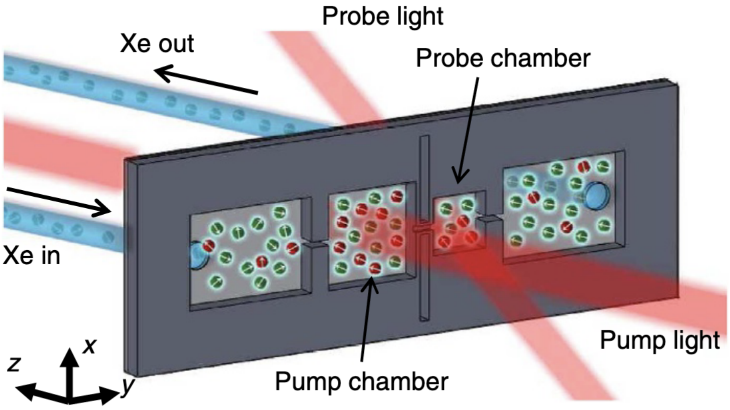

FIGURE 2.5: A schematic diagram of the chip used for spin exchange optical pumping. The image was taken from Ref. [152].

2.3.1.2 Dynamic Nuclear Polarization

Dynamic Nuclear Polarization (DNP) is a technique that utilises unpaired electron spins that are coupled to nearby nuclear spins through hyperfine coupling [154]. This is achieved by perturbing populations of the electron spins by microwave irradiation, which is on resonance with the electron spin transition. This results in a large non-equilibrium spin polarization that is transferred to the coupled nucleus [155]. Several types of DNP have been reported. These include solid-state magic angle spinning (MAS) DNP [156–158], Overhauser DNP [159–161], but the most common is dissolution DNP (d-DNP) [142, 162–165]. In the following section only liquid-state DNP methods, Overhauser DNR and d-DNP, are discussed since solid-state samples pose difficulties in microfluidic device due to channel blockage.

Dissolution DNP requires a sample of free radicals (2,2,6,6-Tetramethylpiperidin-1-yl)oxyl commonly referred to as TEMPO) to be homogeneously distributed in an amorphous matrix then, the sample is cooled down to cryogenic temperatures at high-field. Upon cooling a non-equilibrium electron spin population is created, which is then transferred to a target nucleus via microwave irradiation. Once sufficient polarization is obtained on the nucleus, the sample is rapidly dissolved in a hot solvent and injected to an NMR or MRI spectrometer for observation [154]. Due to the requirement of solid manipulation and cryogenic temperatures, microfluidic implementations of d-DNP are limited. Jeong *et al.* [166]

used a commercially available d-DNP set up to hyperpolarize a metabolite (pyruvate) mixed with with a cell suspension. Then, the suspension was injected into a microfluidic device placed in a 1 T MRI spectrometer to quantify the metabolic flux of the cell suspension. Performing experiments in a microfluidic chip required only $\sim 10^4$ cells to be used in contrast to $\sim 10^7$ cells that are required in conventional set-ups leading to 1000-fold higher sensitivity.

Overhauser DNP is used on samples that cannot be cooled to cryogenic temperatures. These rely on cross-relaxation between the electron and nuclear spins [159, 160]. In an experiment, a sample containing a source of unpaired electrons (such as TEMPO) is irradiated with microwaves at the electron Larmor frequency to drive the Overhauser effect, which causes electron polarization to be transferred to nuclear spins in solvent molecules. Overhauser DNP is best suited for experiments at low to moderate magnetic fields otherwise high microwave excitation are required. Overhauser DNP in conjunction with microfluidics is an attractive prospect to enhance the sensitivity of micro-NMR, especially at low fields as it does not require any solid-state manipulations. Since the efficiency of Overhauser DNP is dependent on the depth that the microwave irradiation can penetrate and the homogeneity of its distribution, it is particularly suited for performing at the microscale since very small volumes are used [21, 155, 167].

Another microfluidic implementation of DNP has been reported utilising rapid-melt DNP [168]. In this work, the sample was shuttled from a 'DNP' area through a melting area to an NMR detection area. In this way, signal enhancement of $\sim$300 was achieved but most importantly this set up allowed for the same sample to be polarized multiple times in a controlled, repeatable manner.

DNP offers the possibility to hyperpolarize a plethora of compounds but the biggest drawback of the method is the instrumentation cost. Additionally, the lifetime of hyperpolarized species is relatively short 1-3 minutes, which limits its applications for biological processes that occur on longer time-scales [169].

2.3.1.3 Chemically Induced Dynamic Nuclear Polarization

Chemically Induced Dynamic Nuclear Polarization (CIDNP) is a hyperpolarization method that requires formation of unstable free radicals that form a radical pair with the hyperpolarization target through a chemical reaction [170, 171]. During the reaction, radical recombination is driven by spin sorting and since different nuclear spin states behave differently this leads to varying product molecules or rates of spin relaxation.

A variant of CIDNP, called photo-CIDNP is widely used where the radicals are generated by light irradiation of the sample. The efficiency of a photochemical reaction depends on the intensity of light and this in turn depends on the distance from the light source. As a result, it is difficult to obtain a homogeneous irradiation of large samples therefore working on a small scale has several advantages for photo-CIDNP as it significantly improves the proportion of sample that is irradiated and the homogeneity of the light dispersion. Additionally, as discussed in Section 2.1.1.5, the efficient heat transfer in microfluidic devices leads to a consistent distribution of the light-induced heating of the sample. Photo-CIDNP was first demonstrated at the micro-scale by Mompeán *et al.* [172]. In their work, 4-fluorophenol was hyperpolarized by a photochemical reaction with flavin mononucleotide. The light source was located outside of the NMR spectrometer and the light was guided to the chip using an optical fibre. The microfluidic chip was made of PDMS with a Y-shaped channel for delivery of substrates, a 1 μL sample detection chamber and a microcoil embedded. The authors were able to demonstrate a remarkable sensitivity of 1 pmol $\sqrt{\text{s}}$.

The main disadvantage of CIDNP is the very specific chemical conditions that are required to induce hyperpolarization. As a result, CIDNP has mainly been utilised for protein structure determination and protein-ligand interactions [173, 21].

2.3.1.4 Brute Force

Brute force hyperpolarization is the simplest method to enhance the sensitivity as it relies on cooling the sample down to a low temperature (< 4K) at a high magnetic field. Proton polarization of 1% has been reported using this technique [174–176]. Once proton polarization has built up, it can be transferred to other nuclei such as ^{13}C. The approach poses many advantages because unlike other methods, it can be generalised since any compound can be cooled and placed in a high magnetic field. Additionally, it does not require any any free radicals, co-solvents or chemical reactions therefore there is no need to filter unwanted contaminants downstream.

The draw back of this method is the long waiting times for the build up of polarization, up to 70 hours, which prohibits high throughput [175]. Additionally, the level of polarization achieved with this method is currently limited to only 10^{-2} at temperatures and magnetic fields available.

2.3.2 Parahydrogen-Induced Polarization

ParaHydrogen-Induced Polarization (PHIP) is a hyperpolarization technique that was discovered by Weitekamp and Bowers [22, 177]. This method utilises parahydrogen ($\mathrm{p-H_2}$), a spin isomer of hydrogen, as a source of polarization. The polarization is transferred from $\mathrm{p-H_2}$ to a target molecule through a chemical reaction, usually in the presence of an organometallic catalyst. Both heterogeneous and homogeneous catalysts can be used for hydrogenation reactions and given that the organometallic catalysts are often toxic for biological cultures utilising heterogeneous catalysts would be ideal as they would not need to be removed post-reaction. However, for a successful polarization transfer, the two protons must remain coupled throughout the reaction, otherwise the polarization is lost. Since heterogeneous catalysis involves adsorption of hydrogen molecules onto the catalyst surface, the probability of the same two protons going through the same catalytic cycle is low. Some examples of heterogeneous PHIP have been demonstrated but the enhancement factors were low [178–180]. This thesis focuses only on homogeneous catalysts.

Fig. 2.6 shows typical reactions for hydrogenative and non-hydrogenative variants of PHIP. The choice of the catalyst is the key for the outcome of a hydrogenation reaction, iridium based organometallic catalysts are utilised in the non-hydrogenative variant of PHIP referred to as Signal Amplification By Reversible Exchange (SABRE)

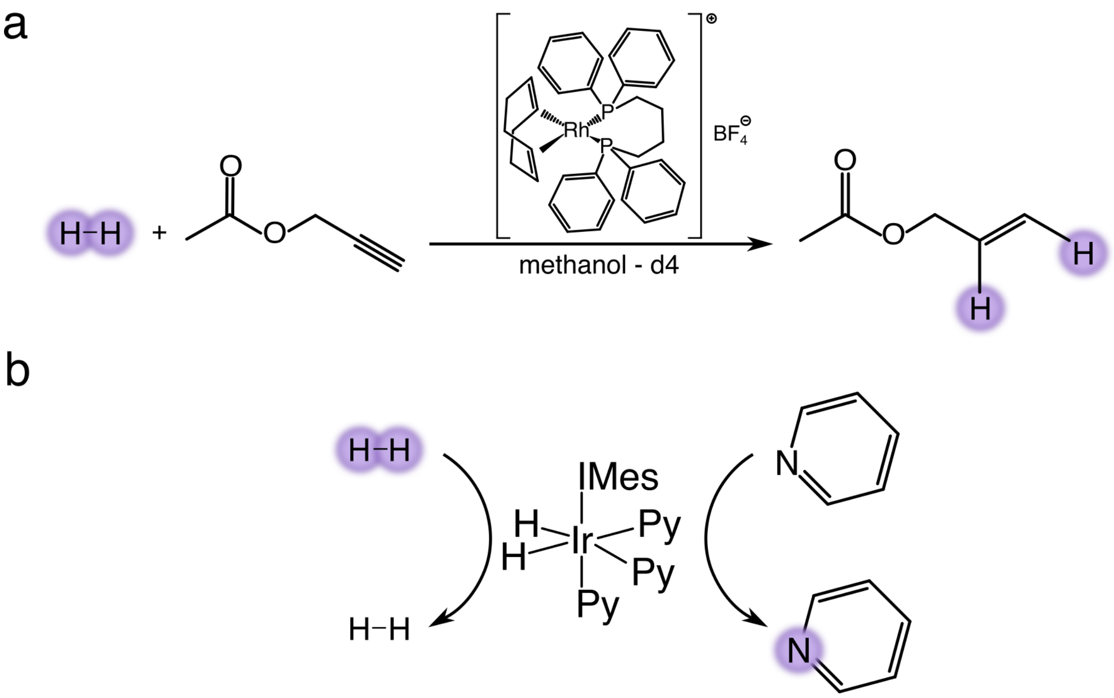

FIGURE 2.6: a) A typical reaction performed during a hydrogenative PHIP experiment where an unsaturated precursor molecule is brought into contact with $p-H_2$ in a presence of a rhodium catalyst. b) A typical reaction performed during a non-hydrogenative PHIP experiment. Both the parahydrogen and the polarization target bind reversibly an iridium catalyst.

because hydrogen and the target molecule reversibly bind to the metal centre [181]. Rhodium based catalysts are most commonly used for the hydrogenative PHIP reactions and the resulting product is a cis isomer. The choice of the metal centre dictates the isomerism, for instance trans isomers can be obtained using ruthenium-based catalysts [182]. Before going into the details of individual methods to transfer polarization from $p-H_2$ the hydrogen molecule itself is examined.

2.3.2.1 Nuclear Spin States of Molecular Hydrogen

The molecule of hydrogen contains two protons (I_1 and I_2), since $I_1 = I_2 = \frac{1}{2}$ then the total spin angular momentum (I_3) is: $I_3 = |I_1 - I_2| = 0$ or $I_3 = |I_1 + I_2| = 1$. Therefore, a H_2 molecule has four nuclear spin states. The $I_3 = 0$ is referred to as the singlet state or parahydrogen ($p-H_2$) and the $I_3 = 3$ states are referred to as the triplet states or orthohydrogen ($o-H_2$).

Since the molecule of hydrogen is symmetrical, the chemical shift of the two protons is identical i.e. $\omega_1 = \omega_2 = \omega$. The Hamiltonian from Eq. 2.35 in the Zeeman basis becomes:

$$\hat{H} = \omega(\hat{I}_{1z} + \hat{I}_{2z}) + 2\pi J_{12}\hat{\boldsymbol{I}}_{\boldsymbol{1}}\hat{\boldsymbol{I}}_{\boldsymbol{2}}. \tag{2.63}$$

The matrix representation in the Zeeman basis is:

$$\hat{H} = \begin{pmatrix} \omega + \frac{J_{12}\pi}{2} & 0 & 0 & 0 \\ 0 & -\frac{J_{12}\pi}{2} & J_{12}\pi & 0 \\ 0 & J_{12}\pi & -\frac{J_{12}\pi}{2} & 0 \\ 0 & 0 & 0 & \frac{J_{12}\pi}{2} - \omega \end{pmatrix}. \tag{2.64}$$

Because this matrix is not diagonal, the Zeeman product states $|\alpha\alpha\rangle$, $|\alpha\beta\rangle$, $|\beta\alpha\rangle$ and $|\beta\beta\rangle$ are not the eigenstates of the Hamiltonian. The Hamiltonian can be diagonalized by choosing a different set of basis states, called the singlet - triplet ($\mathbb{ST}$) basis.

$$\begin{aligned} |S_0\rangle &= \frac{1}{\sqrt{2}}(|\alpha\beta\rangle - |\beta\alpha\rangle) \qquad & |T_{+1}\rangle &= |\alpha\alpha\rangle \\ |T_0\rangle &= \frac{1}{\sqrt{2}}(|\alpha\beta\rangle + |\beta\alpha\rangle) \qquad & |T_{-1}\rangle &= |\beta\beta\rangle\,, \end{aligned} \tag{2.65}$$

where $|T_{+1}\rangle\,, |T_0\rangle$ and $|T_{-1}\rangle$ are referred to as the triplet states and $|S_0\rangle$ is referred to as the singlet state, the subscript refers to the projection along the $z-$axis for instance $I_z\,|T_{+1}\rangle = +1\,|T_{+1}\rangle$.

The Hamiltonian in the $\mathbb{ST}$ basis states becomes:

$$\hat{H} = \begin{pmatrix} -\frac{3}{2}J_{12}\pi & 0 & 0 & 0 \\ 0 & \frac{1}{2}J_{12}\pi + \omega & 0 & 0 \\ 0 & 0 & \frac{1}{2}J_{12}\pi & 0 \\ 0 & 0 & 0 & \frac{1}{2}J_{12}\pi - \omega \end{pmatrix}. \tag{2.66}$$

The $\mathbb{ST}$ basis states are the energy eigenstates of the magnetically equivalent spin pair because the matrix is diagonal. The energy levels are:

$$\begin{aligned}
\hat{H}\left|T_{+1}\right\rangle &= (\omega_0 + \frac{1}{2}\pi J_{12})\left|T_{+1}\right\rangle, \\
\hat{H}\left|T_{0}\right\rangle &= (\frac{1}{2}\pi J_{12})\left|T_{0}\right\rangle, \\
\hat{H}\left|T_{-1}\right\rangle &= (-\omega_0 + \frac{1}{2}\pi J_{12})\left|T_{-1}\right\rangle, \\
\hat{H}\left|S_{0}\right\rangle &= (-\frac{3}{2}\pi J_{12})\left|S_{0}\right\rangle.
\end{aligned} \tag{2.67}$$

The total angular momentum operators of the triplet states can be constructed by adding the angular momentum operators of the two spins:

$$\begin{aligned}
\hat{I}_x &= \hat{I}_{1x} + \hat{I}_{2x}, \\
\hat{I}_y &= \hat{I}_{1y} + \hat{I}_{2y}, \\
\hat{I}_z &= \hat{I}_{1z} + \hat{I}_{2z}.
\end{aligned} \tag{2.68}$$

The total square angular momentum operator is:

$$\hat{I}^2 = \hat{I}_x^2 + \hat{I}_y^2 + \hat{I}_z^2. \tag{2.69}$$

Singlet and triplet states adhere to the following eigenequations:

$$\begin{aligned}
&\hat{I}_z\left|T_M\right\rangle = M\left|T_M\right\rangle, \\
&\hat{I}^2\left|T_M\right\rangle = I(I+1)\left|T_M\right\rangle = 2\left|T_M\right\rangle, \\
&\hat{I}_z\left|S_0\right\rangle = 0, \\
&\hat{I}^2\left|S_0\right\rangle = 0.
\end{aligned} \tag{2.70}$$

2.3.2.2 Enrichment of Hydrogen Gas with Para Isomer

The total wavefunction of molecular hydrogen can be approximated as follows:

$$\Psi^{tot} = \Psi^{elec}\Psi^{vib}\Psi^{rot}\Psi^{spin}, \tag{2.71}$$

where Ψ^{elec}, Ψ^{vib}, Ψ^{rot} and Ψ^{spin} are the electronic, vibrational, rotation, and spin part of the wavefunction, respectively.

The Pauli exclusion principle dictates that the total wave function for half-integer nuclei must remain antrisymmetric with respect to exchange of two identical nuclei. In this work, we are interested in temperatures below 100°C, as a result transitions occur only between the nuclear spin states and the rotational states. The even rotational states are symmetric and the odd states are antisymmetric therefore they must pair with spin states of the opposite symmetry as shown in Table 2.3 [183].

The separation between the two lowest rotational energy levels $E_{J=1} - E_{J=0} \approx 171\text{K}$ [184]. When the temperature is reduced, the available thermal energy is reduced. As a result, molecules tend to occupy their ground-state ($J = 0$), hence $\mathrm{p-H_2}$ gets populated. The fraction of parahydrogen N_{para} at temperature T can be calculated as follows [178]:

$$N_{para} = \frac{1}{Z} \sum_{J=even} (2J+1) e^{-J(J+1)\theta_r/T}, \tag{2.72}$$

where Z is the partition function and θ_r is the rotational temperature ($\theta_r = \frac{\hbar}{2Ik_B} = 87.6\text{K}$), which depends on the moment of inertia I of the hydrogen molecule [185]. At room temperature, the ratio of ortho:para hydrogen is 3:1 as shown in Fig. 2.7. Cooling the gas down to 77 K yields a 50:50 ratio, and at temperatures below 30K, 100% of parahydrogen is obtained. During the cooling process, a catalyst (such as iron (III) oxide) must be present otherwise the ortho to para conversion is extremely slow. The catalyst temporarily breaks the symmetry between the protons allowing population transfer from $J = 1$ to $J = 0$. This transfer is disfavoured without the catalyst because a spin flip is required hence the angular momentum would not be

Label	**Spin State**	**J**	**Rotational States**
para	antisymmetric	0	symmetric
ortho	symmetric	1	antisymmetric
para	antisymmetric	2	symmetric
ortho	symmetric	3	antisymmetric

Table 2.3: Correlation between the spin and symmetry state of the total wavefunction of molecular hydrogen.

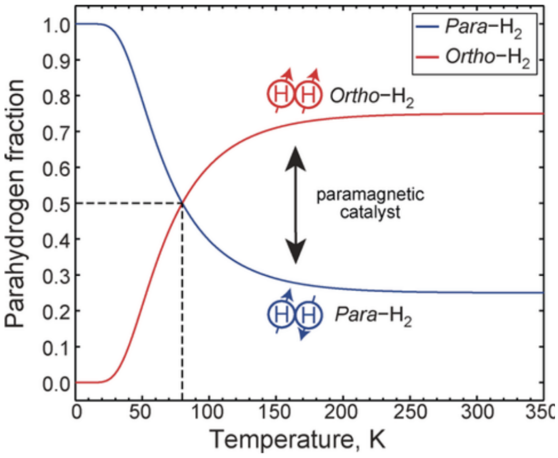

FIGURE 2.7: A plot of para- and orthohydrogen fraction as a function of temperature. The dashed line indicates the 50% parahydrogen enrichment achieved by cooling the hydrogen gas to 77 K with liquid nitrogen. Image modified from Ref. [187]

preserved. Once $\mathrm{p-H_2}$ has been generated it can be stored for weeks at room temperature, therefore hyperpolarization source can be access on-demand [186].

It is convenient to express the density operators for *para−* and *ortho−*spin isomers in the Zeeman basis:

$$\begin{aligned}
|T_{+1}\rangle\langle T_{+1}| &= \begin{pmatrix} 1 & 0 & 0 & 0 \\ 0 & 0 & 0 & 0 \\ 0 & 0 & 0 & 0 \\ 0 & 0 & 0 & 0 \end{pmatrix} \qquad & |T_0\rangle\langle T_0| &= \frac{1}{2}\begin{pmatrix} 0 & 0 & 0 & 0 \\ 0 & 1 & 1 & 0 \\ 0 & 1 & 1 & 0 \\ 0 & 0 & 0 & 0 \end{pmatrix} \\
|T_{-1}\rangle\langle T_{-1}| &= \begin{pmatrix} 0 & 0 & 0 & 0 \\ 0 & 0 & 0 & 0 \\ 0 & 0 & 0 & 0 \\ 0 & 0 & 0 & 1 \end{pmatrix} \qquad & |S_0\rangle\langle S_0| &= \frac{1}{2}\begin{pmatrix} 0 & 0 & 0 & 0 \\ 0 & 1 & -1 & 0 \\ 0 & -1 & 1 & 0 \\ 0 & 0 & 0 & 0 \end{pmatrix}.
\end{aligned} \tag{2.73}$$

The singlet and triplet population operators may be expressed in terms of Cartesian product operators as follows [127]:

$$\begin{aligned}
|T_{+1}\rangle\langle T_{+1}| &= \frac{1}{4}\mathbb{1} + \frac{1}{2}(\hat{I}_{1z} + \hat{I}_{2z} + 2\hat{I}_{1z}\hat{I}_{2z}), \\
|T_{0}\rangle\langle T_{0}| &= \frac{1}{4}\mathbb{1} + \frac{1}{2}(2\hat{I}_{1x}\hat{I}_{2x} + 2\hat{I}_{1y}\hat{I}_{2y} - 2\hat{I}_{1z}\hat{I}_{2z}), \\
|T_{-1}\rangle\langle T_{-1}| &= \frac{1}{4}\mathbb{1} + \frac{1}{2}(-\hat{I}_{1z} - \hat{I}_{2z} + 2\hat{I}_{1z}\hat{I}_{2z}), \\
|S_{0}\rangle\langle S_{0}| &= \frac{1}{4}\mathbb{1} + \frac{1}{2}(-2\hat{I}_{1x}\hat{I}_{2x} - 2\hat{I}_{1y}\hat{I}_{2y} - 2\hat{I}_{1z}\hat{I}_{2z}).
\end{aligned} \tag{2.74}$$

To simplify the notation, one density operator for orthohydrogen ($\hat{\rho}_{ortho}$) and one for parahydrogen ($\hat{\rho}_{para}$) can be defined:

$$\begin{aligned}
\hat{\rho}_{ortho} &= \frac{1}{3}|T_{+1}\rangle\langle T_{+1}| + |T_{0}\rangle\langle T_{0}| + |T_{-1}\rangle\langle T_{-1}| \\
&= \frac{1}{4}\mathbb{1} + \frac{1}{3}(\hat{I}_{1x}\hat{I}_{2x} + \hat{I}_{1y}\hat{I}_{2y} + \hat{I}_{1z}\hat{I}_{2z}) \\
&= \frac{1}{4}\mathbb{1} + \frac{1}{3}\mathbf{I}_1 \cdot \mathbf{I}_2, \\
\hat{\rho}_{para} &= |S_{0}\rangle\langle S_{0}| \\
&= \frac{1}{4}\mathbb{1} - (I_{1x}I_{2x} + I_{1y}I_{2y} + I_{1z}I_{2z}) \\
&= \frac{1}{4}\mathbb{1} - \mathbf{I}_1 \cdot \mathbf{I}_2.
\end{aligned} \tag{2.75}$$

Therefore, a density operator for an ensemble of hydrogen molecules ($\hat{\rho}_{hyd}$) can be defined [188]:

$$\begin{aligned}
\hat{\rho}_{hyd} &= (1 - N_{para})\rho_{ortho} + N_{para}\rho_{para} \\
&= \frac{1}{4}\mathbb{1} - \xi\mathbf{I}_1 \cdot \mathbf{I}_2 - \frac{\epsilon}{4}(\hat{I}_{1z} + \hat{I}_{2z}),
\end{aligned} \tag{2.76}$$

where N_{para} is the parahydrogen fraction. Factor $\xi = (4N_{para} - 1)/3$ and ϵ is the Boltzmann factor.

It is important to notice that at room temperature, the parahydrogen fraction is $\frac{1}{4}$ thus $\xi = 0$, and the second term on the right-hand side disappears. Therefore, Eq. 2.76 reduces to an expression for a density operator of a two spin system in thermal equilibrium. When the fraction of parahydrogen is significant, which is the case during PHIP experiments i.e. $1/2 \leq N_{para} \leq 1$, the expression is dominated by the second term in Eq. 2.76 and the thermal factor can be ignored. The $\hat{\rho}_{para}$ is invariant under rotations therefore, chemical transformations must take place to access the hyperpolarized nuclear spin state.

The key for all PHIP reactions is parahydrogen gas therefore in the following section methods of bring the precursor solution in contact with the gas are discussed.

2.3.2.3 Gas - Liquid Mixers

The challenge in performing liquid phase hydrogenation is the inherently low solubility of hydrogen in solvents. In water, the solubility of hydrogen at 1 atm pressure and room temperature is $0.0016\,\mathrm{g/kg_{H_20}}$ [185], which is 25-times lowered compared with the solubility of oxygen ($0.04\,\mathrm{g/kg_{H_20}}$) [185] and over 930-times lower in comparison to CO_2 ($1.5\,\mathrm{g/kg_{H_20}}$) [189]. The solubility of hydrogen in other commonly used organic solvents is better for instnace, methanol ($0.0095\,\mathrm{g/kg_{methanol}}$), DMSO ($0.0019\,\mathrm{g/kg_{DMSO}}$), and tolune ($0.0068\,\mathrm{g/kg_{toluene}}$) [185]. Since the solubility of gases increases linearly with pressure, working at high pressures greatly increases H_2 concentration.

The most common method of bringing parahydrogen in contact with solution is through bubbling or shaking, which induces turbulent mixing between the two phases. In a shaking experiment, an NMR tube containing a precursor solution is pressurised with hydrogen gas outside of an NMR spectrometer and is followed by vigorous manual shaking to achieve mixing. Then, the tube is placed in a spectrometer for detection [186]. The main drawback of this approach is the lack of reproducibility. This was addressed by developing approaches where $\mathrm{p-H_2}$ is bubbled through the solution. Then the solution is transported into a spectrometer manually or under flow for detection alternatively, the entire experiment can take place inside of a spectrometer. However, it has been demonstrated that bubbling systems reduce the observed levels of polarization possibly due to the reduced mixing efficiency compared with manual shaking [190]. Additionally, introduction of capillaries can result in broadening of NMR signals as the homogeneity of the field is disturbed.

A semi-permeable membrane can be used to facilitate the gas-liquid mixing. One of the early examples of membrane PHIP reactors is XENONIZER [191, 192]. The set up is shown in Fig. 2.8 and it comprises a hollow fibre membrane inserted into an NMR tube. In this way, a molecule of 2-hydroxyethyl acrylate was continuously hydrogenated with $p-H_2$ achieving proton signal enhancement of 2000 and 6000-fold enhancement for ^{13}C polarization [191]. Performing the reaction under continuous flow surpassed another limitation of hyperpolarization methods, which is the fact that hyperpolarized molecules have a limited life time and decay in seconds (^{1}H polarization) or minutes (^{13}C polarization). The continuous flow approach, allows a constant stream of hyperpolarized material to be obtained. However, the set up only allows one to perform reactions in aqueous solutions and since most PHIP catalysts are water insoluble this approach lacks generality.

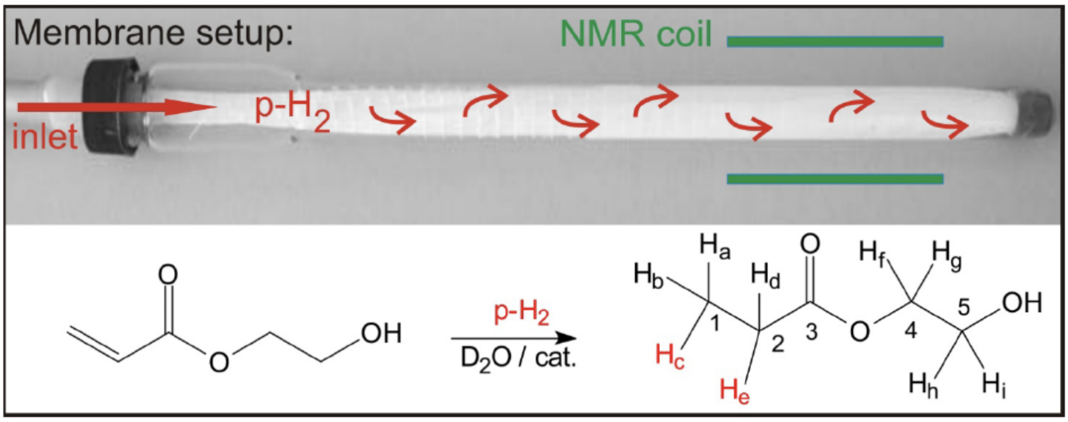

FIGURE 2.8: XENOTIZER set up used in a continuous flow reaction of 2-hydroxyethyl acrylate with $p-H_2$. The signal enhancement of 2000 was achieved. The figure was taken form Ref [191]

Lehmkuhl *et al.* [193] used a commercially available reactor combined with a polymer membrane to facilitate hydrogenation. The reaction was carried out outside of the magnet and the solution was flown into a 5 mm tube for detection. This approach allows the use of a wider variety of solvents and catalysts but the lack of integrated detection region with the device requires to use very high flow rates (3-5 mL/min) in order to detect hyperpolarized products leading to high costs.

As discussed in Section 2.1.1, microfluidic reactors provide a high specific surface area as well as higher mass and heat transfer efficiency, and smaller sample volumes in comparison to conventional reactors. Two most common methods of bringing gas and liquid phases in contact have been developed in microfluidics are: (i) through creating microdispersions where gas micro-bubbles are separated by a liquid plug and (ii) gas is brought in contact with the liquid using a semi-permeable membrane.

Several micromixers have been designed to produce a stream of micro-bubbles these include: T- and Y-junction, flow focusing, multilamination and split-and-recombine. T- and Y-junction mixers bring the two phases in contact at the channel intersection to create a monodispersed suspension of gas bubbles in a liquid phase. Flow focusing micromixers utilise a thin capillary to deliver a gas that is placed in a microchannel filled with a liquid. Gas bubbles are formed when a liquid is forced though orifice near the tip of the capillary due to the pressure drop. This results in a formation of highly homogeneous micro-bubbles [194–196]. A multilamination mixer consists of separate feeding units for the delivery of a fluid, and a gas as well as a collection slit. The feeding unit is designed such that the fluid and liquid lamelle alternate and create a large number of bubbles at the outlet of the feeding channels [197]. In split-and-recombine mixers, as the name suggests, the channels are split into several lamelle which recombine and can incorporate obstacles to enhance mixing efficiency between the phases [198]. The common feature of the aforementioned mixers have is that mixing is achieved through the formation of micro-bubble stream. However, phase changes are not desirable in NMR due to the differences in the magnetic susceptibilities between phases, which destroy the homogeneity of the sample under observation. This can be prevented by designing bubble traps upstream from the observation chamber but they are not 100% effective. Instead, membrane-based reactors have been extensively used to avoid bubble formation in the channels.

Many methods have been developed to integrate membranes microfluidic chips [199]. The simplest approach is to glue or clamp a commercially available membrane with the reactor. Both flat sheet and hollow fibre membranes can be directly purchased and can be functionalised by for instance immobilization of enzymes [200–203] or impregnation with an extraction fluid [204, 205]. The biggest challenge with this method is sealing the device as pores in the membrane can be easily blocked by glue or fluids can become stuck between the layers. Membranes can also be prepared as part of the chip fabrication process where the specific membrane functionality is embedded into the chip. For instance microsives or filters can be fabricated by etching [206]. Lastly, the membrane can be used as the bulk matrial for the chip. As discussed in section 2.1.2 PDMS has been extensively used as a chip fabrication material due to its high gas permeability, known properties, transparency, biocompatibility and high availability. However, the biggest drawback of this material is the lack of compatibility with organic solvents, which cause swelling and deformation.

In the following section chemical reactions that utilise $\mathrm{p-H_2}$ as a hyperpolarization agent are discussed.

2.3.2.4 Non-Hydrogenative PHIP

Signal Amplification By Reversible Exchange (SABRE) is a non-hydrogenative variant of PHIP that utilises iridium based catalysts to reversibly bind parahydrogen and the target molecule [181]. Polarization is transferred from parahydrogen to the target molecule through an RF or B_0 matching field condition while both molecules are bound to the catalyst and experience mutual $J-$coupling. Since all reactions are reversible, the hyperpolarization target is not depleted thus can be reused for many experiments providing that fresh parahydrogen is delivered.

Several biologically relevant compounds such as pyridine and its derivatives [181, 207–209], nitriles [210], schiff bases [211], amines [212, 213] and phosphines [214] have been hyperpolarized using SABRE with efficient polarization transfer to ^{1}H (>50%) [215], ^{13}C (>15%) [208], and ^{15}N (>20%) [216] as well as to ^{19}F [217], ^{29}Si and ^{119}Sn [218]. However, its main limitation remains the biocompatibility of the solvent as most SABRE reactions are performed in an organic solvents. To enhance water solubility, catalysts containing phosphine ligands have been synthesised [219].

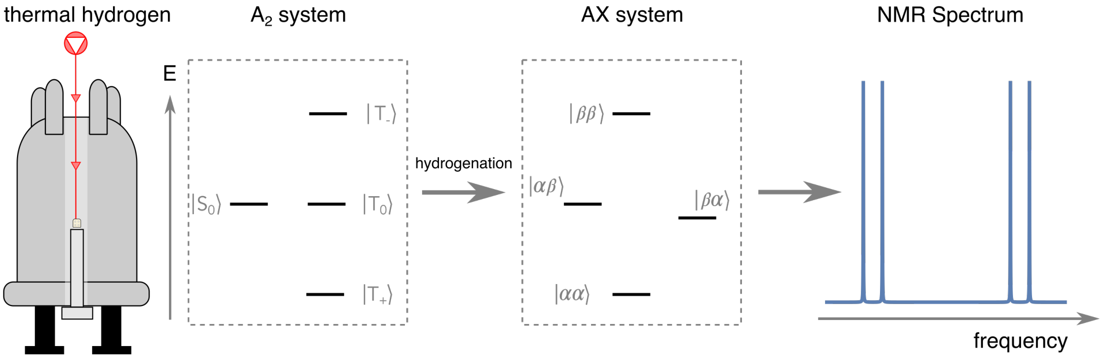

FIGURE 2.9: A hydrogenation experiment inside of a high-field NMR spectrometer using thermally equilibrated hydrogen. In the absence of other spins, hydrogen can be represented as an A_2 system, after addition to an unsaturated molecule, it becomes an AX system. The resulting spectrum shows two doublets. The image adapted from Ref. [178]

Microfluidic implementation of SABRE was demonstrated by Bordonali *et al.* [220]. In their work, a microfluidic polarizer was made of two layers of glass with channels for gas and liquid etched onto it. Parahydrogen diffusion was facilitated by using a semi-permeable membrane interposed between the two glass layers. The polarizer was incorporated into an NMR probe head. The SABRE precursor solution was delivered into the device using a syringe pump located outside of the spectrometer using flow rates between $20 - 30\,\mu\mathrm{L\,min}^{-1}$ while 95% $\mathrm{p-H_2}$ was provided at 2 bar. Hyperpolarized products were detected at a 0.56 μL detection chamber using a Helmholtz pair. Reactions were performed under continuous flow and three substrates were hyperpolarized namely, nicotinamicde, pyridine and 1-methy-1,2,3-triazole with enhancements of $4-$, $1.2-$, and $4.6-$ fold, respectively.

2.3.2.5 Hydrogenative PHIP

Hydrogenative PHIP relies on a pairwise addition of parahydrogen molecules into an unsaturated substrate, meaning that both hydrogen atoms are added onto the same molecule. This is the key for a successful hyperpolarization transfer because if the proton coupling is lost, the hyperpolarized singlet state is also lost. The first demonstration of this technique was performed in 1987 using Wilkinson's catalyst where parahydrogen was added to a molecule of acrylonitrile achieving signal enhancement of 100-200 [22]. Since then a number of metabolites including acetate

[221–223], lactate [224], fumarate [182, 225–227], pyruvate [223, 226, 228] and succinate [229, 230] have been polarized in this way.

When the hydrogenation reaction is carried out using hydrogen in thermal equilibrium, the NMR spectrum is independent of the magnetic field strength. Initially, the hydrogen molecule can be described by the A_2 spin systems and the singlet-triplet eigenfuctions (described by Eq. 2.65) are equally populated ($P = 0.25$) outside of the magnet. Inside of the magnet, the populations change according to the Boltzmann distribution ($\epsilon = \hbar\gamma B_0/kT \approx 10^{-5}$ at RT). After the hydrogenation, the protons form an AX system, and can be described by the Zeeman states (Eq. 2.18) and the NMR spectrum shows two doublets of equal intensity as shown in Fig. 2.9. In the *para*−state of hydrogen, the singlet state is overpopulated by ΔP, and its population is $P + \Delta P$, while populations of individual triplet states are: $P - \frac{\Delta P}{3}$. As a result, the spectrum after reaction with $\mathrm{p-H_2}$ depends on the strength of the field that the hydrogenation reaction and detection is performed. Parahydrogen And Synthesis Allow Dramatically Enhanced Nuclear Alignment (PASADENA) refers to a PHIP variant where the reaction and detection are carried out inside of a high-field spectrometer. Adiabatic Longitudinal Transport After Dissociation Endangers Net Alignment (ALTADENA) refers to an experiment where the hydrogenation is carried out at low field and the sample is transferred to a high-field magnet for detection. In the following section the spin dynamics of PASADENA and ALTADENA are discussed.

PASADENA The initial density operator of parahydrogen is the nuclear singlet order between the protons. Recalling Eq. 2.75, it can be represented by the following density operator:

$$\hat{\rho}_{para} = \frac{1}{4}\mathbb{1} - (\hat{\mathbf{I}}_1 \cdot \hat{\mathbf{I}}_2).$$

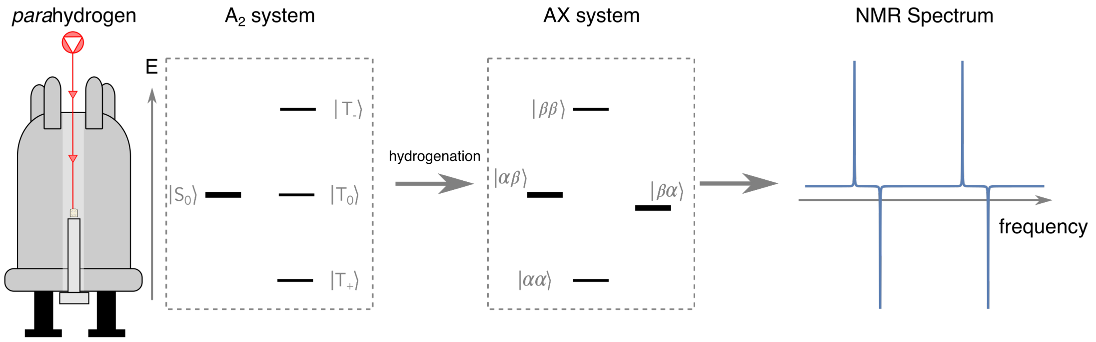

FIGURE 2.10: A PASADENA experiment. The reaction occurs inside of a high-field spectrometer. The presence of parahydrogen is evidenced by an overpopulation of the singlet state $|S_0\rangle$ in the A_2 system. After hydrogenation, the two $|\alpha\beta\rangle$ and $|\beta\alpha\rangle$ states are overpopulated, which results in two antiphase peaks in the NMR spectrum. The image adapted from Ref. [178]

The matrix representation in the Zeeman basis is:

$$\hat{\rho}_{para} = \frac{1}{2}\begin{pmatrix} 0 & 0 & 0 & 0 \\ 0 & 1 & -1 & 0 \\ 0 & -1 & 1 & 0 \\ 0 & 0 & 0 & 0 \end{pmatrix}. \tag{2.77}$$

In order to access the singlet order, a hydrogen molecule is added to a chemically non-equivalent position on the target molecule yielding the weakly coupled J-Hamiltonian, recalling Eq. 2.34:

$$\hat{H} = \omega_1 \hat{I}_{1z} + \omega_2 \hat{I}_{2z} + 2\pi J_{12} \hat{I}_{1z} \hat{I}_{2z}.$$

Immediately after the reaction, the off-diagonal terms (i.e. coherences) in the density matrix begin to evolve at a frequency characterized by the difference in the chemical shifts ($\Delta\omega$). The diagonal elements (i.e. populations) do not evolve because they commute with the Hamiltonian. This is referred to as incoherent averaging and since the coherence evolution is much faster than the hydrogenation period, it yields:

$$\frac{1}{4}\mathbb{1} - \hat{\boldsymbol{I}}_1 \hat{\boldsymbol{I}}_2 \xrightarrow{\textit{incoherent averaging}} \frac{1}{4}\mathbb{1} - \hat{I}_{1z} \hat{I}_{2z}. \tag{2.78}$$

As a matrix in the Zeeman basis:

$$\frac{1}{2}\begin{pmatrix} 0 & 0 & 0 & 0 \\ 0 & 1 & -1 & 0 \\ 0 & -1 & 1 & 0 \\ 0 & 0 & 0 & 0 \end{pmatrix} \xrightarrow{incoherent\ averaging} \frac{1}{2}\begin{pmatrix} 0 & 0 & 0 & 0 \\ 0 & 1 & 0 & 0 \\ 0 & 0 & 1 & 0 \\ 0 & 0 & 0 & 0 \end{pmatrix}. \tag{2.79}$$

The application of a $\frac{\pi}{2}$ x-pulse has the following effect, omitting the unity operator:

$$\hat{R}_y(\frac{\pi}{2})\hat{\rho}_{PAS} = -\hat{I}_{1y}\hat{I}_{2y}, \tag{2.80}$$

i.e. unobservable double quantum coherence. However a $\frac{\pi}{4}$ x-pulse produces:

$$\hat{R}_y(\frac{\pi}{4})\hat{\rho}_{PAS} = -\frac{1}{2}(\hat{I}_{1y}\hat{I}_{2y} + \hat{I}_{1y}\hat{I}_{2z} + \hat{I}_{1z}\hat{I}_{2y} + \hat{I}_{1z}\hat{I}_{2z}). \tag{2.81}$$

Both $\hat{I}_{1z}\hat{I}_{2y}$ and $\hat{I}_{1y}\hat{I}_{2z}$ terms are the observable single quantum coherences that give rise to the anti phase spectral lines as shown in Fig. 2.10.

Signal enhancement (ε) can be calculated by comparing the maximum signal obtained from an experiment with hydrogen in thermal equilibrium to the maximum signal obtained from a PHIP experiment. The ideal enhancement factor as function of the parahydrogen fraction (N_{para}) is formulated by:

$$\varepsilon = \frac{(4N_{para} - 1)2k_BT}{3\gamma\hbar B_0}, \tag{2.82}$$

For a PASDENA experiment where a $\frac{\pi}{4}$ pulse is applied the equation reduces to [1]:

$$\varepsilon = \frac{4N_{para} - 1}{3}\frac{1}{\sqrt{2}}\frac{2k_BT}{\hbar\gamma B_0}, \tag{2.83}$$

where $\frac{1}{\sqrt{2}}$ reflects the use of $\frac{\pi}{4}$ pulse in the experiment. If the parahydrogen fraction of $x_p = 0.5$ with the magnetic field of $B_0 = 11.7$ T and the temperature of T = 298 K are used during an experiment, the ideal enhancement factor is ∼5900 [1].

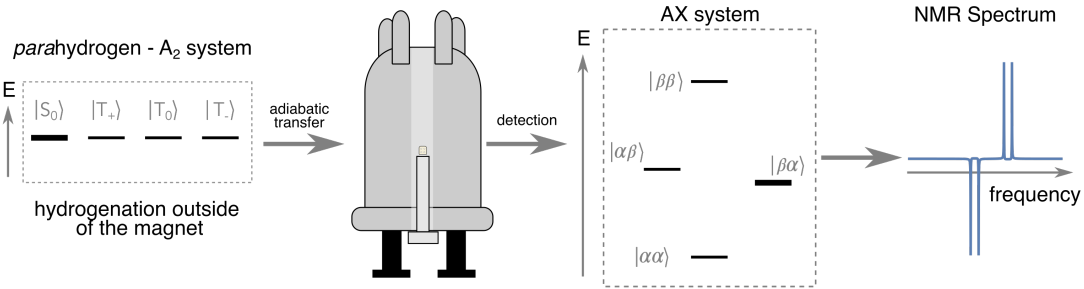

FIGURE 2.11: During an ALTADENA experiment the hydrogenation takes place outside of the magnet then, the sample is adiabatically transferred into a high-field spectrometer for detection. This results in two doublets with opposite phases in the NMR spectrum. The image taken from Ref. [178]

ALTADENA During an ALTATENA experiment, the hydrogenation is carried out at low field for instance in earth's field, where the J-coupling interaction has a comparable magnitude to the chemical shift. To a reasonable approximation only $|S_0\rangle$ is populated therefore there is no evolution and the density operators before and after the hydrogenation are identical. After the hydrogenation, the sample is transferred to the high-field for detection where the chemical shift dominates over the J-coupling. If the transfer is done adiabatically meaning that the rate of change of the magnetic field ($\frac{dB_0}{dt}$) is small with respect to the square of the value of the J-coupling $(J_{12})^2$, the initial $|S_0\rangle$ population will remain in the corresponding Hamiltonian eigenstste at all fields, and completely carried over to an $|\alpha\beta\rangle$ population, meaning that only one of the four states is populated. Fig. 2.12 shows a correlation diagram of the eigenvalues of the Hamiltonian eigenstates as a function of the magnetic field, the singlet state is shown in green.

Mathematically an idealised adiabatic transfer can be expressed as [188]:

$$\frac{1}{4}\mathbb{1} - \hat{\boldsymbol{I}}_1\hat{\boldsymbol{I}}_2 \xrightarrow{adiabatic\, transfer} \frac{1}{4}\mathbb{1} - \hat{I}_{1z}\hat{I}_{2z} + \frac{1}{2}(\hat{I}_{1z} - \hat{I}_{2z}). \tag{2.84}$$

As a matrix in the Zeeman basis:

$$\frac{1}{2}\begin{pmatrix} 0 & 0 & 0 & 0 \\ 0 & 1 & -1 & 0 \\ 0 & -1 & 1 & 0 \\ 0 & 0 & 0 & 0 \end{pmatrix} \xrightarrow{adiabatic\, transfer} \begin{pmatrix} 0 & 0 & 0 & 0 \\ 0 & 0 & 0 & 0 \\ 0 & 0 & 1 & 0 \\ 0 & 0 & 0 & 0 \end{pmatrix}. \tag{2.85}$$

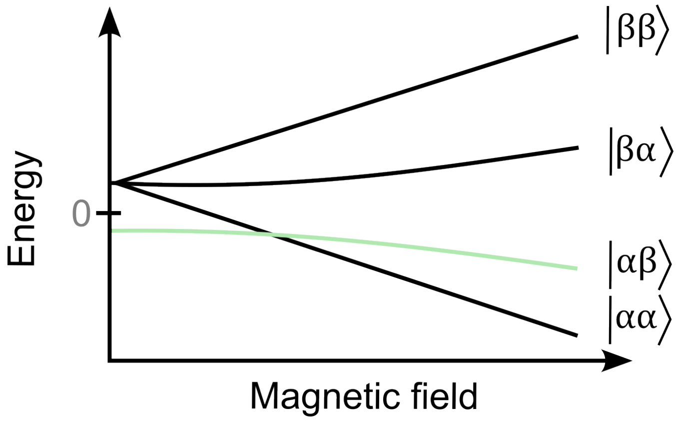

FIGURE 2.12: A plot of the eigenvalues of the Hamiltonian as a function of the magnetic field. At zero magnetic field, the eigenstates are single-triplet states. By gradually increasing the magnetic field, the states transition into the Zeemann states.

The maximum signal for an ALTADENA is obtained by applying a $\frac{\pi}{2}$ x-pulse and a spectrum consists of two doublets with opposite phase as shown in Fig. 2.11 .

Near Equivalence Regime When the chemical shift difference between the two nuclei is much smaller than the J-coupling even at large magnetic fields, the molecule is said to be in the near-equivalence regime [231]. Unlike in the ALTADENA example, the singlet order does not become accessible by simply increasing the magnetic field strength. In this regime a specific pulse sequence such as singlet-to-magnetization (S2M) needs to be used to obtain the observable signal. The S2M pulse sequence is shown in Fig. 2.13 and is composed of two $J-$synchronised echo trains separated by a τ delay and $\frac{\pi}{2}$ pulse. Detailed theoretical descriptions of the S2M pulse sequence have been extensively discussed in the literature [231–234]. Here, only the main events in the pulse sequence are outlined. The initial density operator ($\hat{\rho}_0$), is given by Eq. 2.75. Fig. 2.14 shows the visual representation of the matrix for $\hat{\rho}_0$. The white boxes represent exact zeros while the non-zero elements are rendered in colors proportional to their magnitude. In the $\mathbb{ST}$ basis, only the singlet state is populated.

The application of the first J-synchronised echo train induces an approximate $\frac{\pi}{2}$ rotation about x-axis. As seen in the visual representation of the matrix for $\hat{\rho}_1$ in Fig. 2.16, this creates a coherence between the singlet and the central state $|T_0\rangle$.

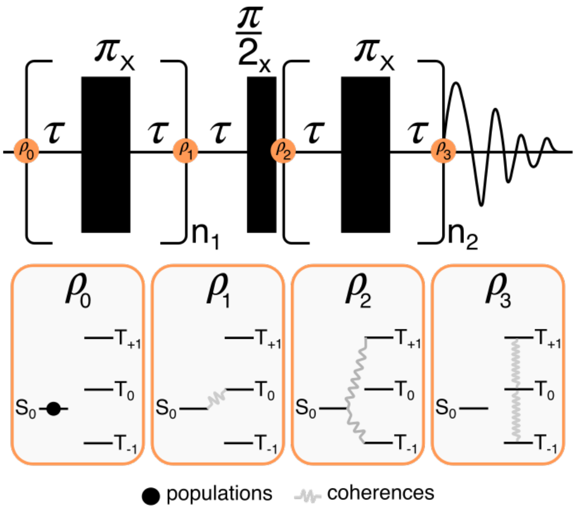

FIGURE 2.13: Singlet-to-magnetization pulse sequence. The main events in the pulse sequence are visualised. The optimal parameters for n_1, n_2 and τ can be calculated as follows: $n_1 = \frac{\pi J}{\Delta\omega}$, $n_2 = 2n_1$, and $\tau = \frac{1}{2\sqrt{(J)^2+\Delta\omega}}$ [232].

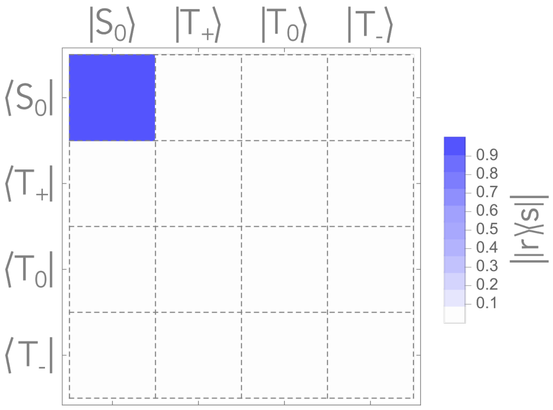

FIGURE 2.14: A visual representation for the matrix of $\hat{\rho}_0$ density operator in the $\mathbb{ST}$ basis. White boxes represent exact zeros while the non-zero elements are rendered in colors proportional to their magnitude. In the $\mathbb{ST}$ basis, only the singlet state is occupied.

The successive τ delay $-$ $\frac{\pi}{2}$ pulse block converts the $|S_0\rangle - |T_0\rangle$ into $|S_0\rangle - |T_+\rangle$ and $|S_0\rangle - |T_-\rangle$ coherences as can be seen in Fig. 2.16.

The next event in the pulse sequence is a second J-synchronised echo train. In this case, the echo train is looped $2n$ times and produces coherences between the inner and outer triplet states as shown in Fig. 2.17. The observable magnetization arises from the following single-quantum coherences [234]:

$$|T_0\rangle\langle T_+| + |T_+\rangle\langle T_0| + |T_-\rangle\langle T_0| + |T_0\rangle\langle T_-| \equiv \hat{I}_x. \tag{2.86}$$

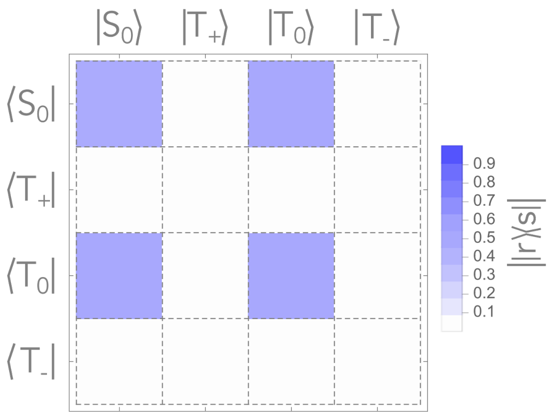

FIGURE 2.15: A visual representation of the matrix for the $\hat{\rho}_1$ density operator in the $\mathbb{ST}$ basis. The first J-synchronised echo train creates coherences between the $|S_0\rangle$ and the $|T_0\rangle$ state.

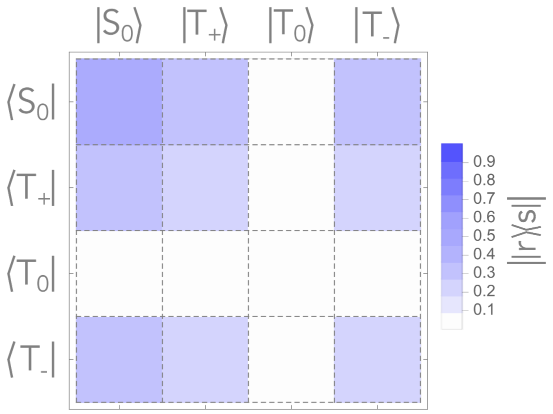

FIGURE 2.16: A visual representation of the matrix for the $\hat{\rho}_2$ density operator in the $\mathbb{ST}$ basis. After the τ delay and the $\frac{\pi}{2}$ pulse coherences between $|S_0\rangle$ and the two outer triplet states, $|T_-\rangle$ and $|T_+\rangle$ are created.

The residual terms do not contribute to the observable signal.

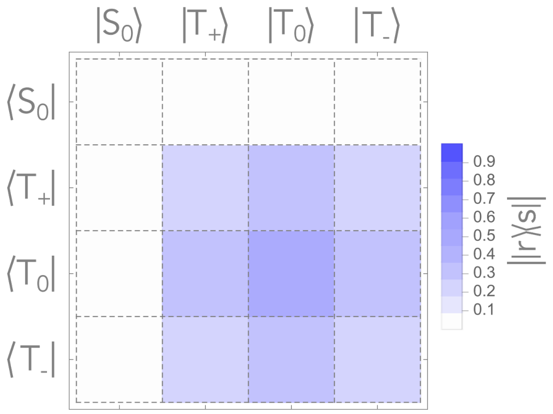

FIGURE 2.17: A visual representation of the matrix for the $\hat{\rho}_3$ density operator in the $\mathbb{ST}$ basis. The second $J-$synchronised echo train creates observable magnetization. This is visualised by the presence of single quantum coherences in the matrix.

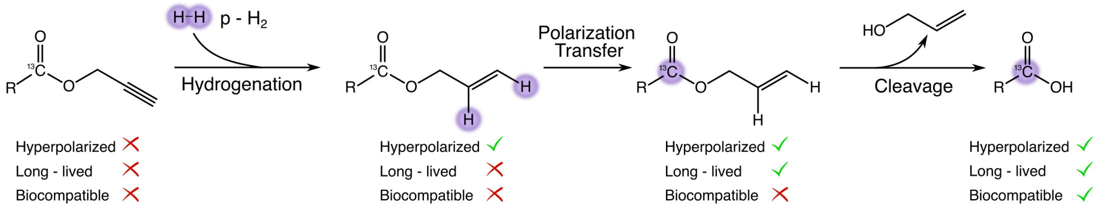

FIGURE 2.18: An overview of steps required to obtain a hyperpolarized, long-lived and biocompatible molecule by side-arm hydrogenation. The image was adapted from Ref. [21]

Side Arm Hydrogenation Parahydrogen induced polarization has been utilised to obtain structural and mechanistic information [23], in drug research [235], and to investigate molecular dynamics [236]. Perhaps the most important application for hyperpolarization methods is in medical diagnostics with the prospect of uncovering metabolic pathways that are currently unattainable due to sensitivity limitations [21]. In order to achieve this goal, the hyperpolarization target must fulfil the following requirements: (i) must be hyperpolarizable, (ii) must be biocompatible, (iii) the life time of the species must be long enough to allow for observation of the desired phenomenon. A widely used approach to overcome these issues is the side-arm hydrogenation (SAH-PHIP). Fig. 2.18 shows the general schematic of a SAH-PHIP reaction.

The first step is a reaction of the para state of hydrogen with an unsaturated precursor molecule in the presence of an organometallic catalyst. This yields a hyperpolarized molecule however, the molecule needs to undergo further transformations to become biologically relevant. Since the hyperpolarized molecules are subject to relaxation, which is of the order of a few seconds for protons, the polarization needs to be transferred a much longer lived nucleus such as carbon (relaxation of a few minutes). Carbon detection has an additional advantage as there are no background signals and it has a larger range of the ppm scale. The polarization transfer can be achieved through the magnetic field cycling [237–239] or application of RF pulses [223, 225, 240]. Once carbon polarized molecule has been created the so called "side-arm" needs to be cleaved and the molecule can be dissolved in an aqueous solvent. This can be achieved by a hydrolysis reaction where a hot solution of sodium hydroxide is added to create two phases. The organic phase contains the catalyst and the ester while the aqueous phase contains the hyperpolarized salt [235]. This yields a biocompatible, long-lived and hyperpolarized molecule.

Since its development in the group of Silivo Aime in 2015 [221], SAH-PHIP has been used to hyperpolarize acetate, pyruvate, and lactate [24].

PHIP@Chip Implementation of the hydrogenative PHIP at the microscale was demonstrated by Eills *et al.* [1]. The microfluidic reactor was made of PMMA and it contained channels for fluid and gas delivery, as well as 2.5 μL sample chamber, where species were detected. The diffusion of hydrogen into the fluid channel was facilitated by using a semi-permeable membrane. The chip and the membrane were held by a pair of screw-tightened 3D-printed holders with fluidic connectors that aligned with those on the microfluidic chip as shown in Fig. 2.19 a. All experiments were performed inside of a high-field NMR spectrometer. The precursor solution containing 5 mM of [1,4-Bis(diphenylphosphino)butane](1,5-cyclooctadiene)rhodium(I) tetrafluoroborate catalyst and 20 mM of propargyl acetate in methanol-d4 was delivered into the chip via a syringe pump located outside of the spectrometer. $\mathrm{p-H_2}$ gas with para-enrichment of 50% was supplied at 5 bar and its flow was controlled using a mass-flow controlled located at the end of the gas outlet as shown in Fig. 2.19 b. Inside of the magnet, the chip was placed in a home-build transmission line probe [138], which provided a planar orientation for the chip (Fig. 2.19 c). The detector was made of two stripline planes and the sample detection chamber was aligned with the constriction of the stripline planes, which is the sensitive area of the detector (Fig. 2.19 d). Using this set up a steady stream of hyperpolarized allyl acetate was obtained and signal enhancement of 1800 was reported, leading to 2.2 pmol $\sqrt{\mathrm{s}}$ mass sensitivity. The volume of the sample chamber was reported at 2.5 μL, therefore the concentration limit of detection of 0.8 μM was obtained. The remarkable stability of the hyperpolarized signal enabled acquisition of 2D-spectra using conventional t1 increments, which is unattainable using conventional set-ups as hyperpolarized signals decay rapidly.

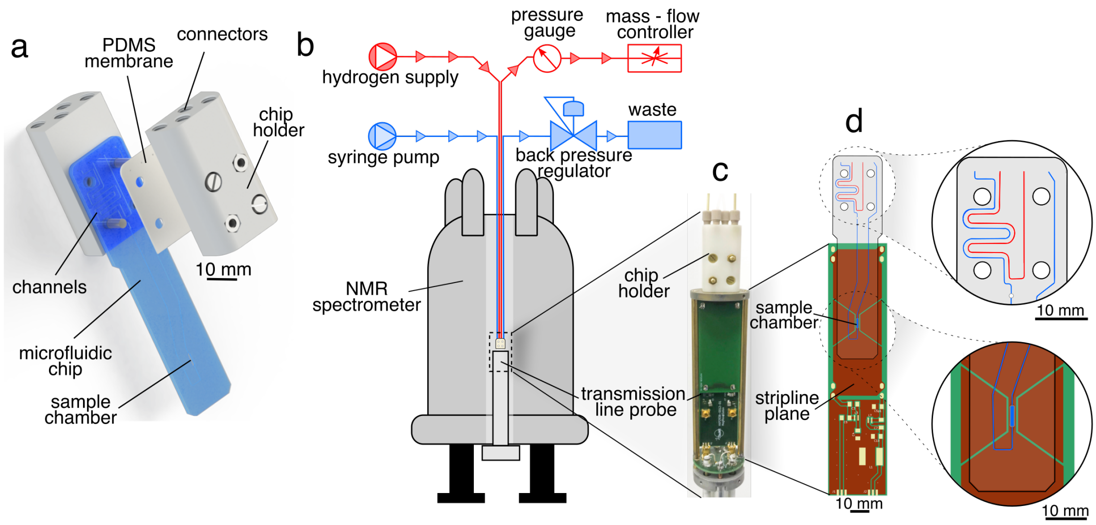

FIGURE 2.19: a) A microfluidic chip assembly. b) A diagram of the experimental set up. c) The transmission line probe provides a planar orientation of the chip. d) A drawing of the microfluidic device aligned with the stripline plane of the detector. The key areas of the drawing are enlarged.

However, the yield of the hyperpolarized material was very low at 2.5%, corresponding to a concentration of ∼0.5 mM of the hydrogenated substrate. Since further transformations and purification steps are needed after the hydrogenation, which would cause further losses, the device proposed by Eills *et al.* is not suitable for applications in the life sciences, unless its yield can be improved significantly. This requires a quantitative understanding of the interplay between the kinetics of the hydrogenation reaction, transport properties of the LoC device and the diffusion of reaction species in the flowing liquid as well as the diffusion of $\mathrm{p-H_2}$ gas through the membrane.

2.4 Computational Modelling

The simulation of a PHIP reaction in a microfluidic chip involves three key components: (i) the reaction kinetics, (ii) the space dynamics (i.e. the flow and diffusion in the chip) and (iii) the spin dynamics of the reaction. The problem generally can be expressed as a direct product of each component [241–243]:

$$[\text{space dynamics}] \otimes [\text{reaction kinetics}] \otimes [\text{spin dynamics}] \tag{2.87}$$

A typical metabolite (e.g. glucose) contains upwards of 10 coupled spins meaning a Liouville space dimension of at least $4^{10} \approx 10^6$, while a typical mesh contains upwards of 100 000 degrees of freedom. The Kronecker product between the spin and spatial dynamics results in a matrix of huge dimensions and the reaction kinetics have not even been taken under consideration. However, since the coupling between the spatial and spin dynamics is limited, these objects can be treated separately. In the following section finite element method is introduced to model the transport properties of the microfluidic device.

2.4.0.1 Finite Element Modelling

Finite element method was coined by Clough [244] in 1960 and it refers to a numerical method for solving partial differential equations. An approximate solution is obtained by discretization meaning that the problem is divided into a limited (finite) number of well-defined components (elements). Fig. 2.20 shows the overview of the finite element method workflow for a simple two-dimensional structure. The simulation domain is divided into smaller components called elements that are connected with each other via nodes. This operation is commonly referred to as meshing. There are many elements that can be used to create a 2D mesh such as triangular or quadrilateral elements. For more complex 3D meshing solid elements are used and very simple structures can even be represented by lines. Once a satisfactory mesh is obtained, each element is treated separately to calculate displacement or fluxes (in fluid mechanics) at each node. Once calculations are completed, the elements are re-assembled and a field solution is obtained.

FEM is a powerful modelling tool to analyse problems such as device design and material, establishing optimal parameters or experimental set up without the expense of laboratory time. Numerical simulations enable the study of conditions which are difficult to accurately measure experimentally, these include for instance the temperature, shear stress, and the velocity [245]. The key operating parameters: fluid flow, mass and heat transport, as well as chemical reaction kinetics can be simulated, providing researchers with an indispensable tool for rapid prototyping [246].

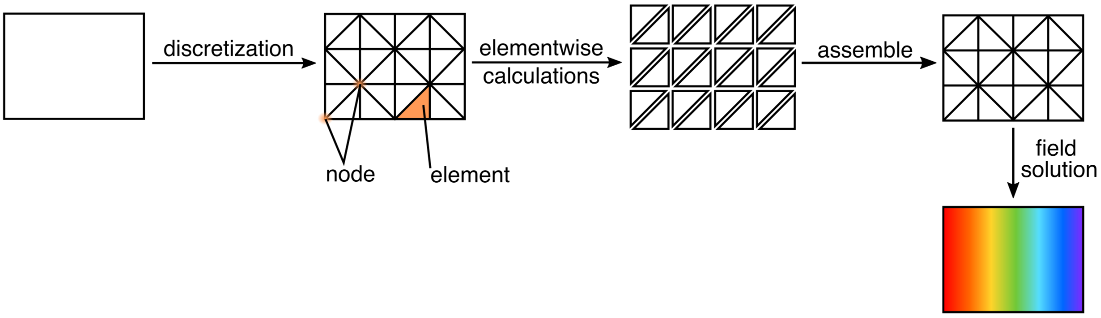

FIGURE 2.20: Workflow for the finite element method.

Computational fluid dynamics calculations have been used to model and simulate many reactors including micro-mixers [247], biosensors [248, 249] and catalytic reactors [250]. Numerical simulations can be particularly useful for biological studies where precise control over the environmental conditions is instrumental to make conclusions about the behaviour of an organism. For instance, the availability of oxygen determines if metabolic efficiency and fluctuations in cellular oxygen can cause changes in phenotype and function [20]. Therefore, determination of oxygen concentration in a cell culture is vital to ensure its stable growth and development. Commercially available oxygen sensors utilise invasive techniques based on electrochemistry that disturb the system, to tackle this issue, Ochs *et al.* [251] developed a computational model for estimating the oxygen consumption of endothelial cells and hepatocytes cultured in a microfluidic device. The model predicted the concentration of oxygen for three device materials: PDMS and two thermoplastics (poly(methyl pentene) and cyclic olefin copolymer). Since PDMS has a high oxygen permeability, the concentration of oxygen remained ∼constant however, hepatocytes consumed all available oxygen within 70 mins in a device made from cyclic olefin copolymer.

Numerical simulations can also be used to model and optimise kinetics of a reaction. For instance, immunoassay biosensors require a specific binding reaction between an analyte-ligand protein pair however, their performance is often limited by diffusion. Electrothermal microstirring has been used to accelerate the binding reaction. The method utilises a non-uniform electric field to induce a pair of vortices that enhance the mixing but the efficiency of this technique is dependent on the proximity of the vortices to the biosensor. Huang *et al.* [252] simulated the effect of varying the

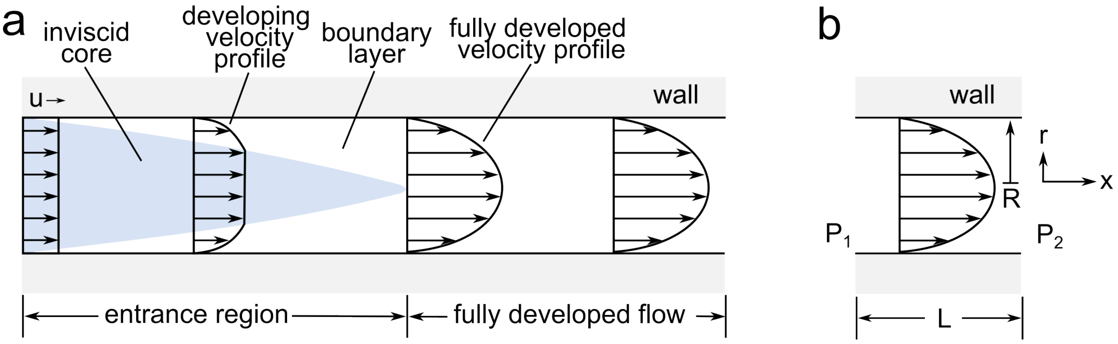

FIGURE 2.21: a) Flow profile in a pipe b) Parameters of the parabolic velocity profile.

condition of electrothermal microsirring to accelerate the binding kinetics of C-reactive protein (CRP) and immunoglobulin G (IgG). In their study, the association and dissociation of the protein pair was simulated to obtain a time-resolved surface concentration profile. Then, the position of the sensor in the microchannel was varied to determine the location where the enhancement of the binding reaction was the largest. Finding the optimal position rised the slope of the analyte-complex association curve by 5.17 for CRP and 1.98 for IgG as well as 3.74 for CRP and 1.28 for IgG in dissociation. The study found that further improvements can be made by optimising the temperature of the reaction and the geometry of the reactor.

To our knowledge, such simulations have not been carried out in the context of a PHIP reaction.

2.4.0.2 Flow

As discussed in Section 2.1.1.1, due to the small channel dimension the Reynolds number in a microfluidic device is low, and since only low flow rates are utilised the flow profile is laminar. When fluid enters a pipe the velocity is uniformly distributed resulting in a flat flow profile as shown in Fig. 2.21 a. However, at the fluid/wall boundary there is a significant shear stress due to the friction between fluid particles that leads to deceleration of the fluid adjacent to the boundary layer. This layer grows as the fluid travels down the pipe leading to a velocity gradient but at the core of the developing profile, shown in blue in Fig. 2.21 a, the shear stress is negligible therefore the velocity profile appears flat. At the end of the entrance region, the velocity profile is said to be fully developed and has a parabolic shape, which is characteristic for the laminar flow regime . The shear stress encompasses the entire flow profile, the average velocity does not change change, and the velocity at the wall is zero because of no-slip boundary. The parabolic velocity profile can be described by the Poiseuille flow [36]:

$$u = -\frac{\Delta P}{L}\frac{1}{4\mu}(R^2 - r^2), \tag{2.88}$$

where $\Delta P = P_1 - P_2$ is the pressure difference between the inlet and the outlet of the channel, L is the length of the channel, μ is the dynamic viscosity, and R is the radius of the channel as shown in Fig. 2.21 b.

In this work only incompressible fluids are considered, meaning that the density of such fluid is approximately uniform and the heat transfer can be neglected. As a result, equations describing the conservation of mass and momentum are sufficient to describe the fluid flow [253]. Conservation of mass equation, also referred to as the continuity equation, states that the mass of a fluid contained within a control volume stays constant:

$$\nabla \cdot (\rho \mathbf{u}) = 0, \tag{2.89}$$

where $\mathbf{u}$ is the velocity of the fluid, $\nabla\cdot$ is the divergence and ρ is the density. Since ρ is uniform for incompressible flow, this simplifies to:

$$\nabla \cdot \mathbf{u} = 0 \tag{2.90}$$

Conservation of momentum for a Newtonian fluid can be described by the Navier-Stokes equation [40]:

$$\rho\frac{\partial \mathbf{u}}{\partial t} + \rho\mathbf{u}\cdot\nabla\mathbf{u} = -\nabla p + \eta\nabla^2\mathbf{u}, \tag{2.91}$$

where the changes in momentum ($\rho\frac{\partial \mathbf{u}}{\partial t}$) are caused by the net momentum convected out of the control volume by the fluid flow ($\rho\mathbf{u}\cdot\nabla\mathbf{u}$), the surface ($\nabla p$), and the body forces $\eta\nabla^2\mathbf{u}$.

2.4.0.3 Diffusion-Convection-Reaction

Diffusion and convection facilitate the transport of a scalar, here we are concerned with chemical species (Δc), in or out of the control volume [254, 255]. Diffusion is a passive movement of molecules down the concentration gradient due to random thermal fluctuations. Fick's first law relates the diffusive flux to the chemical species gradient and their diffusivity in the solvent (D):

$$\mathbf{j}_{diff} = -D\Delta c, \tag{2.92}$$

where $\mathbf{j}_{diff}$ is the diffusive flux density (i.e. the net amount of species diffusing across per unit area per unit time). Alongside the random fluctuations due to thermal motions, molecules are transported due to fluid convection that leads to a convective flux:

$$\mathbf{j}_{conv} = \mathbf{u}c, \tag{2.93}$$

where $\mathbf{j}_{conv}$ is the convective flux density of chemical species (i.e. the net amount of species convecting across per unit area per unit time). The application of fluxes $\mathbf{j}_{conv}$ and $\mathbf{j}_{diff}$ to a control volume leads to the covection-diffusion equation for chemical species c_i:

$$\frac{\partial c_i}{\partial t} + \mathbf{u} \cdot \nabla c_i = D\nabla^2 c_i, \tag{2.94}$$

where ∇^2 is the Laplace operator. If chemical reactions are taking place in the flowing fluid this can be accounted for by adding a reaction term R_i such that Eq. 2.94 becomes a convection-diffusion-reaction equation:

$$\frac{\partial c_i}{\partial t} = -\mathbf{u} \cdot \nabla c_i + D\nabla^2 c_i + R_i. \tag{2.95}$$

For a simple reaction:

$$A + B \xrightarrow{k_1} P \tag{2.96}$$

The rate equation are:

$$\begin{aligned}\frac{\mathrm{d}[\mathbf{A}]}{\mathrm{d}t} &= -k_1[\mathbf{A}],\\ \frac{\mathrm{d}[\mathbf{B}]}{\mathrm{d}t} &= -k_1[\mathbf{B}],\\ \frac{\mathrm{d}[\mathbf{P}]}{\mathrm{d}t} &= +k_1[\mathbf{P}].\end{aligned} \tag{2.97}$$

Therefore Eq. 2.95 for species A becomes:

$$\frac{\partial[\mathbf{A}]}{\partial t} = -\mathbf{u}\cdot\nabla[\mathbf{A}] + D\nabla^2[\mathbf{A}] - k_1[\mathbf{A}]. \tag{2.98}$$

Chapter 3

Materials and Methods

3.1 Device Fabrication

Microfluidic devices were designed in AutoCad 2019. In this work, microfluidic devices were manufactured from polycarbonate (PC) (Self Adhesive Supplies, United Kingdom) in contrast to poly(methyl methacrylate) (PMMA) material used for the $\alpha-$chip reported by Eills *et al.* [1]. The material was changed to improve the durability as PMMA has a lower chemical resistance and is brittle which led to frequent leakages and breakages during experiments. As shown in Fig 3.1 a, devices were fabricated from three layers of PC (Self Adhesive Supplies, United Kingdom) with 0.25, 0.5, and 0.25 mm thickness for the top, middle, and bottom layers, respectively. The layers were cut out from PC sheets using a LS3040 CO_2 laser cutter (HPC Laser Ltd, United Kingdom). The channels were cut through the top layer and engraved in the middle layer. The sample chamber was cut through the middle layer. Unlike the $\alpha-$chip, the $\beta-$chip design has channels engraved in the bottom layer. To bond a device, one side of each layer was plasma activated (Electro-Technic Products, USA) and coated with 18 μL of a plasticiser solution (5 v/v% dibuthyl phalate in isopropyl alcohol). Then the layers were placed in a 65°C oven for 15 mins to dry. After that time, the layers were aligned and placed in a heat press (85°C, 5 tonnes) for 20 mins. A PDMS membrane was cut out from a 1 mm thick PDMS sheet (Shielding Solutions, United Kingdom) using the CO_2 laser cutter described above. The membrane was placed over

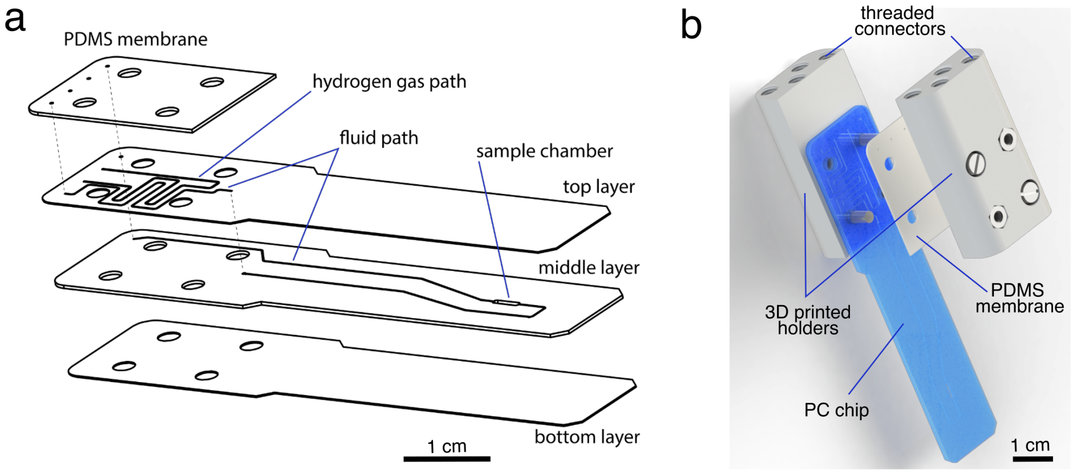

FIGURE 3.1: a) An illustration of the three layers of a microfluidic chip with the channels cut through the top layer and engraved in the middle layer. The sample chamber is cut through the middle layer. The $\beta-$chip design has channels engraved in the bottom layer. b) A rendering of the chip assembly consisting of a PC device and a PDMS membrane, which are held together using a screw-tightened 3D printed holders. The holders contain threaded connectors for 1/16" capillaries.

the top half of the chip to seal the channels and allow hydrogen to diffuse from the gas into the liquid channel. The chip and the membrane were held together by 3D printed holders (ProtoLabs, United Kingdom) that attached threaded connectors for 1/16" capillaries (Cole-Parmer, United Kingdom) to the four access points on the chip for gas and liquid inlets and outlets as shown in Fig. 3.1 b.

3.2 Microfluidic Set up

All micro-NMR experiments were performed using an 11.7 T magnet equipped with a Bruker AVANCE III spectrometer system. The precursor solution was delivered into the chip using a syringe pump (Cole-Parmer, United Kingdom) located outside of the NMR spectrometer as illustrated in Fig. 3.2 a. Hydrogen gas (gas purity 99.995%) was delivered from a cyliner located outside of the spectrometer at a flow rate set to 20 mL min^{-1} controlled using a mass-flow controller at the end of the gas line. As a result, the chemical reaction took place in the microfluidic device. In the magnet, the device was placed in a home-built transmission line probe [138] and the reaction products were detected in a 2.5 μL sample chamber. The chamber of the chip was

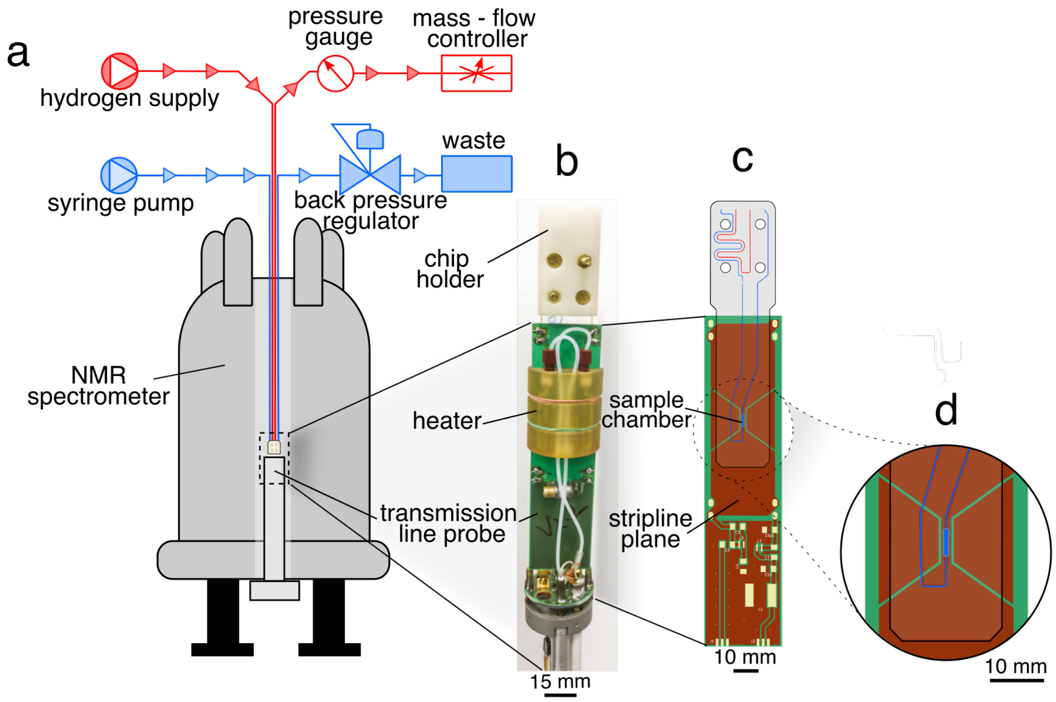

FIGURE 3.2: The experimental set up for the PHIP on a chip experiment. a) All experiments were preformed inside of a high-filed NMR spectrometer. The precursor solution was delivered to the device via a syringe pump located outside of the spectrometer. Hydrogen was delivered from a cyliner located outside of the spectrometer and its flow was controlled using a mass-flow controller at the end of the gas line. b) Inside of the magnet, the device sat in a home build transmission line probe [138] and the temperature at the sample chamber was regulated by a heater clamped outside of the detector. c) The sample chamber of the chip aligns with the constriction at the stripine plane. d) Enlarged view of the sensitive area of the chip.

aligned with the constriction of the striplane plane, which is the sensitive region of the detector as illustrated in Fig. 3.2 c and d [138]. The temperature at the sample chamber was regulated by a PID controlled water heater equipped with a thermistor (RS components, United Kingdom) that was clamped outside of the detector as shown in Fig. 3.2 b. The heated area did not include the chip holders since the solubility of hydrogen decreases with increasing temperature. The temperature recorded by the heater was calibrated against the temperature at the sample chamber of the chip by determining the chemical shift difference of water and DSS peaks (10 mM). The error was estimated by taking the variation in the width of the water peak.

3.3 Experimental Procedures

All chemicals were purchased from Merck KGaA (Germany) and were used as purchased.

3.3.1 Standard Bubbling Experiments

The precursor solution was prepared by dissolving 20 mM (10 μL) of propargyl acetate and 5 mM (18 mg) of [1,4-bis(diphenylphosphino)butane](1,5-cyclooctadiene)rhodium(I) tetrafluoroborate in 5 mL methanol-d4. 400 μL of the solution was pipetted into a 5 mm Wilmad® quick pressure valve NMR tube (Merck KGaA, Germany). The reaction was performed by pressurising the tube with 5 bar of hydrogen in thermal equilibrium (purity 99.995%) and bubbling the gas at 400 mL min^{-1} for 10 s inside a 9.4 T Oxford AS400 magnet equipped with Bruker AVANCE Neo console. After bubbling, the sample was left to settle for 25 s and a spectrum was acquired. The nutation frequency for RF pulses was 20.8 kHz for protons. 32 k data points were acquired over 3.3 s for proton 1D spectra. A total of 19 spectra were acquired. Hydrogen was bubbled prior every acquisition. The bubbling set up used in this work is described in detail by Dagys *et al.* [256]. The concentration profile for species involved in the reaction was obtained by integrating a corresponding region in a ^{1}H NMR spectrum. Propargyl acetate: 2.85 to 2.95 ppm; allyl acetate 5.00 to 5.50 ppm; propyl acetate 3.97 to 4.06 ppm; catalyst 2.49 to 2.64 ppm. Integrals were calibrated against the concentration of propargyl acetate peak at 2.85 to 2.95 ppm, which was 20 mM.

3.3.2 Hydrogen Uptake into $\beta-$chip

The uptake of hydrogen into the $\beta-$chip was quantified by flowing a solution of methanol-d4 doped with 20 mM of sodium acetate. In the gas channel, hydrogen in thermal equilibrium was flowed at 5 bar. The flow rate was varied from 2 to 20 $\mu\text{L}\,\text{min}^{-1}$ in steps of 2 $\mu\text{L}\,\text{min}^{-1}$ and the solution was left to equilibrate for

10 minutes at each flow rate. Then, 64 scans were acquired after the application of a $\frac{\pi}{2}$ pulse with a recycle delay of 20 s.

3.3.3 Microscale Propargyl Acetate Hydrogenation

The precursor solution contained 5 mM of [1,4-bis(diphenylphospino)butane](1,5-cycloctadiene) rhodium (I) tetrafluoroborate and 20 mM of propargyl acetate in methanol-d4. Parahydrogen gas at 50% enrichment was generated by flowing hydrogen gas (99.995% purity) through a home-built parahydrogen generator, which contained iron (III) oxide cooled to 77K with liquid nitrogen. The gas pressure was set to 5 bar. The nutation frequency for RF pulses was 125 kHz for protons. Spectra were collected with a 16 ppm spectral width and 8 k data points. Data was acquired continuously while varying the flow rate from 2 to 12 $\mu\mathrm{L\,min^{-1}}$ in steps of 1 $\mu\mathrm{L\,min^{-1}}$ and from 14 to 20 $\mu\mathrm{L\,min^{-1}}$ in steps of 2 $\mu\mathrm{L\,min^{-1}}$. At each flow rate, 20 single scan spectra were acquired after the application of a $\frac{\pi}{4}$ pulse with a recycle delay of 30 s. At these experimental conditions, it took ~2 minutes for the hyperpolarized signal to build up and stabilise therefore the first 10 transients at each flow rate were discarded to ensure that only steady-state data was taken into consideration.

Spectral integrals were derived by fitting two Lorentzian functions to the H^h signal. This is illustrated in Fig. 3.3, where the blue line represents the experimental data and the black solid line is the fit. Only the positive lobe of the antiphase peak was integrated, which is indicated as the shaded region. Each data point reported in Fig. 5.5 represents a mean of 10 integrals. Error in the data is the mean error of fit. Julia 1.6 [257] with NMR package written by Marcel Utz [258] was used to perform the fitting routine.

Reference spectra were obtained using hydrogen in thermal equilibrium instead of parahydrogen. 10 mM of IPA was added as the concentration standard, all other conditions remained identical. The solution was flowed at 5, 7 and 9 $\mu\mathrm{L\,min^{-1}}$ for 25°C, 37°C and 47°C, respectively. Each reference spectrum is an average of 512 transients with a 30 s recycle delay. The yield of allyl acetate was found by comparing

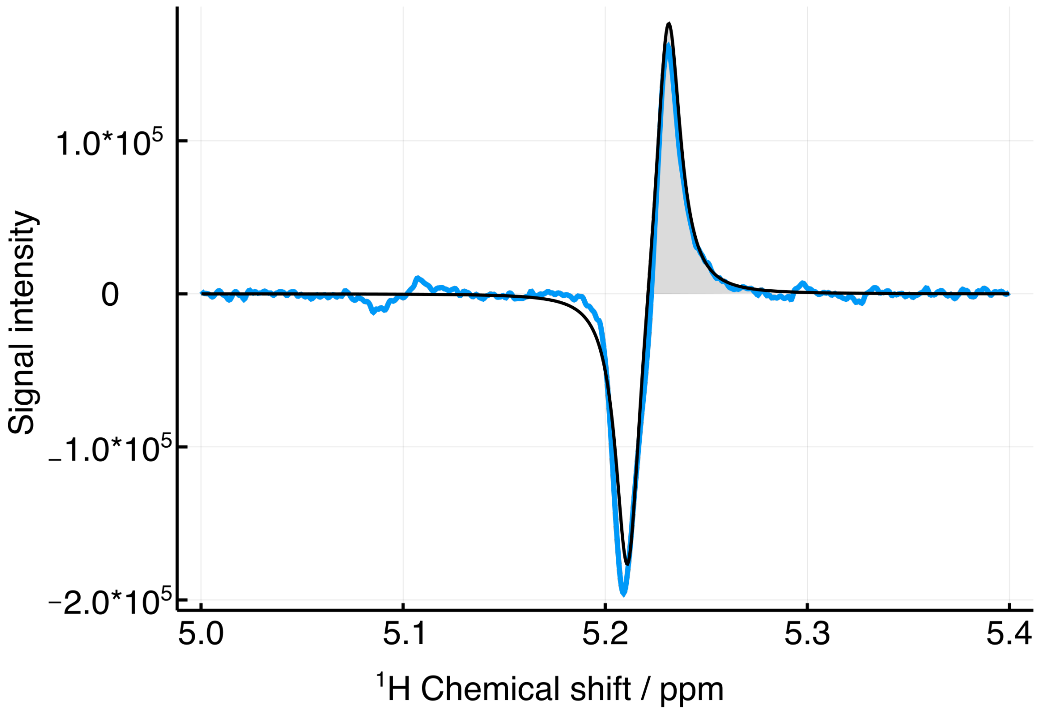

Figure 3.3: An illustration of the fitting routine used to obtain the integral values from PASADENA experiments. The hyperpolarized spectrum of allyl acetate is shown in blue while the fitted Lorentzian function is shown in black. The integral was obtained by taking the area under the positive lobe of the antiphase peak, which is indicated as the grey shaded region.

the integral of signal H^f peak at 5.9 ppm to the intensity of the IPA peak at 1.1 ppm and accounting for the difference in the number of protons. The yield of propyl acetate was calculated as described above, from the integral of H^i peak at 4.33 ppm to the intensity of the IPA peak. The enhancement factor was obtained by calculating the SNR in the thermal and reference spectra and accounting for the difference in the number of scans.

3.3.4 Microscale Acetylene Dicarboxylic Acid [1-^{13}C] Disodium Salt Hydrogenation

The precursor solution contained 100 mM acetylene dicarboxylic acid [1-^{13}C] disodium salt, 6 mM [RuCp*(CH_3CN)$_3$]PF_6 catalyst and 200 mM sodium sulfite dissolved in D_2O at 50°C. ^{1}H experiments were carried out with the temperature of the water heater set to 50°C. *Para*-enriched hydrogen gas (gas purity 99.995%) was continuously produced by a Bruker parahydrogen generator BPHG90, with a specified parahydrogen content of 89%. Flow rates from 2 to 2 μL min^{-1} in steps of 2 μL min^{-1} were studied. The probe delivered nutation frequencies for ^{1}H RF pulses of 100 kHz. Spectra were collected with a 16 ppm spectral width, and 8 k data points were acquired.

Proton singlet order in [1-^{13}C]fumarate was converted into the observable magnetisation using the singlet-to-magnetisation (S2M) pulse sequence. The maximum efficiency was achieved using the following parameters: $\tau = 15.6$ ms, $n_2 = 14$, $n_1 = 7$. The repetition delay was set to 60 s.

The CW-S2M experiments were performed by applying continuous wave irradiation for 20 s at 0.488 and 1.935 kHz, while changing the resonance offset from 20 to -20 ppm. θ-S2M experiments were performed by applying a hard pulse of varying flip angle prior the S2M pulse sequence. This was achieved by varying the pulse duration from 0 to 8 μs in steps of 0.22 μs.

The reference spectrum was obtained using hydrogen in thermal equilibrium. The ^{1}H spectrum was obtained by applying a $\frac{\pi}{2}$ pulse and averaging over 400 scans with a recycle delay of 20 s. The enhancement factor was calculated by comparing the integral of H$^{\text{a}}$ peak in the hyperpolarized and the reference spectrum and accounting for the difference in the number of scans.

An identical precursor solution was used for ^{13}C experiments. Hydrogen gas with 50% *para*-enrichment was generated form the aforementioned home-build parahydrogen generator. The gas pressure was set to 6 bar. The heater temperature was set to 58°C. Flow rates from 2 to 18 μL min^{-1} in steps of 2 μL min^{-1} were studied. The probe delivered nutation frequencies for ^{13}C RF pulses of 12.5 kHz. Spectra were collected with a 200 ppm spectral width, and 8 k data points were acquired. Proton singlet order in [1-^{13}C]fumarate was converted into the observable magnetisation using the singlet-to-heteronuclear-magnetisation (S2hM) pulse sequence. The maximum efficiency was achieved using the following parameters: $\tau = 15.7$ ms, $n_2 = 6$, $n_1 = 6$. The repetition delay was set to 60 s. To calculate the enhancement factor for carbon polarization, the SNR of in the hyperpolarized spectrum was compared with the SNR obtained form a spectrum of 1M D-glucose-1-^{13}C averaged over 32 scans.

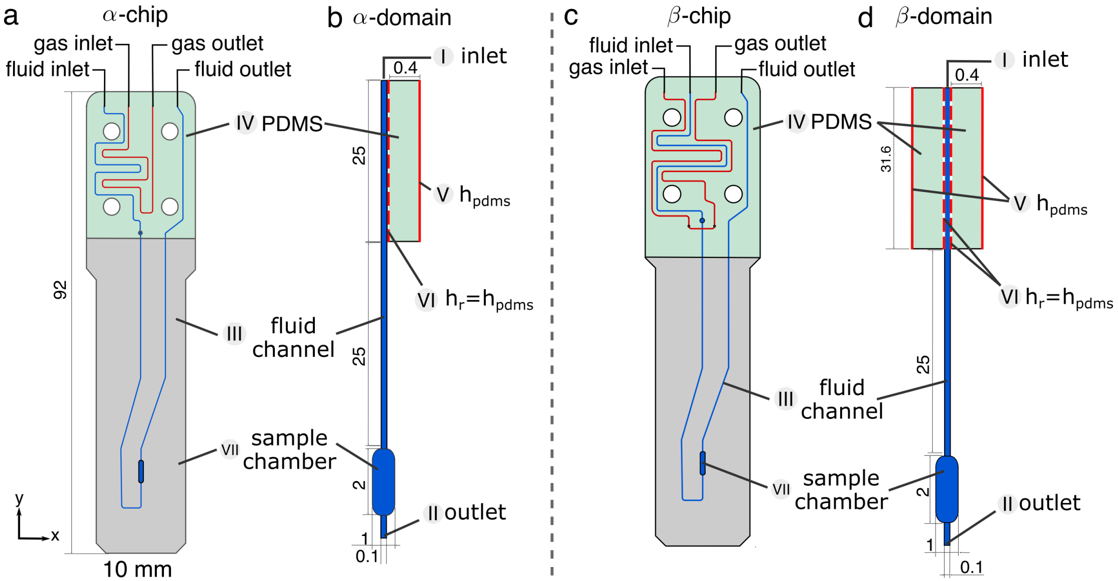

FIGURE 3.4: a) The top view of the $\alpha-$chip. b) The finite element simulation domain representing the $\alpha-$chip. c) The top view of the $\beta-$chip. d) The FEM simulation domain representing the $\beta-$chip.

3.4 Simulations

Rate equations for 5 irreversible reactions 4.1a - 4.1e were generated in Mathematica version 12 (Wolfram Research, Inc.) using a home-built Kinetics Toolbox [259]. Fitting of the experimental data obtained from the macroscopic bubbling experiments reported in Fig. 4.5 was done using the non-linear model fit function built into Mathematica.

3.4.1 COMSOL Simulations

Finite element simulations were performed using COMSOL Multiphysics version 5.4. The top view of the $\alpha-$chip reported in Ref. [1] is shown in Fig. 3.4 a. The key functional parts of the chip are: the gas channel, the fluid channel, the sample chamber and the PDMS membrane. The simulation domain consisted of a fluid channel III (50 mm length, 0.1 mm width) with a sample chamber VII (2 mm length, 1 mm width) and a PDMS membrane IV (25 mm length, 0.4 mm width). The entrance thickness was set to $120 * 10^{-5}$ m, which resulted in a chip volume of 8.5 μL. Fig. 3.1 c shows the top view of the $\beta-$chip where an additional hydrogen channel was added to increase the uptake of hydrogen into the chip. To simulate an additional hydrogen channel, a PDMS membrane, h_{pdms} and h_r boundaries were added in the β simulation

Simulation Parameters / units	
Flow Rate / $\mu\mathrm{L\,min^{-1}}$	$2\ldots50$
Diffusion Coefficient / $\mathrm{m^2\,s^{-1}}$	$1\cdot10^{-9}$
Concentration of Analyte $[\mathbf{2}]_0$ / mol $\mathrm{m^{-3}}$	20
Temperature / K	298.15

TABLE 3.1: Parameters used in COMSOL simulations for hydrogen uptake in the $\alpha-$ and $\beta-$domains.

domain as shown in Fig. 3.1 d. Furthermore, the length of the fluid pathway in contact with the PDMS membrane and the membrane itself were elongated by 6.6 mm. The total volume of the $\beta-$chip was calculated as 7 μL. A simple 2D representation of the chips was used in order to reduce the computation time and allow to explore a wider parameter space. The Laminar Flow module in COMSOL was used to find the flow pattern in the fluid channel. This was done by solving the Navier-Stokes equations for laminar flow regime for incompressible fluid, recalling the conservation of mass Eq. 2.90:

$$\nabla\cdot\mathbf{u}=0,$$

where $\nabla\cdot$ is the divergence and $\mathbf{u}$ is the flow velocity. The conservation of momentum is given by Eq. 2.91:

$$\rho\frac{\partial\mathbf{u}}{\partial t}+\rho\mathbf{u}\cdot\nabla\mathbf{u}=-\nabla p+\eta\nabla^2\mathbf{u},$$

where the changes in momentum ($\rho\frac{\partial\mathbf{u}}{\partial t}$) are caused by the net momentum convected out of the control volume by the fluid flow ($\rho\mathbf{u}\cdot\nabla\mathbf{u}$), the surface ($\nabla p$), and the body forces $\eta\nabla^2\mathbf{u}$.

The Transport of Dilute Species module was used to simulate the uptake of hydrogen into the chips. The gas channel was not explicitly modelled instead a constant hydrogen concentration condition was imposed on the outer boundary of the PDMS membrane V shown as $\mathrm{h_{pdms}}$, $[\mathbf{2}]=$ 20mM in Fig. 3.4 b. In order to couple the membrane to the reaction pathway, another condition $\mathrm{h_r}=\mathrm{h_{pdms}}$ was imposed on the boundary between PDMS membrane and the reaction channel marked as VI. The convection-diffusion Eq. 2.94 for hydrogen becomes:

Simulation Parameters / units	**Values**
Flow Speed / $\mu\text{L}\,\text{min}^{-1}$	$2 \dots 50$
Diffusion coefficients / $\text{m}^2\,\text{s}^{-1}$	$1 \cdot 10^{-9}$
Concentration of Analyte $[\mathbf{1}]_0$ / mol m^{-3}	5
Concentration of Analyte $[\mathbf{2}]_0$ / mol m^{-3}	20
Concentration of Analyte $[\mathbf{3}]_0$ / mol m^{-3}	20
Concentration of Analyte $[\mathbf{1c}]_0, [\mathbf{3a}]_0, [\mathbf{4}]_0, [\mathbf{4a}]_0, [\mathbf{4rx}]_0, [\mathbf{5}]_0, [\mathbf{6}]_0$ / mol m^{-3}	0
k_1 $\text{mM}^{-1}\,\text{s}^{-1}$	0.0015
k_2 / $\text{mM}^{-1}\,\text{s}^{-1}$	0.5016
k_3 / $\text{mM}^{-1}\,\text{s}^{-1}$	0.0056
k_4 / $\text{mM}^{-1}\,\text{s}^{-1}$	0.0014
k_5 / $\text{mM}^{-1}\,\text{s}^{-1}$	0.0038
k_6 / s^{-1}	0.14
Temperature / K	298.15

TABLE 3.2: Parameters used in COMSOL for simulating the propargyl acetate hydrogenation reaction in $\alpha-$ and $\beta-$domains.

$$\frac{\partial c_{H_2}}{\partial t} = D\nabla^2 c_{H_2} - \mathbf{u} \cdot \nabla c_{H_2}, \tag{3.1}$$

All simulation parameters are listed in Table 3.1.

The Transport of Dilute Species module in COMSOL was also used to simulate the chemical reaction in the flowing fluid, the velocity distribution was used in the diffusion-convection-reaction Eq. 2.95:

$$\frac{\partial c_i}{\partial t} = -\mathbf{u} \cdot \nabla c + D\nabla^2 c + R_j,$$

c_i is the concentration of species i, R_i are the rates of species involved in the reaction. Reaction rates for 10 species defined by Eq. 4.2a to Eq. 4.2j and their rate constants together with other simulation parameters are listed in Table. 3.2.

Physics-controlled mesh was automatically generated with the element size set to fine. Overall, the $\alpha-$chip mesh consisted of 45210 elements, and the computation involved 312446 independent degrees of freedom. The $\beta-$domain mesh consisted of 45469 elements, and the computation involved 271077 independent degrees of freedom. PARDISO stationary solver was used.

Chapter 4

Spatially Resolved Kinetic Model of PHIP in a Microfluidic Chip

This chapter is an extended version of S. J. Ostrowska, A. Rana, M. Utz, Spatially Resolved Kinetic Model of Parahydrogen Induced Polarisation (PHIP) in a Microfluidic Chip, *ChemPhysChem*, 22(19), 2004-2013, 2021 [2].

4.1 Introduction

Integration of catalytic hydrogenation and product detection onto a single LoC platform, enables performance of PHIP reactions in a highly controlled and repeatable manner [220, 1]. As discussed in the background section, Eills *et al.* [1] reported a microfluidic PHIP set up that achieved signal enhancements of 1800, leading to pmol $\sqrt{\text{s}}$ mass sensitivity. However, the yield of the hyperpolarized material was very low at ∼2.5%, corresponding to a concentration of ∼0.5 mM of the hydrogenated product. Since further transformation and purification steps are needed after the hydrogenation, which would cause further losses, the proposed device is not suitable for applications in the life sciences, unless its yield can be improved significantly. This requires quantitative understanding of the interplay between the kinetics of the hydrogenation reaction, the transport properties of the LoC device and the diffusion of

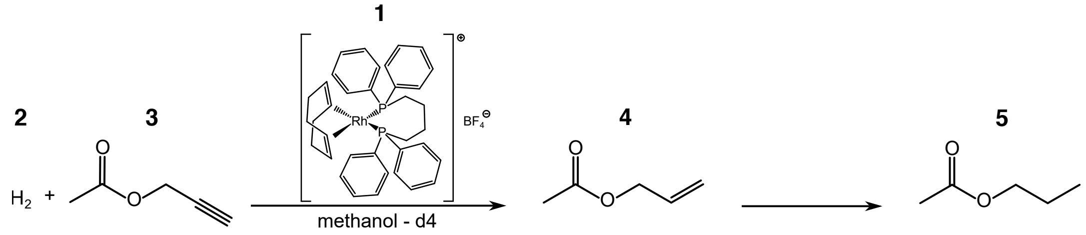

FIGURE 4.1: A schematic of the hydrogenation reaction studied. $[Rh(dppb)COD]BF_4$ **1** catalyses the reaction of hydrogen gas **2** and propargyl acetate **3** to produce allyl acetate **4**. Upon further hydrogenation propyl acetate **5** is formed.

reaction species in the flowing liquid as well as the diffusion of $p-H_2$ gas through the membrane.

In this chapter, the development of a spatially resolved kinetic model of a PHIP reaction in the device proposed by Eills *et al.* [1], here referred to as the $\alpha-$chip, is discussed. The reaction modelled is displayed in Fig 4.1 where $[Rh(dppb)COD]BF_4$ **1** catalyses the reaction of hydrogen gas **2** with propargyl acetate **3** in a microfluidic device.

The model development proceeded in two phases. First, a kinetic model of the reaction itself was developed. A set of kinetic equations was derived from the known reaction mechanism [260–267]. Although kinetic data can be obtained using microfluidic devices, such measurements are much more cumbersome due to the limited signal-to-noise ratio in the microfluidic system with thermal hydrogen. Additionally, the time scale for formation of propyl acetate is difficult to reach in flow and extremely low flow rates would be required. Therefore, the experimental kinetic data was obtained in conventional scale NMR tubes, where thermal hydrogen gas **2** was bubbled through the solution of propargyl acetate **3** and the catalyst **1**, and the evolving concentrations of the reaction products were monitored by NMR. In phase two, a coupled convection-diffusion-reaction finite element model was developed, using the rate constants obtained from the macroscopic experiments. In the remainder of this paper, the computational model is explained in detail, and the experimental results for the microscopic reaction of propargyl acetate with parahydrogen are discussed. Finally, the resulting FEM calculations are compared to the experimental data reported by Eills *et al.* [1].

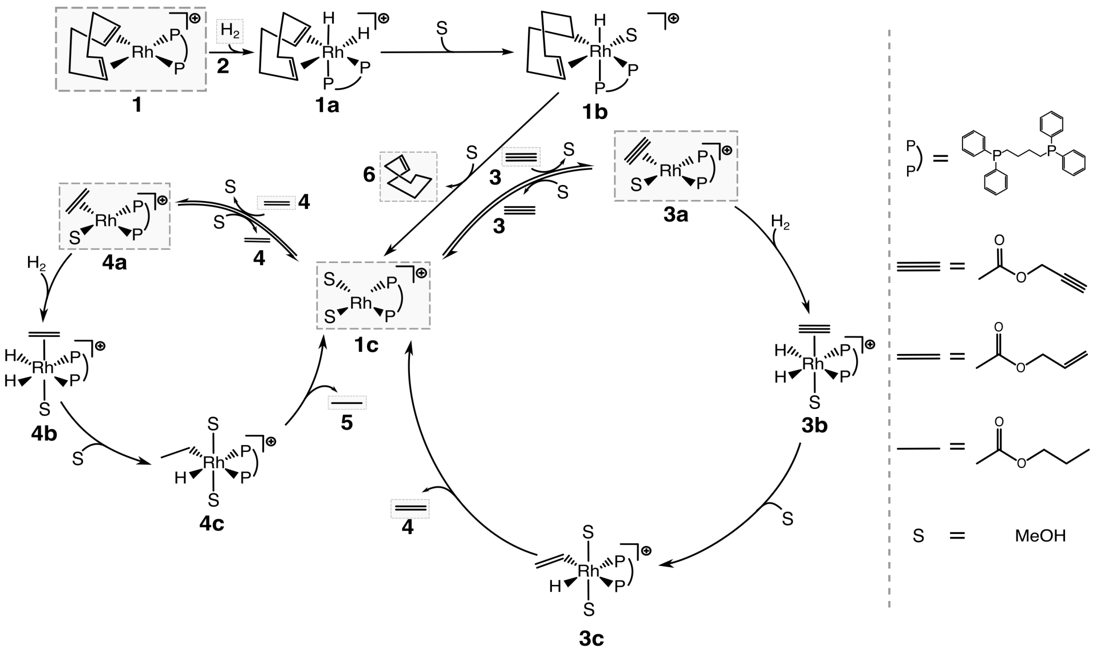

FIGURE 4.2: The full reaction mechanisms of the propargyl acetate hydrogenation reaction in the presence of [Rh(dppb)COD]BF_4 catalyst. The key species in the mechanisms are highlighted.

4.2 Reaction Mechanism and Kinetic Model

At the start of the reaction, the catalyst is in its inactive form **1** as shown in Fig. 4.2. The activation takes place through an oxidative addition reaction, where a hydrogen molecule **2** binds to the metal centre, creating a highly unstable octahedral complex **1a**. In order to return to the stable square planar configuration, the η^2-η^2 cyclooctadiene ligand gets reduced to κ^3 - cyclooct-4-enyl ligand (complex **1b**) [260]. Lastly, the reduced ligand dissociates, creating a highly active, electron poor Rh^+ centre i.e the active catalyst **1c**. The catalytic cycle starts through an association of a propargyl acetate molecule **3** to the active catalyst to create complex **3a** [261]. This step is followed by an oxidative addition of hydrogen (complex **3b**) and subsequent reduction of propargyl acetate to allyl acetate (complex **3c**). The last step in this cycle is the elimination of allyl acetate **4** from the complex [262]. Since the catalyst is non-selective, allyl acetate can re-enter the cycle to get hydrogenated fully to propyl acetate (**5**) in the same manner.

This mechanism has many steps and is too complex to determine the rate constants

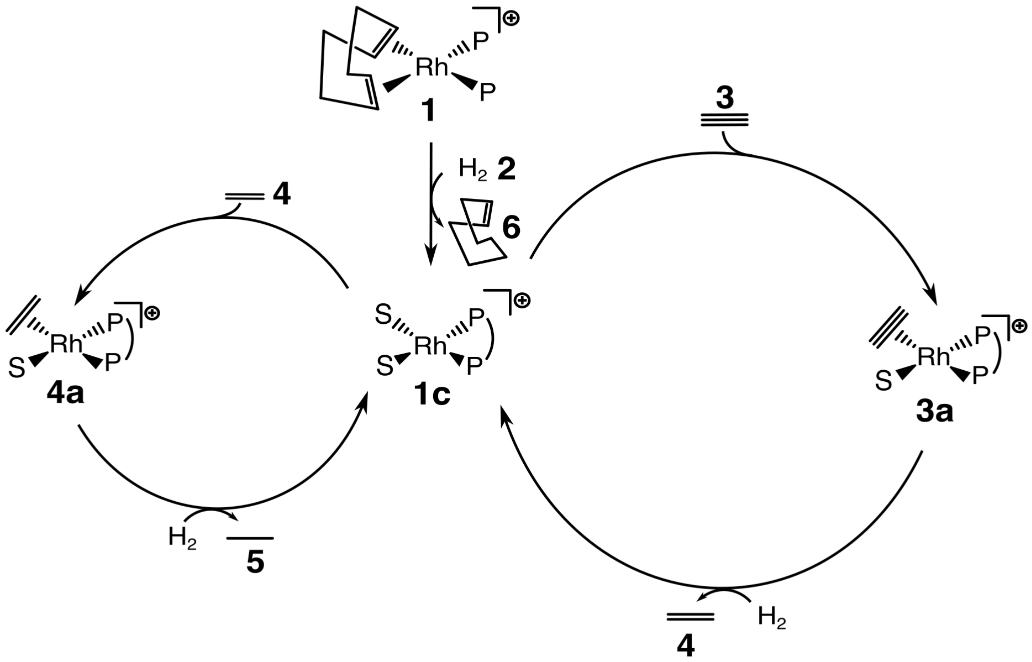

FIGURE 4.3: The simplified reaction mechanism for the propargyl acetate hydrogenation displayed in Fig. 4.1. The placement of the unsaturated molecules in species **3a** and **4a** was drawn schematically for convenience.

from the experimental data. For this reason, some simplifying assumptions were made for the current model. The induction period was reduced to a single step, where the catalyst **1** reacts with a hydrogen molecule **2** to yield the active catalyst complex **1c** and cyclooctene **6** as shown in Fig. 4.3. The catalytic cycle starts by propargyl acetate **3** binding to the active catalyst **1c** to create complex **3a**. The reduction of the catalyst-bound propargyl acetate to allyl acetate **4** and its elimination from the catalyst was assumed to proceed as a concerted reaction. Since the catalyst is not selective, allyl acetate **4** can re-enter the cycle and get reduced to propyl acetate **5** in the same manner. This leads to a kinetic model consisting of 5 irreversible reactions, each associated with a forward rate constant:

$$\mathbf{1} + \mathbf{2} \xrightarrow{k_1} \mathbf{1c} + \mathbf{6} \tag{4.1a}$$

$$\mathbf{1c} + \mathbf{3} \xrightarrow{k_2} \mathbf{3a} \tag{4.1b}$$

$$\mathbf{3a} + \mathbf{2} \xrightarrow{k_3} \mathbf{4} + \mathbf{1c} \tag{4.1c}$$

$$\mathbf{1c} + \mathbf{4} \xrightarrow{k_4} \mathbf{4a} \tag{4.1d}$$

$$\mathbf{4a} + \mathbf{2} \xrightarrow{k_5} \mathbf{5} + \mathbf{1c} \tag{4.1e}$$

The corresponding rate equations are

$$\frac{\mathrm{d}[\mathbf{1}]}{\mathrm{d}t} = -k_1[\mathbf{1}][\mathbf{2}], \tag{4.2a}$$

$$\frac{\mathrm{d}[\mathbf{1c}]}{\mathrm{d}t} = +k_1[\mathbf{1}][\mathbf{2}] - k_2[\mathbf{1c}][\mathbf{3}] + k_3[\mathbf{3a}][\mathbf{2}] - k_4[\mathbf{1c}][\mathbf{4}] + k_5[\mathbf{4a}][\mathbf{2}], \tag{4.2b}$$

$$\frac{\mathrm{d}[\mathbf{2}]}{\mathrm{d}t} = -k_1[\mathbf{1}][\mathbf{2}] - k_3[\mathbf{3a}][\mathbf{2}] - k_5[\mathbf{4a}][\mathbf{2}], \tag{4.2c}$$

$$\frac{\mathrm{d}[\mathbf{3}]}{\mathrm{d}t} = -k_2[\mathbf{1c}][\mathbf{3}], \tag{4.2d}$$

$$\frac{\mathrm{d}[\mathbf{3a}]}{\mathrm{d}t} = +k_2[\mathbf{1c}][\mathbf{3}] - k_3[\mathbf{3a}][\mathbf{2}], \tag{4.2e}$$

$$\frac{\mathrm{d}[\mathbf{4}]}{\mathrm{d}t} = +k_3[\mathbf{3a}][\mathbf{2}] - k_4[\mathbf{1c}][\mathbf{4}], \tag{4.2f}$$

$$\frac{\mathrm{d}[\mathbf{4a}]}{\mathrm{d}t} = +k_4[\mathbf{1c}][\mathbf{4}] - k_5[\mathbf{4a}][\mathbf{2}], \tag{4.2g}$$

$$\frac{\mathrm{d}[\mathbf{5}]}{\mathrm{d}t} = +k_5[\mathbf{4a}][\mathbf{2}], \tag{4.2h}$$

$$\frac{\mathrm{d}[\mathbf{6}]}{\mathrm{d}t} = +k_1[\mathbf{1}][\mathbf{2}]. \tag{4.2i}$$

4.3 Results and Discussion

Hydrogenation was performed in a valved NMR tube with a threaded capillary to allow for the hydrogen gas delivery. The precursor solution contained 20 mM of propargyl acetate **3** and 5 mM of rhodium catalyst **1**. Thermal hydrogen **2** was bubbled at 5 bar for 10 s at 400 $\mathrm{mL\,min^{-1}}$ then the solution was left to settle for 25 s and a transient was acquired. As a result, a single-scan proton spectrum was acquired every 40 s. The bubble-wait-acquire procedure was repeated until the reaction reached completion. A total of 19 spectra were acquired. Fig. 4.4 a shows two spectra at 0 s and 120 s with peak assignments. Fig. 4.4 b shows the NMR spectra as the reaction proceeds, with the peaks that display the most significant change labelled. At time = 0 s the sample contains propargyl acetate as evidenced by the H^c peak at 2.9 ppm. After one bubbling event i.e at 40 s the H^c peak has decreased by 60% and has completely disappeared by 80 s. The conversion of propargyl acetate **3** to allyl acetate **4** is very rapid, while the secondary hydrogenation to form propyl acetate **5** is a much slower process. The H^j peak firstly appears at 3.9 ppm at 80 s and grows until 640 s, by which point the peaks associated with **4** have completely disappeared thus the

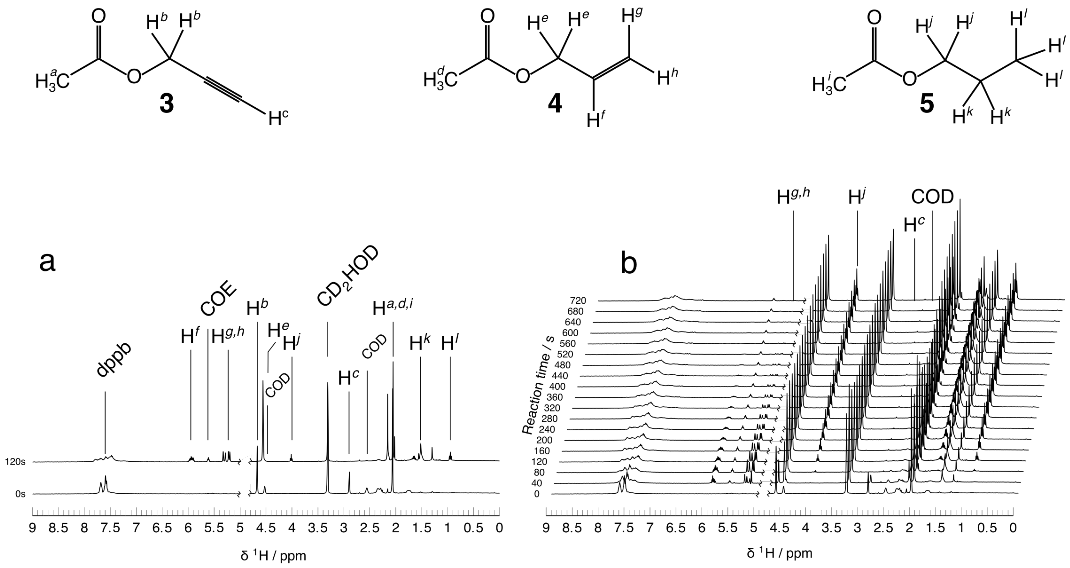

FIGURE 4.4: a) Assignment of species present in the solution. b) Experimental data obtained by bubbling thermal hydrogen **2** (5 bar) for 10 s between each acquisition through a solution of 20 mM propargyl acetate **3** and 5 mM of catalyst **1**. A transient was acquired every 40 s until 720 s. Methanol peak at 4.78 ppm was suppressed.

reaction reached completion. The peak associated with dissolved hydrogen was not observed thus hydrogen is rapidly consumed in the reaction.

The catalyst activation can be followed in the region of 7.4 to 7.7 ppm, which corresponds to the aromatic protons on the 1,4 - bis(diphenylphosphino)butane (dppb) ligand. Initially there are two broad peaks, which slowly split to four peaks that are observed at 120 s. The region remains unchanged until 460 s. After 460 s, the four peaks slowly decline and broaden. This may be due to the degradation of the catalyst, possibly by oxidation.

By integrating the H^c, $H^{g,h}$, H^j and COD peaks highlighted in Fig. 4.4 b, time-resolved concentration data was extracted, which is shown in Fig. 4.5. Squares indicate propargyl acetate, triangles - allyl acetate, circles propyl acetate and diamonds represent the catalyst region. Error bars were calculated from the small variation in the SNR in the spectra.

The conversion from propargyl acetate **3** to allyl acetate **4** and lastly to propyl acetate **5** was simulated by solving differential equations (4.2a) to (4.2i), and assuming a steady state hydrogen concentration of 20 mM. This assumption was made because

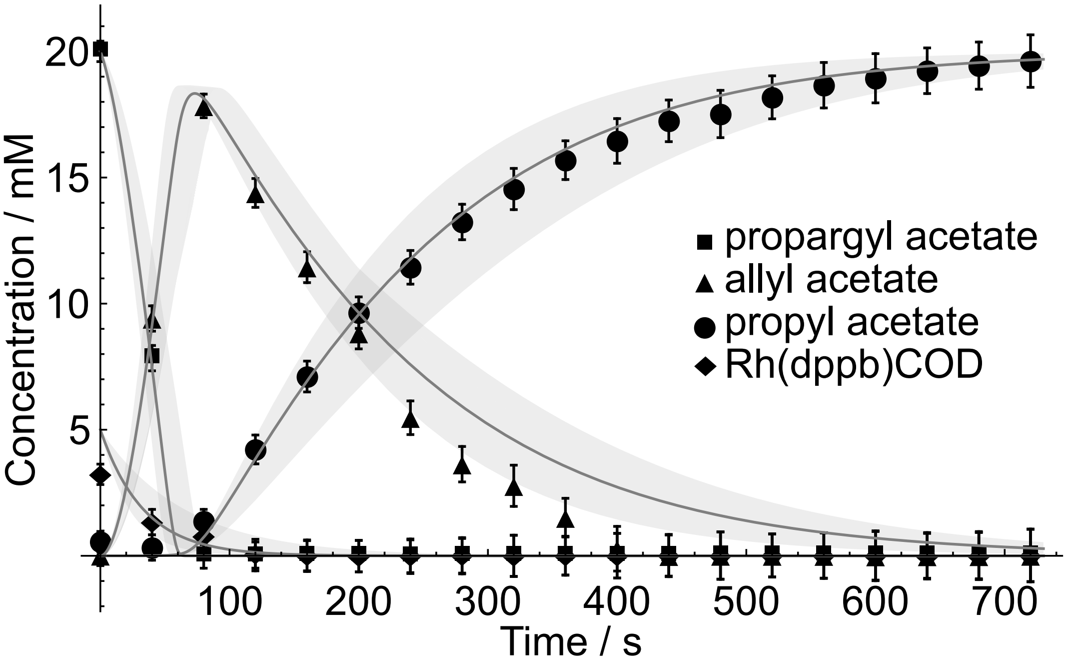

FIGURE 4.5: Concentration vs time data of propargyl acetate **3** (square), allyl acetate **4** (triangle), propyl acetate **5** (circle) and the catalyst **1** (diamond). The solid lines represent the best fit to the experimental model, the shadows are the 95 % confidence intervals of the reaction rate constants.

Reaction	**Rate Constant** / $\mathrm{mM^{-1}\,s^{-1}}$	**95% Confidence Interval**
$\mathbf{1} + \mathbf{2} \rightarrow \mathbf{1c} + \mathbf{6}$	$k_1 = 0.0015$	(0.0008,0.0022)
$\mathbf{1c} + \mathbf{3} \rightarrow \mathbf{3a}$	$k_2 = 0.5016$	(0.4659,0.5373)
$\mathbf{3a} + \mathbf{2} \rightarrow \mathbf{1c} + \mathbf{4}$	$k_3 = 0.0056$	(0.0035,0.0077)
$\mathbf{1c} + \mathbf{4} \rightarrow \mathbf{4a}$	$k_4 = 0.0014$	(0.0013,0.0019)
$\mathbf{4a} + \mathbf{2} \rightarrow \mathbf{1c} + \mathbf{5}$	$k_5 = 0.0038$	(0.0013,0.0063)

TABLE 4.1: Reaction equations and rate constants obtained by non-linear model fit to the experimental data with their 95% confidence intervals.

hydrogen solubility in methanol at room temperature is 4 mM/bar and the experiments were carried out at 5 bar [268]. The starting concentrations of **3** and **1** were 20 mM and 5 mM, respectively; all other initial concentrations were zero. The reaction rate constants were obtained by non-linear least squares model fitting in Mathematica. The solid lines in Fig. 4.5 represent the best fit of the data; the shaded regions correspond to the boundaries of the 95% confidence intervals. The resulting reaction rate constants are listed in Table 4.1 along with their 95% confidence intervals.

The catalyst induction period is slow with a rate constant of $k_1 = 0.0015\,\mathrm{mM^{-1}\,s^{-1}}$.

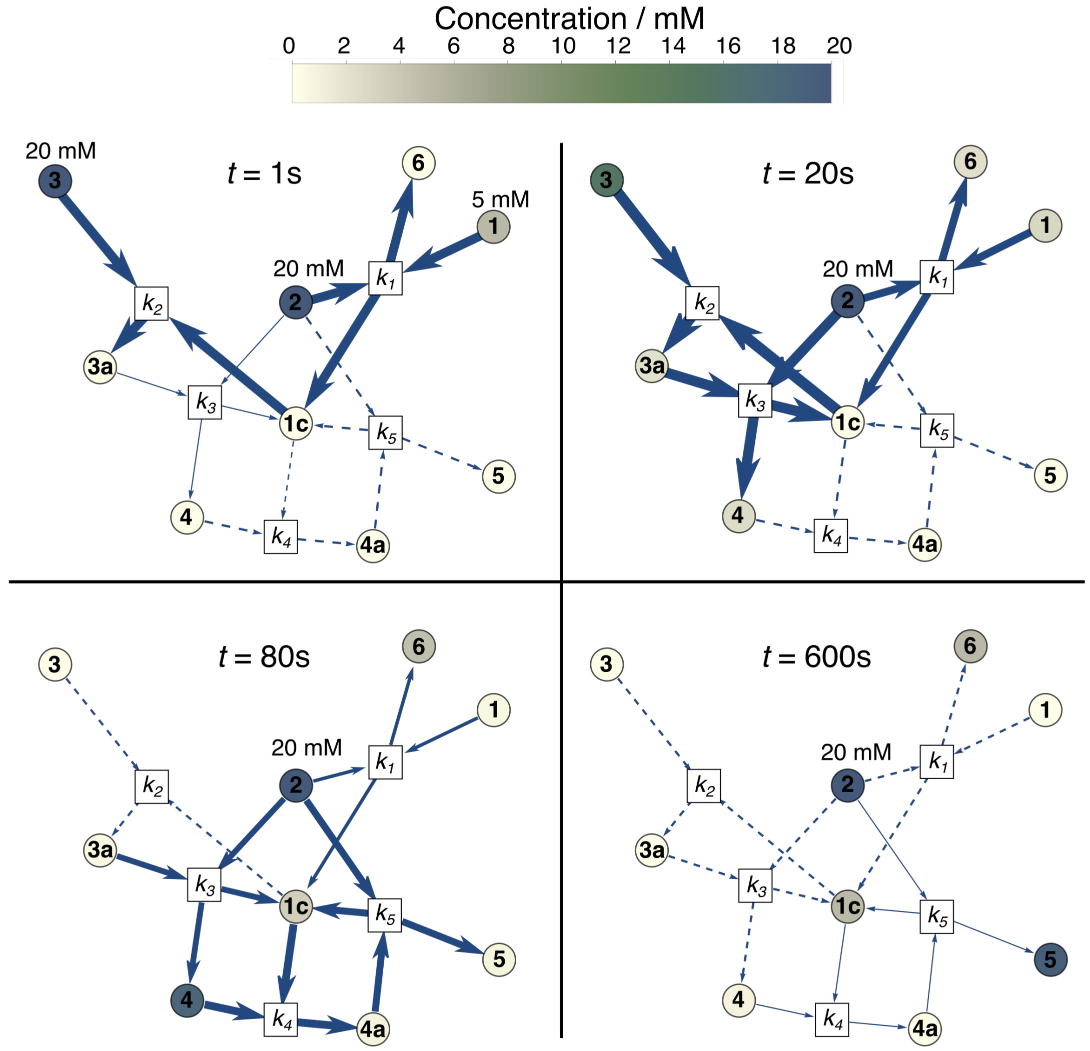

FIGURE 4.6: The kinetic model of the propargyl acetate hydrogenation reaction. The intensity of the colour from cream to navy indicates the concentration of species. The thickness of the arrow indicates the flux. The dashed arrow corresponds to no flux. t = 1 s the model assumes 20 mM steady state hydrogen **2** concentration, 5 mM of the pre-catalyst **1** and 20 mM of propargyl acetate **3**. The concentration of all other species was set to zero. At t = 1 s, he reaction is dominated by k_1 and k_2. t = 20 s, an early stage of the reaction, k_2 and k_3 are the dominant reaction rate constants. t = 80, there is very little flux to k_1 and no flux to k_2 while k_4 and k_5 dominate. t = 600 s is the late stage of the reaction, there is no flux at k_1, k_2 and k_3 while k_4 and k_5 are very slow.

Once **1a** reaches sufficient concentration, creation of the catalyst-substrate complex is comparatively fast, with $k_2 = 0.5016\,\mathrm{mM^{-1}\,s^{-1}}$. Elimination of the first hydrogenation product **4** proceeds with a reaction rate constant $k_3 = 0.0056\,\mathrm{mM^{-1}\,s^{-1}}$. Coordination of **4** to **1a** is a much slower process compared with the production of compound **3a** as $k_4 = 0.0014\,\mathrm{mM^{-1}\,s^{-1}}$. Lastly, elimination of **5** proceeds with $k_5 = 0.0038\,\mathrm{mM^{-1}\,s^{-1}}$. The simulation predicts very well the first hydrogenation event however, there is a minor discrepancy in the prediction of the reduction of allyl acetate to propyl acetate.

The experimental data shows a near linear (pseudo-zeroth order) consumption of **4** from 120 s to 480 s, whereas the simulation predicts a more gradual (pseudo-first order) decline between 320 s and 600 s. This discrepancy most likely arose due to measurement error. Fig. 4.6 illustrates the reaction network represented by the kinetic model. The intensity of the colour from cream to navy indicates the concentration of species. The arrow thickness represents flux. If there is no flux a dashed arrow is used. During the early stage i.e $t = 1$ s, the reaction is dominated by k_1 and k_2; there is no flux to k_4 and k_5. In the next stage, $t = 20$ s, the catalyst activation characterised by k_1 slows down. The reaction is dominated by k_2 and k_3, which correspond to the consumption of propargyl acetate **3** to produce allyl acetate **4**. At $t = 80$ s, k_4 and k_5 rates are driving the reaction. In the last stage of the reaction, $t = 600$ s there is no flux at k_1, k_2, and k_3. The reaction is driven by k_4 and k_5 and is very slow.

The next step in the modelling of the PHIP reaction involved simulating the mass transport properties of the LoC device. The microfluidic reactor used in Ref [1] is shown in Fig. 4.7 a. The precursor solution containing 20 mM propargyl acetate **3** and 5 mM [Rh(dppb)COD]BF_4 **1** in methanol-d_4 is delivered into the fluid channel marked blue via a syringe pump. Hydrogen gas **2** is delivered via a separate channel, marked in red. The transport of hydrogen into the liquid channel is facilitated by the use of a semi - permeable PDMS membrane. The membrane acts as a bridge between the two channels as shown in Fig. 4.7 b allowing hydrogen to diffuse into the solution. The reaction products are detected at the 2.5 μL sample detection chamber labelled VII. In order to keep the computational cost manageable, a 2D finite element representation of the LoC was constructed rather than a full 3D model. The use of a simple 2D model reduced the computation time to less than 30 minutes and therefore allowed exploration of a wider range of parameters. The simulation domain of the $\alpha-$chip is shown in Fig. 4.7 c and it consists of an inlet I, outlet II, a fluid channel III with a sample chamber VII and a PDMS membrane IV. The flow pattern in the channel was found by solving the Navier-Stokes equations for incompressible fluids for each flow rate. The resulting velocity distribution was used in a reaction-diffusion-convection simulation of the hydrogenation reaction in the channel. The reaction equations and rates were obtained from the space independent model and are listed in Table 4.1. The gas channel was not modelled explicitly but a constant concentration condition was applied to the outer boundary of the PDMS membrane marked as h_{pmds} V in Fig. 4.7 c. The hydrogen diffusion into the channel was facilitated by coupling the PDMS membrane to the flowing liquid through another concentration condition, marked $h_r = h_{\mathrm{pmds}}$ VI, imposed on the boundary between the membrane and the channel. In order to simulate the volume of the chip, the depth of the domain was fixed to 1.2 mm in the simulation parameters.

The 2D model has been designed to ensure that the residence time of the fluid in contact with the PDMS membrane, inside of the transport channel and in the sample chamber agree with the experimental device. Physics-controlled mesh was automatically generated with the element size set to fine and a sample of the mesh is shown in 4.7 d.

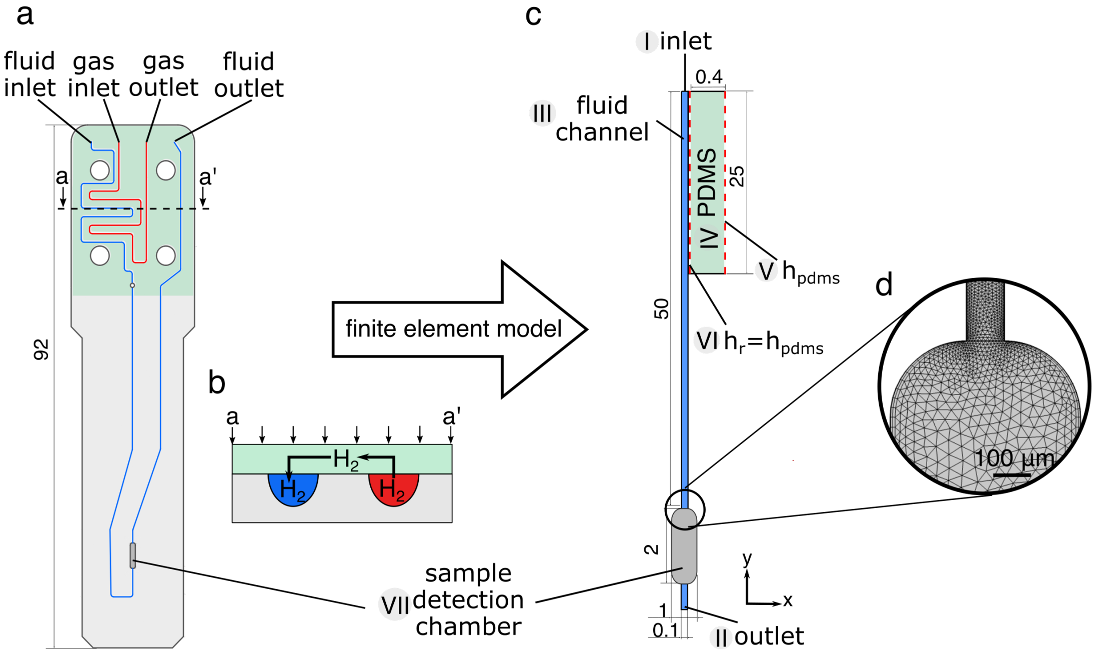

FIGURE 4.7: a) The top view of the $\alpha-$chip. b) An illustration of the hydrogen diffusion from the gas channel (red) into the solution channel (blue). The PDMS membrane (green) acts as a bridge between the two channels. c) The finite element simulation domain; $h_{\mathrm{pdms}} = [\mathbf{2}] = 20$ mM is the concentration of hydrogen at outer boundary of the PDMS membrane, h_r is the hydrogen concentration in the fluid channel. d) A sample of the mesh at the sample chamber/fluid channel boundary obtained from COMSOL.

In a first step, the model was used to predict the uptake of hydrogen into methanol as a function of flow rate in the absence of the catalyst and substrates. This was accomplished by setting all reaction rate constants and the initial concentrations of all species to zero, with the only exception being the hydrogen concentration in the PDMS membrane h_{pmds} = [**2**]= 20 mM. An assumption was made that no hydrogen is lost from the solution after passing the membrane because the residence time of hydrogen in the chip is too short to diffuse through the plastic. Fig. 4.8 a shows the concentration of hydrogen in the sample chamber as a function of flow rate. The empty circles correspond to the experimental data reported by Ref [1] and the solid black line represents the results of the 2D simulation. The experimental data indicate a slow decrease in hydrogen concentration until 10 $\mu\mathrm{L\,min^{-1}}$. Above 10 $\mu\mathrm{L\,min^{-1}}$, the concentration steeply declines. The 2D simulation predicts that methanol flowing in the channel is saturated with hydrogen only at low flow rates (below 2 $\mu\mathrm{L\,min^{-1}}$). As the flow rate increases, the uptake of hydrogen steadily declines and at high flow rates such as 20 $\mu\mathrm{L\,min^{-1}}$ only 4 mM of hydrogen dissolves in the flowing fluid. Very similar simulation results were presented by Eills *et al.* [1] and are shown in Fig. 4.8 a as the solid blue line. In distinction to the current work, 3D calculations were carried out for the full chip geometry. Simulations for the hydrogen flux at the PDMS/liquid interface in the 2D model are in quantitative agreement with the 3D simulations. In both sets, at flow rates below 10 $\mu\mathrm{L\,min^{-1}}$ the uptake of hydrogen into the fluid is predicted well and the simulated result agrees with the experimental data within the error bars. However, there is an increasing discrepancy at high flow rates. The simulations predict a steady decline of the hydrogen concentration in the sample chamber with an increasing flow rate, whereas the experimental data falls off very rapidly after 10 $\mu\mathrm{L\,min^{-1}}$. This discrepancy is not yet understood. Eills *et al.* [1] suggested that this could be due to the deformation of the PDMS membrane.

Fig. 4.8 b shows the calculated hydrogen concentration distribution in the chip. The green shaded area corresponds to the region where the reaction pathway is in contact with the PDMS membrane. This is the only region where hydrogen can be uptaken into the chip. At very low flow rates such as 0.5 $\mu\mathrm{L\,min^{-1}}$ hydrogen flux occurs at only at the first few millimeters of the PDMS/liquid boundary before the liquid reaches saturation. As the flow rate increases, the part of the boundary at which flux occurs gradually expands. However, since the amount of liquid per unit time increases

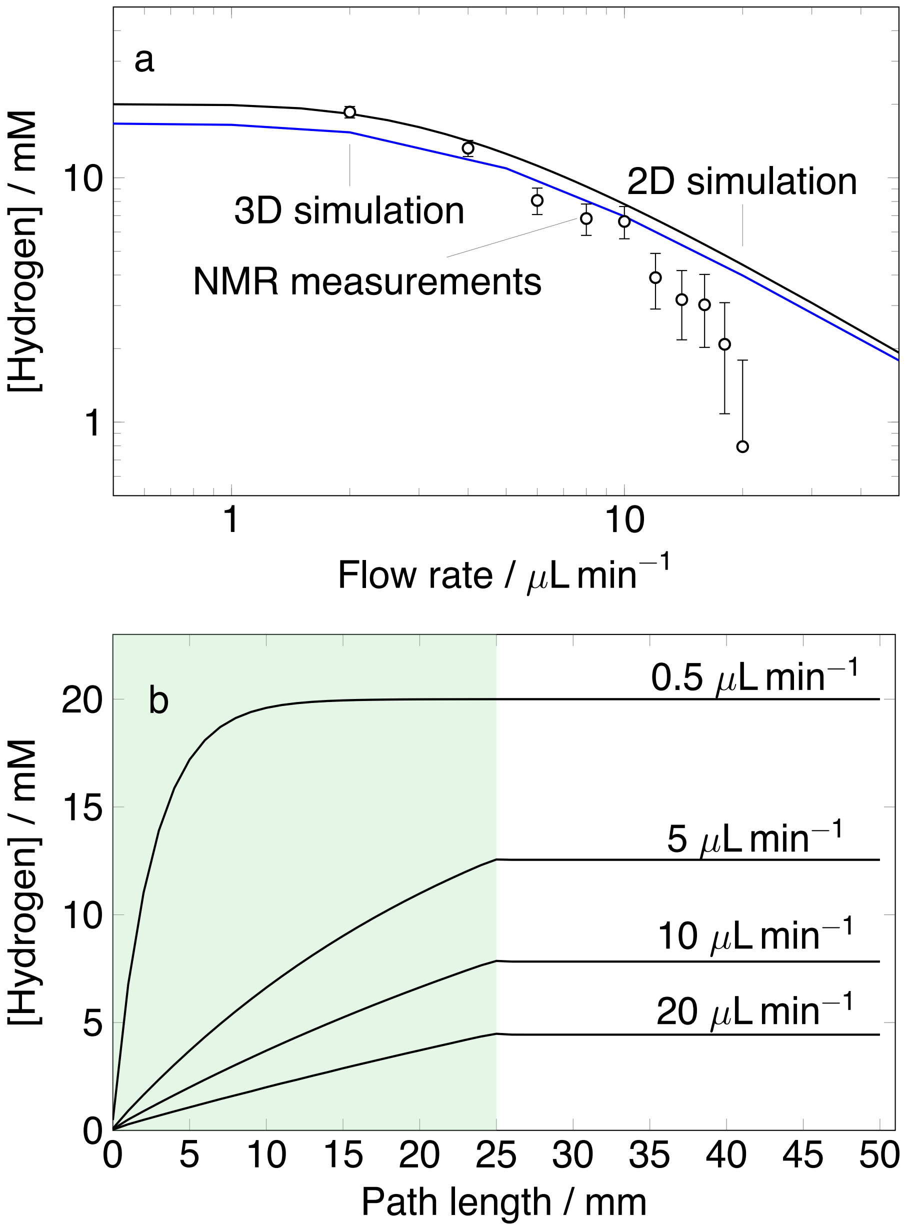

FIGURE 4.8: a) Hydrogen concentration in the sample chamber as a function of flow rate. Empty circle corresponds to the experimental data and the solid blue line represents the 3D simulation both obtained from Ref [1], the solid black line is the 2D simulation. b) The distribution of [hydrogen] throughout the length of the fluid channel in the $\alpha-$chip. The green shaded area corresponds to the region where the fluid channel is in contact with the PDMS membrane.

as well, this results in a decreasing concentration of hydrogen after contact. At very high flow rates, 20 μL min^{-1} this issue becomes very prominent with the pathway saturation reaching only 4.5 mM.

Hydrogenation experiments in the LoC device reported in Ref [1] were performed using *para* – enriched hydrogen. Hyperpolarized molecules have a limited life-time and relax with a time-constant T_1. The kinetic model proposed in Fig. 4.6 does not account for the relaxation of the hyperpolarized species as the calibration experiments were performed with thermal hydrogen. In order to approximately account for this process, an additional reaction was added:

$$\mathbf{4} \xrightarrow{k_6} \mathbf{4rx} \tag{4.1f}$$

where k_6 is the nuclear spin-lattice relaxation rate constant. It has been reported that the ^{1}H T_1 relaxation time of similar compounds is ∼7 s, therefore the relaxation rate of k_6 was set to 0.14 s^{-1} [269]. Accounting for the relaxation results in the following changes to rate equations:

$$\frac{\mathrm{d}[\mathbf{1c}]}{\mathrm{d}t} = +k_1[\mathbf{1}][\mathbf{2}] - k_2[\mathbf{1c}][\mathbf{3}] + k_3[\mathbf{3a}][\mathbf{2}] - k_4[\mathbf{1c}][\mathbf{4rx}] + k_5[\mathbf{4a}][\mathbf{2}], \tag{4.2b'}$$

$$\frac{\mathrm{d}[\mathbf{4}]}{\mathrm{dt}} = +k_3[\mathbf{3a}][\mathbf{2}] - k_6[\mathbf{4}] \tag{4.2f'}$$

$$\frac{\mathrm{d}[\mathbf{4a}]}{\mathrm{dt}} = +k_4[\mathbf{1c}][\mathbf{4rx}] - k_5[\mathbf{4a}][\mathbf{4}] \tag{4.3g'}$$

Moreover, the following equation was added

$$\frac{\mathrm{d}[\mathbf{4rx}]}{\mathrm{dt}} = -k_4[\mathbf{1c}][\mathbf{4rx}] + k_6[\mathbf{4}]. \tag{4.2j}$$

The remaining equations were unchanged.

To perform the finite element simulation, the initial concentrations of propargyl acetate **3** and the catalyst **1** were set to 20 mM and 5 mM respectively ($[\mathbf{3}]_0$ = 20 mM, $[\mathbf{1}]_0$ = 5 mM). Hydrogen supply was modelled as a constant concentration condition, $\mathrm{h}_{\mathrm{pmds}} = [\mathbf{2}]$ = 20 mM. The initial concentrations of all other species were set to zero. Fig. 4.9 shows the concentration of hyperpolarized allyl acetate at the sample chamber as a function of flow rate. The empty circles represent the experimental data obtained from Ref [1], the black solid line represents the 2D simulation. The experimental data

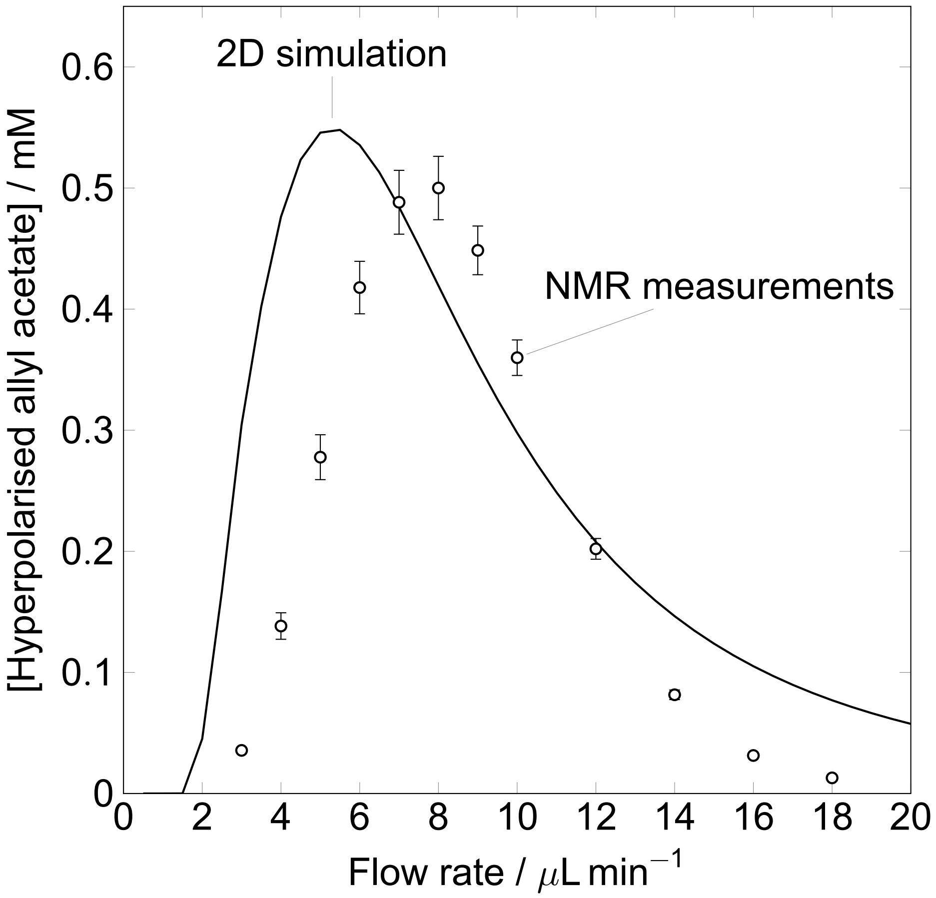

FIGURE 4.9: Hyperpolarized allyl acetate concentration in the sample chamber of the chip as a function of flow rate. The empty circles represent the experimental data obtained from ref [1], the black solid line is the 2D simulation.

shows that as the flow rate increases from 3 μL min^{-1} the concentration of the product increases in the sample chamber until it reaches the maximum at 8 μL min^{-1}. Once the maximum is reached the concentration of hyperpolarized allyl acetate falls rapidly. The simulation predicts a very similar trend, with an initial rise of the concentration of the product. The maximum is reached at 5.5 μL min^{-1} and is followed by a steep decline in the yield of the product, which tails off at flow rates beyond 12 μL min^{-1}. At flow rates below the maximum, the time it takes for the hyperpolarized product to arrive at the sample chamber is greater than its relaxation time. Therefore, at very low flow rates, the product is formed upstream from the sample chamber and on the way, it undergoes relaxation processes. The steep increase in the product from 2 μL min^{-1} until the maximum is due to the fact that the product is delivered faster to the sample chamber therefore less of it is lost due to relaxation. This is illustrated in Fig. 4.10, which shows the predicted concentration of hyperpolarized allyl acetate in the sample

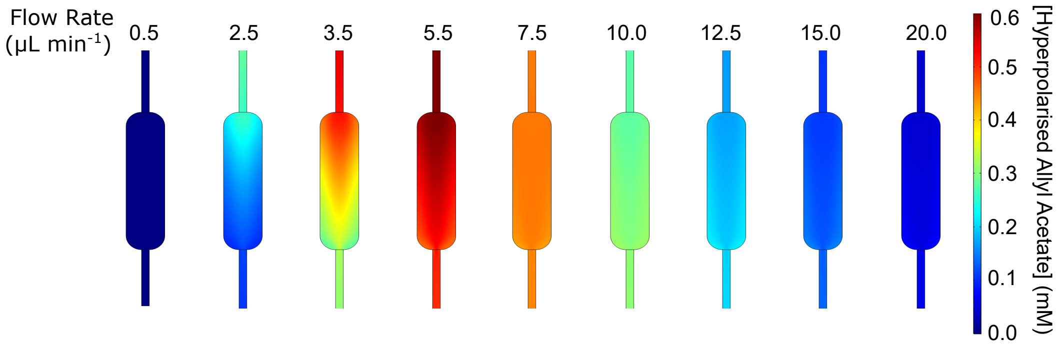

FIGURE 4.10: Distribution of the hyperpolarized allyl acetate in the sample chamber of the microfluidic chip at varying flow rates.

chamber at different flow rates. At very low flow rates, 0.5 μL min^{-1}, there is no product being formed in the sample chamber. As the flow rate increases there is an influx into the sample chamber, which can be seen as a colour gradient at flow rates from 2.5 μL min^{-1} to 5.5 μL min^{-1}. At 5.5 μL min^{-1}, the maximum is reached signified by the deep red colour. As the flow rate increases further, the concentration of the product gradually decreases to 0 mM at flow rates of 20 μL min^{-1}. As discussed previously, at flow rates above the optimum, hydrogen concentration in the reaction channel is less than 10 mM. Low hydrogen concentration results in a significant reduction in the efficiency of the allyl acetate production as two key reactions, namely 4.1 a and 4.1 c, rely on the supply of hydrogen.

There is a discrepancy in the location of the maximum between the experimental data and the simulation. The position of the maximum depends on the volume of the chip as shown in Fig. 4.11. As discussed previously, the total volume of the chip modelled was calculated based on the chip used by Eills *et al.* [1]. The experimental data contains a fabrication error due to the imperfect bonding of the chip layers that can result in increased volume of the chip. Fig. 4.11 shows three simulations at different total volumes of the chip. The dashed, solid and dotted black lines correspond to volumes of 4.5 μL, 8.5 μL, and 12.5 μL, respectively. As the volume of the chip is increased the position of the maximum shifts to the higher flow rate. There is also a notable change in the product formation kinetics. At the very small chip volumes such as 4.5 μL the maximum product concentration is formed at 2 μL min^{-1} and is followed by a near immediate fall in the concentration, where at 4 μL min^{-1} there is only 0.1

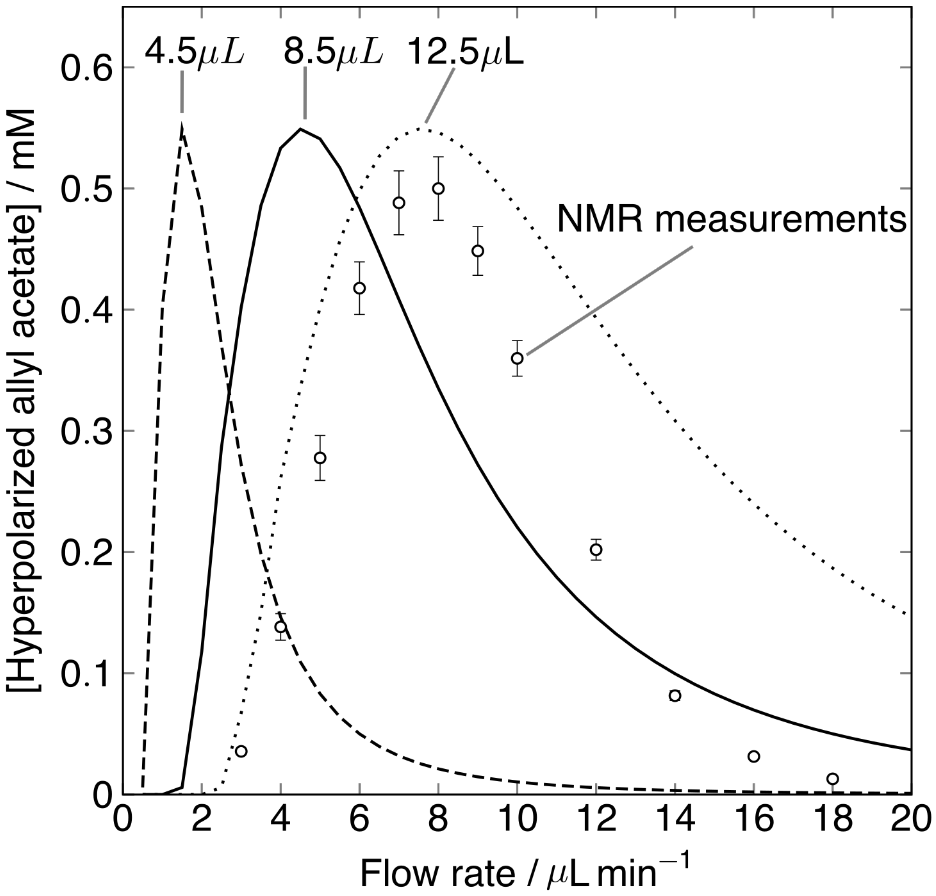

FIGURE 4.11: Simulation of the effect of chip volume on the kinetics of the reaction. Hyperpolarized allyl acetate concentration in the sample chamber of the chip as a function of flow rate. The dashed, solid and dotted black lines show simulations for a chip with a total volume of 4.5 μL, 8.5 μL, and 12.5 μL, respectively. The empty circles represent the experimental data obtained from Ref. [1].

mM of the product in the sample chamber. At very low chip volumes, the residence time of the liquid in contact with the PDMS membrane is very short. Flowing at 2 μL min^{-1} the solution spends 30 s in contact with the membrane. As the flow rate increases, this time is further reduced to only 10 s. Such short time is insufficient to dissolve a substantial amount of hydrogen. In contrast, at high chip volumes, the solution spends a long time in contact with the PDMS membrane. Flowing at 2 μL min^{-1} equates to 150 s contact time with the membrane however, at such long reaction times relaxation of the hyperpolarized product becomes an issue.

In order to improve the yield of hyperpolarized allyl acetate in the chip several scenarios were simulated. Fig. 4.12 shows the change in the concentration of the four key species, protected catalyst **1** (dashed line) hydrogen **2** (dash-dotted line),

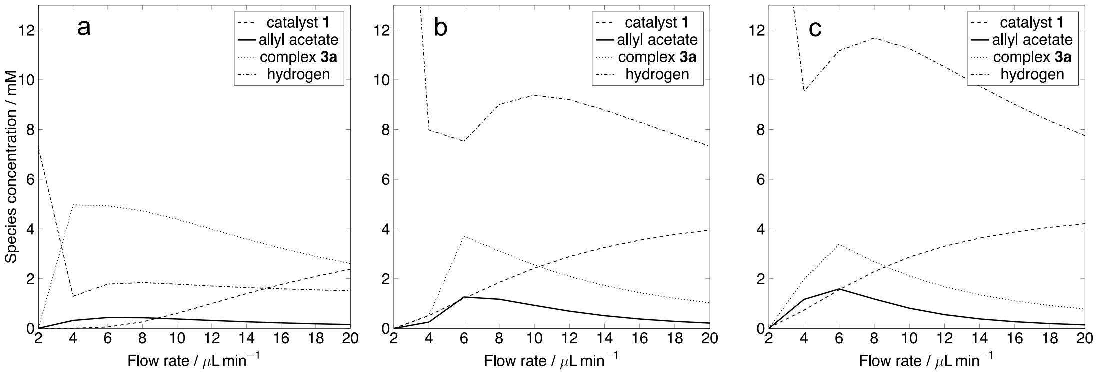

FIGURE 4.12: Change in the concentration of the four key species: protected catalyst **1** (dashed line), hyperpolarized allyl acetate **3** (solid line), complex **3a** (dotted line), and hydrogen **2** (dash-dotted line) in the sample chamber as a function of flow rate predicted by the finite element model when a) k_1 was increased tenfold to $k_1' = 0.015\ \mathrm{s}^{-1}\,\mathrm{mM}^{-1}$. b) The concentration of hydrogen was doubled to [**2**] = 40 mM; the reaction rate constants were unchanged. c) The sample detection chamber was mocved upstream by 12.5 mm; the concentration of hydrogen [**2**] = 40 mM and the reaction rate constants were unchanged.

hyperpolarized allyl acetate **3** (solid line) and complex **3a** (dotted line), in the sample chamber as a function of flow rate in three different scenarios. Since the kinetic model predicts that the slowest step in the formation of allyl acetate is the catalyst deprotection step with $k_1 = 0.0015\ \mathrm{s}^{-1}\,\mathrm{mM}^{-1}$, in the simulation, the rate of the reaction was accelerated by increasing k_1 tenfold to $k_1' = 0.015\ \mathrm{s}^{-1}\,\mathrm{mM}^{-1}$. Fig. 4.12 a shows that all of the available hydrogen is used for the catalyst deprotection step. Therefore, the reaction of complex **3a** with hydrogen **2** becomes rate limiting. Experimentally, this could be achieved by pre-activating the catalyst however, the stability of such complex could be an issue. In another simulation, shown in Fig. 4.12 b the concentration of hydrogen was doubled to [**2**] = 40 mM, all reaction rate constants remained unchanged. Doubling the concentration of hydrogen led to doubling of the hyperpolarized allyl acetate however, the yield remains low at [**3**] = 1.2 mM. Hyperpolarized species are subject to relaxation therefore in an attempt to minimise this effect the sample detection chamber was moved upstream by 12.5 mm. The concentration of hydrogen [**2**] was kept at 40 mM and the reaction rate constants were unchanged. The result of this simulation is shown in Fig. 4.12 c. The yield of hyperpolarized allyl acetate was increased by further 0.5 mM.

The most drastic increase in hyperpolarized allyl acetate production was observed when more hydrogen was supplied to the chip. Therefore a device that maximise the uptake of hydrogen need to be designed.

4.4 Conclusions

In this chapter, a spatially resolved kinetic model of a PHIP reaction in a LoC device was developed. In a first step, a space independent kinetic model was developed and was calibrated against the independently acquired experimental data. Then, a 2D finite element model of the LoC device was created. The model had no adjustable parameters. In order to test the performance of the finite element model, hydrogen flux from the PDMS membrane was simulated. The simulation successfully predicted the hydrogen uptake at flow rates below 10 $\mu\text{L}\,\text{min}^{-1}$. Above that, the simulation over predicted the amount of hydrogen taken up by the chip. This discrepancy is not yet understood. Following that, the full reaction of propargyl acetate hydrogenation was simulated. This was done by utilising the reaction rates obtained from the macroscopic measurement in a finite element convection-diffusion-reaction simulation. The model successfully predicted the yield of hyperpolarized allyl acetate in the sample chamber of the device as a function of flow rate. Lastly, the model was used to predict the concentration of hyperpolarized allyl acetate when some of the conditions were changed. A condition were the concentration of hydrogen was doubled gave the most noticeable increase in the reaction yield thus a device that optimises the uptake of hydrogen needs to be designed. In this work we showed that a simple 2D representation of a microfluidic device can be used to predict the outcome of a hyperpolarized reaction. This a powerful method to test many hypothetical conditions without the expense of laboratory time. The model can be used to test other reactions providing that kinetic parameters are known.

Chapter 5

An Optimised Microfluidic Device for Yield Maximisation

5.1 Introduction

Microfluidic implementation of PHIP reported by Eills *et al.* [1] enabled incorporation of the hydrogenation reaction and detection onto a single microfluidic platform. However, since further transformations such as purification and cleavage are required in order to utilise the hyperpolarized product for biological applications, the reaction yield needs to be improved.

In Chapter 4, a spatially resolved kinetic finite element model of the reaction shown in Fig. 5.1 a was developed. It involved the hydrogenation of propargyl acetate **3** with parahydrogen gas **2** in the presence of a rhodium catalyst **1** to obtain allyl acetate **4**. The black bar in Fig.5.1 b represents the yield of **4** obtained from Ref. [1], while the grey bars correspond to three scenarios predicted by the model developed in Chapter 4. In the first scenario the temperature was increased by 10°C, in the second case the concentration of hydrogen was doubled, and lastly the catalyst activation rate was increased 10 times. The corresponding yield of **4** was 0.6 mM, 1.2 mM, and 0.45 mM. Since the only significant concentration increase was observed by increasing the

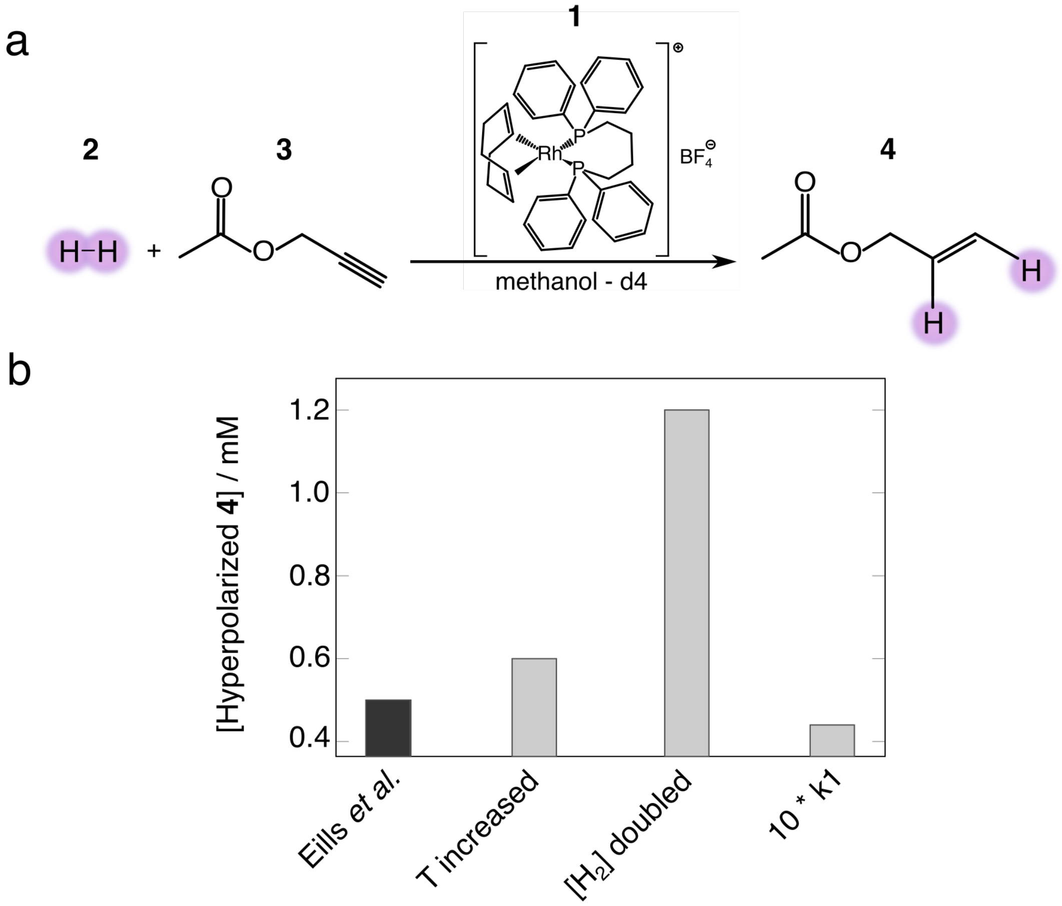

FIGURE 5.1: a) The reaction investigated in this work. Propargyl acetate **3** reacts with parahydrogen **2** in the presence of rhodium catalyst **1** to produce allyl acetate **4** with two protons in a hyperpolarized state. b) A comparison of the yield of hyperpolarized **4** obtained from Eills *et al.* [1] and three scenarios predicted by the model developed in Chapter 4.

concentration of hydrogen, it was concluded that in order to increase the yield of **4**, hydrogen uptake into the chip must be improved.

In this chapter, the finite element model was extended to simulate the uptake of hydrogen into the chip where the simulation domain included an additional hydrogen channel. To experimentally confirm the simulation, a prototype, referred to as the $\beta-$chip, was built where the channel network was re-designed to include an additional hydrogen channel. Then, the $\beta-$chip was used to perform the PHIP reaction. Lastly, the reaction was studied at three different temperatures.

5.2 Results and Discussion

An insufficient uptake of hydrogen into the $\alpha-$chip was identified as the cause of the low yield of the PHIP reaction shown in Fig. 5.1 a [2]. Simply elevating hydrogen pressure to increase the concentration of hydrogen in the chip is not a viable solution due to engineering challenges such chip delamination, which leads to leakages. Additionally, working with high hydrogen pressures poses as increased safety hazard. Instead, the channel network can be modified to maximise the gas uptake. To simulate the effect of introducing an additional hydrogen channel finite element simulations were performed.

The $\alpha-$domain, shown in Fig. 5.2 a, represents the simulation domain for the $\alpha-$chip and it consists of an inlet I, an outlet II, a fluid channel III with a sample chamber VII and a PDMS membrane IV. To simulate the gas channel, a steady-state hydrogen concentration of 20 mM was imposed on the outer boundary of the PDMS membrane marked as $\mathrm{h}_{\mathrm{pdms}}$ V. A h_{r} boundary VI was imposed at the PDMS/fluid channel interface to couple the membrane with the channel. In order to simulate the effect of an increased hydrogen concentration, another hydrogen channel was introduced to the simulation domain. As shown in Fig 5.2 b, this was represented by introducing a second PDMS membrane with new $\mathrm{h}_{\mathrm{pdms}}$ and h_{r} boundaries marked as V and VI. Additionally, the fluid pathway in contact with the PDMS membrane was increased by 30%.

Fig 5.2 c shows hydrogen concentration as a function of the channel length. The green, shaded area represents the part of the channel in contact with the PDMS membrane. The dash-dotted and solid black lines represent results for the $\alpha-$ and $\beta-$domains, respectively. As seen in the previous section, at very low flow rates such as 0.5 $\mu\mathrm{L\,min^{-1}}$, hydrogen flux occurs only at the first few millimeters of the PDMS/liquid boundary before reaching saturation. The saturation of the fluid channel with hydrogen in the $\beta-$domain occurs at ∼5 mm, while the hydrogen reaches saturation ∼10 mm for the $\alpha-$domain. As the flow rate increases, the area where hydrogen flux occurs expands. However, since the amount of liquid per unit time increases as well,

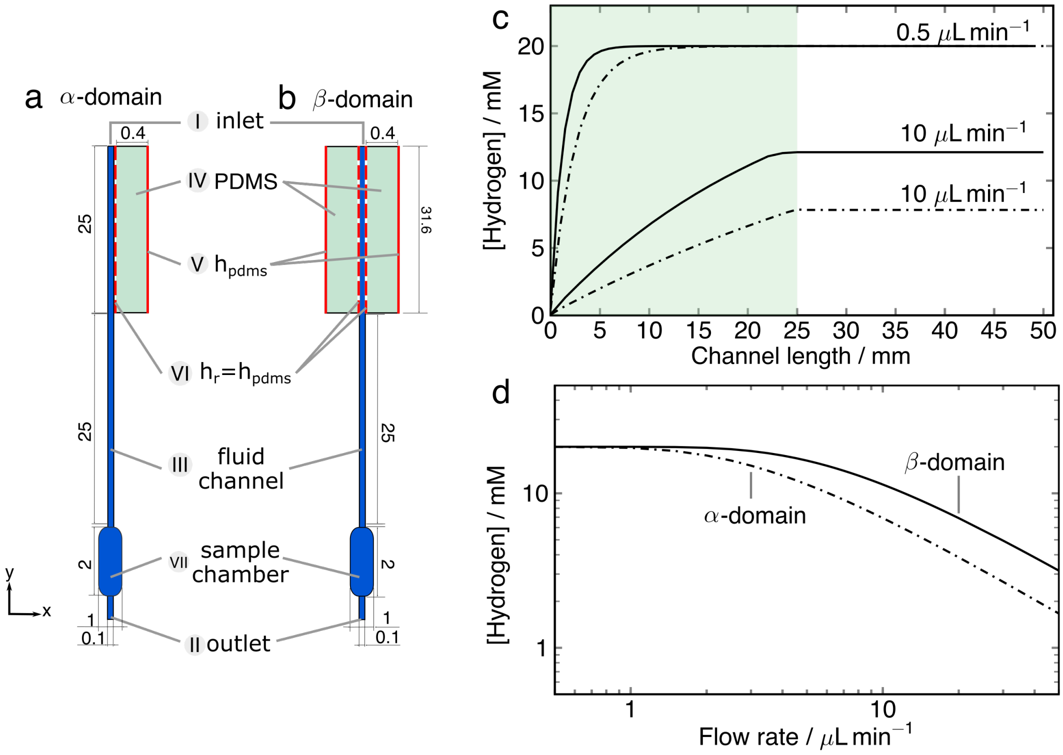

FIGURE 5.2: a) The simulation domain for the $\alpha-$chip. It consists of an inlet I, an outlet II, a fluid channel III with a sample chamber VII and a PDMS membrane IV. A gas channel is represented by imposing a constant hydrogen concentration to the outer boundary V of the PDMS membrane marked as $\mathrm{h_r} = \mathrm{h_{pdms}}$. The membrane and the fluid channel were coupled through the boundary $\mathrm{h_r} = \mathrm{h_{pdms}}$ VI this allowed hydrogen to dissolve in the fluid channel. b) The simulation domain for the $\beta-$chip. An additional PDMS membrane was added with $\mathrm{h_{pdms}}$ and $\mathrm{h_r}$ boundaries to signify an additional hydrogen channel. The fluid pathway in contact with the PDMS membrane was extended by 30%. c) The uptake of hydrogen at 0.5 and 10 μL min^{-1} flow rates as a function of the fluid channel length. The dash-dotted line line represents the $\alpha-$domain and the black solid line corresponds to results for the $\beta-$domain. d) Simulation results of hydrogen concentration in the sample chamber as a function of flow rate. The dash-dotted line represents the $\alpha-$domain and the black solid line corresponds to results for the $\beta-$domain.

this results in a decreasing concentration of hydrogen after contact. At 10 μL min^{-1} only ~8 mM of hydrogen dissolves in the fluid channel for the $\alpha-$domain, while ~13 mM dissolves in the $\beta-$domain. Fig. 5.2 d shows simulation results for hydrogen concentration in the sample chamber as a function of flow rate for the $\alpha-$ and $\beta-$domains represented by the dash-dotted and solid lines, respectively. At 2 μL min^{-1} the time that the fluid spends in contact with the PDMS membrane is very long. Therefore, the fluid becomes fully saturated with hydrogen. As the flow rate increases, that contact time decreases therefore the amount of hydrogen dissolved in the channel decreases. Already at 6 μL min^{-1} the simulation predicts that the concentration of

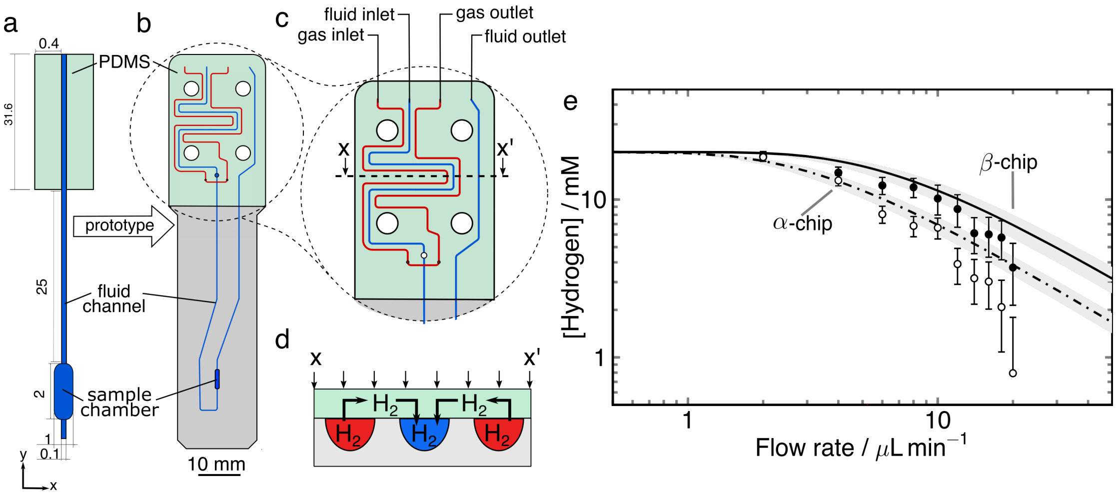

FIGURE 5.3: a) The simulation domain used in the finite element modelling of the $\beta-$chip. b) The top view of the $\beta-$chip where the fluid channel was interposed between two gas channels in order to increase the uptake of hydrogen into the chip. c) The key area of the chip enlarged. d) The cross section of the chip illustrating hydrogen diffusion of from the gas channel (red) to the solution channel (blue) e) Hydrogen uptake into the chip as a function flow rate. The black circles represent NMR data and the error bars were calculated form the SNR variation. The black solid line is the result of an FEM simulation. The grey shadow is the ±1.5 μL error in the volume of the chip.

hydrogen is only 8 mM in the $\alpha-$domain while in the $\beta-$domain it is nearly double, at 15.6 mM. At 20 μL min^{-1} the concentration of hydrogen in the $\alpha-$domain is only 3 mM, while in the $\beta-$domain it is 7 mM.

In order to introduce an additional gas channel into the device, the fluid channel was interposed between two gas channels as shown in Fig 5.3 b and c. In this way, the area of the fluid channel in contact with the PDMS membrane was doubled. To measure the uptake of hydrogen gas into the $\beta-$chip, methanol was flowed into the fluid channel by means of a syringe pump located outside of the NMR spectrometer. Hydrogen gas was delivered into the gas channel (marked in red) at 5 bar and its flow was controlled using a mass-flow controller set to 20 mL min^{-1}. A semi-permeable PDMS membrane was used to seal the chip and allow for hydrogen to dissolve in the gas channel as illustrated in Fig. 5.3 d. The chip and PDMS membrane were held together by screw-tightened 3D printed holders and the chip was placed in a home-build transmission line probe. Species of interest were detected in the 2.5 μL sample chamber on the chip. Fig 5.3 e shows the concentration of hydrogen in the sample chamber as a function of flow rate; 20 mM of sodium acetate was used as the concentration standard. The solid empty and black circles represent the NMR data for

$\alpha-$ and $\beta-$chips, respectively. Error bars were calculated from the SNR variation. Data for the $\alpha-$chip was obtained from Ref. [1]. At the flow rate of 2 $\mu\text{L}\,\text{min}^{-1}$ the concentration of hydrogen was found to be ~20 mM in both chips thus they are fully saturated with hydrogen. However, as the flow rate increased to 10 $\mu\text{L}\,\text{min}^{-1}$, the concentration of hydrogen in the $\beta-$chip was 11.3 mM but it's only 6 mM in the $\alpha-$chip. At higher flow rates, at 18 $\mu\text{L}\,\text{min}^{-1}$ there was 3 times more hydrogen dissolved in the $\beta-$chip compared to $\alpha-$chip. The solid and dash-dotted lines are the FEM simulations and the grey shadows represent a ±1.5 μL error in the volume of the chips. Simulations for both $\alpha-$ and $\beta-$chip are in good agreement for flow rates up to 10 $\mu\text{L}\,\text{min}^{-1}$. Above this flow rate, the behaviour is not predicted well. This discrepancy is not well understood yet, it was proposed that this could be due to the deformation of the PDMS membrane [1].

The PHIP reaction was performed by flowing the precursor solution containing 20 mM of propargyl acetate **3** and 5 mM of rhodium catalyst **1** into the solution channel and delivering 5 bar of *para*-enriched hydrogen gas **2** into the gas channel. Fig 5.4 a shows a single scan proton NMR spectrum acquired after a $\frac{\pi}{4}$ pulse obtained from a steady-state experiment where the solution was flowed at 5 $\mu\text{L}\,\text{min}^{-1}$. The hyperpolarized spectrum contains an antiphase doublet at 5.2 ppm corresponding to protons H^h and an antiphase multiplet at 5.9 ppm corresponding to protons H^f. This is compared with a 512-scans reference spectrum obtained with hydrogen in thermal equilibrium shown in Fig 5.4 b. Each scan was acquired after a $\frac{\pi}{2}$ pulse with a recycle delay of 30 s. From the ratio of the signal intensity in the reference and hyperpolarized spectra, the ^{1}H polarization was estimated. In the reference spectrum, the SNR was found to be 9:1, while it was 300:1 in the hyperpolarized spectrum. Since the reference spectrum was obtained using 512 scans, the SNR resulting from a single scan would be $9/\sqrt{512} \approx 0.40$. Therefore, the signal enhancement factor is $\varepsilon \approx 300/0.4 \approx 750$. At the field of 11.7 T and temperature of 25°C this corresponds to 3% ^{1}H polarization.

To estimate the yield of allyl acetate, 10 mM of propan-2-ol (IPA) was added into the precursor solution. At 5 $\mu\text{L}\,\text{min}^{-1}$ flow rare, the concentration of propargyl acetate was 4.9 ± 0.2 mM, which corresponds to 24.5 ± 0.25% yield. This was calculated by

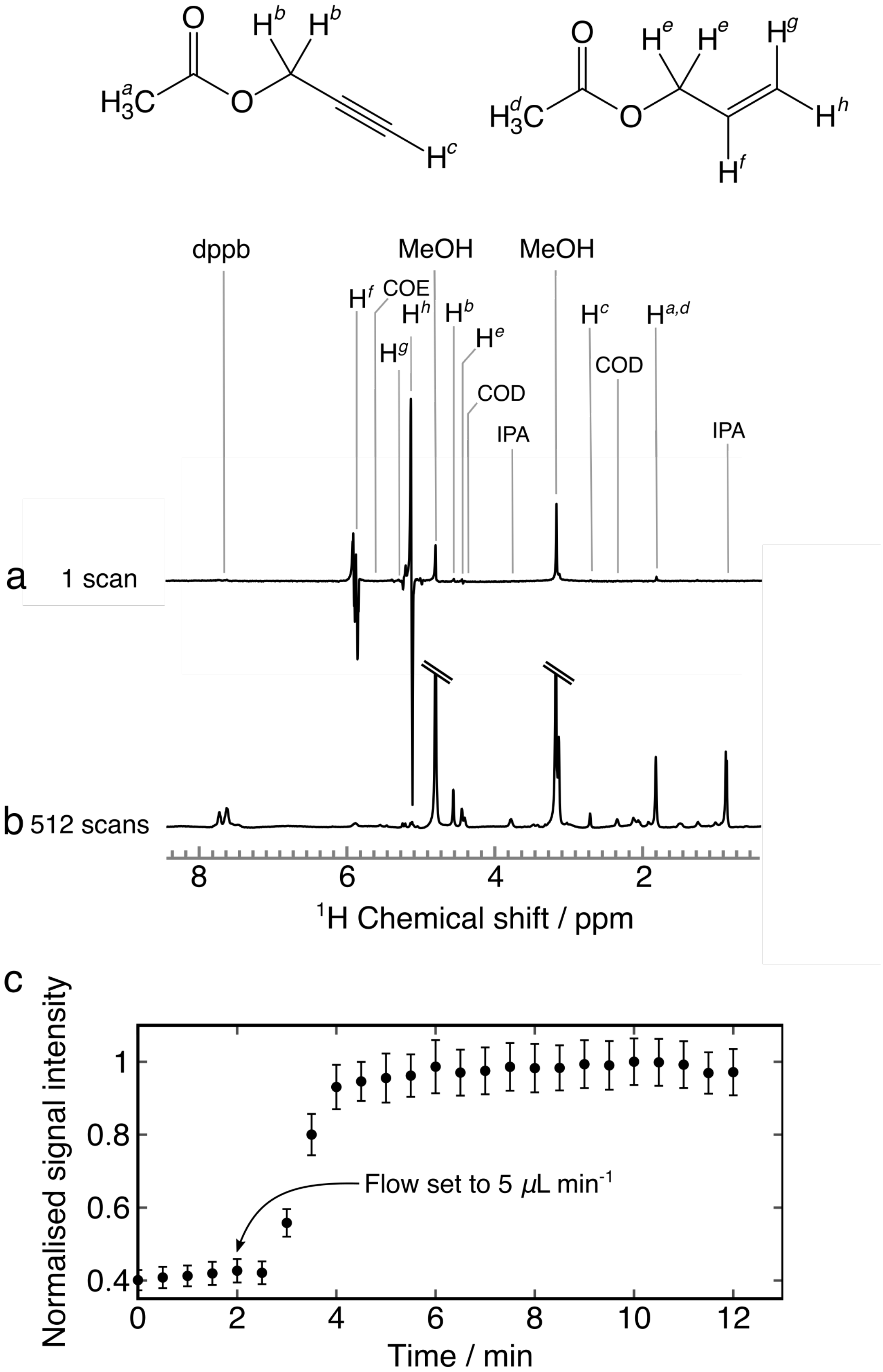

FIGURE 5.4: a) A single scan proton spectrum obtained with parahydrogen. b) A reference spectrum obtained with hydrogen in thermal equilibrium. Methanol peaks have been suppressed for clarity. c) The buildup of the hyperpolarized signal (H^h) after changing the flow rate from 4 to 5 μL min^{-1}. Error bars represent the error of fit.

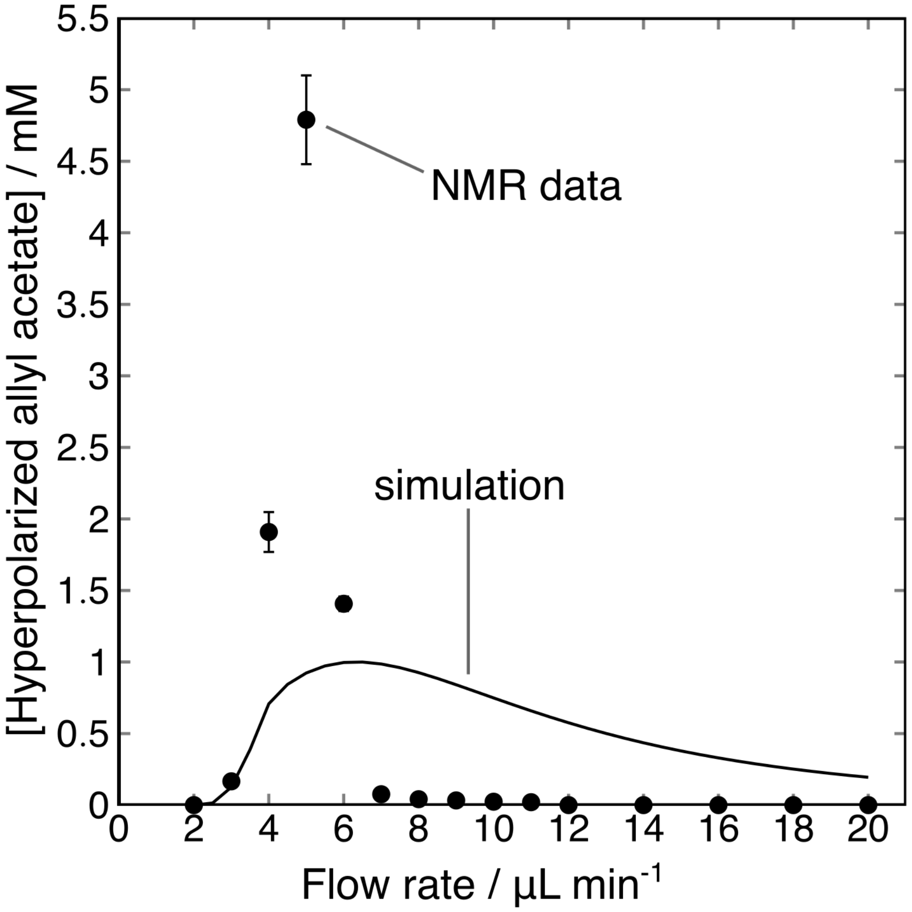

FIGURE 5.5: Steady-state signal intensity as a function of flow rate. The solid circles correspond to the NMR data for the $\beta-$chip and the solid line is the finite element simulation of the PHIP reaction. Error bars represent error of fit

comparing the intensity of the IPA peak at 1.14 ppm in the reference spectrum to the intensity of the H^f peak and accounting for the difference in the number of protons.

Fig 5.4 c shows the buildup of a hyperpolarized signal H^h after changing the flow rate from 4 to 5 $\mu\mathrm{L\,min}^{-1}$. NMR spectra were acquired every 30 s using a $\frac{\pi}{4}$ excitation pulse. The signal intensity begins to rise 30 s after the target flow rate was set to 5 $\mu\mathrm{L\,min}^{-1}$ and it reaches a steady-state after 2 minutes. Similar results were shown in Ref [1] where the signal intensity also took just 2 minutes to buildup. After reaching a steady-state the system provides a remarkable stability of the signal.

The steady-state PHIP signal in the sample chamber of the $\beta-$chip as a function of flow rate is shown in Fig. 5.5. The solid circles represent the experimental data while the solid line represents the finite element simulation. The experimental data represent the integral of the hyperpolarized peak H^h that has been determined using the fitting routine described in the Experimental Section 3.3.3 and each data point plotted represents a mean of 10 experimental data points. Data was normalised to the concentration of allyl acetate, which was calculated to be 4.9 ± 0.2 mM. By introducing an additional hydrogenation pathway the yield of allyl acetate was increased over 15-fold compared with the $\alpha-$chip. Similarly to the data reported by Eills *et al.* [1] there is an initial steep rise in the product formation with increased flow rate that is followed by a maximum. The maximum for the $\alpha-$chip appeared at 8 $\mu\mathrm{L\,min^{-1}}$ and at 5 $\mu\mathrm{L\,min^{-1}}$ for the $\beta-$chip. After that, the yield of the product falls rapidly. As shown in the previous chapter, the reaction profile is dependent on the volume of the chip. The $\alpha-$chip was made of PMMA, which has a very poor resistance to methanol. In this work, the material was replaced by PC because it has a much higher chemical resistance and creates stronger bonding. However, the channels in PC are shallower therefore the total volume of the chip is lower, at around 7 μL as compared to 8.5 μL in the $\alpha-$chip.

To perform the finite element simulation of the PHIP reaction in the $\beta-$chip, the initial concentrations of propargyl acetate **3** and the catalyst **1** were set to 20 mM and 5 mM respectively ($[\mathbf{3}]_0$ = 20 mM, $[\mathbf{1}]_0$ = 5 mM). The supply of hydrogen was modelled as a constant concentration condition, $\mathrm{h_{pmds}} = [\mathbf{2}] = 20$ mM. The initial concentrations of all other species were set to zero. The simulation results are shown as the solid black line in Fig. 5.5. Initially there is a steep increase in the product formation, with a maximum at 6 $\mu\mathrm{L\,min^{-1}}$ corresponding to 1.2 mM. As the flow rate is increased, the concentration of allyl acetate steadily declines. The FEM fits only the first two data points at the lowest flow rates after that the model vastly under-predicts the concentration of allyl acetate formed in the chip. The model also does not predict the kinetics of the reaction, at flow rates above 10 $\mu\mathrm{L\,min^{-1}}$, the experimental data shows a steep decline in the product concentration, while the simulation predicts a steady decrease in the concentration. This is likely because simplistic 2D geometry does not capture mixing that occurs in the chip. Straight, long rectangular channels are used in the $\beta-$domain to represent the fluid channel, while the prototype uses serpentine channels to increase the surface area and enhance the on-chip mixing. However, a simple 2D representation of a microfluidic device allowed to identify the limiting steps

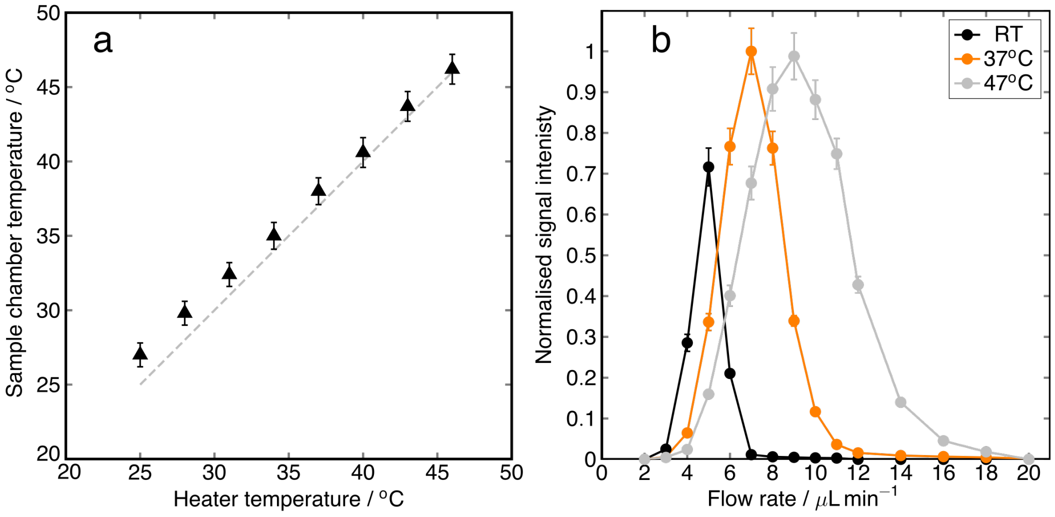

Figure 5.6: a) Temperature calibration curve showing the heater box temperature read by a sensor placed inside of one of the water heaters plotted against the temperature at the sample chamber of the chip determined by the chemical shift difference of the water and DSS peaks. Error was estimated by taking the variation in water peak's width. b) Flow-rate dependence of the hyperpolarized allyl acetate yield at three different temperatures. Black, orange and orange dots represent the experimental data for data obtained at 25°C, 37°C and 47°C respectively.

of the reaction and aided design of a more optimized microfluidic device. The model has no adjustable parameters, and simulations for the uptake of hydrogen into both the $\alpha-$ and $\beta-$chips are in quantitative agreement with the experimental data.

Another way of accelerating the reaction rates is by increasing the temperature of the reaction. In order to heat the sample chamber, the stripline detector was interposed between a pair of water heaters such that only the sample chamber of the chip was heated. Fig. 5.6 a shows the temperature at the sample chamber versus the temperature displayed by the heater. The temperature calibration curve was determined by the chemical shift difference between water and DSS peaks. Overall, the sample chamber of the chip is efficiently heated to a desired temperature with a temperature variation of ± 3 °C from the target temperature, which sufficient for this application. Appendix I shows the temperature log from the heater.

Fig. 5.6 b shows the normalised signal intensity of proton (H^h) as a function of flow rate at three different temperatures. The black, orange and grey solid circles correspond to the experimental data obtained at 25°C, 37°C and 47°C. As the temperature is increased form 25 to 37 °C, the maximum of the signal increases by

30%. Upon further 10°C increase, the maximum signal decreased by ~2%. Increasing the temperature by 10°C shifts the position of the maximum to a higher flow rate by 2 μL min^{-1}. At 25°C the maximum is located at 5 μL min^{-1}, while at 47°C it is at 9 μL min^{-1}. The position of the maximum represents a balance between the rate of relaxation of the hyperpolarized product and the hydrogen uptake into the chip. At low flow rates such as 2 μL min^{-1}, the residence time of the hyperpolarized product in the fluid channel is very long therefore it fully relaxes before it reaches the sample chamber. As the flow rate increases, the product is delivered faster to the sample chamber and less of it is lost due to relaxation hence the steep spike from 2 μL min^{-1} until the maximum. As the temperature increases so do the reaction rates hence the position of the maximum shifts to a higher flow rate as the product needs to be delivered faster into the sample chamber.

In order to determine the yield of allyl acetate at the optimum flow rate, the experiment was repeated using hydrogen in thermal equilibrium. 10 mM IPA was used as the concentration standard and the thermal spectra are shown in Fig. 5.7. The results are listed in Table 5.1.

The concentration of allyl acetate at 25°C was found to be 4.9 ± 0.2 mM, which corresponds to 24.5 ± 1% yield. The same calculations were repeated for data obtained at 37°C and 47°C. The concentration of allyl acetate at the optimal flow at 37°C was found to be 7.0 ± 0.2 mM, resulting in the yield of 35.0 ± 1.0%. This is a further increase of 10% in the yield. Increasing the temperature further to 47°C resulted in a drop in the concentration of **4** to 5.4 ± 0.2 mM. At 37°C the reaction is most efficient and even leads to the formation of propyl acetate, as evidence by a H^{i} peak at 4.33 ppm in Fig. 5.1, which is absent at other temperatures. The concentration of propyl acetate was calculated as 1.2 mM ± 0.2 mM.

T / °C	**q / μL min^{-1}**	**[4] / mM**	ε	**^{1}H polarization / %**	**Molar polarization / μM**
25	5	4.9 ± 0.2	750	3.0	147 ± 6
37	7	7.0 ± 0.2	1060	4.1	287 ± 8
47	9	5.2 ± 0.2	930	3.5	182 ± 7

TABLE 5.1: Experimental results for the PHIP reaction in the $\beta-$chip performed at 25°C, 37°C, and 47°C.

From the ratio of the signal intensity in the reference and hyperpolarized spectra, the ^{1}H polarisation was estimated. Accounting for the difference in the number of scans, the signal enhancement was calculated as 750. At the field of 11.7 T and temperature of 25°C this corresponds to 3.0% ^{1}H polarisation. The enhancement factor for reactions performed at 37°C and 47°C was found to be 1060 and 930, respectively. This corresponds to the ^{1}H polarisation of 4.1% and 3.5%, respectively. The polarization level for the $\alpha-$chip was reported as 8% [1], which is a much higher polarization than obtained in the $\beta-$chip. This is due to the fact that polarization is calculated in relation to the yield obtained. For that reason polarization level or signal enhancement alone are not good indicators of the total signal intensity available from the hyperpolarized species. Instead, molar polarization should be considered, which is defined as the product of the polarization level and the concentration of the species [270]. Molar polarization for the $\beta-$chip was calculated as 147 ± 6, 287 ± 8, 182 ± 7 μM, for reactions preformed at 25°C, 37°C, and 47 °C, respectively, while the molar polarization for the $\alpha-$chip was less than 40 μM. By implementing an additional hydrogenation pathway in the $\beta-$chip the molar polarization has nearly quadrupled compared with the $\alpha-$chip. Elevating temperature of the reaction by 10 °C further ~doubled the molar polarization. However at 47 °C, molar polarization decreased.

5.3 Conclusions

In this work finite element simulations and modelling was used to aid design of an optimized microfluidic device for performing a PHIP reaction at the microscale. The FEM of the chip discussed in Chapter 4 identified that an inadequate uptake of hydrogen into the device is the limiting factor for the reaction, which resulted in sub-milimolar product concentration. Since simply increasing the hydrogen pressure at which the device operate is not a viable option due to engineering challenges, a scenario in which hydrogen is increased by introducing an additional hydrogen channel was first simulated. Introduction of an additional hydrogenation channel resulted in at least 2-fold increase in hydrogen uptake into the device and consequently led to a 15-fold increased in the yield of hyperpolarized allyl acetate compared with the

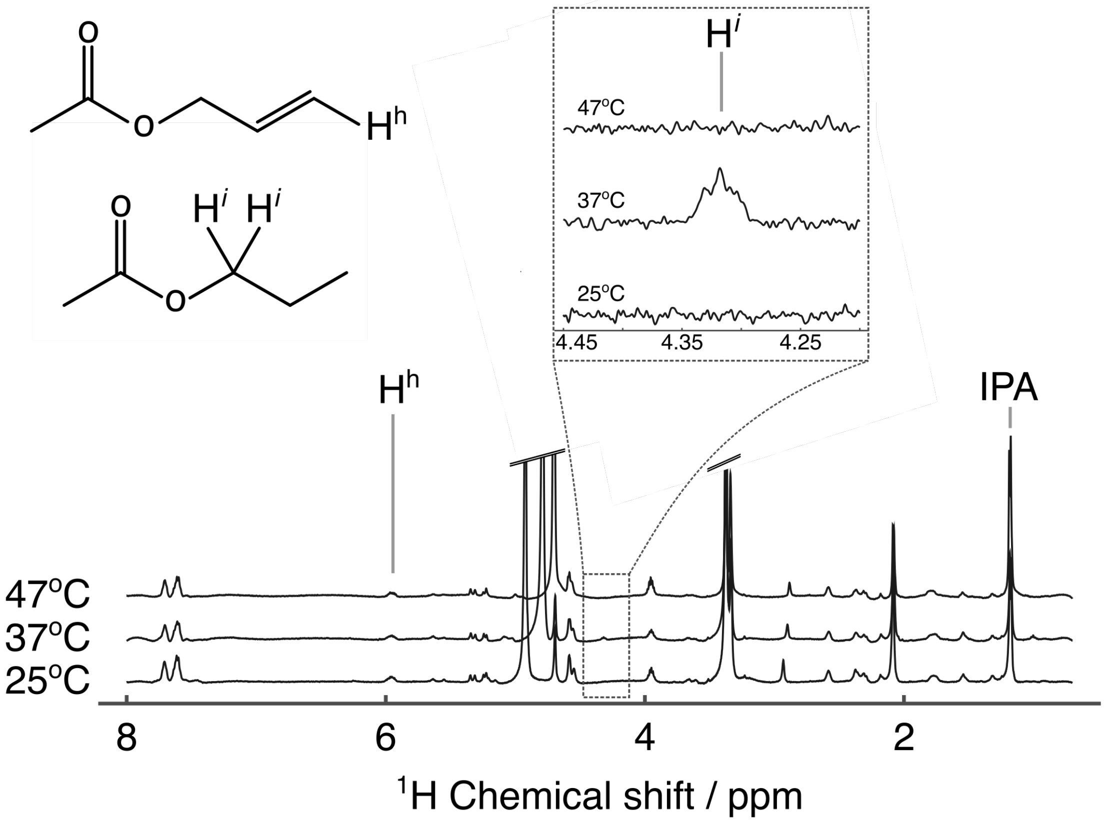

FIGURE 5.7: 512 scan proton spectra obtained after the reaction of propargyl acetate with hydrogen in thermal equilibrium at 25°C, 37°C, and 47°C. Spectra were obtained at steady-state flow rate of 5, 7, and 9 μL min^{-1}, respectively. The key species used in the yield calculations are highlighted. 10x magnification of the 4.20 - 4.35 ppm region reveals the propyl acetate peak H^i.

previously reported $\alpha-$chip [1]. Heating the sample chamber of the chip to 37°Cled to further 10% increase in the yield.

Although the simple 2D representation of the $\alpha-$chip provided an invaluable insight into the complex spatially resolved kinetics occurring inside of the device it has reached its limits with a more complex geometry. The model predicts well the interplay of the chemical kinetics and the transport properties of the chip however, it fails to predict the complex interactions of the catalyst, the hydrogen and the precursor as well as to include detailed spin dynamics unique to this spin system. That is an inherent limitation of the software, COMSOL Multiphysics 5.4, used to simulate this reaction as it does not allow to include spin dynamics of the system. This can potentially be achieved by simulation these conditions using Flokke Planck formalism discussed in details in Ref [243, 241].

Chapter 6

PHIP ^{13}C Hyperpolarized Metabolite in a Microfluidic Chip

This chapter is an extended version of S. J.Barker, L. Dagys, W. Hale, B. Ripka, J. Eills, M. Sharma, M. H. Levitt, M. Utz, Direct Production of a Hyperpolarized Metabolite on a Microfluidic Chip, *Analytical Chemistry*, 94(7), 3260-3267, 2022 [3].

6.1 Introduction

Microfluidic systems are commonly used as scaffolds for cell [271–275] and organ [14, 276–281] culture. Through a careful design of the channel network, LoC can mimic physiological environment in a highly controlled and repeatable manner, providing valuable models for supporting the development of diagnostics [15, 16], therapies [14] and drug safety testing [17, 18] but can also be used as microreactors [282–284] for chemical reaction monitoring [285], separations or the detection of various compounds [276, 286, 287].

Carbon (^{13}C) NMR and imaging (MRI) is an attractive technique for real-time and non-invasive metabolic studies of living organisms as carbon is the backbone for nearly all organic molecules [288]. Additionally, ^{13}C detection offers significant advantages for biological applications due to longer longitudinal relaxation times than ^{1}H, larger chemical shift dispersion, and reduced overlap with background signals. The challenge lies in its low natural abundance at 1.1%. Implementing hyperpolarization methods offers an opportunity to enhance the ^{13}C signals by more than 10 000, enabling studies of metabolic and physiological processes, especially in volume limited systems such as LoC. For instance, hyperpolarized fumarate is widely used as a contrast agent for *in vivo* detection of necrosis [226, 227, 270, 289–295].

In this chapter, [1-^{13}C]fumarate is formed via trans-hydrogenative PHIP in a microfluidic chip under continuous-flow conditions, performing the chemical reaction in one part of the chip and NMR detection in another. To our knowledge, this is the first demonstration of ^{13}C-hyperpolarized metabolite production in a microfluidic device by PHIP. While the current implementation on the chip is not yet ready for use with biological systems due to the presence of the catalyst and other residues, the stability of the microfluidic implementation allows systematic studies of complex kinetic effects.

PHIP utilises a chemical reaction to transfer parahydrogen-derived spin order onto the target molecule, and the reaction is usually mediated by an organometallic catalyst such as rhodium or ruthenium. The presence of the catalyst significantly complicates the reaction chemistry and often leads to the formation of unwanted intermediates. In particular, the interaction of parahydrogen with the catalyst breaks the symmetry of $\mathrm{p-H_2}$ and if the life-time of such complexes is long enough this can lead to a significant leakage of the singlet state population into the central triplet state (called singlet-triplet mixing), which can substantially hinder the achievable polarization. PHIP is conventionally implemented by bubbling hydrogen gas enriched in the para spin isomer through a solution containing a suitable substrate and catalyst, either directly at high magnetic field (PASADENA experiments) [22] or outside of the magnet at low (μT) fields, followed by an adiabatic increase of the magnetic field (ALTADENA experiments) [296]. Such experiments are effective, but quite difficult to repeat accurately. This complicates systematic studies of the interplay between reaction kinetics and nuclear spin relaxation processes. Microfluidic implementation of hydrogenative PHIP utilises a semi-permeable PDMS membrane to bring the parahydrogen gas in contact with the PHIP solution. This enables experiments to be

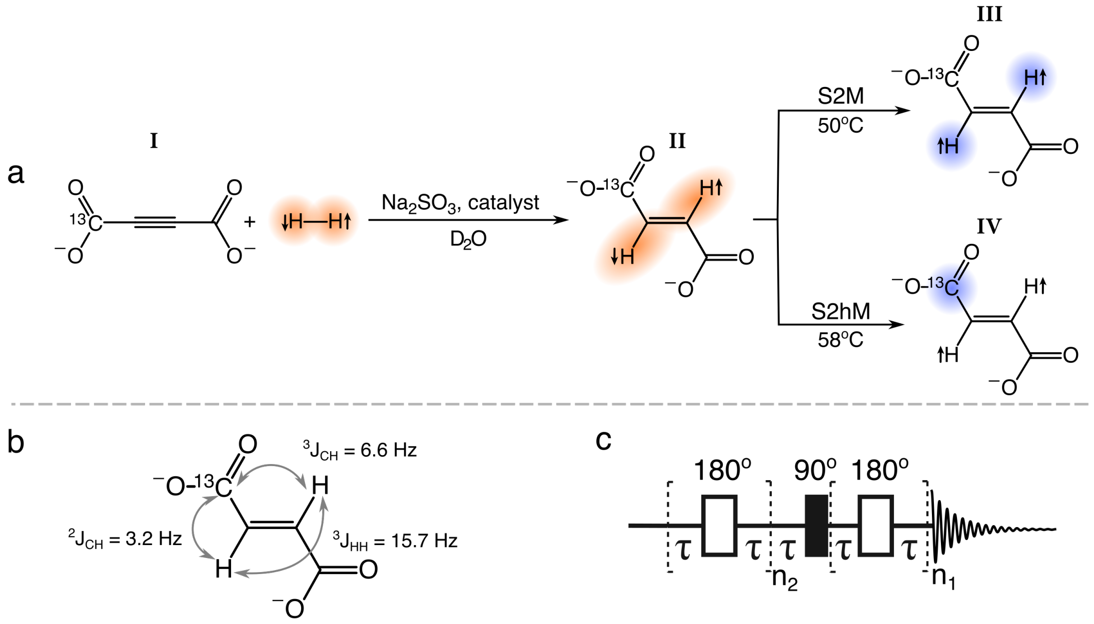

FIGURE 6.1: a) The reaction investigated in this work. acetylene dicarboxylic acid [1-^{13}C] disodium salt labelled as molecule **I** reacts with parahydrogen in the presence of sodium sulfite and the catalyst [RuCp*$(CH_3CN)_3$]PF_6 in D_2O. The reaction results in a production of disodium [1-^{13}C]fumarate, molecule **II**, with the two protons in a singlet state. Application of the S2M or S2hM pulse sequence converts the singlet state into a state that is magnetic and hence observable. b) The $J-$coupling network of [1-^{13}C]fumarate. The $J-$coupling values were taken from Ref. [182]. c) A general schematic representation of the S2M pulse sequence.

performed under continuous flow, with a stable stationary level of hyperpolarization established in the chip.

Singlet-triplet mixing has been reported to hinder the achievable polarization of [1-^{13}C]fumarate at high field [227, 297, 256]. In the following, the PHIP-on-a-chip platform is utilised to quantify how effectively two different RF pulse methods mitigate the problem of ST mixing and the findings are supported with computational spin dynamics simulations. Then the optimized pulse sequence is used to generate carbon hyperpolarization in the $\beta-$chip. Lastly, quantitative data on the kinetics and yield of [1-^{13}C]fumarate from acetylene dicarboxylic acid [1-^{13}C] disodium salt are discussed.

6.2 Background

Hyperpolarized fumarate can be generated through a hydrogenation of acetylene dicarboxylic acid [1-^{13}C] disodium salt **I** with parahydrogen in the presence of a

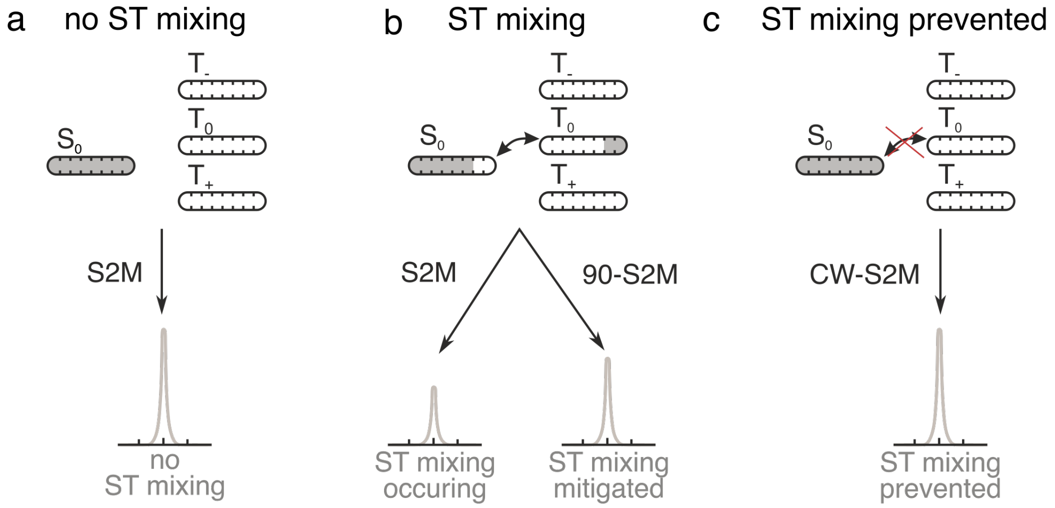

FIGURE 6.2: a) An illustration of the ideal case where no ST mixing occurs; only $|S_0\rangle$ is populated b) A case where ST mixing occurs leading to a leak of $|S_0\rangle$ population to the $|T_0\rangle$ state. ST mixing is negated by applying a purge pulse prior the S2M, which distributes the $|T_0\rangle$ population to $|T_+\rangle$ and $|T_-\rangle$ c) A case where ST mixing is avoided by applying a CW pulse during the hydrogenation reaction.

ruthenium catalyst, which results in a trans-hydrogenated molecule of fumarate **II** as shown in Fig 6.1 a. Since protons in the fumarate molecule are magnetically and chemically equivalent, they are NMR silent. To access the hyperpolarized state, a ^{13}C label was introduced into one of the carboxylate groups to break the symmetry and introduce ^{1}H$-^{13}$C $J-$couplings, which are listed in Fig. 6.1 b [182, 298]. The slight magnetic inequivalence due to the difference in the couplings makes it possible to convert the singlet order into observable hyperpolarized magnetisation through the use of RF pulse sequences. The singlet-to-magnetisation (S2M) [231–234] and singlet-to-heteronuclear magnetization (S2hM) [182, 299] pulse sequences can be used to convert the singlet order into observable magnetisation (see Fig. 6.1 c). Such sequences are robust against field inhomogeneities in contrast to alternative methods [231], which is an important factor because magnetic field inhomogeneities are present in the chip due to differences in magnetic susceptibility of the chip and the solvent [300]. Applying S2M sequence after the chemical reaction with parahydrogen results in high magnetisation of the two protons giving rise to a hyperpolarized substance **III**, while S2hM enables polarization transfer to a carbon nucleus **IV**.

The polarization that is generated on the target molecules can be attenuated by singlet-triplet (ST) mixing (sometimes called ST leakage) [301]. In an ideal case, there is no ST mixing and the population of the $|S_0\rangle$ is converted into a large hyperpolarized signal as shown in Fig. 6.2 a. However, in some cases hydrogen molecules can form intermediate hydride species with the catalyst metal center, where the two hydrogen atoms take up inequivalent positions, such that they experience a chemical shift difference at high field. If the lifetime of this intermediate complex is long enough, there can be a significant leakage from the H_2 proton singlet state to the central triplet state $|T_0\rangle$, which generally reduces the resulting PHIP signals [301–303]. The S2M sequence converts both the $|S_0\rangle$ and the $|T_0\rangle$ states to magnetisation, but with opposite phases. The $|T_0\rangle$ population therefore *reduces* the resulting NMR signal, as illustrated in Fig. 6.2 b. This process sometimes gives rise to a partially-negative line (PNL) in the ^{1}H NMR spectra [304]. It is also known to occur in non-hydrogenative PHIP experiments, and has been noted to give rise to 'spontaneous' polarization on the target molecules [305], although generally ST mixing is undesirable.

Two methods have been shown to suppress ST mixing: spin locking on the hydride resonance during the chemical reaction [24, 230, 297, 304, 306–312], and applying a hard $\pi/2$ purge pulse to deplete the $|T_0\rangle$ state prior to the polarization transfer step [24, 304, 306, 312–315]. These two methods are illustrated in Fig. 6.1 b and c.

Probing ST mixing in hydrogenative PHIP experiments is very challenging as it requires stable and reproducible conditions, which are difficult to achieve using conventional bubbling or shaking experiments. Additionally, since hydrogenative PHIP relies on irreversible chemical reactions, the chemical kinetics influence the observed spectra, and the sample under study needs to be replaced upon the reaction reaching completion. This is a particular issue if the samples are scarce or expensive due to isotopic enrichment. Finally, since hyperpolarized nuclei are in a non-equilibrium state, the NMR signals relax on a timescale of seconds to tens of seconds, unique to each molecular species and nuclear spin site, which can convolute the observed results. This is especially problematic if the signals relax quickly compared to the time it takes for a shaken tube to be placed in the NMR magnet, or for bubbles to settle in solution. Conversely, the study of ST mixing is greatly facilitated by microfluidic PHIP, since instabilities associated with bubbling experiments are avoided. Once a steady-state is established, stable and reproducible experimental conditions are provided.

6.3 Results and Discussion

In order to obtain hyperpolarized [1-^{13}C]fumarate, 100 mM acetylene dicarboxylic acid [1-^{13}C] disodium salt was reacted with parahydrogen at 5 bar in the presence of a ruthenium catalyst. Direct application of the S2hM pulse sequence in the $\alpha-$chip did not result in any observable ^{13}C signals therefore, in order to gain insight into the probable cause, proton spectra were investigated. Fig. 6.3 a depicts a 400-scan reference spectrum obtained after the application of a $\frac{\pi}{2}$ pulse in a steady-state flow experiment using hydrogen in thermal equilibrium (i.e., not *para*-enriched). This is compared to a single-scan proton NMR spectrum obtained after the S2M pulse sequence in a steady-state flow experiment with para-enriched H_2 depicted in Fig. 6.3 b.

The hyperpolarized spectra contain a peak at 6.6 ppm that corresponds to the fumarate protons H^a. From the ratio of the signal intensity in the reference and hyperpolarized spectra, the ^{1}H polarization was estimated. Accounting for the difference in the number of scans, the signal enhancement was calculated as 190 ± 10. At the field of 11.7 T and temperature of 50°C this corresponds to $0.7 \pm 0.1\%$ ^{1}H polarization. At 10 $\mu\mathrm{L\,min^{-1}}$ flow rate, the concentration of fumarate was 1.2 ± 0.5 mM , which corresponds to 1.2 ± 0.5 % yield. This was calculated by comparing the intensity of the Cp* peak in the reference spectrum to the intensity of the fumarate peak and accounting for the difference in the number of protons.

The reaction kinetics can be probed by varying the flow rate. Fig. 6.3 c shows the steady state signal intensity of the proton H^a peak as a function of flow rate. As the flow rate increases from 2 to 10 $\mu\mathrm{L\,min^{-1}}$, there is a steady increase in the product formation. The signal intensity plateaus at 10-12 $\mu\mathrm{L\,min^{-1}}$ and steadily declines below 14 $\mu\mathrm{L\,min^{-1}}$. The reaction profile is much more steady in comparison to the propargyl acetate reaction discussed in the previous chapters. This most likely stems form the fact that this reaction is much slower compared with the propargyl acetate hydrogenation. It has been reported that at 60°C, it takes 2000s to reach the maximum of the product [227].

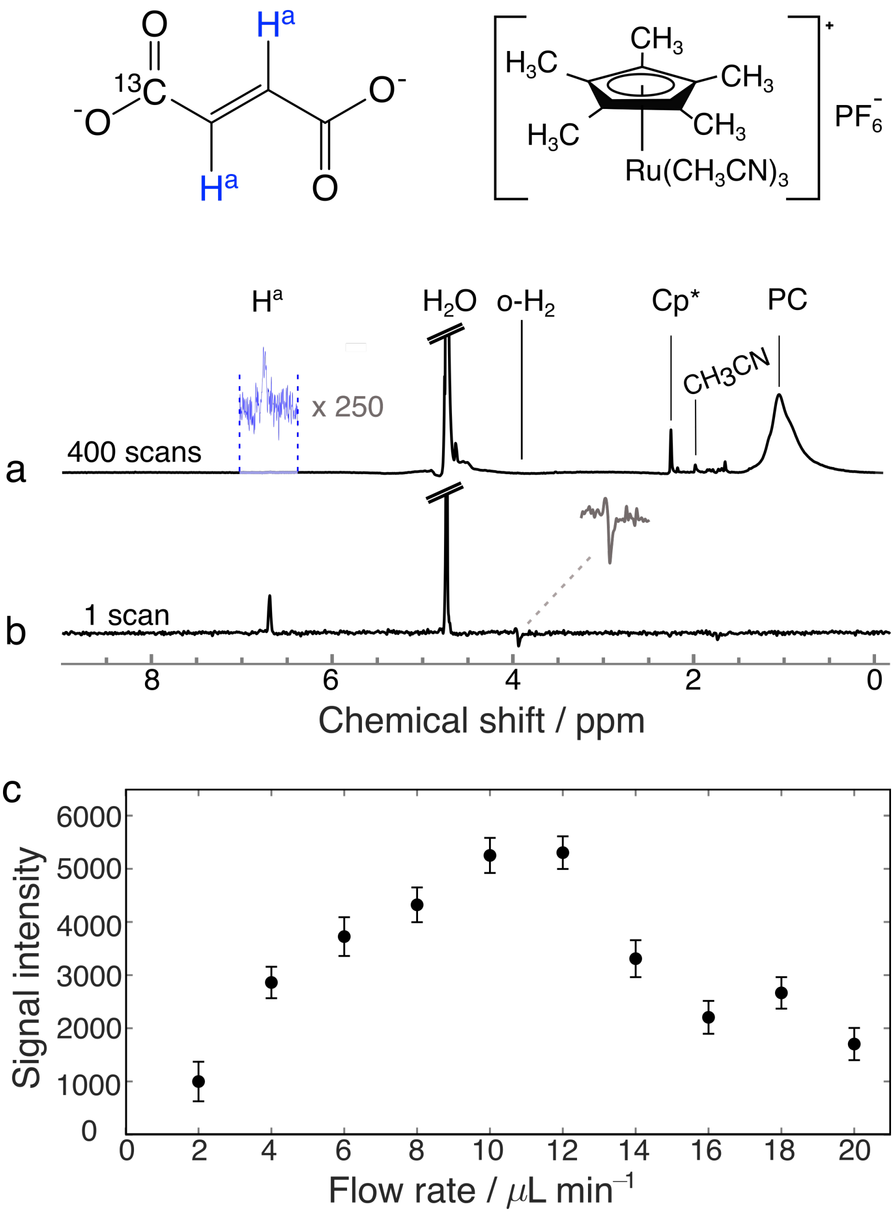

FIGURE 6.3: The steady state ^{1}H NMR spectra of [1-^{13}C]fumarate sample flowing at 10 μL min^{-1} in the $\alpha-$chip. a) The 400-scan reference spectrum obtained after application of a $\frac{\pi}{2}$ pulse in a reaction with hydrogen in thermal equilibrium. b) A single-scan spectrum after application of the S2M pulse sequence from a reaction with parahydrogen. The trace displays a hyperpolarized [1-^{13}C]fumarate peak at 6.6 ppm. The presence of exchanging hydrogen species is indicated at 4 ppm ($\mathrm{o-H_2}$). Cp*: catalyst methyl protons; PC: background signal from the polycarbonate chip material. c) The steady-state signal intensity of H^a protons as a function of flow rate.

The hyperpolarized spectrum features the aforementioned partially negative line at 4 ppm labelled $\mathrm{o-H_2}$. The heavy metal catalyst and dissolved molecular hydrogen

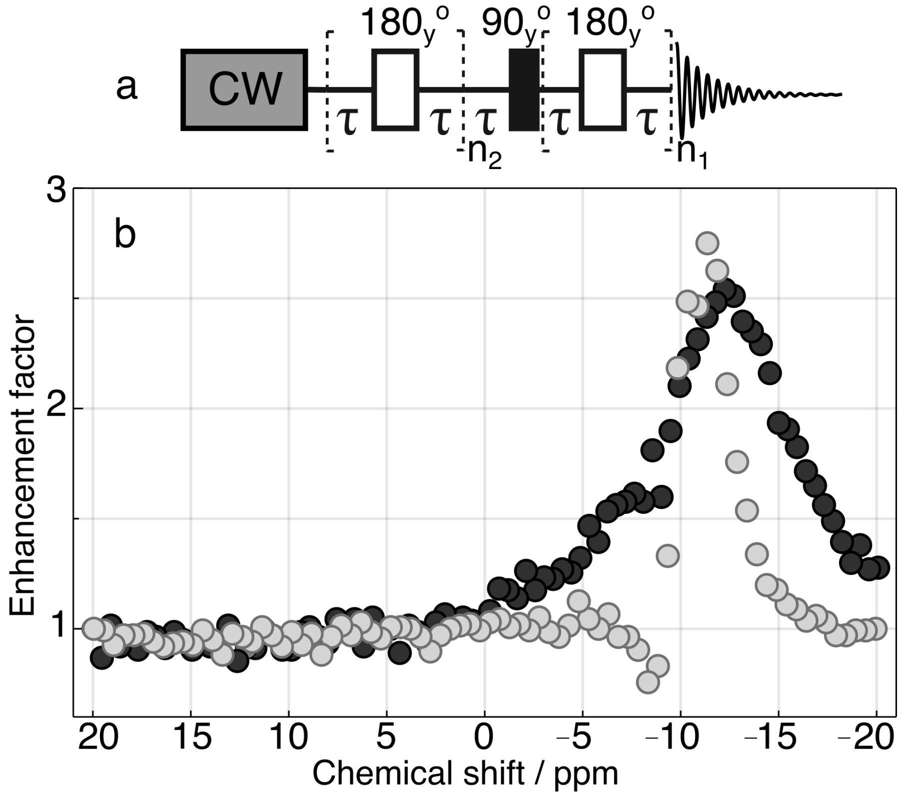

FIGURE 6.4: a) The singlet-to-magnetisation pulse sequence with spin-locking field applied during the recycle delay. The following parameters were found to be optimal for the sequence: $\tau = 0.0156$ ms, $n_1 = 7$, $n_2 = 14$. b) Integral of the hyperpolarized proton of [1-^{13}C]fumarate as a function of the resonance offset of the spin-locking field. Experiments were preformed with two CW amplitudes, corresponding to 2 kHz and 0.5 kHz nutation frequency shown as black and grey data points, respectively. The signal amplitude was normalised to the S2M signal without the spin locking field.

form intermediate complexes where the two hydrogen nuclei occupy chemically inequivalent positions. At high magnetic field this introduces a chemical shift difference between the two protons, which causes singlet state population to leak into the population of the central triplet state. In addition, the chemical shift difference lifts the degeneracy of the two triplet state transitions. In rapid exchange, this leads to a small partially negative line in the dissolved H_2 signal [304, 305, 311, 313], as displayed in the spectrum in Fig. 6.3 b.

To suppress the effects of ST mixing we performed experiments in which we applied continuous-wave (CW) irradiation to the sample for 20 s prior to the application of S2M and signal acquisition. The pulse sequence is shown in Fig 6.4 a. The resulting integral of the fumarate signal intensity at 6.6 ppm is plotted as a function of CW offset frequency in Fig. 6.4 b. Experiments were performed with two different CW amplitudes, corresponding to 0.5 kHz and 2 kHz nutation frequency on protons shown as grey and black circles, respectively.

The profiles of signal intensity against the CW irradiation frequency display a peak at around −11 ppm. This is a typical chemical shift of hydride species for ruthenium complexes [316], indicating that ST mixing does indeed occur for the hydride species, and is suppressed by CW irradiation. The ^{1}H spectra can be used to observe ST mixing and this has been shown in case of SABRE by either applying a single hard pulse after CW irradiation or a pulse sequence designed to probe higher spin-order if hydride species undergo very fast chemical exchange [304, 305]. In the present case, hydride species are not directly observable due to fast exchange and low sensitivity. The signal is enhanced by a factor of ∼3 when the spin-locking amplitude is set to either to 0.5 kHz or 2 kHz applied at −11 ppm. The peak width in each case corresponds roughly to the excitation bandwidth, resulting in a narrower peak at the lower CW amplitude.

The CW-irradiation method was contrasted with another method, which has been used to address ST mixing effects: applying a hard pulse (which we will refer to as the purge pulse) to the protons prior to polarization transfer and signal acquisition. Application of a $\pi/2$ purge pulse on the proton channel depletes the $|T_0\rangle$ state, which partially reconstitutes the population difference between the $|S_0\rangle$ and $|T_0\rangle$ states. [24, 304, 306, 313–315].

Fig. 6.5 a depics the pulse sequence used to investigate the phenomenon, and Fig. 6.5 b shows the hyperpolarized H^a proton signals obtained experimentally by varying the flip angle θ from 0° to 360° in steps of 10°. The signal shows an oscillatory dependence on the flip angle of the purge pulse, with maxima occurring at 90° and 270°, and no improvement seen near 180°. The signal at 270° is about 15% less than at 90°. This is partially due to B_1 inhomogeneities in the probe. However, the $\frac{A_{90}}{A_{810}}$ signal ratio for this probe is better than 92% [138], and we therefore suspect that additional factors may be contributing.

The spectral peaks in the Fig 6.5 b also display phase distortions depending on the flip angle of the purge pulse. The origin of the effect was confirmed by numerical

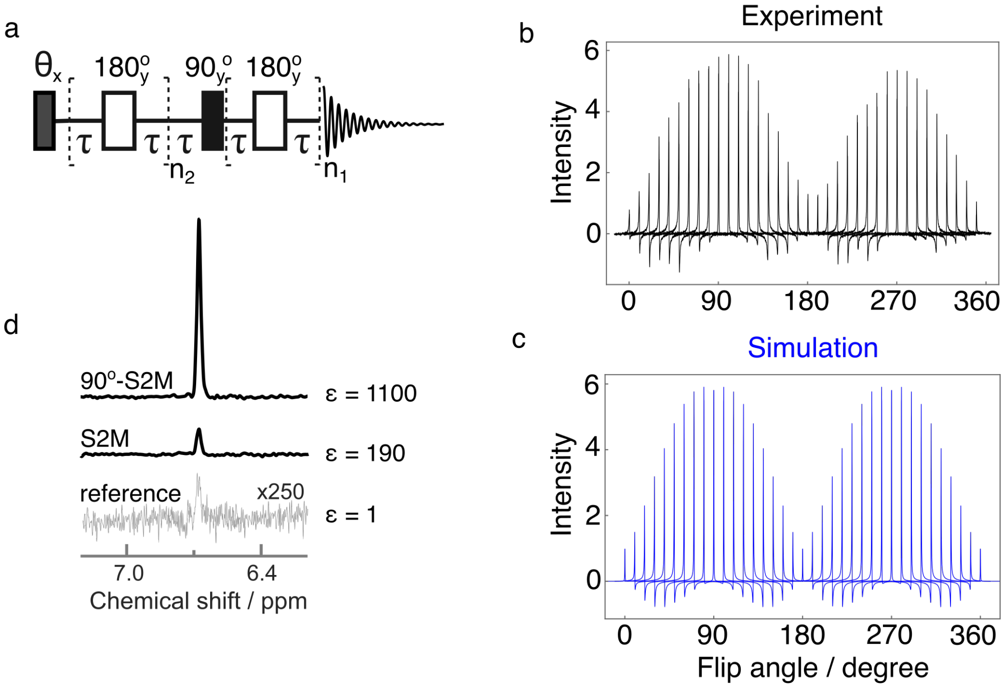

FIGURE 6.5: a) θ - S2M pulse sequence. The θ angle was arrayed from 0° to 360° in steps of 10°. $\tau = 15.6$ ms, $n_1 = 7$, $n_2 = 14$ b) Experimentally obtained H^a signals of [1-^{13}C]fumarate as a function of the purge pulse angle. The y-axis shows the improvement of the enhancement factor compared to the S2M without the purge pulse. c) Computational simulation of the spin system using SpinDynamica software [317] d) Comparison of the signal intensity of fumarate protons (H^a) between the reference spectrum, pure S2M and $90° - $S2M.

simulations using software package SpinDynamica [317] and the result is shown in Fig 6.5 c. The simulation assumes that before the application of the sequence depicted in Fig 6.5 a, the $|S_0\rangle$ and $|T_0\rangle$ states are populated by 55% and 45%, respectively. The other triplet states are neglected. The agreement between experimental data and numerical simulation is striking. The phase distortions, are caused by triplet-triplet coherences excited by the first pulse, when its flip angle is not an integer multiple of 90 degrees. Both experiments and simulations show phase distortions when the flip angle is not an integer multiple of 90 degrees. These phase distortions arise as follows: When the first pulse has a flip angle of 90 degrees, the pulse transfers the population of the central triplet state $|T_0\rangle$ to the outer triplet states $|T_{\pm1}\rangle$, increasing the population difference between the singlet state $|S_0\rangle$ and the central triplet state $|T_0\rangle$, and hence enhancing the hyperpolarized NMR signal at the end of the pulse sequence. However, the flip angle of the first pulse is not a multiple of 90 degrees, the transport of populations between the triplet state is accompanied by the excitation of single-quantum triplet-triplet coherences, of the form $|T_{\pm 1}\rangle\langle T_0|$ and $|T_0\rangle\langle T_{\pm 1}|$. These coherences persist throughout the pulse sequence, and appear as out-of-phase signal components in the observed spectrum, which have the effect of an undesirable phase shift of the observed peak.

In Fig. 6.5 d a comparison is shown between the reference spectrum obtained with 400 scans and single scan NMR spectra of protons $\mathrm{H^a}$ after applying the S2M sequence with a purge pulse of 0° and 90°. The enhancement in the latter case was calculated to be 1100 ± 10 in contrast to 190 ± 10 without applying the purge pulse. This corresponds to $4.0 \pm 0.1\%$ ^{1}H polarization, and hence a nearly 6-fold improvement in the achievable fumarate signal. The enhancement factor was calculated by comparing the integral of the $\mathrm{H^a}$ peak in the hyperpolarized and reference spectrum, accounting for the difference in the number of scans between the two spectra.

The hard-pulse method yielded a 6-fold improvement in the achievable fumarate signal, compared to 3-fold improvement for the spin-locking method. This was unexpected since the spin-locking method can in principle lead to higher signal enhancements as it should mitigate the effect of ST mixing entirely. We believe the lower efficiency provided by spin locking is due to the micro-NMR probe design where the RF field is concentrated exclusively onto the sample chamber as shown in Fig. 3.2 d. Therefore the solution outside of the sample chamber is not affected by the RF irradiation, and thus ST mixing cannot be suppressed for molecules of fumarate that formed in the channels before reaching the sample chamber. This is not a problem for the hard-pulse method since the pulse is applied after the chemical reaction.

The results obtained show a remarkable reproducibility and stability of the chemical reactions performed in the microfluidic device over the course of hours. A steady-state between the rate of chemical reaction to form the hyperpolarized product and the rate of relaxation was established, and without the confounding influence of these external factors it is possible to study and optimise pulse sequences in hyperpolarized NMR experiments. An additional benefit of working on a microfluidic scale is the small sample volumes required, meaning expensive or scarce samples can be more readily used. For example, the data in Fig. 6.5 b required 40 minutes of experimental time, consuming 400 μL of solution, which is the approximate volume required for a single PHIP experiment in a conventional 5 mm NMR tube.

The yield of fumarate in the $\alpha-$chip was 1.2 ± 0.5 %. This low yield of the reaction is most likely due to the limited uptake of hydrogen into the flowing solution as well as a slow reaction time. As discussed in Chapter 4, when methanol is flowed through the $\alpha-$chip at 10 $\mu\mathrm{L\,min^{-1}}$ at a partial pressure of 5 bar, only 10 mM of hydrogen dissolves in the fluid. Since in this work water was used as the solvent, the concentration of hydrogen dissolved is expected to be lower due to poorer solubility of hydrogen in water.

In order to improve the yield, the reaction was repeated in the $\beta-$chip, which increases hydrogen uptake. As discussed in the Chapter 5, at 10 $\mu\mathrm{L\,min^{-1}}$ the concentration of hydrogen in the chip doubled compared to the $\alpha-$chip. Additionally, the temperature of the reaction was increased to 58°C, which is the maximum temperature that we were able to obtain using the home-built water heater. Utilising the new chip design and elevated temperature, the concentration of fumarate was increased to 3.0 ± 0.2 mM.

Similarly to the S2M sequence, the efficiency of the S2hM pulse sequence can be improved by mitigating the effects of ST mixing. The $90-$S2hM sequence is shown in Fig. 6.6 a, where the purge pulse is applied to the proton channel just like in the S2M sequence, then the polarization is transferred using the $J-$coupling network in fumarate and is followed by ^{13}C detection.

Fig. 6.6 b shows single scan carbon spectra of ^{13}C-hyperpolarized fumarate at different flow rates. At 2 $\mu\mathrm{L\,min^{-1}}$, the carbon signal is barely distinguishable from the noise but as the flow rate increases, the signal intensity increases. The change in signal intensity as a function of flow rate is displayed in Fig. 6.6 c. Until 8 $\mu\mathrm{L\,min^{-1}}$, there is a near-linear increase in the product formation then the signal intensity plateaus. This reaction profile is markedly different to the ones reported in the previous chapters. At very low flow rates, the time it takes for the product to be delivered into the sample chamber is greater that the relaxation time therefore, the product is formed upstream from the sample chamber and is passively carried into the detection chamber. As a result, increasing the flow rate results in a faster delivery of the product however since

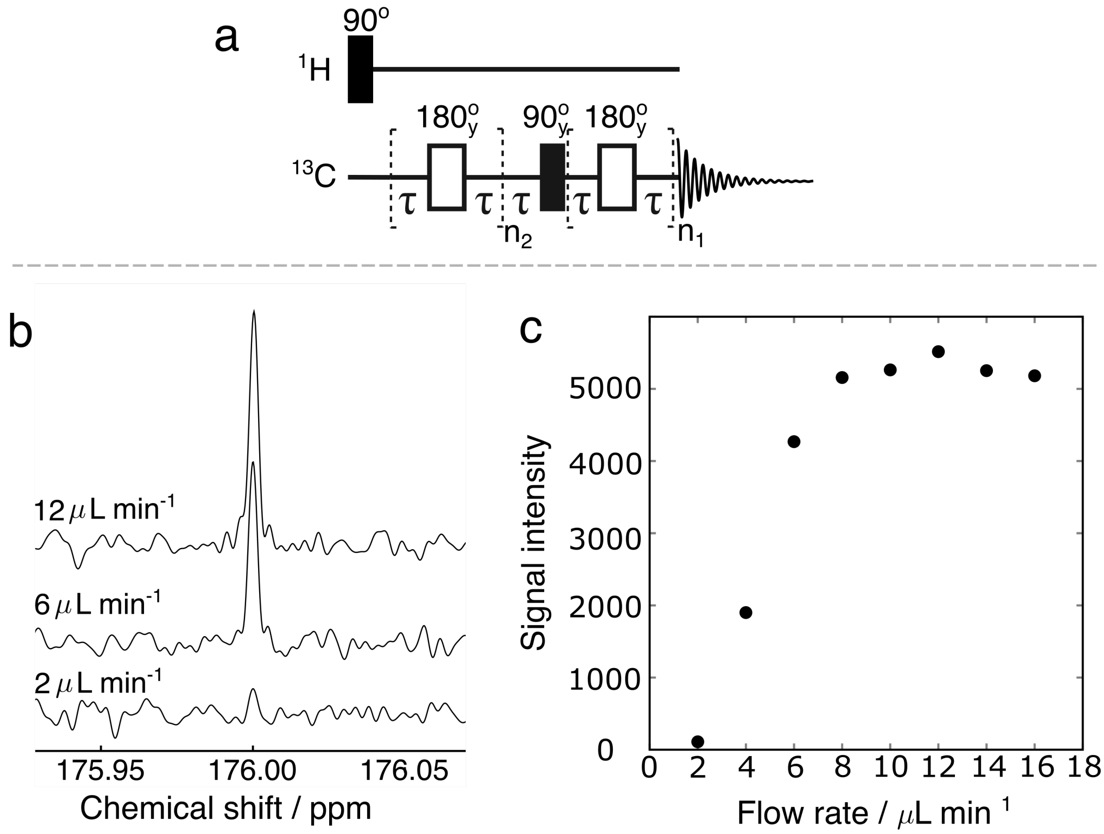

FIGURE 6.6: a) S2hM pulse sequence used to transfer the polarization from the proton singlet state to carbon. The following parameters were found to be optimal for the sequence: $\tau = 0.0158$ ms, $n_1 = 7$, $n_2 = 7$. b) ^{13}C spectra of [1-^{13}C]fumarate at different flow rates. c) A plot of the signal intensity of [1-^{13}C]fumarate as a function of flow rate.

carbon nuclei relax at much slower rate compared to proton nuclei the initial reaction profile is much smoother compared with the reaction profile discussed in the previous chapter. After 8 μL min^{-1} flow rate, the intensity of the signal ∼plateaus. This is likely due to the fact that the reaction is slow and uptake of hydrogen into the chip is no longer limiting the rate of the reaction.

Detection of ^{13}C signals arising from thermally polarized fumarate was not possible using our home-built transmission line probe due to the limited sensitivity. To estimate the signal enhancement, the hyperpolarized spectrum was compared with a spectrum of 1M D-glucose-1-^{13}C obtained after the application of $\frac{\pi}{2}$ pulse; shown in Appendix III. The SNR in the glucose spectrum is 2:1, while in the hyperpolarized spectrum of fumarate the SNR is 9:1. Since glucose spectrum was obtained from 32 number of scans, the SNR in a single scan is $\frac{2}{\sqrt{32}} \approx 0.35$. Accounting for the fact that glucose spectrum was obtained from 1 M sample and spectrum of fumarate was obtained from 3 mM sample, this leads to the signal enhancement factor of $\varepsilon = \frac{9}{0.35} * \frac{1000}{3} \approx 8500$. Leading to ∼8% carbon polarization.

6.4 Conclusions

In this work we employed a microfluidic chip to perform PHIP reactions, incorporating the hydrogenation, sample transport, RF excitation and signal detection steps onto a single device. This system was used to investigate pulsed NMR methods that reduce the detrimental effects of singlet-triplet mixing in this PHIP reaction. We showed that the application of continuous wave irradiation prior to applying the S2M pulse sequence leads to a 3-fold improvement to the fumarate proton polarization, and also allowed us to locate the chemical shift of the catalyst complex on which singlet-triplet mixing occurs. We contrasted that with application of a $\pi/2$ pulse prior to applying the S2M sequence, which led to a 6-fold improvement to the proton polarization. The same principle can be applied to improve the efficiency of the S2hM pulse sequence however, applying $90 - \mathrm{S2hM}$ in the $\alpha-$chip we did not observe any ^{13}C signals. This is likely due to very low yield of fumarate in the $\alpha-$chip, as only ∼1 % of product was obtained. Performing the reaction in the $\beta-$chip and raising the temperature to 58°C improved the reaction yield to ∼3% and ∼8% carbon polarization was obtained.

Chapter 7

Conclusions

In this work, a spatially resolved kinetic finite element model of a PHIP reaction in a microfluidic chip was developed. The model informed design of an optimised microfluidic device that enabled the formation, sample transport, RF excitation and observation of ^{13}C-hyperpolarized metabolites on a single, compact microfluidic device at the μL scale.

Chapter 4 described the development of the spatially-resolved kinetic model of the $\alpha-$chip where firstly, a kinetic model of the propargyl acetate reaction with hydrogen in thermal equilibrium has been established and its rate constants have been calibrated using macroscopic kinetic measurements. Then the kinetic model was coupled with a 2D finite element representation of the chip. In order to test the performance of the finite element model, hydrogen flux from from the PDMS membrane was simulated. The simulation successfully predicted the hydrogen uptake at flow rates below 10 $\mu\mathrm{L\,min}^{-1}$. Above that, the simulation over predicted the amount of hydrogen taken up by the chip. This discrepancy is not yet understood. Following that, the full reaction of propargyl acetate hydrogenation was simulated. This was done by utilising reaction rates obtained from macroscopic measurement in a finite element convection-diffusion-reaction simulation. The model successfully predicted the yield of hyperpolarized allyl acetate in the sample chamber of the device as a function of flow rate. The results were in quantitative agreement with published experimental data. Lastly, the model was used to predict the concentration of hyperpolarized allyl acetate when some of the conditions were changed. It was identified that the concentration of hyperpolarized allyl acetate was ∼proportional to the concentration of hydrogen present in the chip therefore, designing a device that maximises its uptake was required to improve the yield. This chapter demonstrated that simple 2D representation of a microfluidic device can be used to predict the outcome of a hyperpolarized reaction and to our knowledge this was the first demonstration of such simulation for a PHIP reaction. This a powerful method to test many hypothetical conditions without the expense of laboratory time.

Chapter 5 described the engineering of the $\beta-$chip which improved the yield of the PHIP reaction. Firstly, an additional hydrogen channel was introduced in the finite element domain to simulate the effect. The simulation predicted that this modification will lead to doubling of the concentration at the flow rate of interest. Following these encouraging simulation results, the $\beta-$chip was manufactured. The additional gas channel was introduced by interposing the fluid channel between two gas channels. The experimental results confirmed that an additional hydrogenation channel resulted in at least 2-fold increase in hydrogen uptake into the device and consequently led to a 15-fold increase in the yield (at 25°C) of the hyperpolarized allyl acetate compared with the previously reported $\alpha-$chip design [1]. Lastly, the reaction was studied at RT, 37°C, and 47°C. Heating the sample chamber of the chip to 37 °C led to a further increase in the yield to 7.0 ±0.2 mM. However, a further increase to 47°C led to a drop in the reaction yield to 5.2 ±0.2 mM. The enhancement factors of 750, 1060 and 930 were calculated for each temperature, which are much lower to what previously has been reported in the same device. This is most likely due to relaxation.

Although the simple 2D representation of the $\alpha-$chip provided invaluable insight into the complex spatially resolved kinetics occurring inside of the device it has reached its limit with a more complex geometry. To fully understand the interplay of the spin-dynamics, reaction kinetics and transport properties in the chip. This can potentially be achieved by simulation these conditions using Flokke Planck formalism discussed in details in Ref [243, 241].

Increasing the yield of the propargyl acetate hydrogenation reaction from 2% to 35% is a vital step towards implementing all steps of the PHIP-SAH reaction in a single microfluidic device and such yield should be sufficient for further transformations. Other modifications in the channel network can be performed to enhance the yield in LoC if required however, the device fabrication method needs to be changed. The current method involves laser cutting PC, which leads to melting of the material rater than straight cuts. This prevents from being able to cut complex pathways to increase the surface area of the device.

In the last experimental Chapter 6, the first demonstration of a ^{13}C-hyperpolarized metabolite by PHIP is reported. The metabolite was generated from acetylene dicarboxylic acid [1-^{13}C] disodium salt in the presence of a ruthenium-based catalyst, which resulted in a trans-hydrogenated [1-^{13}C]fumarate, and the S2M and S2hM pulse sequences were used to generate in-phase proton and carbon magnetisation for observation in the 2.5 $\mu\mathrm{L\,min}^{-1}$ sample chamber.

The system was used to investigate pulsed NMR methods that reduce the detrimental effects of singlet-triplet mixing in this PHIP reaction. It was demonstrated that the application of the continuous wave irradiation prior to applying the S2M pulse sequence leads to a 3-fold improvement to the fumarate proton polarization, and also allowed location of the chemical shift of the catalyst complex on which singlet-triplet mixing occurs. The method was contrasted with the application of a $\pi/2$ pulse prior to applying the S2M sequence, which led to a 6-fold improvement to the proton polarization leading to 3% ^{1}H polarization. The same principle applies to the S2hM sequence thus the application of the pre-pulse should in-principle combat the detrimental effects of the ST mixing. However, simply applying the $90 - $S2M sequence to the precursor solution flowing in the $\alpha-$chip did not yield any observable carbon signals. One possible problem could be the low yield as only 1% of fumarate was generated. Utilising the $\beta-$chip tripled the obtained yield and lead to 8% carbon polarization.

The continuous-flow PHIP approach allows one to establish a constant stream of a hyperpolarized product, providing stable and reproducible conditions for the study of complex chemical and spin-dynamical phenomena in a well-controlled environment. This is an important step towards the observation of metabolism in biological systems by hyperpolarized NMR on a single microfluidic device. By bringing hydrogen gas into solution through a membrane as opposed to bubbling or shaking, the chemical reaction is more stable and reaches a steady-state with a variation in the concentration of reaction product of 3%. By operating at a small volume-scale (microliters), the consumption of expensive materials is significantly reduced as compared to performing reactions in NMR tubes.

Not only does microfluidic implementation aid in the development of hyperpolarized NMR methods, but incorporating hyperpolarization to enhance NMR signals opens the door to the use of NMR as a detection method to study biological systems in microfluidic devices. Methods such as fluorescence spectroscopy require using specific fluorescent tags to track molecules, and UV-visible spectroscopy offers limited ability to identify molecules. The molecular specificity and non-destructive nature of NMR spectroscopy makes it an ideal technique to track metabolic reactions, and direct production of hyperpolarized fumarate in a microfluidic chip is an important step towards this goal. However, further developments are required to make this dream a reality, such as the removal of toxic chemicals after the hyperpolarization process.

A prerequisite of using PHIP-polarized metabolites for biological studies is the ability to remove the catalyst and reaction side-products from the solution. This has been shown to be possible for [1-^{13}C]fumarate via a precipitation procedure [270], and for a variety of other PHIP-polarized metabolites via the side-arm hydrogenation procedure [24]. Precipitation procedures are not feasible in microfluidic devices as the solid would block the fluidic channels. One possible solution would be to use scavenger compounds that bind the catalyst could potentially be used for this purpose [318, 319].

I thoroughly enjoyed working on this project and I look forward to seeing further advancements.

Chapter 8

Appendix I

Fig. 8.1 shows the temperature recorded by the heater during the propargyl acetate hydrogenation reactions reported in Chapter 5 as a function of time. Three temperatures were recorded 25 °C, 37 °C, and 47 °C. It took ∼40 minutes for the heater to stabilise at the set temperature and 0.1°C variation in temperature was recorded.

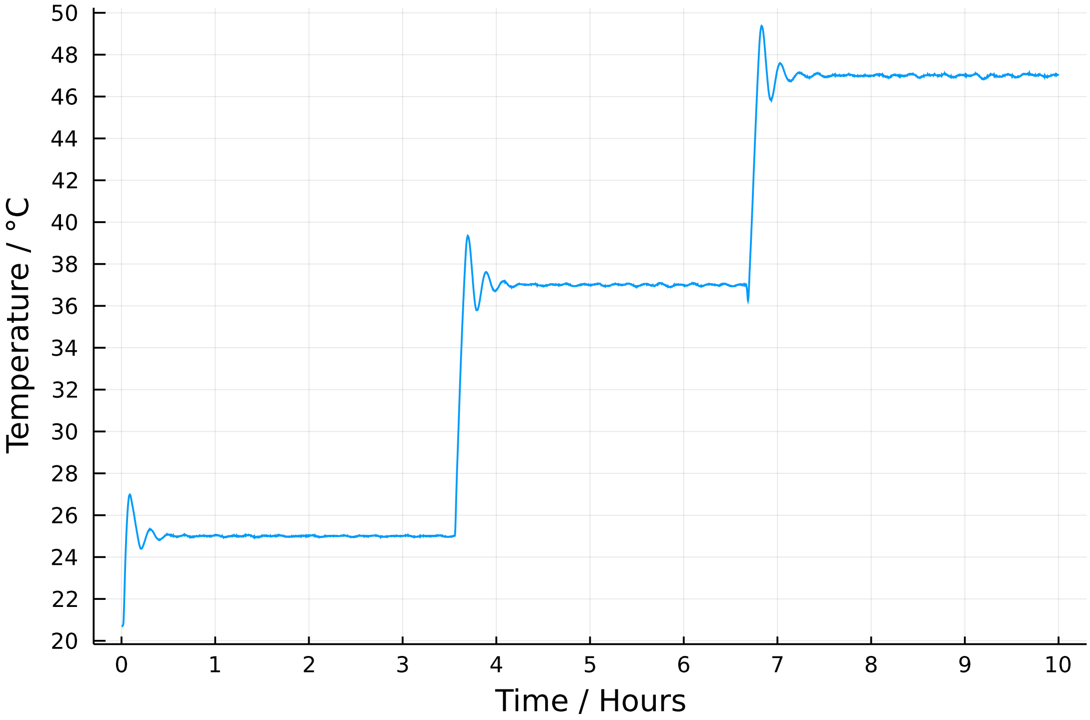

FIGURE 8.1: Temperature log for the hydrogenation of propargyl acetate shown in Chapter 5.

Chapter 9

Appendix II

A log of temperature for the hydrogenation of acetylene dicarboxylic acid [1-^{13}C] disodium salt with parahydrogen reported in Chapter 6. Similarly to the temperature log reported in Appendix 8, it took ~45 mins for the heater to reach temperature of 58°C. Once the heater reached the desired temperature, a 0.1°C variation was recorded.

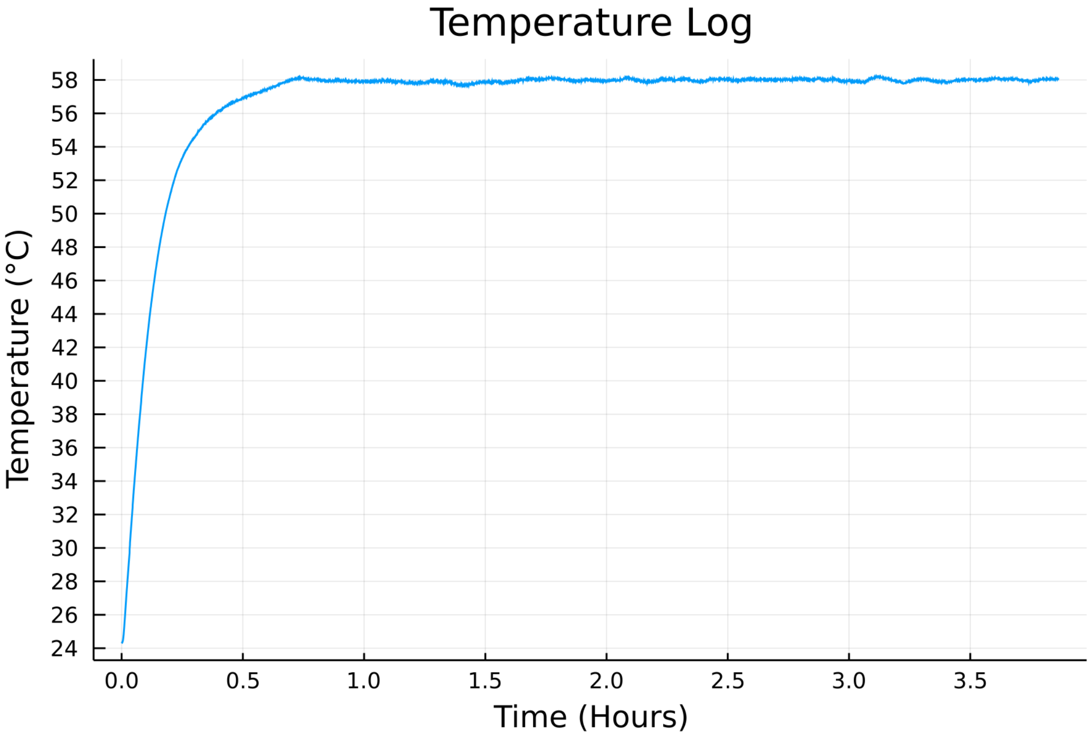

FIGURE 9.1: Temperature log for the hydrogenation of acetylene dicarboxylic acid [1-^{13}C] disodium salt shown in Chapter 6

Chapter 10

Appendix III

A ^{13}C spectrum of 1M D-Glucose-1-^{13}C.

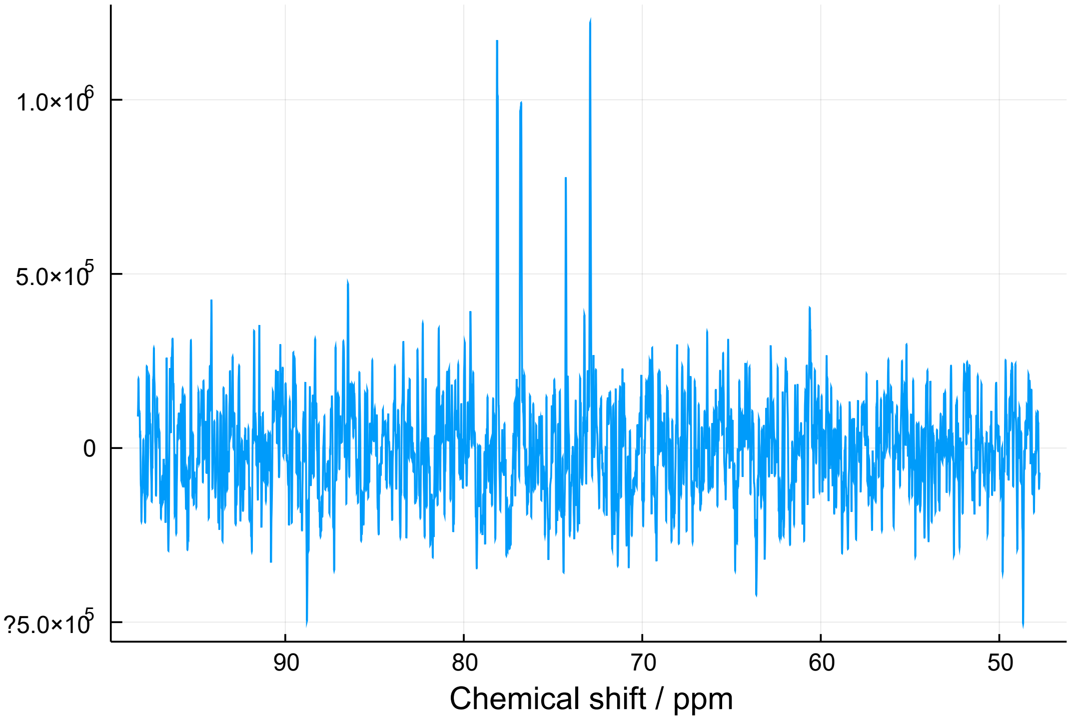

FIGURE 10.1: ^{13}C spectrum of 1M D-Glucose-1-^{13}C.

Chapter 11

Appendix IV

This Appendix contains SpinDynamica and Mathematica code used to produce some of the Figures in this Thesis. The following documents are included:

1. Simulation of a spectrum obtained with thermally equilibrated hydrogen shown in Fig. 2.9
2. Simulation of a PASADENA spectrum spectrum shown in Fig. 2.10
3. Simulation of an ALTADENA spectrum spectrum shown in Fig. 2.11
4. Simulations of the S2M pulse sequence shown in Fig. 2.14 − 2.17
5. Simulations of the 90-S2M pulse sequence where the phases of the pre-pulse and S2M block differ for [1-^{13}C]fumarate shown in Fig. 6.5.

H_2 in Thermal Equilibrium Simulations

```
In[•]:= SetSpinSystem[2]

        SetSpinSystem: the spin system has been set to {{1, 1/2}, {2, 1/2}}

In[•]:= H = 50 opI[1, "z"] + -50 opI[2, "z"] + 13 opI[1, "z"].opI[2, "z"]
Out[•]= 13 (I1 z•I2 z) + 50 I1 z - 50 I2 z

In[•]:= ρthermal = UnityOperator[]  + opI[1, "z"] + opI[2, "z"]
Out[•]= I1 z + I2 z + 𝟙

In[•]:= SigThermal = Signal1D[{{2 π 40, "2k"}}, InitialDensityOperator → ρthermal,
          BackgroundGenerator → H, Preparation → RotationSuperoperator[{π/2, "x"}]]
        Signal1D: Using SignalCalculationMethod → Diagonalization

        Signal1D: Using LineBroadening → 2π × 28.6583×10^-3 rad s^-1.
Out[•]= Signal[ {0, 51.15, 25.×10^-3} , { Lorentzian ,<< 4 >>}]

In[•]:= ListPlot[Re@FT@SigThermal, Frame → False]
Out[•]=
```

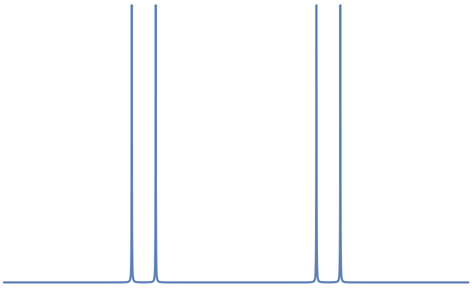

PASADENA Simulations

```
In[∘]:= SetSpinSystem[2]
```

SetSpinSystem: the spin system has been set to $\left\{\left\{1, \frac{1}{2}\right\}, \left\{2, \frac{1}{2}\right\}\right\}$

```
In[∘]:= H = 50 opI[1, "z"] + - 50 opI[2, "z"] + 13 opI[1, "z"].opI[2, "z"]
```

Out[∘]= $13\ (\mathrm{I}_{1\,z}\bullet\mathrm{I}_{2\,z}) + 50\ \mathrm{I}_{1\,z} - 50\ \mathrm{I}_{2\,z}$

```
In[∘]:= ρPASADENA = UnityOperator[] - 0.5 opI[1, "z"].opI[2, "z"]
```

Out[∘]= $-0.5\ (\mathrm{I}_{1\,z}\bullet\mathrm{I}_{2\,z}) + \mathbb{1}$

```
In[∘]:= SigPASADENA = Signal1D[{{2 π 40, "2k"}}, InitialDensityOperator → ρPASADENA,
          BackgroundGenerator → H, Preparation → RotationSuperoperator[{π / 4, "x"}]]
```

Signal1D: Using SignalCalculationMethod → Diagonalization

Signal1D: Using LineBroadening → $2\pi \times 28.6583\times 10^{-3}$ rad s^{-1}.

Out[∘]= Signal[$\{0, 51.15, 25.\times 10^{-3}\}$, { Lorentzian ,<< 4 >>}]

```
In[∘]:= ListPlot[Re@FT@SigPASADENA, Frame → False]
```

Out[∘]=

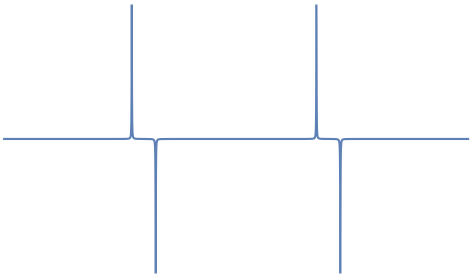

ALTADENA Simulations

```
In[∘]:= SetSpinSystem[2]

        SetSpinSystem: the spin system has been set to {{1, 1/2}, {2, 1/2}}

        SetBasis: the state basis has been set to ZeemanBasis[{{1, 1/2}, {2, 1/2}}, BasisLabels → Automatic].

In[∘]:= H = 50 opI[1, "z"] + -50 opI[2, "z"] + 13 opI[1, "z"].opI[2, "z"]

Out[∘]= 13 (I1z•I2z) + 50 I1z - 50 I2z

In[∘]:= ρ0 = 1/4 UnityOperator[] - opI[1].opI[2]

Out[∘]= -(I1x•I2x) - I1y•I2y - I1z•I2z + 𝟙/4

In[∘]:= BμT[B_] := B * 10^-6;
        {Λsys, Σsys} = CorrelatedEigensystems[
           -BμT[B] × GyromagneticRatio[1] (opI[1, "z"] - opI[2, "z"]) +
            2 π 15 opI[1].opI[2], {B, 0, 1, 1 / 20}];
        First[Σsys]
        Last[Σsys] // Simplify

Out[∘]= {0, {0.707107 |βα⟩ - 0.707107 |αβ⟩, 1. |αα⟩, 0.707107 |βα⟩ + 0.707107 |αβ⟩, 1. |ββ⟩}}

Out[∘]= {1, {-0.08707 |βα⟩ + 0.996202 |αβ⟩, 1. |αα⟩, 0.996202 |βα⟩ + 0.08707 |αβ⟩, 1. |ββ⟩}}

In[∘]:= t = ListPlot[Λsys, PlotLegends -> Automatic, PlotRange -> Full]

Out[∘]=
```

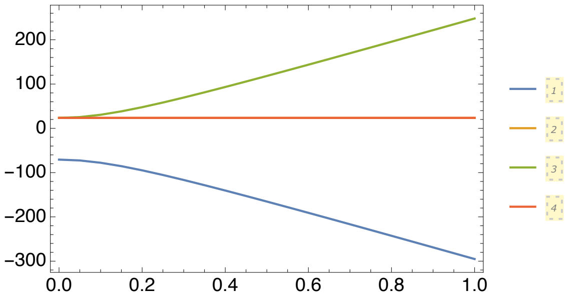

```
In[∘]:= ρALTADENA = NPropagate[{Function[t,
              +I 2 π (100 t + 0.01) CommutationSuperoperator[(opI[1, "z"] - opI[2, "z"])]],
            5, PropagationMethod -> Adiabatic, EventSampling -> {500}},
          BackgroundGenerator -> 2 π 15 opI[1].opI[2]][ρ0];
```

In[∘]:=
```
ListPlot[Re[FT[Signal1D[{{2 π 100, "2k"}},
    InitialDensityOperator -> ρALTADENA, BackgroundGenerator -> H]]]]
```

```
Signal1D: Using SignalCalculationMethod → Diagonalization
Signal1D: Using LineBroadening → 2π × 71.6457×10^-3 rad s^-1.
```

Out[∘]=

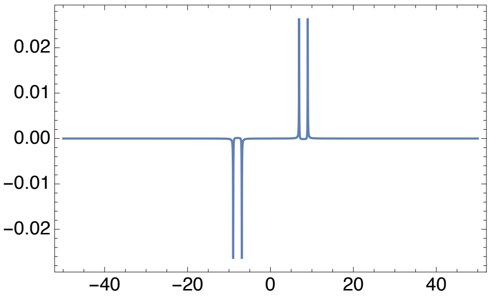

S2M Simulations

```
In[∘]:= SetSpinSystem[2]

        SetSpinSystem: the spin system has been set to {{1, 1/2}, {2, 1/2}}

In[∘]:= SetBasis[SingletTripletBasis[]]

        SetBasis: the state basis has been set to SingletTripletBasis[{{1, 1/2}, {2, 1/2}}, BasisLabels → Automatic].

In[∘]:= HS2M[Δ_, J_] := 2 π J opI[1].opI[2] + π Δ (opI[1, "z"] - opI[2, "z"])

In[∘]:= θST[Δ_, J_] := ArcTan[Δ / J]

In[∘]:= S2M1[Δ_, J_] :=
         {Repeat[{{None, 1 / (4 * 100)}, Pulse[{π, π / 2}], {None, 1 / (4 * 100)}},
           Round[π / (4 θST[Δ, J])]]}

In[∘]:= S2M2[Δ_, J_] := {{None, 1 / (4 × 100)}, Pulse[{π / 2, 0}]}

In[∘]:= S2M3[Δ_, J_] :=
         {Repeat[{{None, 1 / (4 * 100)}, Pulse[{π, π / 2}], {None, 1 / (4 * 100)}},
           Round[π / (2 θST[Δ, J])]]}

In[∘]:= SetBasis[SingletTripletBasis[]]

        SetBasis: The basis is already set to SingletTripletBasis[{{1, 1/2}, {2, 1/2}}, BasisLabels → Automatic]. No action has been
             taken.

In[∘]:= ρ0 = 1/4 UnityOperator[] - opI[1].opI[2]

Out[∘]= -(I1x•I2x) - I1y•I2y - I1z•I2z + 𝟙/4

In[∘]:= ρ0 // MatrixRepresentation // MatrixForm
Out[∘]//MatrixForm=
        1  0  0  0
        0  0  0  0
        0  0  0  0
        0  0  0  0
```

In[•]:=
```
MatPlot = MatrixPlot[Abs@MatrixRepresentation[ρ0],
  Mesh -> All, MeshStyle → Directive[Gray, Dashed],
  ColorFunction → (Blend[{White, Lighter@Blue}, #] &[Rescale[#, {0, 1}]] &),
  ColorFunctionScaling → False, PlotLegends → BarLegend[
    {(Blend[{White, Lighter@Blue}, #] &[Rescale[#, {0, 1}]] &), {0, 1}}, 9]]
```

Out[•]=

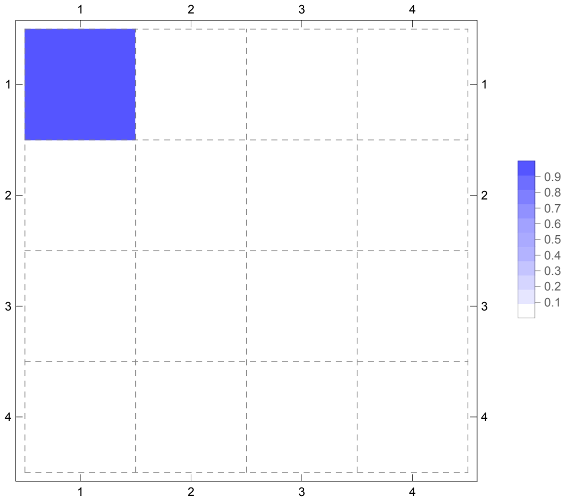

In[•]:=
```
ρ1 = NPropagate[S2M1[1, 100], BackgroundGenerator -> HS2M[1, 100] ] [ρ0] //
  ExpressOperator
```

```
OperatorBasis : The current operator basis is inappropriate for the current spin system or the current spin state basis.
```

SetOperatorBasis : the operator basis has been set to ShiftAndZOperatorBasis$\left[\left\{\left\{1, \frac{1}{2}\right\}, \left\{2, \frac{1}{2}\right\}\right\}, \text{Sorted} \to \text{CoherenceOrder}\right]$.

Out[•]=

$$(0.00459748 - 0.499978\, i)\,(I_1^- \bullet I_2^+) + (0.00459748 + 0.499978\, i)\,(I_1^+ \bullet I_2^-) - 1.\,(I_{1z} \bullet I_{2z}) + 0.00108289\, I_{1z} - 0.00108289\, I_{2z} + 0.25\, \mathbb{1}$$

In[•]:=
```
ρ1 // MatrixRepresentation // MatrixForm
```

Out[•]//MatrixForm=

$$\begin{pmatrix} 0.495403 & 0 & 0.00108289 + 0.499978\, i & 0 \\ 0 & 0 & 0 & 0 \\ 0.00108289 - 0.499978\, i & 0 & 0.504597 & 0 \\ 0 & 0 & 0 & 0 \end{pmatrix}$$

```
In[•]:= MatrixPlot[Abs@MatrixRepresentation[ρ1],
         Mesh -> All, MeshStyle → Directive[Gray, Dashed],
         ColorFunction → (Blend[{White, Lighter@Blue}, #] &[Rescale[#, {0, 1}]] &),
         ColorFunctionScaling → False, PlotLegends → BarLegend[
           {(Blend[{White, Lighter@Blue}, #] &[Rescale[#, {0, 1}]] &), {0, 1}}, 9]]
```

Out[•]=

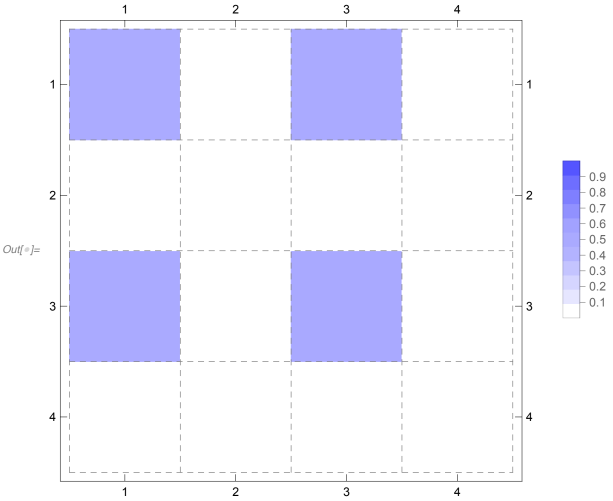

```
In[•]:= ρ2 = NPropagate[S2M2[1, 100], BackgroundGenerator -> HS2M[1, 100] ] [ρ1] //
          ExpressOperator
```

Out[•]=

$$0.254804\,(I_1^-\cdot I_2^-) - 0.245196\,(I_1^-\cdot I_2^+) + 0.000997596\,(I_1^-\cdot I_{2z}) - 0.245196\,(I_1^+\cdot I_2^-) + 0.254804\,(I_1^+\cdot I_2^+) + 0.000997596\,(I_1^+\cdot I_{2z}) - 0.000997596\,(I_{1z}\cdot I_2^-) - 0.000997596\,(I_{1z}\cdot I_2^+) + 0.0192148\,(I_{1z}\cdot I_{2z}) + (0. + 0.249953\,i)\,I_1^- - (0. + 0.249953\,i)\,I_1^+ - (0. + 0.249953\,i)\,I_2^- + (0. + 0.249953\,i)\,I_2^+ + 0.25\,\mathbb{1}$$

```
In[•]:= ρ2 // MatrixRepresentation // MatrixForm
```

Out[•]//MatrixForm=

$$\begin{pmatrix} 0.490393 & -0.000705407 - 0.353487\,i & 0 & -0.000705407 - 0.353487\,i \\ -0.000705407 + 0.353487\,i & 0.254804 & 0 & 0.254804 \\ 0 & 0 & 0 & 0 \\ -0.000705407 + 0.353487\,i & 0.254804 & 0 & 0.254804 \end{pmatrix}$$

```
In[•]:= MatrixPlot[Abs@MatrixRepresentation[ρ2],
         Mesh -> All, MeshStyle → Directive[Gray, Dashed],
         ColorFunction → (Blend[{White, Lighter@Blue}, #] &[Rescale[#, {0, 1}]] &),
         ColorFunctionScaling → False, PlotLegends → BarLegend[
           {(Blend[{White, Lighter@Blue}, #] &[Rescale[#, {0, 1}]] &), {0, 1}}, 9]]
```

Out[•]=

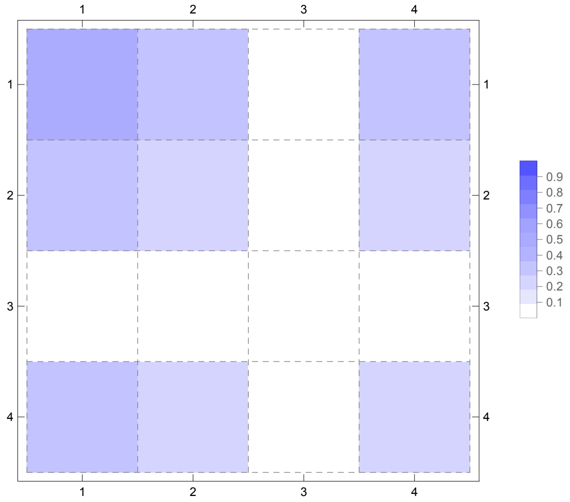

```
In[•]:= ρ3 = NPropagate[S2M3[1, 100], BackgroundGenerator -> HS2M[1, 100] ] [ρ2] //
          ExpressOperator
```

Out[•]=

$$
\begin{aligned}
&0.254804\,\left(I_1^-\bullet I_2^-\right)+\left(0.245194-0.000392429\,\mathbb{i}\right)\,\left(I_1^-\bullet I_2^+\right)-\\
&\left(0.00107362+0.000997593\,\mathbb{i}\right)\,\left(I_1^-\bullet I_{2\,z}\right)+\left(0.245194+0.000392429\,\mathbb{i}\right)\,\left(I_1^+\bullet I_2^-\right)+\\
&0.254804\,\left(I_1^+\bullet I_2^+\right)-\left(0.00107362-0.000997593\,\mathbb{i}\right)\,\left(I_1^+\bullet I_{2\,z}\right)+\\
&\left(0.00107362-0.000997593\,\mathbb{i}\right)\,\left(I_{1\,z}\bullet I_2^-\right)+\left(0.00107362+0.000997593\,\mathbb{i}\right)\,\left(I_{1\,z}\bullet I_2^+\right)+\\
&0.0192148\,\left(I_{1\,z}\bullet I_{2\,z}\right)+\left(0.249953-0.000198952\,\mathbb{i}\right)\,I_1^-+\\
&\left(0.249953+0.000198952\,\mathbb{i}\right)\,I_1^++0.0010524\,I_{1\,z}+\left(0.249953+0.000198952\,\mathbb{i}\right)\,I_2^-+\\
&\left(0.249953-0.000198952\,\mathbb{i}\right)\,I_2^+-0.0010524\,I_{2\,z}+0.25\,\mathbb{1}
\end{aligned}
$$

```
In[•]:= ρ3 // MatrixRepresentation // MatrixForm
```

Out[•]//MatrixForm=

```
(        2.57254 × 10^-6        0.000759163 + 0.00028136 i   0.0010524 + 0.000392429 i  0.0
 0.000759163 - 0.00028136 i            0.254804              0.353486 + 0.000705405 i
  0.0010524 - 0.000392429 i    0.353486 - 0.000705405 i              0.49039              0.
 0.000759163 - 0.00028136 i            0.254804              0.353486 + 0.000705405 i
```

```
In[◦]:= MatrixPlot[Abs@MatrixRepresentation[ρ3],
         Mesh -> All, MeshStyle → Directive[Gray, Dashed],
         ColorFunction → (Blend[{White, Lighter@Blue}, #] &[Rescale[#, {0, 1}]] &),
         ColorFunctionScaling → False, PlotLegends → BarLegend[
           {(Blend[{White, Lighter@Blue}, #] &[Rescale[#, {0, 1}]] &), {0, 1}}, 9]]
```

Out[◦]=

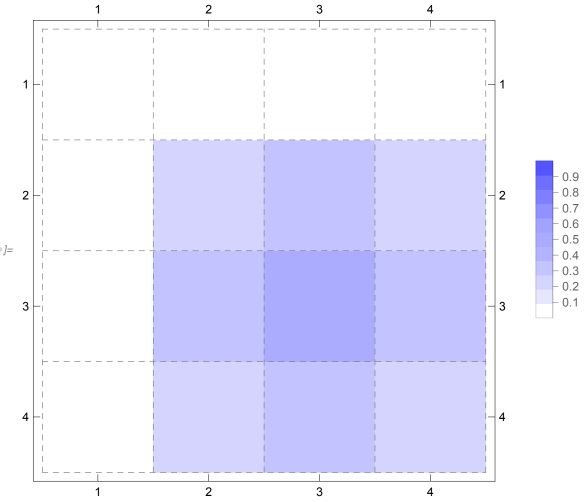

Fumarate Simulations

```
In[∘]:= SetSpinSystem[3]
```

SetSpinSystem: the spin system has been set to $\left\{\left\{1, \frac{1}{2}\right\}, \left\{2, \frac{1}{2}\right\}, \left\{3, \frac{1}{2}\right\}\right\}$

SetBasis: the state basis has been set to ZeemanBasis$\left[\left\{\left\{1, \frac{1}{2}\right\}, \left\{2, \frac{1}{2}\right\}, \left\{3, \frac{1}{2}\right\}\right\}\right.$, BasisLabels → Automatic$\left.\right]$.

```
In[∘]:= SetBasis[ProductBasis[SingletTripletBasis[{1, 2}], ZeemanBasis[{3}]]]
```

CheckBasis: State basis is orthonormal.

SetBasis: the state basis has been set to

ProductBasis$\left[\left\{\right.\right.$SingletTripletBasis$\left[\left\{\left\{1, \frac{1}{2}\right\}, \left\{2, \frac{1}{2}\right\}\right\}\right.$, BasisLabels → Automatic$\left.\right]$, ZeemanBasis$\left[\left\{\left\{3, \frac{1}{2}\right\}\right\}\right.$, BasisLabels → Automatic$\left.\left.\right\}\right]$, $\left\{\left\{1, \frac{1}{2}\right\}, \left\{2, \frac{1}{2}\right\}, \left\{3, \frac{1}{2}\right\}\right\}$, Validity → True$\left.\right]$.

```
In[∘]:= BasisKets[]
```

Out[∘]= $$\left\{\frac{-|\beta\alpha\alpha\rangle + |\alpha\beta\alpha\rangle}{\sqrt{2}}, |\alpha\alpha\alpha\rangle, \frac{|\beta\alpha\alpha\rangle + |\alpha\beta\alpha\rangle}{\sqrt{2}}, |\beta\beta\alpha\rangle, \frac{-|\beta\alpha\beta\rangle + |\alpha\beta\beta\rangle}{\sqrt{2}}, |\alpha\alpha\beta\rangle, \frac{|\beta\alpha\beta\rangle + |\alpha\beta\beta\rangle}{\sqrt{2}}, |\beta\beta\beta\rangle\right\}$$

```
In[∘]:= BasisBras[]
```

Out[∘]= $$\left\{\frac{-\langle\beta\alpha\alpha| + \langle\alpha\beta\alpha|}{\sqrt{2}}, \langle\alpha\alpha\alpha|, \frac{\langle\beta\alpha\alpha| + \langle\alpha\beta\alpha|}{\sqrt{2}}, \langle\beta\beta\alpha|, \frac{-\langle\beta\alpha\beta| + \langle\alpha\beta\beta|}{\sqrt{2}}, \langle\alpha\alpha\beta|, \frac{\langle\beta\alpha\beta| + \langle\alpha\beta\beta|}{\sqrt{2}}, \langle\beta\beta\beta|\right\}$$

```
In[∘]:= Hspins = {1, 2}
Out[∘]= {1, 2}
```

```
In[∘]:= Cspins = {3}
Out[∘]= {3}
```

```
In[∘]:= H0 = 2 π J12 opI[1].opI[2] +
          2 π J13 opI[1, "z"].opI[3, "z"] + 2 π J23 opI[2, "z"].opI[3, "z"]
```

Out[∘]= $2\,J12\,\pi\left(I_{1x}\bullet I_{2x} + I_{1y}\bullet I_{2y} + I_{1z}\bullet I_{2z}\right) + 2\,J13\,\pi\left(I_{1z}\bullet I_{3z}\right) + 2\,J23\,\pi\left(I_{2z}\bullet I_{3z}\right)$

```
In[∘]:= params = {J12 → 15.9, J13 → 3.3, J23 → 5.9, λ → 1}
Out[∘]= {J12 → 15.9, J13 → 3.3, J23 → 5.9, λ → 1}
```

```
In[∘]:= ρstart[p_] := Evaluate[
           p PopulationOperator[1] + (1 - p) PopulationOperator[3] - UnityOperator[] / 4 //
             ExpressOperator // Simplify];
```

OperatorBasis: The current operator basis is inappropriate for the current spin system or the current spin state basis.

SetOperatorBasis: the operator basis has been set to

ShiftAndZOperatorBasis$\left[\left\{\left\{1, \frac{1}{2}\right\}, \left\{2, \frac{1}{2}\right\}, \left\{3, \frac{1}{2}\right\}\right\}\right.$, Sorted → CoherenceOrder$\left.\right]$.

```
In[∘]:= Off1 = {#[[1]], #[[2]] + 0.002} & /@ Sig1;

In[∘]:= τ = π / (2 Sqrt[(2 π J12)^2 + (2 π (J23 - J13))^2]) /. params

Out[∘]= 0.0155172

In[∘]:= n = Round[π / (4 ArcTan[(J23 - J13) / J12])] /. params

Out[∘]= 5

In[∘]:= S2M90[τ_, n1_, n2_, θ_] := {
          RotationSuperoperator[{1, 2}, {θ, "y"}],
          Repeat[{
             {None, τ},
             RotationSuperoperator[{1, 2}, {π, "y"}],
             {None, τ}
            }, n2],
          {None, τ},
          RotationSuperoperator[{1, 2}, {π / 2, "y"}],
          Repeat[{
             {None, τ},
             RotationSuperoperator[{1, 2}, {π, "y"}],
             {None, τ}
            }, n1]
         }

In[∘]:= S2M902[τ_, n1_, n2_, θ_] := {
          RotationSuperoperator[{1, 2}, {θ, "x"}],
          Repeat[{
             {None, τ},
             RotationSuperoperator[{1, 2}, {π, "y"}],
             {None, τ}
            }, n2],
          {None, τ},
          RotationSuperoperator[{1, 2}, {π / 2, "y"}],
          Repeat[{
             {None, τ},
             RotationSuperoperator[{1, 2}, {π, "y"}],
             {None, τ}
            }, n1]
         }
```

```
In[•]:= SigTable = Table[Re@FT@Signal1D[{{2 π 1200, "2k"}},
            InitialDensityOperator → ρstart[5.8 / (5.8 + 4.8)],
            BackgroundGenerator → (H0 /. params), Preparation → S2M902[0.0158, 14, 7, x],
            PlotRange → All, LineBroadening → 40], {x, 0, 2 π, 2 π / 36}];
```

```
Signal1D: Using SignalCalculationMethod → Diagonalization

Signal1D: Using SignalCalculationMethod → Diagonalization

Signal1D: Using SignalCalculationMethod → Diagonalization

General: Further output of Signal1D::reportscm will be suppressed during this calculation.
```

```
In[•]:= OffTable = Table[{+ (#[[1]] + 300 * (i - 1)) / (3600 * 3) * 360, #[[2]] / 0.0004} & /@
          SigTable[[i]], {i, 1, 37, 1}];
```

```
In[•]:= ListPlot[OffTable, PlotStyle → {{Blue, Thickness[0.001]}},
         PlotRange → {{-20, 380}, All},
         FrameTicks → {{{0, 2, 4, 6}, None}, {{0, 90, 180, 270, 360}, None}}]
```

Out[•]=

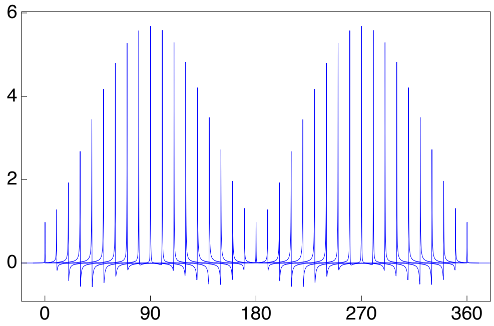

```
In[•]:= SigTable2 = Table[Re@FT@Signal1D[{{2 π 1200, "2k"}},
            InitialDensityOperator → ρstart[5.8 / (5.8 + 4.8)],
            BackgroundGenerator → (H0 /. params), Preparation → S2M90[0.0158, 14, 7, x],
            PlotRange → All, LineBroadening → 40], {x, 0, 2 π, 2 π / 36}];
```

```
Signal1D: Using SignalCalculationMethod → Diagonalization

Signal1D: Using SignalCalculationMethod → Diagonalization

Signal1D: Using SignalCalculationMethod → Diagonalization

General: Further output of Signal1D::reportscm will be suppressed during this calculation.
```

```
In[•]:= OffTable2 = Table[{(#[[1]] + 300 * (i - 1)) / (3600 * 3) * 360, #[[2]] / 0.0004} & /@
          SigTable2[[i]], {i, 1, 37, 1}];
```

In[∘]:=
```
ListPlot[OffTable2, PlotStyle → {{Blue, Thickness[0.001]}},
 PlotRange → {{-20, 380}, All},
 FrameTicks → {{{0, 2, 4, 6}, None}, {{0, 90, 180, 270, 360}, None}}]
```

Out[∘]=

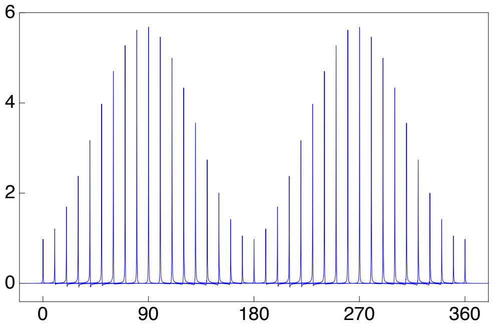

References

[1] James Eills, William Hale, Manvendra Sharma, Matheus Rossetto, Malcolm H. Levitt, and Marcel Utz. High-Resolution Nuclear Magnetic Resonance Spectroscopy with Picomole Sensitivity by Hyperpolarization on a Chip. *Journal of the American Chemical Society*, 141(25):9955–9963, 2019.

[2] Sylwia J. Ostrowska, Aabidah Rana, and Marcel Utz. Spatially Resolved Kinetic Model of Parahydrogen Induced Polarisation (PHIP) in a Microfluidic Chip. *ChemPhysChem*, 22(19):2004–2013, 2021.

[3] Sylwia J. Barker, Laurynas Dagys, William Hale, Barbara Ripka, James Eills, Manvendra Sharma, Malcolm H. Levitt, and Marcel Utz. Direct Production of a Hyperpolarized Metabolite on a Microfluidic Chip. *Analytical Chemistry*, 94(7):3260–3267, 2022.

[4] Lingling Shui, Albert van den Berg, and Jan C. T. Eijkel. Scalable Attoliter Monodisperse Droplet Formation Using Multiphase Nano-microfluidics. *Microfluidics and Nanofluidics*, 11(1):87–92, 2011.

[5] George M. Whitesides. The Origins and the Future of Microfluidics. *Nature*, 442:368–373, 2006.

[6] J. Tirén, L. Tenerz, and B. Hök. A Batch-Fabricated Non-Reverse Valve with Cantilever Beam Manufactured by Micromachining of Silicon. *Sensors and Actuators*, 18(3):389–396, 1989.

[7] Shuichi Shoji, Masayoshi Esashi, and Tadayuki Matsuo. Prototype Miniature Blood Gas Analyser Fabricated on a Silicon Wafer. *Sensors and Actuators*, 14(2):101–107, 1988.

[8] Neil Convery and Nikolaj Gadegaard. 30 Years of Microfluidics. *Micro and Nano Engineering*, 2:76–91, 2019.

[9] H. T. G. van Lintel, F. C. M. van De Pol, and S. Bouwstra. A Piezoelectric Micropump Based on Micromachining of Silicon. *Sensors and Actuators*, 15(2):153–167, 1988.

[10] F. C. M. van de Pol, D. G. J. Wonnink, M. Elwenspoek, and J. H. J. Fluitman. A Thermo-Pneumatic Actuation Principle for a Microminiature Pump and Other Micromechanical Devices. *Sensors and Actuators*, 17(1):139–143, 1989.

[11] A. Manz, N. Graber, and H. M. Widmer. Miniaturized Total Chemical Analysis Systems: A Novel Concept for Chemical Sensing. *Sensors and Actuators B: Chemical*, 1(1):244–248, 1990.

[12] Neda Azizipour, Rahi Avazpour, Derek H. Rosenzweig, Mohamad Sawan, and Abdellah Ajji. Evolution of Biochip Technology: A Review from Lab-on-a-Chip to Organ-on-a-Chip. *Micromachines*, 11(6):599, 2020.

[13] Longlong Si, Haiqing Bai, Melissa Rodas, Wuji Cao, Crystal Yuri Oh, Amanda Jiang, Rasmus Moller, Daisy Hoagland, Kohei Oishi, Shu Horiuchi, Skyler Uhl, Daniel Blanco-Melo, Randy A. Albrecht, Wen-Chun Liu, Tristan Jordan, Benjamin E. Nilsson-Payant, Ilona Golynker, Justin Frere, James Logue, Robert Haupt, Marisa McGrath, Stuart Weston, Tian Zhang, Roberto Plebani, Mercy Soong, Atiq Nurani, Seong Min Kim, Danni Y. Zhu, Kambez H. Benam, Girija Goyal, Sarah E. Gilpin, Rachelle Prantil-Baun, Steven P. Gygi, Rani K. Powers, Kenneth E. Carlson, Matthew Frieman, Benjamin R. TenOever, and Donald E. Ingber. A Human-Airway-on-a-Chip for the Rapid Identification of Candidate Antiviral Therapeutics and Prophylactics. *Nature Biomedical Engineering*, 5:815–829, 2021.

[14] Qirui Wu, Jinfeng Liu, Xiaohong Wang, Lingyan Feng, Jinbo Wu, Xiaoli Zhu, Weijia Wen, and Xiuqing Gong. Organ-on-a-chip: Recent Breakthroughs and Future Prospects. *BioMedical Engineering OnLine*, 19(1):1–19, 2020.

[15] Nikunja Kolluri, Catherine M. Klapperich, and Mario Cabodi. Towards Lab-on-a-Chip Diagnostics for Malaria Elimination. *Lab on a Chip*, 18(1):75–94, 2017.

[16] Jiandong Wu, Meili Dong, Claudio Rigatto, Yong Liu, and Francis Lin. Lab-on-Chip Technology for Chronic Disease Diagnosis. *npj Digital Medicine*, 1(7):1–11, 2018.

[17] Yasamin A. Jodat, Min Gyeong Kang, Kiavash Kiaee, Gyeong Jin Kim, Angel Flores Huidobro Martinez, Aliza Rosenkranz, Hojae Bae, and Su Ryon Shin. Human-Derived Organ-on-a-Chip for Personalized Drug Development. *Current Pharmaceutical Design*, 24(45):5471–5486, 2018.

[18] Ye Cong, Xiahe Han, Youping Wang, Zongzheng Chen, Yao Lu, Tingjiao Liu, Zhengzhi Wu, Yu Jin, Yong Luo, and Xiuli Zhang. Drug Toxicity Evaluation Based on Organ-on-a-chip Technology: A Review. *Micromachines*, 11(4):381, 2020.

[19] Job Komen, Eiko Y. Westerbeek, Ruben W. Kolkman, Julia Roesthuis, Caroline Lievens, Albert van den Berg, and Andries D. van der Meer. Controlled Pharmacokinetic Anti-Cancer Drug Concentration Profiles Lead to Growth Inhibition of Colorectal Cancer Cells in a Microfluidic Device. *Lab on a Chip*, 20(17):3167–3178, 2020.

[20] Asieh Emami Nejad, Simin Najafgholian, Alireza Rostami, Alireza Sistani, Samaneh Shojaeifar, Mojgan Esparvarinha, Reza Nedaeinia, Shaghayegh Haghjooy Javanmard, Marjan Taherian, Mojtaba Ahmadlou, Rasoul Salehi, Bahman Sadeghi, and Mostafa Manian. The Role of Hypoxia in the Tumor Microenvironment and Development of Cancer Stem Cell: A Novel Approach to Developing Treatment. *Cancer Cell International*, 21(1):1–26, 2021.

[21] James Eills, William Hale, and Marcel Utz. Synergies Between Hyperpolarized NMR and Microfluidics: A Review. *Progress in Nuclear Magnetic Resonance Spectroscopy*, 128:44–69, 2022.

[22] C. Russell Bowers and Daniel P. Weitekamp. Parahydrogen and Synthesis Allow Dramatically Enhanced Nuclear Alignment. *Journal of the American Chemical Society*, 109(18):5541–5542, 1987.

[23] Simon B. Duckett and Christopher J. Sleigh. Applications of the Parahydrogen Phenomenon: A Chemical Perspective. *Progress in Nuclear Magnetic Resonance Spectroscopy*, 34(1):71–92, 1999.

[24] Francesca Reineri, Eleonora Cavallari, Carla Carrera, and Silvio Aime. Hydrogenative-PHIP Polarized Metabolites for Biological Studies. *Magnetic Resonance Materials in Physics, Biology and Medicine*, 34(1):25–47, 2021.

[25] Eleonora Cavallari, Carla Carrera, Silvio Aime, and Francesca Reineri. Studies to Enhance the Hyperpolarization Level in PHIP-SAH-produced ^{13}C-Pyruvate. *Journal of Magnetic Resonance*, 289:12–17, 2018.

[26] Darwin R. Reyes, Dimitri Iossifidis, Pierre-Alain Auroux, and Andreas Manz. Micro Total Analysis Systems. 1. Introduction, Theory, and Technology. *Analytical Chemistry*, 74(12):2623–2636, 2002.

[27] Todd M. Squires and Stephen R. Quake. Microfluidics: Fluid Physics at the Nanoliter Scale. *Reviews of Modern Physics*, 77(3):977–1026, 2005.

[28] Rosamund Daw and Joshua Finkelstein. Lab on a Chip. *Nature*, 442:367, 2006.

[29] Peter Mitchell. Microfluidics–Downsizing Large-Scale Biology. *Nature Biotechnology*, 19(8):717–721, 2001.

[30] Huanhuan Shi, Kaixuan Nie, Bo Dong, Mengqiu Long, Hui Xu, and Zhengchun Liu. Recent Progress of Microfluidic Reactors for Biomedical Applications. *Chemical Engineering Journal*, 361:635–650, 2019.

[31] Nongnoot Wongkaew, Marcel Simsek, Christian Griesche, and Antje J. Baeumner. Functional Nanomaterials and Nanostructures Enhancing

Electrochemical Biosensors and Lab-on-a-Chip Performances: Recent Progress, Applications, and Future Perspective. *Chemical Reviews*, 119(1):120–194, 2019.

[32] Pavel Sengupta, Kalap Khanra, Amit Roy Chowdhury, and Pallab Datta. Lab-on-a-Chip Sensing Devices for Biomedical Applications. In *Bioelectronics and Medical Devices*, pages 47–95. Woodhead Publishing, Buckingham, England, UK, 2019.

[33] Reynolds Osborne. XXIX. An Experimental Investigation of the Circumstances which Determine Whether the Motion of Water Shall be Direct or Sinuous, and of the Law of Resistance in Parallel Channels. *Philosophical Transactions of the Royal Society of London*, 174:935–982, 1883.

[34] Bastian E. Rapp. Chapter 9 - Fluids. In *Microfluidics: Modelling, Mechanics and Mathematics*, pages 243–263. Elsevier, Walthm, MA, USA, 2017.

[35] Ryan L. Hartman, Jonathan P. McMullen, and Klavs F. Jensen. Deciding Whether To Go with the Flow: Evaluating the Merits of Flow Reactors for Synthesis. *Angewandte Chemie International Edition*, 50(33):7502–7519, 2011.

[36] Oliver Geschke, Henning Klank, and Pieter Telleman. *Microsystem Engineering of Lab-on-a-Chip Devices.* John Wiley & Sons, Ltd, 2003.

[37] Natalija Schmelzer, Jürgen Einfeldt, and Manfred Grigo. Measurements of the Electrolyte Conductivity of Alkali-Metal Perchlorates and $LiNO_3$ in Acetone at 25 °C. *Journal of the Chemical Society, Faraday Transactions 1*, 84(4):931–939, 1988.

[38] John D. Cutnell, Kenneth W. Johnson, David Young, and Shane Stadler. *Physics, 10th Edition.* Wiley, Hoboken, NJ, USA, 2014.

[39] L. B. Romero-Zerón, L. Li, S. Ongsurakul, and B. Balcom. Visualization of Waterflooding through Unconsolidated Porous Media Using Magnetic Resonance Imaging. *Petroleum Science and Technology*, 27(17):1993–2009, 2009.

[40] Brian J. Kirby. *Micro- and Nanoscale Fluid Mechanics: Transport in Microfluidic Devices.* Cambridge University Press, Cambridge, England, UK, 2010.

[41] Siddharth Misra and Yuteng Jin. Chapter 5 - Effects of Wettability of Conductive and Nonconductive Particles on the Multifrequency Electromagnetic Response of Porous Material. In *Multifrequency Electromagnetic Data Interpretation for Subsurface Characterization*, pages 145–170. Elsevier, Walthm, MA, USA, 2021.

[42] Luoran Shang, Yao Cheng, and Yuanjin Zhao. Emerging Droplet Microfluidics. *Chemical Reviews*, 117(12):7964–8040, 2017.

[43] Timothy Noël. Micro Flow Chemistry: New Possibilities for Synthetic Chemists. In *Discovering the Future of Molecular Sciences*, pages 137–164. John Wiley & Sons, Ltd, 2014.

[44] Mohini Joshi and J. D. Deshpande. Polymerase Chain Reaction: Methods, Principles and Application. *International Journal of Biomedical Research*, 2(1):81–97, 2011.

[45] Christopher J. Easley, James M. Karlinsey, Joan M. Bienvenue, Lindsay A. Legendre, Michael G. Roper, Sanford H. Feldman, Molly A. Hughes, Erik L. Hewlett, Tod J. Merkel, Jerome P. Ferrance, and James P. Landers. A Fully Integrated Microfluidic Genetic Analysis System with Sample–in–answer–out capability. *Proceedings of the National Academy of Sciences of the United States of America*, 103(51):19272–19277, 2006.

[46] Timothy Noël, Yuanhai Su, and Volker Hessel. Beyond Organometallic Flow Chemistry: The Principles Behind the Use of Continuous-Flow Reactors for Synthesis. In *Organometallic Flow Chemistry*, pages 1–42. Springer, Cham, Switzerland, 2015.

[47] A. Udaya Kumar, D. Sai Ganesh, T. Vamsi Krishna, B. Sashank, and Talam Satyanarayana. Modeling and Investigation on Mixing Characteristics of T & Y-Shaped Micromixers for Microfluidic Devices. *Materials Today: Proceedings*, 59:501–505, 2022.

[48] Shou-Shing Hsieh, Jyun-Wei Lin, and Jyun-Hong Chen. Mixing Efficiency of Y-Type Micromixers with Different Angles. *International Journal of Heat and Fluid Flow*, 44:130–139, 2013.

[49] Chih-Yung Huang, Shaw-An Wan, and Yu-Hsiang Hu. Oxygen and Nitrogen Gases Mixing in T-Type Micromixers Visualized and Quantitatively Characterized Using Pressure-Sensitive Paint. *International Journal of Heat and Mass Transfer*, 111:520–531, 2017.

[50] Wentan Wang, Shufang Zhao, Ting Shao, Yong Jin, and Yi Cheng. Visualization of Micro-Scale Mixing in Miscible Liquids Using μ-LIF Technique and Drug Nano-Particle Preparation in T-Shaped Micro-Channels. *Chemical Engineering Journal*, 192:252–261, 2012.

[51] Afzal Husain, F. A. Khan, Noorul Huda, and M. A. Ansari. Mixing Performance of Split-and-Recombine Micromixer with Offset Inlets. *Microsystem Technologies*, 24(3):1511–1523, 2018.

[52] Mubashshir Ahmad Ansari, Kwang-Yong Kim, Khalid Anwar, and Sun Min Kim. A Novel Passive Micromixer Based on Unbalanced Splits and Collisions of Fluid Streams. *Journal of Micromechanics and Microengineering*, 20(5):055007, 2010.

[53] S. C. Terry, J. H. Jerman, and J. B. Angell. A Gas Chromatographic Air Analyzer Fabricated on a Silicon Wafer. *IEEE Transactions on Electron Devices*, 26(12):1880–1886, 1979.

[54] Charles W. Hull and Uvp Inc. Apparatus for Production of Three-Dimensional Objects by Stereolithography, 1984. [Online; Accessed 12 Aug 2022].

[55] A. Manz, Y. Miyahara, J. Miura, Y. Watanabe, H. Miyagi, and K. Sato. Design of an Open-Tubular Column Liquid Chromatograph Using Silicon Chip Technology. *Sensors and Actuators B: Chemical*, 1(1):249–255, 1990.

[56] Harold Swerdlow and Raymond Gesteland. Capillary Gel Electrophoresis for Rapid, High Resolution DNA Sequencing. *Nucleic Acids Research*, 18(6):1415–1419, 1990.

[57] Eric K. Sackmann, Anna L. Fulton, and David J. Beebe. The Present and Future Role of Microfluidics in Biomedical Research. *Nature*, 507:181–189, 2014.

[58] A. T. Woolley and R. A. Mathies. Ultra-High-Speed DNA Fragment Separations Using Microfabricated Capillary Array Electrophoresis Chips. *Proceedings of the National Academy of Sciences of the United States of America*, 91(24):11348–11352, 1994.

[59] Adam T. Woolley and Richard A. Mathies. Ultra-High-Speed DNA Sequencing Using Capillary Electrophoresis Chips. *Analytical Chemistry*, 67(20):3676–3680, 1995.

[60] Peter C. Simpson, David Roach, Adam T. Woolley, Todd Thorsen, Rick Johnston, George F. Sensabaugh, and Richard A. Mathies. High-Throughput Genetic Analysis Using Microfabricated 96-Sample Capillary Array Electrophoresis Microplates. *Proceedings of the National Academy of Sciences of the United States of America*, 95(5):2256–2261, 1998.

[61] Enoch Kim, Younan Xia, and George M. Whitesides. Polymer Microstructures Formed by Moulding in Capillaries. *Nature*, 376:581–584, 1995.

[62] Xu Hou, Yu Shrike Zhang, Grissel Trujillo-de Santiago, Mario Moisés Alvarez, João Ribas, Steven J. Jonas, Paul S. Weiss, Anne M. Andrews, Joanna Aizenberg, and Ali Khademhosseini. Interplay Between Materials and Microfluidics. *Nature Reviews Materials*, 2(17016):1–15, 2017.

[63] Kiran Raj M and Suman Chakraborty. PDMS Microfluidics: A Mini Review. *Journal of Applied Polymer Science*, 137(27):48958, 2020.

[64] Kangning Ren, Yin Chen, and Hongkai Wu. New Materials for Microfluidics in Biology. *Current Opinion in Biotechnolog*, 25:78–85, 2014.

[65] Ismail Emre Araci and Stephen R. Quake. Microfluidic Very Large Scale Integration (mVLSI) with Integrated Micromechanical Valves. *Lab on a Chip*, 12(16):2803–2806, 2012.

[66] Frank B. Myers, Richard H. Henrikson, Jennifer Bone, and Luke P. Lee. A Handheld Point-of-Care Genomic Diagnostic System. *PLoS One*, 8(8):e70266, 2013.

[67] Keil J. Regehr, Maribella Domenech, Justin T. Koepsel, Kristopher C. Carver, Stephanie J. Ellison-Zelski, William L. Murphy, Linda A. Schuler, Elaine T. Alarid, and David J. Beebe. Biological Implications of Polydimethylsiloxane-Based Microfluidic Cell Culture. *Lab on a Chip*, 9(15):2132–2139, 2009.

[68] Camilla Luni, Stefano Giulitti, Elena Serena, Luca Ferrari, Alessandro Zambon, Onelia Gagliano, Giovanni G. Giobbe, Federica Michielin, Sebastian Knöbel, Andreas Bosio, and Nicola Elvassore. High-Efficiency Cellular Reprogramming with Microfluidics. *Nature Methods*, 13:446–452, 2016.

[69] Haiwa Wu, Jing Zhu, Yao Huang, Daming Wu, and Jingyao Sun. Microfluidic-Based Single-Cell Study: Current Status and Future Perspective. *Molecules*, 23(9):2347–2370, 2018.

[70] Jeremy D. Caplin, Norma G. Granados, Myra R. James, Reza Montazami, and Nastaran Hashemi. Microfluidic Organ-on-a-Chip Technology for Advancement of Drug Development and Toxicology. *Advanced Healthcare Materials*, 4(10):1426–1450, 2015.

[71] Dongeun Huh, Benjamin D. Matthews, Akiko Mammoto, Martín Montoya-Zavala, Hong Yuan Hsin, and Donald E. Ingber. Reconstituting Organ-Level Lung Functions on a Chip. *Science*, 328(5986):1662–1668, 2010.

[72] Seung-A. Lee, Da Yoon No, Edward Kang, Jongil Ju, Dong-Sik Kim, and Sang-Hoon Lee. Spheroid-Based Three-Dimensional Liver-on-a-Chip to Investigate Hepatocyte–Hepatic Stellate Cell Interactions and Flow Effects. *Lab on a Chip*, 13(18):3529–3537, 2013.

[73] Li-Dong Ma, Yi-Tong Wang, Jing-Rong Wang, Jian-Lin Wu, Xian-Sheng Meng, Ping Hu, Xuan Mu, Qiong-Lin Liang, and Guo-An Luo. Design and Fabrication of a Liver-on-a-Chip Platform for Convenient, Highly Efficient, and Safe *in situ*

Perfusion Culture of 3D Hepatic Spheroids. *Lab on a Chip*, 18(17):2547–2562, 2018.

[74] Kyung-Jin Jang, Ali Poyan Mehr, Geraldine A. Hamilton, Lori A. McPartlin, Seyoon Chung, Kahp-Yang Suh, and Donald E. Ingber. Human Kidney Proximal Tubule-on-a-Chip for Drug Transport and Nephrotoxicity Assessment. *Integrative Biology*, 5(9):1119–1129, 2013.

[75] Anna Marsano, Chiara Conficconi, Marta Lemme, Paola Occhetta, Emanuele Gaudiello, Emiliano Votta, Giulia Cerino, Alberto Redaelli, and Marco Rasponi. Beating Heart-on-a-Chip: A Novel Microfluidic Platform to Generate Functional 3D Cardiac Microtissues. *Lab on a Chip*, 16(3):599–610, 2016.

[76] Maierdanjiang Wufuer, GeonHui Lee, Woojune Hur, Byoungjun Jeon, Byung Jun Kim, Tae Hyun Choi, and SangHoon Lee. Skin-on-a-Chip Model Simulating Inflammation, Edema and Drug-Based Treatment. *Scientific Reports*, 6(37471):1–12, 2016.

[77] Hyun Jung Kim, Hu Li, James J. Collins, and Donald E. Ingber. Contributions of Microbiome and Mechanical Deformation to Intestinal Bacterial Overgrowth and Inflammation in a Human Gut-on-a-Chip. *Proceedings of the National Academy of Sciences of the United States of America*, 113(1):E7–E15, 2016.

[78] Hyun Jung Kim, Dongeun Huh, Geraldine Hamilton, and Donald E. Ingber. Human Gut-on-a-Chip Inhabited by Microbial Flora that Experiences Intestinal Peristalsis-like Motions and Flow. *Lab on a Chip*, 12(12):2165–2174, 2012.

[79] Sasan Jalili-Firoozinezhad, Rachelle Prantil-Baun, Amanda Jiang, Ratnakar Potla, Tadanori Mammoto, James C. Weaver, Thomas C. Ferrante, Hyun Jung Kim, Joaquim M. S. Cabral, Oren Levy, and Donald E. Ingber. Modeling Radiation Injury-Induced Cell Death and Countermeasure Drug Responses in a Human Gut-on-a-Chip. *Cell Death & Disease*, 9(2):223., 2018.

[80] Min Seo Jeon, Yoon Young Choi, Sung Jun Mo, Jang Ho Ha, Young Seo Lee, Hee Uk Lee, Soo Dong Park, Jae-Jung Shim, Jung-Lyoul Lee, and Bong Geun

Chung. Contributions of the Microbiome to Intestinal Inflammation in a Gut-on-a-Chip. *Nano Convergence*, 9(1):1–13, 2022.

[81] JiSoo Park, Bo Kyeong Lee, Gi Seok Jeong, Jung Keun Hyun, C. Justin Lee, and Sang-Hoon Lee. Three-Dimensional Brain-on-a-Chip with an Interstitial Level of Flow and its Application as an *in vitro* Model of Alzheimer's Disease. *Lab on a Chip*, 15(1):141–150, 2014.

[82] Juan Eduardo Sosa-Hernández, Angel M. Villalba-Rodríguez, Kenya D. Romero-Castillo, Mauricio A. Aguilar-Aguila-Isaías, Isaac E. García-Reyes, Arturo Hernández-Antonio, Ishtiaq Ahmed, Ashutosh Sharma, Roberto Parra-Saldívar, and Hafiz M. N. Iqbal. Organs-on-a-Chip Module: A Review from the Development and Applications Perspective. *Micromachines*, 9(10), 2018.

[83] Donald E. Ingber. Human Organs-on-Chips for Disease Modelling, Drug Development and Personalized Medicine. *Nat. Rev. Genet.*, 23:467–491, 2022.

[84] Amid Shakeri, Shadman Khan, and Tohid F. Didar. Conventional and Emerging Strategies for the Fabrication and Functionalization of PDMS-Based Microfluidic Devices. *Lab on a Chip*, 21(16):3053–3075, 2021.

[85] Ali Yilmaz and Marcel Utz. Characterisation of Oxygen Permeation into a Microfluidic Device for Cell Culture by *in situ* NMR Spectroscopy. *Lab on a Chip*, 16(11):2079–2085, 2016.

[86] X. Chen, T. Li, and J. Shen. CO2 Laser Ablation of Microchannel on PMMA Substrate for Effective Fabrication of Microfluidic Chips. *International Polymer Processing*, 31(2):233–238, 2016.

[87] Caitlin Howell, Thy L. Vu, Christopher P. Johnson, Xu Hou, Onye Ahanotu, Jack Alvarenga, Daniel C. Leslie, Oktay Uzun, Anna Waterhouse, Philseok Kim, Michael Super, Michael Aizenberg, Donald E. Ingber, and Joanna Aizenberg. Stability of Surface-Immobilized Lubricant Interfaces Under Flow. *Chemistry of Materials*, 27(5):1792–1800, 2015.

[88] Jiwoon Park, Vijaya Sunkara, Tae-Hyeong Kim, Hyundoo Hwang, and Yoon-Kyoung Cho. Lab-on-a-Disc for Fully Integrated Multiplex Immunoassays. *Analytical Chemistry*, 84(5):2133–2140, 2012.

[89] Curtis D. Chin, Tassaneewan Laksanasopin, Yuk Kee Cheung, David Steinmiller, Vincent Linder, Hesam Parsa, Jennifer Wang, Hannah Moore, Robert Rouse, Gisele Umviligihozo, Etienne Karita, Lambert Mwambarangwe, Sarah L. Braunstein, Janneke van de Wijgert, Ruben Sahabo, Jessica E. Justman, Wafaa El-Sadr, and Samuel K. Sia. Microfluidics-Based Diagnostics of Infectious Diseases in the Developing World. *Nature Medicine*, 17:1015–1019, 2011.

[90] Jacob B. Nielsen, Robert L. Hanson, Haifa M. Almughamsi, Chao Pang, Taylor R. Fish, and Adam T. Woolley. Microfluidics: Innovations in Materials and Their Fabrication and Functionalization. *Analytical Chemistry*, 92(1):150–168, 2020.

[91] Carla B. Goy, Roberto E. Chaile, and Rossana E. Madrid. Microfluidics and Hydrogel: A Powerful Combination. *Reactive & Functional Polymers*, 145:104314, 2019.

[92] Fahima Akther, Peter Little, Zhiyong Li, Nam-Trung Nguyen, and Hang T. Ta. Hydrogels as Artificial Matrices for Cell Seeding in Microfluidic Devices. *RSC Advances*, 10(71):43682–43703, 2020.

[93] Kyu-Young Shim, Dongwook Lee, Jeonghun Han, Nam-Trung Nguyen, Sungsu Park, and Jong Hwan Sung. Microfluidic Gut-on-a-Chip with Three-Dimensional Villi Structure. *Biomedical Microdevices*, 19(2):1–10, 2017.

[94] Andres W. Martinez, Scott T. Phillips, Manish J. Butte, and George M. Whitesides. Patterned Paper as a Platform for Inexpensive, Low-Volume, Portable Bioassays. *Angewandte Chemie International Edition*, 46(8):1318–1320, 2007.

[95] Julie Credou and Thomas Berthelot. Cellulose: From Biocompatible to Bioactive Material. *Journal of Materials Chemistry B*, 2(30):4767–4788, 2014.

[96] Ganesan Sriram, Mahesh P. Bhat, Pravin Patil, Uluvangada T. Uthappa, Ho-Young Jung, Tariq Altalhi, Tushar Kumeria, Tejraj M. Aminabhavi, Ranjith Krishna Pai, Madhuprasad, and Mahaveer D. Kurkuri. Paper-Based Microfluidic Analytical Devices for Colorimetric Detection of Toxic Ions: A Review. *TrAC Trends in Analytical Chemistry*, 93:212–227, 2017.

[97] Sarah J. Vella, Patrick Beattie, Rebecca Cademartiri, Anna Laromaine, Andres W. Martinez, Scott T. Phillips, Katherine A. Mirica, and George M. Whitesides. Measuring Markers of Liver Function Using a Micropatterned Paper Device Designed for Blood from a Fingerstick. *Analytical Chemistry*, 84(6):2883–2891, 2012.

[98] Nira R. Pollock, Jason P. Rolland, Shailendra Kumar, Patrick D. Beattie, Sidhartha Jain, Farzad Noubary, Vicki L. Wong, Rebecca A. Pohlmann, Una S. Ryan, and George M. Whitesides. A Paper-Based Multiplexed Transaminase Test for Low-Cost, Point-of-Care Liver Function Testing. *Science Translational Medicine*, 4(152):152ra129, 2012.

[99] Shreyas Vasantham, Ruby Alhans, Chaitali Singhal, Shalini Nagabooshanam, Sumaya Nissar, Tinku Basu, Sekhar C. Ray, Shikha Wadhwa, Jagriti Narang, and Ashish Mathur. Paper Based Point of Care Immunosensor for the Impedimetric Detection of Cardiac Troponin I Biomarker. *Biomedical Microdevices*, 22(1):1–9, 2020.

[100] Julien Reboud, Gaolian Xu, Alice Garrett, Moses Adriko, Zhugen Yang, Edridah M. Tukahebwa, Candia Rowell, and Jonathan M. Cooper. Paper-Based Microfluidics for DNA Diagnostics of Malaria in Low Resource Underserved Rural Communities. *Proceedings of the National Academy of Sciences of the United States of America*, 116(11):4834–4842, 2019.

[101] Roberto Raiteri, Massimo Grattarola, Hans-Jürgen Butt, and Petr Skládal. Micromechanical Cantilever-Based Biosensors. *Sensors and Actuators B: Chemical*, 79(2):115–126, 2001.

[102] Aviru Kumar Basu, Adreeja Basu, and Shantanu Bhattacharya. Micro/Nano Fabricated Cantilever Based Biosensor Platform: A Review and Recent Progress. *Enzyme and Microbial Technology.*, 139:109558, 2020.

[103] Ribu Mathew and A. Ravi Sankar. A Review on Surface Stress-Based Miniaturized Piezoresistive SU-8 Polymeric Cantilever Sensors. *Nano-Micro Letters*, 10(2):1–41, 2018.

[104] Bernard Ouma Alunda and Yong Joong Lee. Review: Cantilever-Based Sensors for High Speed Atomic Force Microscopy. *Sensors*, 20(17):4784, 2020.

[105] Joseph Wang. Electrochemical Biosensors: Towards Point-of-Care Cancer Diagnostics. *Biosensors and Bioelectronics*, 21(10):1887–1892, 2006.

[106] Noel Nesakumar, Srinivasan Kesavan, Chen-Zhong Li, and Subbiah Alwarappan. Microfluidic Electrochemical Devices for Biosensing. *Journal of Analysis and Testing*, 3(1):3–18, 2019.

[107] Miren Ruiz de Eguilaz, Loanda R. Cumba, and Robert J. Forster. Electrochemical Detection of Viruses and Antibodies: A Mini Review. *Electrochemistry Communications*, 116:106762, 2020.

[108] Pin-Chuan Chen, Wei-Zhe Zhang, Wei-Ru Chen, Yung-Cheng Jair, Yi-Hsin Wu, Yi-Hsin Liu, Pei-Zhen Chen, Lian-Yu Chen, and Pai-Shan Chen. Engineering an Integrated System with a High Pressure Polymeric Microfluidic Chip Coupled to Liquid Chromatography-Mass Spectrometry (LC-MS) for the Analysis of Abused Drugs. *Sensors and Actuators B: Chemical*, 350:130888, 2022.

[109] Izabella J. Jahn, Olga Žukovskaja, Xiao-Shan Zheng, Karina Weber, Thomas W. Bocklitz, Dana Cialla-May, and Jürgen Popp. Surface-Enhanced Raman Spectroscopy and Microfluidic Platforms: Challenges, Solutions and Potential Applications. *Analyst*, 142(7):1022–1047, 2017.

[110] Gustavo Ochoa-Vazquez, Boris Kharisov, Ana Arizmendi-Morquecho, Anaïs Cario, Cyril Aymonier, Samuel Marre, and Israel López. Microfluidics and Surface-Enhanced Raman Spectroscopy: A Perfect Match for New Analytical Tools. *IEEE Transactions on NanoBioscience*, 18(4):558–566, 2019.

[111] Jun Li, Helena Šimek, David Ilioae, Nicole Jung, Stefan Bräse, Hans Zappe, Roland Dittmeyer, and Bradley P. Ladewig. *In situ* Sensors for Flow Reactors – A Review. *Reaction Chemistry & Engineering*, 6(9):1497–1507, 2021.

[112] Frank B. Myers and Luke P. Lee. Innovations in Optical Microfluidic Technologies for Point-of-Care Diagnostics. *Lab on a Chip*, 8(12):2015–2031, 2008.

[113] Yu Tian, Michelle M. Martinez, and Dimitri Pappas. Fluorescence Correlation Spectroscopy: A Review of Biochemical and Microfluidic Applications. *Applied Spectroscopy*, 65(4):115A, 2011.

[114] Yong Zhao, Xu-guang Hu, Sheng Hu, and Yun Peng. Applications of Fiber-Optic Biochemical Sensor in Microfluidic Chips: A Review. *Biosensors and Bioelectronics*, 166:112447, 2020.

[115] Antoine Dupré, Ka-Meng Lei, Pui-In Mak, Rui P. Martins, and Weng Kung Peng. Micro- and Nanofabrication NMR Technologies for Point-of-Care Medical Applications – A Review. *Microelectronic Engineering*, 209:66–74, 2019.

[116] P. J. M. van Bentum, J. W. G. Janssen, and A. P. M. Kentgens. Towards Nuclear Magnetic Resonance μ-Spectroscopy and μ-Imaging. *Analyst*, 129(9):793–803, 2004.

[117] Nuno Miguel Matos Pires, Tao Dong, Ulrik Hanke, and Nils Hoivik. Recent Developments in Optical Detection Technologies in Lab-on-a-Chip Devices for Biosensing Applications. *Sensors*, 14(8):15458, 2014.

[118] Daniel Măriuţa, Stéphane Colin, Christine Barrot-Lattes, Stéphane Le Calvé, Jan G. Korvink, Lucien Baldas, and Jürgen J. Brandner. Miniaturization of Fluorescence Sensing in Optofluidic Devices. *Microfluidics and Nanofluidics*, 24(9):1–28, 2020.

[119] Petra S. Dittrich and Andreas Manz. Single-Molecule Fluorescence Detection in Microfluidic Channels–The Holy Grail in μTAS? *Analytical and Bioanalytical Chemistry*, 382(8):1771–1782, 2005.

[120] Yu Shrike Zhang, João Ribas, Akhtar Nadhman, Julio Aleman, Šeila Selimović, Sasha Cai Lesher-Perez, Ting Wang, Vijayan Manoharan, Su-Ryon Shin, Alessia Damilano, Nasim Annabi, Mehmet Remzi Dokmeci, Shuichi Takayama, and Ali Khademhosseini. A Cost-Effective Fluorescence Mini-Microscope for Biomedical Applications. *Lab on a Chip*, 15(18):3661–3669, 2015.

[121] Kunal K. Ghosh, Laurie D. Burns, Eric D. Cocker, Axel Nimmerjahn, Yaniv Ziv, Abbas El Gamal, and Mark J. Schnitzer. Miniaturized Integration of a Fluorescence Microscope. *Nature Methods*, 8(10):871–878, 2011.

[122] Witold Nawrot, Kamila Drzozga, Sylwia Baluta, Joanna Cabaj, and Karol Malecha. A Fluorescent Biosensors for Detection Vital Body Fluids' Agents. *Sensors*, 18(8):2357, 2018.

[123] Martin D. Brennan, Megan L. Rexius-Hall, Laura Jane Elgass, and David T. Eddington. Oxygen Control with Microfluidics. *Lab on a Chip*, 14(22):4305–4318, 2014.

[124] Jun Yue, Jaap C. Schouten, and T. Alexander Nijhuis. Integration of Microreactors with Spectroscopic Detection for Online Reaction Monitoring and Catalyst Characterization. *Industrial & Engineering Chemistry Research*, 51(45):14583–14609, 2012.

[125] Saratchandra Shanmukh, Les Jones, Jeremy Driskell, Yiping Zhao, Richard Dluhy, and Ralph A. Tripp. Rapid and Sensitive Detection of Respiratory Virus Molecular Signatures Using a Silver Nanorod Array SERS Substrate. *Nano Letters*, 6(11):2630–2636, 2006.

[126] Robin Fortt, Robert C. R. Wootton, and Andrew J. de Mello. Continuous-Flow Generation of Anhydrous Diazonium Species: Monolithic Microfluidic Reactors for the Chemistry of Unstable Intermediates. *Organic Process Research & Development*, 7(5):762–768, 2003.

[127] Malcolm H. Levitt. *Spin Dynamics: Basics of Nuclear Magnetic Resonance, 2nd Edition*. Wiley, Hoboken, NJ, USA, 2008.

[128] P. A. M. Dirac. A New Notation for Quantum Mechanics. *Mathematical Proceedings of the Cambridge Philosophical Society*, 35(3):416–418, 1939.

[129] David I. Hoult. Sensitivity of the NMR Experiment. In *eMagRes*. John Wiley & Sons, Ltd, Chichester, England, UK, 2007.

[130] Joël Mispelter, Mihaela Lupu, and André Briguet. *NMR Probeheads for Biophysical and Biomedical Experiments*. World Scientific Publishing Company, London, England, UK, 2011.

[131] Santosh Kumar Bharti and Raja Roy. Quantitative ^{1}H NMR spectroscopy. *TrAC Trends in Analytical Chemistry*, 35:5–26, 2012.

[132] Vlad Badilita, Robert Ch. Meier, Nils Spengler, Ulrike Wallrabe, Marcel Utz, and Jan G. Korvink. Microscale Nuclear Magnetic Resonance: A Tool for Soft Matter Research. *Soft Matter*, 8(41):10583–10597, 2012.

[133] Meghan E. Halse. Perspectives for Hyperpolarisation in Compact NMR. *TrAC Trends in Analytical Chemistry*, 83:76–83, 2016.

[134] Abdul-Hamid Emwas, Raja Roy, Ryan T. McKay, Leonardo Tenori, Edoardo Saccenti, G. A. Nagana Gowda, Daniel Raftery, Fatimah Alahmari, Lukasz Jaremko, Mariusz Jaremko, and David S. Wishart. NMR Spectroscopy for Metabolomics Research. *Metabolites*, 9(7):123, 2019.

[135] A. Abragam. *The Principles of Nuclear Magnetism*. Oxford University Press, Oxford, England, UK, 1961.

[136] D. I. Hoult and R. E. Richards. The Signal-to-Noise Ratio of the Nuclear Magnetic Resonance Experiment. *Journal of Magnetic Resonance (1969)*, 24(1):71–85, 1976.

[137] P. J. M. van Bentum, J. W. G. Janssen, A. P. M. Kentgens, J. Bart, and J. G. E. Gardeniers. Stripline Probes for Nuclear Magnetic Resonance. *Journal of Magnetic Resonance*, 189(1):104–113, 2007.

[138] Manvendra Sharma and Marcel Utz. Modular Transmission Line Probes for Microfluidic Nuclear Magnetic Resonance Spectroscopy and Imaging. *Journal of Magnetic Resonance*, 303:75–81, 2019.

[139] Robert Ch. Meier, Jens Höfflin, Vlad Badilita, Ulrike Wallrabe, and Jan G. Korvink. Microfluidic Integration of Wirebonded Microcoils for On-Chip Applications in Nuclear Magnetic Resonance. *Journal of Micromechanics and Microengineering*, 24(4):045021, 2014.

[140] Nils Spengler, Jens Höfflin, Ali Moazenzadeh, Dario Mager, Neil MacKinnon, Vlad Badilita, Ulrike Wallrabe, and Jan G. Korvink. Heteronuclear Micro-Helmholtz Coil Facilitates μm-Range Spatial and Sub-Hz Spectral Resolution NMR of nL-Volume Samples on Customisable Microfluidic Chips. *PLoS One*, 11(1):e0146384, 2016.

[141] William G. Hale. *Applications of Microfluidics in Nuclear Magnetic Resonance.* PhD thesis, University of Southampton, 2019.

[142] Arthur C. Pinon, Andrea Capozzi, and Jan Henrik Ardenkjær-Larsen. Hyperpolarization via Dissolution Dynamic Nuclear Polarization: New Technological and Methodological Advances. *Magnetic Resonance Materials in Physics, Biology and Medicine*, 34(1):5–23, 2021.

[143] Wai Tung Lee, Gang Zheng, Cavin L. Talbot, Xin Tong, Tim D'Adam, Steven R. Parnell, Michael de Veer, Graham Jenkin, Graeme R. Polglase, Stuart B. Hooper, Bruce R. Thompson, Francis Thien, and Gary F. Egan. Hyperpolarised Gas Filling Station for Medical Imaging Using Polarised ^{129}Xe and ^{3}He. *Magnetic Resonance Imaging*, 79:112, 2021.

[144] Thad G. Walker and William Happer. Spin-Exchange Optical Pumping of Noble-Gas Nuclei. *Reviews of Modern Physics*, 69(2):629–642, 1997.

[145] B. Lancor and T. G. Walker. Effects of Nitrogen Quenching Gas on Spin-Exchange Optical Pumping of ^{3}He. *Physical Review A*, 82(4):043417, 2010.

[146] B. Driehuys, G. D. Cates, E. Miron, K. Sauer, D. K. Walter, and W. Happer. High-Volume Production of Laser-Polarized ^{129}Xe. *Applied Physics Letters*, 69(12):1668–1670, 1996.

[147] I. C. Ruset, S. Ketel, and F. W. Hersman. Optical Pumping System Design for Large Production of Hyperpolarized ^{129}Xe. *Physical Review Letters*, 96(5):053002, 2006.

[148] Panayiotis Nikolaou, Aaron M. Coffey, Laura L. Walkup, Brogan M. Gust, Nicholas Whiting, Hayley Newton, Scott Barcus, Iga Muradyan, Mikayel Dabaghyan, Gregory D. Moroz, Matthew S. Rosen, Samuel Patz, Michael J. Barlow, Eduard Y. Chekmenev, and Boyd M. Goodson. Near-Unity Nuclear Polarization with an Open-Source ^{129}Xe Hyperpolarizer for NMR and MRI. *Proceedings of the National Academy of Sciences of the United States of America*, 110(35):14150–14155, 2013.

[149] N. R. Newbury, A. S. Barton, P. Bogorad, G. D. Cates, M. Gatzke, B. Saam, L. Han, R. Holmes, P. A. Souder, J. Xu, and D. Benton. Laser Polarized Muonic Helium. *Physical Review Letters*, 67(23):3219–3222, 1991.

[150] Leif Schröder. Xenon for NMR Biosensing – Inert but Alert. *Physica Medica*, 29(1):3–16, 2013.

[151] P. L. Anthony, R. G. Arnold, H. R. Band, H. Borel, P. E. Bosted, V. V Breton, G. D. Cates, T. E. Chupp, F. S. Dietrich, J. Dunne, R. Erbacher, J. Fellbaum, H. Fonvieille, R. Gearhart, R. Holmes, E. W. Hughes, J. R. Johnson, D. Kawall, C. Keppel, S. E. Kuhn, R. M. Lombard-Nelsen, J. Marroncle, T. Maruyama, W. Meyer, Z. Meziani, H. Middleton, J. Morgenstern, N. R. Newbury, G. G. Petratos, R. Pitthan, R. Prepost, Y. Roblin, S. E. Rock, S. H. Rokni, G. Shapiro, T. Smith, P. A. Souder, M. Spengos, F. Staley, L. M. Stuart, Z. M. Szalata, Y. Terrien, A. K. Thompson, J. L. White, M. Woods, J. Xu, C. C. Young, and G. Zapalac. Determination of the Neutron Spin Structure Function. *Physical Review Letters*, 71(7):959–962, 1993.

[152] Ricardo Jiménez-Martínez, Daniel J. Kennedy, Michael Rosenbluh, Elizabeth A. Donley, Svenja Knappe, Scott J. Seltzer, Hattie L. Ring, Vikram S. Bajaj, and John Kitching. Optical Hyperpolarization and NMR Detection of ^{129}Xe on a Microfluidic Chip. *Nature Communications*, 5(3908):1–6, 2014.

[153] Daniel J. Kennedy, Scott J. Seltzer, Ricardo Jiménez-Martínez, Hattie L. Ring, Nicolas S. Malecek, Svenja Knappe, Elizabeth A. Donley, John Kitching, Vikram S. Bajaj, and Alexander Pines. An Optimized Microfabricated Platform for the Optical Generation and Detection of Hyperpolarized ^{129}Xe. *Scientific Reports*, 7:43994., 2017.

[154] A. Abragam and M. Goldman. Principles of Dynamic Nuclear Polarisation. *Reports on Progress in Physics*, 41(3):395–467, 1978.

[155] Jan G. Krummenacker, Vasyl P. Denysenkov, Maxim Terekhov, Laura M. Schreiber, and Thomas F. Prisner. DNP in MRI: An In-Bore Approach at 1.5T. *Journal of Magnetic Resonance*, 215:94–99, 2012.

[156] Lino R. Becerra, Gary J. Gerfen, Richard J. Temkin, David J. Singel, and Robert G. Griffin. Dynamic Nuclear Polarization with a Cyclotron Resonance Maser at 5 T. *Physical Review Letters*, 71(21):3561–3564, 1993.

[157] G. J. Gerfen, L. R. Becerra, D. A. Hall, R. G. Griffin, R. J. Temkin, and D. J. Singel. High Frequency (140 GHz) Dynamic Nuclear Polarization: Polarization Transfer to a Solute in Frozen Aqueous Solution. *The Journal of Chemical Physics*, 102(24):9494–9497, 1995.

[158] Ümit Akbey and Hartmut Oschkinat. Structural Biology Applications of Solid State MAS DNP NMR. *Journal of Magnetic Resonance*, 269:213–224, 2016.

[159] Albert W. Overhauser. Polarization of Nuclei in Metals. *Physical Review*, 92(2):411–415, 1953.

[160] T. R. Carver and C. P. Slichter. Polarization of Nuclear Spins in Metals. *Physical Review*, 92(1):212–213, 1953.

[161] C. Griesinger, M. Bennati, H. M. Vieth, C. Luchinat, G. Parigi, P. Höfer, F. Engelke, S. J. Glaser, V. Denysenkov, and T. F. Prisner. Dynamic Nuclear Polarization at High Magnetic Fields in Liquids. *Progress in Nuclear Magnetic Resonance Spectroscopy*, 64:4–28, 2012.

[162] Jan H. Ardenkjær-Larsen, Björn Fridlund, Andreas Gram, Georg Hansson, Lennart Hansson, Mathilde H. Lerche, Rolf Servin, Mikkel Thaning, and Klaes Golman. Increase in Signal-to-Noise Ratio of $>$ 10,000 Times in Liquid-State NMR. *Proceedings of the National Academy of Sciences of the United States of America*, 100(18):10158–10163, 2003.

[163] Björn Corzilius. High-Field Dynamic Nuclear Polarization. *Annual Review of Physical Chemistry*, 71(1):143–170, 2020.

[164] Guoquan Liu, Marcel Levien, Niels Karschin, Giacomo Parigi, Claudio Luchinat, and Marina Bennati. One-Thousand-Fold Enhancement of High Field Liquid Nuclear Magnetic Resonance Signals at Room Temperature. *Nature Chemistry*, 9:676–680, 2017.

[165] Karel Kouřil, Hana Kouřilová, Samuel Bartram, Malcolm H. Levitt, and Benno Meier. Scalable Dissolution-Dynamic Nuclear Polarization with Rapid Transfer of a Polarized Solid. *Nature Communications*, 10(1733):1–6, 2019.

[166] Sangmoo Jeong, Roozbeh Eskandari, Sun Mi Park, Julio Alvarez, Sui Seng Tee, Ralph Weissleder, Michael G. Kharas, Hakho Lee, and Kayvan R. Keshari. Real-Time Quantitative Analysis of Metabolic Flux in Live Cells Using a Hyperpolarized Micromagnetic Resonance Spectrometer. *Science Advances*, 3(6):e1700341, 2017.

[167] Sebastian Z. Kiss, Neil MacKinnon, and Jan G. Korvink. Microfluidic Overhauser DNP Chip for Signal-Enhanced Compact NMR. *Scientific Reports*, 11(4671):1–11, 2021.

[168] M. Sharma, G. Janssen, J. Leggett, A. P. M. Kentgens, and P. J. M. van Bentum. Rapid-Melt Dynamic Nuclear Polarization. *Journal of Magnetic Resonance*, 258:40–8, 2015.

[169] Thomas Theis, Gerardo X. OrtizJr., Angus W. J. Logan, Kevin E. Claytor, Yesu Feng, William P. Huhn, Volker Blum, Steven J. Malcolmson, Eduard Y. Chekmenev, Qiu Wang, and Warren S. Warren. Direct and Cost-Efficient Hyperpolarization of Long-Lived Nuclear Spin States on Universal $^{15}N_2$-Diazirine Molecular Tags. *Science Advances*, 2(3):e1501438, 2016.

[170] R. Kaptein and J. L. Oosterhoff. Chemically Induced Dynamic Nuclear Polarization II: (Relation with Anomalous ESR Spectra). *Chemical Physics Letters*, 4(4):195–197, 1969.

[171] Gerhard L. Closs. Mechanism Explaining Nuclear Spin Polarizations in Radical Combination Reactions. *Journal of the American Chemical Society*, 91(16):4552–4554, 1969.

[172] Miguel Mompeán, Rosa M. Sánchez-Donoso, Antonio de la Hoz, Vittorio Saggiomo, Aldrik H. Velders, and M. Victoria Gomez. Pushing Nuclear Magnetic Resonance Sensitivity Limits with Microfluidics and Photo-Chemically Induced Dynamic Nuclear Polarization. *Nature Communications*, 9(1):108., 2018.

[173] K. Hun Mok, Toshio Nagashima, Iain J. Day, Jonathan A. Jones, Charles J. V. Jones, Christopher M. Dobson, and P. J. Hore. Rapid Sample-Mixing Technique for Transient NMR and Photo-CIDNP Spectroscopy: Applications to Real-Time Protein Folding. *Journal of the American Chemical Society*, 125(41):12484–12492, 2003.

[174] Matthew L. Hirsch, Bryce A. Smith, Mark Mattingly, Artem G. Goloshevsky, Melanie Rosay, and James G. Kempf. Transport and Imaging of Brute-Force ^{13}C Hyperpolarization. *Journal of Magnetic Resonance*, 261:87–94, 2015.

[175] Matthew L. Hirsch, Neal Kalechofsky, Avrum Belzer, Melanie Rosay, and James G. Kempf. Brute-Force Hyperpolarization for NMR and MRI. *Journal of the American Chemical Society*, 137(26):8428–8434, 2015.

[176] David T. Peat, Matthew L. Hirsch, David G. Gadian, Anthony J. Horsewill, John R. Owers-Bradley, and James G. Kempf. Low-Field Thermal Mixing in

[1-^{13}C] Pyruvic Acid for Brute-Force Hyperpolarization. *Physical Chemistry Chemical Physics*, 18(28):19173–19182, 2016.

[177] C. Russell Bowers and Daniel P. Weitekamp. Transformation of Symmetrization Order to Nuclear-Spin Magnetization by Chemical Reaction and Nuclear Magnetic Resonance. *Physical Review Letters*, 57(21):2645–2648, 1986.

[178] Kirill V. Kovtunov, Vladimir V. Zhivonitko, Ivan V. Skovpin, Danila A. Barskiy, and Igor V. Koptyug. Parahydrogen-Induced Polarization in Heterogeneous Catalytic Processes. In *Hyperpolarization Methods in NMR Spectroscopy*, pages 123–180. Springer, 2012.

[179] Kirill V. Kovtunov, Danila A. Barskiy, Oleg G. Salnikov, Roman V. Shchepin, Aaron M. Coffey, Larisa M. Kovtunova, Valerii I. Bukhtiyarov, Igor V. Koptyug, and Eduard Y. Chekmenev. Toward Production of Pure ^{13}C Hyperpolarized Metabolites Using Heterogeneous Parahydrogen-Induced Polarization of Ethyl[1-^{13}C]acetate. *RSC Advances*, 6(74):69728–69732, 2016.

[180] Ekaterina V. Pokochueva, Kirill V. Kovtunov, Oleg G. Salnikov, Max E. Gemeinhardt, Larisa M. Kovtunova, Valerii I. Bukhtiyarov, Eduard Y. Chekmenev, Boyd M. Goodson, and Igor V. Koptyug. Heterogeneous Hydrogenation of Phenylalkynes with Parahydrogen: Hyperpolarization, Reaction Selectivity, and Kinetics. *Physical Chemistry Chemical Physics*, 21(48):26477–26482, 2019.

[181] Ralph W. Adams, Juan A. Aguilar, Kevin D. Atkinson, Michael J. Cowley, Paul I. P. Elliott, Simon B. Duckett, Gary G. R. Green, Iman G. Khazal, Joaquín López-Serrano, and David C. Williamson. Reversible Interactions with Para-Hydrogen Enhance NMR Sensitivity by Polarization Transfer. *Science*, 323(5922):1708–1711, 2009.

[182] Barbara Ripka, James Eills, Hana Kouřilová, Markus Leutzsch, Malcolm H. Levitt, and Kerstin Münnemann. Hyperpolarized Fumarate *via* Parahydrogen. *Chemical Communications*, 54(86):12246–12249, 2018.

[183] Walter Köckenberger and Jörg Matysik. Hyperpolarization Methods and Applications in NMR. In *Encyclopedia of Spectroscopy and Spectrometry (Second Edition)*, pages 963–970. Academic Press, Cambridge, MA, USA, 2010.

[184] B. P. Stoicheff. High Resolution Raman Spectroscopy of Gases: XI. Spectra of H_2, HD and D_2. *Canadian Journal of Physics*, 35(6):730–741, 1957.

[185] Sebastian Kiss, Lorenzo Bordonali, Jan G. Korvink, and Neil MacKinnon. Microscale Hyperpolarization. In *Micro and Nano Scale NMR*, pages 297–351. John Wiley & Sons, Ltd, 2018.

[186] Peter M. Richardson, Scott Jackson, Andrew J. Parrott, Alison Nordon, Simon B. Duckett, and Meghan E. Halse. A Simple Hand-Held Magnet Array for Efficient and Reproducible SABRE Hyperpolarisation Using Manual Sample Shaking. *Magnetic Resonance in Chemistry*, 56(7):641–650, 2018.

[187] Danila A. Barskiy, Aaron M. Coffey, Panayiotis Nikolaou, Dmitry M. Mikhaylov, Boyd M. Goodson, Rosa T. Branca, George J. Lu, Mikhail G. Shapiro, Ville-Veikko Telkki, Vladimir V. Zhivonitko, Igor V. Koptyug, Oleg G. Salnikov, Kirill V. Kovtunov, Valerii I. Bukhtiyarov, Matthew S. Rosen, Michael J. Barlow, Shahideh Safavi, Ian P. Hall, Leif Schröder, and Eduard Y. Chekmenev. NMR Hyperpolarization Techniques of Gases. *Chemistry (Weinheim an der Bergstrasse, Germany)*, 23(4):725, 2017.

[188] Lisandro Buljubasich, María Belén Franzoni, and Kerstin Münnemann. Parahydrogen Induced Polarization by Homogeneous Catalysis: Theory and Applications. *Topics in Current Chemistry*, 338:33–74, 2013.

[189] Rosa Crovetto. Evaluation of Solubility Data of the System CO_2–H_2O from 273K to the Critical Point of Water. *Journal of Physical and Chemical Reference Data*, 20(3):575–589, 1991.

[190] Ryan E. Mewis, Kevin D. Atkinson, Michael J. Cowley, Simon B. Duckett, Gary G. R. Green, Richard A. Green, Louise A. R. Highton, David Kilgour, Lyrelle S. Lloyd, Joost A. B. Lohman, and David C. Williamson. Probing Signal

Amplification by Reversible Exchange Using an NMR Flow System. *Magnetic Resonance in Chemistry*, 52(7):358–369, 2014.

[191] Meike Roth, Petra Kindervater, Hans-Peter Raich, Joachim Bargon, Hans W. Spiess, and Kerstin Münnemann. Continuous ^{1}H and ^{13}C Signal Enhancement in NMR Spectroscopy and MRI Using Parahydrogen and Hollow-Fiber Membranes. *Angewandte Chemie International Edition*, 49(45):8358–8362, 2010.

[192] N. Amor, P. P. Zänker, Peter Blümler, F. M. Meise, L. M. Schreiber, A. Scholz, Jörg Schmiedeskamp, Hans Wolfgang Spiess, and Kerstin Münnemann. Magnetic Resonance Imaging of Dissolved Hyperpolarized ^{129}Xe Using a Membrane-Based Continuous Flow System. *Journal of Magnetic Resonance*, 201(1):93–99, 2009.

[193] Sören Lehmkuhl, Martin Wiese, Lukas Schubert, Mathias Held, Markus Küppers, Matthias Wessling, and Bernhard Blümich. Continuous Hyperpolarization with Parahydrogen in a Membrane Reactor. *Journal of Magnetic Resonance*, 291:8–13, 2018.

[194] A. M. Gañán-Calvo and J. M. Gordillo. Perfectly Monodisperse Microbubbling by Capillary Flow Focusing. *Physical Review Letters*, 87(27):Pt, 2001.

[195] Eleanor Stride, Tim Segers, Guillaume Lajoinie, Samir Cherkaoui, Thierry Bettinger, Michel Versluis, and Mark Borden. Microbubble Agents: New Directions. *Ultrasound in Medicine and Biology*, 46(6):1326–1343, 2020.

[196] Piotr Garstecki, Irina Gitlin, Willow DiLuzio, George M. Whitesides, Eugenia Kumacheva, and Howard A. Stone. Formation of Monodisperse Bubbles in a Microfluidic Flow-Focusing Device. *Applied Physics Letters*, 85(13):2649–2651, 2004.

[197] Patrick Löb, Helmut Pennemann, and Volker Hessel. g/l-Dispersion in Interdigital Micromixers with Different Mixing Chamber Geometries. *Chemical Engineering Journal*, 101(1):75–85, 2004.

[198] F. Schönfeld, V. Hessel, and C. Hofmann. An Optimised Split-and-Recombine Micro-Mixer with Uniform Chaotic Mixing. *Lab on a Chip*, 4(1):65–69, 2004.

[199] J. de Jong, R. G. H. Lammertink, and M. Wessling. Membranes and Microfluidics: A Review. *Lab on a Chip*, 6(9):1125–1139, 2006.

[200] Hao Zhang, Zhao-Yu Wu, Yin-Zhen Wang, Dong-Dong Zhou, Feng-Qing Yang, and De-Qiang Li. On-Line Immobilized Trypsin Microreactor for Evaluating Inhibitory Activity of Phenolic Acids by Capillary Electrophoresis and Molecular Docking. *Food Chemistry*, 310:125823, 2020.

[201] Jonathan W. Cooper, Jinzhi Chen, Yan Li, and Cheng S. Lee. Membrane-Based Nanoscale Proteolytic Reactor Enabling Protein Digestion, Peptide Separation, and Protein Identification Using Mass Spectrometry. *Analytical Chemistry*, 75(5):1067–1074, 2003.

[202] Sandro Matosevic, Nicolas Szita, and Frank Baganz. Fundamentals and Applications of Immobilized Microfluidic Enzymatic Reactors. *Journal of Chemical Technology & Biotechnology*, 86(3):325–334, 2011.

[203] Mohammad Rafiq Khan. Immobilized Enzymes: A Comprehensive Review. *Bulletin of the National Research Centre*, 45(1):1–13, 2021.

[204] Xiaoyan Wang, Chutarat Saridara, and Somenath Mitra. Microfluidic Supported Liquid Membrane Extraction. *Analytica Chimica Acta*, 543(1):92–98, 2005.

[205] Mina Alidoust, Mahroo Baharfar, Mahshid Manouchehri, Yadollah Yamini, Mohammad Tajik, and Shahram Seidi. Emergence of Microfluidic Devices in Sample Extraction; An Overview of Diverse Methodologies, Principals, and Recent Advancements. *TrAC Trends in Analytical Chemistry*, 143:116352, 2021.

[206] Jan C. T. Eijkel and Albert van den Berg. Nanotechnology for Membranes, Filters and Sieves. A Series of Mini-Reviews Covering New Trends in Fundamental and Applied Research, and Potential Applications of Miniaturised Technologies. *Lab on a Chip*, 6(1):19–23, 2006.

[207] Thomas Theis, Milton L. Truong, Aaron M. Coffey, Roman V. Shchepin, Kevin W. Waddell, Fan Shi, Boyd M. Goodson, Warren S. Warren, and Eduard Y. Chekmenev. Microtesla SABRE Enables 10% Nitrogen-15 Nuclear

Spin Polarization. *Journal of the American Chemical Society*, 137(4):1404–1407, 2015.

[208] Danila A. Barskiy, Roman V. Shchepin, Christian P. N. Tanner, Johannes F. P. Colell, Boyd M. Goodson, Thomas Theis, Warren S. Warren, and Eduard Y. Chekmenev. The Absence of Quadrupolar Nuclei Facilitates Efficient ^{13}C Hyperpolarization via Reversible Exchange with Parahydrogen. *ChemPhysChem*, 18(12):1493–1498, 2017.

[209] Roman V. Shchepin, Milton L. Truong, Thomas Theis, Aaron M. Coffey, Fan Shi, Kevin W. Waddell, Warren S. Warren, Boyd M. Goodson, and Eduard Y. Chekmenev. Hyperpolarization of "Neat" Liquids by NMR Signal Amplification by Reversible Exchange. *The Journal of Physical Chemistry Letters*, 6(10):1961–1967, 2015.

[210] Ryan E. Mewis, Richard A. Green, Martin C. R. Cockett, Michael J. Cowley, Simon B. Duckett, Gary G. R. Green, Richard O. John, Peter J. Rayner, and David C. Williamson. Strategies for the Hyperpolarization of Acetonitrile and Related Ligands by SABRE. *The Journal of Physical Chemistry B*, 119(4):1416–1424, 2015.

[211] Angus W. J. Logan, Thomas Theis, Johannes F. P. Colell, Warren S. Warren, and Steven J. Malcolmson. Hyperpolarization of Nitrogen-15 Schiff Bases by Reversible Exchange Catalysis with para-Hydrogen. *Chemistry*, 22(31):10777–10781, 2016.

[212] Wissam Iali, Peter J. Rayner, and Simon B. Duckett. Using Para Hydrogen to Hyperpolarize Amines, Amides, Carboxylic Acids, Alcohols, Phosphates, and Carbonates. *Science Advances*, 4(1):eaao6250, 2018.

[213] Wissam Iali, Peter J. Rayner, Adel Alshehri, A. Jonathan. Holmes, Amy J. Ruddlesden, and Simon B. Duckett. Direct and Indirect Hyperpolarisation of Amines Using Parahydrogen. *Chemical Science*, 9(15):3677–3684, 2018.

[214] Soumya S. Roy, Kate M. Appleby, Elizabeth J. Fear, and Simon B. Duckett. SABRE-Relay: A Versatile Route to Hyperpolarization. *The Journal of Physical Chemistry Letters*, 9(5):1112–1117, 2018.

[215] Peter J. Rayner, Michael J. Burns, Alexandra M. Olaru, Philip Norcott, Marianna Fekete, Gary G. R. Green, Louise A. R. Highton, Ryan E. Mewis, and Simon B. Duckett. Delivering Strong ^{1}H Nuclear Hyperpolarization Levels and Long Magnetic Lifetimes Through Signal Amplification by Reversible Exchange. *Proceedings of the National Academy of Sciences of the United States of America*, 114(16):3188–3194, 2017.

[216] Danila A. Barskiy, Roman V. Shchepin, Aaron M. Coffey, Thomas Theis, Warren S. Warren, Boyd M. Goodson, and Eduard Y. Chekmenev. Over 20% ^{15}N Hyperpolarization in Under One Minute for Metronidazole, an Antibiotic and Hypoxia Probe. *Journal of the American Chemical Society*, 138(26):8080–8083, 2016.

[217] Roman V. Shchepin, Boyd M. Goodson, Thomas Theis, Warren S. Warren, and Eduard Y. Chekmenev. Toward Hyperpolarized ^{19}F Molecular Imaging via Reversible Exchange with Parahydrogen. *ChemPhysChem*, 18(15):1961–1965, 2017.

[218] Alexandra M. Olaru, Alister Burt, Peter J. Rayner, Sam J. Hart, Adrian C. Whitwood, Gary G. R. Green, and Simon B. Duckett. Using Signal Amplification by Reversible Exchange (SABRE) to Hyperpolarise ^{119}Sn and ^{29}Si NMR Nuclei. *Chemical Communications*, 52(100):14482–14485, 2016.

[219] Marianna. Fekete, Clèmentine Gibard, Gordon J. Dear, Gary G. R. Green, Alexander J. J. Hooper, Andrew D. Roberts, Federico Cisnetti, and Simon B. Duckett. Utilisation of Water Soluble Iridium Catalysts for Signal Amplification by Reversible Exchange. *Dalton Transactions*, 44(17):7870–7880, 2015.

[220] Lorenzo Bordonali, Nurdiana Nordin, Erwin Fuhrer, Neil MacKinnon, and Jan G. Korvink. Parahydrogen Based NMR Hyperpolarisation Goes Micro: An Alveolus for Small Molecule Chemosensing. *Lab on a Chip*, 19(3):503–512, 2019.

[221] Francesca Reineri, Tommaso Boi, and Silvio Aime. ParaHydrogen Induced Polarization of ^{13}C Carboxylate Resonance in Acetate and Pyruvate. *Nature Communications*, 6:5858, 2015.

[222] Sergey Korchak, Salvatore Mamone, and Stefan Glöggler. Over 50 % ^{1}H and ^{13}C Polarization for Generating Hyperpolarized Metabolites—A *para*-Hydrogen Approach. *ChemistryOpen*, 7(9):672–676, 2018.

[223] Sergey Korchak, Shengjun Yang, Salvatore Mamone, and Stefan Glöggler. Pulsed Magnetic Resonance to Signal-Enhance Metabolites within Seconds by Utilizing *para*-Hydrogen. *ChemistryOpen*, 7(5):344–348, 2018.

[224] Eleonora Cavallari, Carla Carrera, Silvio Aime, and Francesca Reineri. ^{13}C MR Hyperpolarization of Lactate by Using ParaHydrogen and Metabolic Transformation *in vitro*. *Chemistry – A European Journal*, 23(5):1200–1204, 2017.

[225] James Eills, Eleonora Cavallari, Carla Carrera, Dmitry Budker, Silvio Aime, and Francesca Reineri. Real-Time Nuclear Magnetic Resonance Detection of Fumarase Activity Using Parahydrogen-Hyperpolarized [1-^{13}C]fumarate. *Journal of the American Chemical Society*, 141(51):20209–20214, 2019.

[226] T. H. Witney, M. I. Kettunen, D-e Hu, F. A. Gallagher, S. E. Bohndiek, R. Napolitano, and K. M. Brindle. Detecting Treatment Response in a Model of Human Breast Adenocarcinoma Using Hyperpolarised [1-^{13}C]pyruvate and [1,4-$^{13}C_2$]fumarate. *British Journal of Cancer*, 103(9):1400, 2010.

[227] Laura Wienands, Franziska Theiß, James Eills, Lorenz Rösler, Stephan Knecht, and Gerd Buntkowsky. Optimizing the Reaction Conditions for the Formation of Fumarate via Trans-Hydrogenation. *Applied Magnetic Resonance*, 53(3):615–634, 2022.

[228] Eleonora Cavallari, Carla Carrera, Matteo Sorge, Gisèle Bonne, Antoine Muchir, Silvio Aime, and Francesca Reineri. The ^{13}C Hyperpolarized Pyruvate Generated by ParaHydrogen Detects the Response of the Heart to Altered Metabolism in Real Time. *Scientific Reports*, 8(1):1–9, 2018.

[229] Aaron M. Coffey, Roman V. Shchepin, Milton L. Truong, Ken Wilkens, Wellington Pham, and Eduard Y. Chekmenev. Open-Source Automated Parahydrogen Hyperpolarizer for Molecular Imaging Using ^{13}C Metabolic Contrast Agents. *Analytical Chemistry*, 88(16):8279–8288, 2016.

[230] Stephan Berner, Andreas B. Schmidt, Mirko Zimmermann, Andrey N. Pravdivtsev, Stefan Glöggler, Jürgen Hennig, Dominik von Elverfeldt, and Jan-Bernd Hövener. SAMBADENA Hyperpolarization of ^{13}C-Succinate in an MRI: Singlet-Triplet Mixing Causes Polarization Loss. *ChemistryOpen*, 8(6):728–736, 2019.

[231] Pileio Giuseppe, Carravetta Marina, and H. Levitt Malcolm. Storage of Nuclear Magnetization as Long-Lived Singlet Order in Low Magnetic Field. *Proceedings of the National Academy of Sciences of the United States of America*, 107(40):17135–17139, 2010.

[232] Giuseppe Pileio. Singlet NMR Methodology in Two-Spin-1/2 Systems. *Progress in Nuclear Magnetic Resonance Spectroscopy*, 98-99:1–19, 2017.

[233] Malcolm H. Levitt. Singlet Nuclear Magnetic Resonance. *Annual Review of Physical Chemistry*, 63(1):89–105, 2012.

[234] Michael C. D. Tayler and Malcolm H. Levitt. Singlet Nuclear Magnetic Resonance of Nearly-Equivalent Spins. *Physical Chemistry Chemical Physics*, 13(13):5556–5560, 2011.

[235] Francesca Reineri, Eleonora Cavallari, Carla Carrera, and Silvio Aime. Hydrogenative-PHIP Polarized Metabolites for Biological Studies. *Magnetic Resonance Materials in Physics, Biology and Medicine.*, 34(1):25–47, 2021.

[236] Pratip Bhattacharya, Eduard Y. Chekmenev, Wanda F. Reynolds, Shawn Wagner, Niki Zacharias, Henry R. Chan, Rolf Bünger, and Brian D. Ross. Parahydrogen-Induced Polarization (PHIP) Hyperpolarized MR Receptor Imaging *in vivo*: A Pilot Study of ^{13}C Imaging of Atheroma in Mice. *NMR in Biomedicine*, 24(8):1023–1028, 2011.

[237] Eleonora Cavallari, Carla Carrera, Tommaso Boi, Silvio Aime, and Francesca Reineri. Effects of Magnetic Field Cycle on the Polarization Transfer from Parahydrogen to Heteronuclei through Long-Range J-Couplings. *The Journal of Physical Chemistry B*, 119(31):10035–10041, 2015.

[238] Haukur Jóhannesson, Oskar Axelsson, and Magnus Karlsson. Transfer of Para-Hydrogen Spin Order into Polarization by Diabatic Field Cycling. *Comptes Rendus Physique*, 5(3):315–324, 2004.

[239] James Eills, John W. Blanchard, Teng Wu, Christian Bengs, Julia Hollenbach, Dmitry Budker, and Malcolm H. Levitt. Polarization Transfer via Field Sweeping in Parahydrogen-Enhanced Nuclear Magnetic Resonance. *The Journal of Chemical Physics*, 150(17):174202, 2019.

[240] Jan-Bernd Hövener, Eduard Y. Chekmenev, Kent C. Harris, William H. Perman, Larry W. Robertson, Brian D. Ross, and Pratip Bhattacharya. PASADENA Hyperpolarization of ^{13}C Biomolecules: Equipment Design and Installation. *Magnetic Resonance Materials in Physics, Biology, and Medicine*, 22(2):111–121, 2009.

[241] Ahmed J. Allami, Maria Grazia Concilio, Pavan Lally, and Ilya Kuprov. Quantum Mechanical MRI Simulations: Solving the Matrix Dimension Problem. *Science Advances*, 5(7):eaaw8962., 2019.

[242] S. A. Smith, T. O. Levante, B. H. Meier, and R. R. Ernst. Computer Simulations in Magnetic Resonance. An Object-Oriented Programming Approach. *Journal of Magnetic Resonance, Series A*, 106(1):75–105, 1994.

[243] Ilya Kuprov. Fokker-Planck Formalism in Magnetic Resonance Simulations. *Journal of Magnetic Resonance*, 270:124–135, 2016.

[244] R. Clough. The Finite Element Method in Plane Stress Analysis. *in: Proceedings of the Second ASCE Conference on Electronic Computation*, 1960.

[245] Violeta Carvalho, Raquel O. Rodrigues, Rui A. Lima, and Senhorinha Teixeira. Computational Simulations in Advanced Microfluidic Devices: A Review. *Micromachines*, 12(10), 2021.

[246] Zohreh Sheidaei, Pooria Akbarzadeh, and Navid Kashaninejad. Advances in Numerical Approaches for Microfluidic Cell Analysis Platforms. *Journal of Science: Advanced Materials and Devices*, 5(3):295–307, 2020.

[247] Joelle Aubin, David F Fletcher, and Catherine Xuereb. Design of Micromixers Using CFD Modelling. *Chemical Engineering Science*, 60(8-9):2503–2516, 2005.

[248] Hasnia Hajji, Lioua Kolsi, Walid Hassen, Abdullah A. A. A. Al-Rashed, Mohamed Naceur Borjini, and Mohamed Ahmed Aichouni. Finite Element Simulation of Antigen-Antibody Transport and Adsorption in a Microfluidic Chip. *Physica E: Low-dimensional Systems and Nanostructures*, 104:177–186, 2018.

[249] Hassnia Hajji, Lioua Kolsi, Kaouther Ghachem, Chemseddine Maatki, and Mohamed Naceur Borjini. Numerical Simulation of a Microfluidic Biosensor for C-reactive Protein Detection into a Microchannel with Considering Electrothermal Effect. *Alexandria Engineering Journal*, 59(3):1649–1659, 2020.

[250] Hui An, Ang Li, Agus P Sasmito, Jundika C Kurnia, Sachin V Jangam, and Arun S Mujumdar. Computational Fluid Dynamics (CFD) Analysis of Micro-Reactor Performance: Effect of Various Configurations. *Chemical Engineering Science*, 75:85–95, 2012.

[251] Christopher J. Ochs, Junichi Kasuya, Andrea Pavesi, and Roger D. Kamm. Oxygen Levels in Thermoplastic Microfluidic Devices During Cell Culture. *Lab on a Chip*, 14(3):459–462, 2013.

[252] Kuan-Rong Huang, Jeng-Shian Chang, Sheng D. Chao, Kuang-Chong Wu, Chih-Kai Yang, Cheng-Yu Lai, and Shyh-Haur Chen. Simulation on Binding Efficiency of Immunoassay for a Biosensor with Applying Electrothermal Effect. *Journal of Applied Physics*, 104(6):064702, 2008.

[253] J. D. Anderson. Governing Equations of Fluid Dynamics. In *Computational Fluid Dynamics*, pages 15–51. Springer, Berlin, Germany, 1992.

[254] Bashar Ibrahim and Richard Henze. Active Transport Can Greatly Enhance Cdc20:Mad2 Formation. *International Journal of Molecular Sciences*, 15(10):19074–19091, 2014.

[255] Bashar Ibrahim. *In silico* Spatial Simulations Reveal that MCC Formation and Excess BubR1 are Required for Tight Inhibition of the Anaphase-Promoting Complex. *Molecular BioSystems*, 11(11):2867–2877, 2015.

[256] Laurynas Dagys, Barbara Ripka, Markus Leutzsch, Gamal A. I. Moustafa, James Eills, Johannes F. P. Colell, and Malcolm H. Levitt. Geminal Parahydrogen-Induced Polarization: Accumulating Long-Lived Singlet Order on Methylene Proton Pairs. *Journal of Magnetic Resonance*, 1(2):175–186, 2020.

[257] Stefan Karpinski Jeff Bezanson. The Julia Programming Language, 2022. [Online; Accessed 19 Dec 2022].

[258] Marcel Utz. NMR Package for Julia Programming Language. `https://github.com/marcel-utz/NMR.jl.git`, 2021. [Online; Accessed 19 Dec 2022].

[259] Marcel Utz. Kinetics Toolbox. `https://github.com/marcel-utz/kinetics-toolbox`, 2020. [Online; Accessed 19 Dec 2022].

[260] Ekaterina M. Kozinets, Marianna Fekete, Oleg A. Filippov, Natalia V. Belkova, Elena S. Shubina, Rinaldo Poli, Simon B. Duckett, and Eric Manoury. Activation of a (Cyclooctadiene) Rhodium (I) Complex Supported by a Chiral Ferrocenyl Phosphine Thioether Ligand for Hydrogenation Catalysis: A Combined Para Hydrogen NMR and DFT Study. *Dalton Transactions*, 42(32):11720–11730, 2013.

[261] Luis A. Oro and Daniel Carmona. Rhodium. In *The Handbook of Homogeneous Hydrogenation*, pages 2–30. WILEY-VCH Verlag GmbH & Co. KGaA, Weinheim, Germany, 2006.

[262] Francesca Reineri, Silvio Aime, Roberto Gobetto, and Carlo Nervi. Role of the Reaction Intermediates in Determining PHIP (Parahydrogen Induced

Polarization) Effect in the Hydrogenation of Acetylene Dicarboxylic Acid with the Complex [Rh (dppb)]+(dppb: 1, 4-bis (diphenylphosphino) butane). *The Journal of Chemical Physics*, 140(9):094307, 2014.

[263] Jingwei Luo, Robin Theron, Laura J. Sewell, Thomas N. Hooper, Andrew S. Weller, Allen G. Oliver, and J. Scott McIndoe. Rhodium-Catalyzed Selective Partial Hydrogenation of Alkynes. *Organometallics*, 34(12):3021–3028, 2015.

[264] Jack Halpern, Dennis P. Riley, Albert S. C. Chan, and Joseph J. Pluth. Novel Coordination Chemistry and Catalytic Properties of Cationic 1,2-bis(diphenylphosphino)ethanerhodium(I) Complexes. *Journal of the American Chemical Society*, 99(24):8055–8057, 1977.

[265] O. Bondar, E. Cavallari, C. Carrera, S. Aime, and F. Reineri. Effect of the Hydrogenation Solvent in the PHIP-SAH Hyperpolarization of [1-^{13}C]pyruvate. *Catalysis Today*, 397-399:94–102, 2022.

[266] Roberto A. Sánchez-Delgado and Merlin Rosales. Kinetic Studies as a Tool for the Elucidation of the Mechanisms of Metal Complex-Catalyzed Homogeneous Hydrogenation Reactions. *Coordination Chemistry Reviews*, 196(1):249–280, 2000.

[267] Marino Itoda, Yuki Naganawa, Makoto Ito, Hiroshi Nonaka, and Shinsuke Sando. Structural Exploration of Rhodium Catalysts and Their Kinetic Studies for Efficient Parahydrogen-Induced Polarization by Side Arm Hydrogenation. *RSC Advances*, 9(32):18183–18190, 2019.

[268] K. Radhakrishnan, P. A. Ramachandran, P. H. Brahme, and R. V. Chaudhari. Solubility of Hydrogen in Methanol, Nitrobenzene, and their Mixtures Experimental Data and Correlation. *Journal of Chemical & Engineering Data*, 28(1):1–4, 1983.

[269] Oleg G. Salnikov, Nikita V. Chukanov, Roman V. Shchepin, Isaac V. Manzanera Esteve, Kirill V. Kovtunov, Igor V. Koptyug, and Eduard Y. Chekmenev. Parahydrogen-Induced Polarization of 1-^{13}C-Acetates and

1-^{13}C-Pyruvates Using Sidearm Hydrogenation of Vinyl, Allyl, and Propargyl Esters. *The Journal of Physical Chemistry C*, 123(20):12827–12840, 2019.

[270] Stephan Knecht, John W. Blanchard, Danila Barskiy, Eleonora Cavallari, Laurynas Dagys, Erik Van Dyke, Maksim Tsukanov, Bea Bliemel, Kerstin Münnemann, Silvio Aime, Francesca Reineri, Malcolm H. Levitt, Gerd Buntkowsky, Alexander Pines, Peter Blümler, Dmitry Budker, and James Eills. Rapid Hyperpolarization and Purification of the Metabolite Fumarate in Aqueous Solution. *Proceedings of the National Academy of Sciences of the United States of America*, 118(13):e2025383118, 2021.

[271] Bishnubrata Patra, Manvendra Sharma, William Hale, and Marcel Utz. Time-Resolved Non-Invasive Metabolomic Monitoring of a Single Cancer Spheroid by Microfluidic NMR. *Scientific Reports*, 11(53):1–11, 2021.

[272] Maria Laura Coluccio, Gerardo Perozziello, Natalia Malara, Elvira Parrotta, Peng Zhang, Francesco Gentile, Tania Limongi, Pushparani Michael Raj, Gianni Cuda, Patrizio Candeloro, and Enzo Di Fabrizio. Microfluidic Platforms for Cell Cultures and Investigations. *Microelectronic Engineering*, 208:14–28, 2019.

[273] Matthias Mehling and Sava Tay. Microfluidic Cell Culture. *Current Opinion in Biotechnology*, 25:95–102, 2014.

[274] Guansheng Du, Qun Fang, and Jaap M. J. den Toonder. Microfluidics for Cell-Based High Throughput Screening Platforms — A Review. *Analytica Chimica Acta*, 903:36–50, 2016.

[275] Bin Xiong, Kangning Ren, Yiwei Shu, Yin Chen, Bo Shen, and Hongkai Wu. Recent Developments in Microfluidics for Cell Studies. *Advanced Materials*, 26(31):5525–5532, 2014.

[276] Sherif I. Hamdallah, Randa Zoqlam, Peer Erfle, Mark Blyth, Alaaldin M. Alkilany, Andreas Dietzel, and Sheng Qi. Microfluidics for Pharmaceutical Nanoparticle Fabrication: The Truth and the Myth. *International Journal of Pharmaceutics*, 584:119408, 2020.

[277] Kyung-Jin Jang and Kahp-Yang Suh. A Multi-Layer Microfluidic Device for Efficient Culture and Analysis of Renal Tubular Cells. *Lab on a Chip*, 10(1):36–42, 2010.

[278] Andreas O. Stucki, Janick D. Stucki, Sean R. R. Hall, Marcel Felder, Yves Mermoud, Ralph A. Schmid, Thomas Geiser, and Olivier T. Guenat. A Lung-on-a-Chip Array with an Integrated Bio-Inspired Respiration Mechanism. *Lab on a Chip*, 15(5):1302–1310, 2015.

[279] Carl-Fredrik Mandenius. Conceptual Design of Micro-Bioreactors and Organ-on-Chips for Studies of Cell Cultures. *Bioengineering*, 5(3):56., 2018.

[280] Wujin Sun, Zhimin Luo, Junmin Lee, Han-Jun Kim, KangJu Lee, Peyton Tebon, Yudi Feng, Mehmet R. Dokmeci, Shiladitya Sengupta, and Ali Khademhosseini. Organ-on-a-Chip for Cancer and Immune Organs Modeling. *Advanced Healthcare Materials*, 8(4):e1801363, 2019.

[281] Ehsanollah Moradi, Sasan Jalili-Firoozinezhad, and Mehran Solati-Hashjin. Microfluidic Organ-on-a-Chip Models of Human Liver Tissue. *Acta Biomaterialia*, 116:67–83, 2020.

[282] Preena Shrimal, Girirajsinh Jadeja, and Sanjaykumar Patel. A Review on Novel Methodologies for Drug Nanoparticle Preparation: Microfluidic Approach. *Chemical Engineering Research and Design*, 153:728–756, 2020.

[283] Yujun Song, Josef Hormes, and Challa S. S. R. Kumar. Microfluidic Synthesis of Nanomaterials. *Small*, 4(6):698–711, 2008.

[284] Liang-Jun Pan, Jia-Wei Tu, Hao-Tian Ma, Yu-Jun Yang, Zhi-Quan Tian, Dai-Wen Pang, and Zhi-Ling Zhang. Controllable Synthesis of Nanocrystals in Droplet Reactors. *Lab on a Chip*, 18(1):41–56, 2017.

[285] Bing Wu, Sebastian von der Ecken, Ian Swyer, Chunliang Li, Amy Jenne, Franck Vincent, Daniel Schmidig, Till Kuehn, Armin Beck, Falko Busse, Henry Stronks, Ronald Soong, Aaron R. Wheeler, and André Simpson. Rapid Chemical Reaction Monitoring by Digital Microfluidics-NMR: Proof of Principle Towards

an Automated Synthetic Discovery Platform. *Angewandte Chemie International Edition*, 58(43):15372–15376, 2019.

[286] Adelina-Gabriela Niculescu, Cristina Chircov, Alexandra Cătălina Bîrcă, and Alexandru Mihai Grumezescu. Fabrication and Applications of Microfluidic Devices: A Review. *International Journal of Molecular Sciences*, 22(4), 2021.

[287] Jihong Hwang, Young Hak Cho, Min Soo Park, and Bo Hyun Kim. Microchannel Fabrication on Glass Materials for Microfluidic Devices. *International Journal of Precision Engineering and Manufacturing*, 20(3):479–495, 2019.

[288] Zhen J. Wang, Michael A. Ohliger, Peder E. Z. Larson, Jeremy W. Gordon, Robert A. Bok, James Slater, Javier E. Villanueva-Meyer, Christopher P. Hess, John Kurhanewicz, and Daniel B. Vigneron. Hyperpolarized ^{13}C MRI: State of the Art and Future Directions. *Radiology*, 291(2):273, 2019.

[289] Christoffer Laustsen, Per Mose Nielsen, Haiyun Qi, Mette Hadberg Løbner, Johan Palmfeldt, and Lotte Bonde Bertelsen. Hyperpolarized [1,4-^{13}C]fumarate Imaging Detects Microvascular Complications and Hypoxia Mediated Cell Death in Diabetic Nephropathy. *Scientific Reports*, 10(9650):1–10, 2020.

[290] Ferdia A. Gallagher, Mikko I. Kettunen, De-En Hu, Pernille R. Jensen, René In 't Zandt, Magnus Karlsson, Anna Gisselsson, Sarah K. Nelson, Timothy H. Witney, Sarah E. Bohndiek, Georg Hansson, Torben Peitersen, Mathilde H. Lerche, and Kevin M. Brindle. Production of Hyperpolarized [1,4-^{13}C$_2$]malate from [1,4-^{13}C$_2$]fumarate is a Marker of Cell Necrosis and Treatment Response in Tumors. *Proceedings of the National Academy of Sciences of the United States of America*, 106(47):19801, 2009.

[291] Sarah E. Bohndiek, Mikko I. Kettunen, De-en Hu, Timothy H. Witney, Brett W. C. Kennedy, Ferdia A. Gallagher, and Kevin M. Brindle. Detection of Tumor Response to a Vascular Disrupting Agent by Hyperpolarized ^{13}C Magnetic Resonance Spectroscopy. *Molecular Cancer Therapeutics*, 9(12):3278–3288, 2010.

[292] Menna R. Clatworthy, Mikko I. Kettunen, De-En Hu, Rebeccah J. Mathews, Timothy H. Witney, Brett W. C. Kennedy, Sarah E. Bohndiek, Ferdia A.

Gallagher, Lorna B. Jarvis, Kenneth G. C. Smith, and Kevin M. Brindle. Magnetic Resonance Imaging with Hyperpolarized [1,4-$^{13}C_2$]fumarate Allows Detection of Early Renal Acute Tubular Necrosis. *Proceedings of the National Academy of Sciences of the United States of America*, 109(33):13374–13379, 2012.

[293] Lionel Mignion, Prasanta Dutta, Gary V. Martinez, Parastou Foroutan, Robert J. Gillies, and Bénédicte F. Jordan. Monitoring Chemotherapeutic Response by Hyperpolarized ^{13}C-Fumarate MRS and Diffusion MRI. *Cancer Research*, 74(3):686–694, 2014.

[294] Jack J. Miller, Angus Z. Lau, Per Mose Nielsen, Giles McMullen-Klein, Andrew J. Lewis, Nichlas Riise Jespersen, Vicky Ball, Ferdia A. Gallagher, Carolyn A. Carr, Christoffer Laustsen, Hans Erik Bøtker, Damian J. Tyler, and Marie A. Schroeder. Hyperpolarized [1,4-$^{13}C_2$]Fumarate Enables Magnetic Resonance-Based Imaging of Myocardial Necrosis. *JACC: Cardiovascular Imaging*, 11(11):1594–1606, 2018.

[295] J. Eills, E. Cavallari, R. Kircher, G. Di Matteo, C. Carrera, L. Dagys, M. H. Levitt, K. L. Ivanov, S. Aime, F. Reineri, K. Münnemann, D. Budker, G. Buntkowsky, and S. Knecht. Singlet-Contrast Magnetic Resonance Imaging: Unlocking Hyperpolarization with Metabolism. *Angewandte Chemie International Edition*, 60(12):6791–6798, 2021.

[296] Michael G. Pravica and Daniel P. Weitekamp. Net NMR Alignment by Adiabatic Transport of Parahydrogen Addition Products to High Magnetic Field. *Chemical Physics Letters*, 145(4):255–258, 1988.

[297] Bogdan A. Rodin, Vitaly P. Kozinenko, Alexey S. Kiryutin, Alexandra V. Yurkovskaya, James Eills, and Konstantin L. Ivanov. Constant-Adiabaticity Pulse Schemes for Manipulating Singlet Order in 3-Spin Systems with Weak Magnetic Non-Equivalence. *Journal of Magnetic Resonance*, 327:106978, 2021.

[298] James Eills, Gabriele Stevanato, Christian Bengs, Stefan Glöggler, Stuart J. Elliott, Javier Alonso-Valdesueiro, Giuseppe Pileio, and Malcolm H. Levitt. Singlet Order Conversion and Parahydrogen-Induced Hyperpolarization of ^{13}C

Nuclei in Near-Equivalent Spin Systems. *Journal of Magnetic Resonance*, 274:163–172, 2017.

[299] Gabriele Stevanato, James Eills, Christian Bengs, and Giuseppe Pileio. A Pulse Sequence for Singlet to Heteronuclear Magnetization Transfer: S2hM. *Journal of Magnetic Resonance*, 277:169–178, 2017.

[300] William Hale, Gabriel Rossetto, Rachael Greenhalgh, Graeme Finch, and Marcel Utz. High-Resolution Nuclear Magnetic Resonance Spectroscopy in Microfluidic Droplets. *Lab on a Chip*, 18(19):3018–3024, 2018.

[301] P. Kating, A. Wandelt, R. Selke, and J. Bargon. Nuclear Singlet/Triplet Mixing During Hydrogenations with Parahydrogen: An *in situ* NMR Method to Investigate Catalytic Reaction Mechanisms and their Kinetics. 2. Homogeneous Hydrogenation of 1,4-dihydro-1,4-epoxynaphthalene Using Different Rhodium Catalysts. *The Journal of Physical Chemistry*, 97(50):13313–13317, 1993. Publisher: American Chemical Society.

[302] J. Bargon, J. Kandels, and P. Kating. Nuclear Magnetic Resonance Studies of Homogeneous Catalysis Using Parahydrogen: Analysis of Nuclear Singlet-Triplet Mixing as a Diagnostic Tool to Characterize Intermediates. *The Journal of Chemical Physics*, 98(8):6150–6153, 1993. Publisher: American Institute of Physics.

[303] Laurynas Dagys, Christian Bengs, and Malcolm H. Levitt. Low-Frequency Excitation of Singlet–Triplet Transitions. Application to Nuclear Hyperpolarization. *The Journal of Chemical Physics*, 155(15):154201, 2021.

[304] Alexey S. Kiryutin, Grit Sauer, Alexandra V. Yurkovskaya, Hans-Heinrich Limbach, Konstantin L. Ivanov, and Gerd Buntkowsky. Parahydrogen Allows Ultrasensitive Indirect NMR Detection of Catalytic Hydrogen Complexes. *The Journal of Physical Chemistry C*, 121(18):9879–9888, 2017.

[305] Stephan Knecht, Alexey S. Kiryutin, Alexandra V. Yurkovskaya, and Konstantin L. Ivanov. Mechanism of Spontaneous Polarization Transfer in

High-Field SABRE Experiments. *Journal of Magnetic Resonance*, 287:74–81, 2018.

[306] Danila A. Barskiy, Stephan Knecht, Alexandra V. Yurkovskaya, and Konstantin L. Ivanov. SABRE: Chemical Kinetics and Spin Dynamics of the Formation of Hyperpolarization. *Progress in Nuclear Magnetic Resonance Spectroscopy*, 114-115:33–70, 2019.

[307] Ewoud Vaneeckhaute, Sophie De Ridder, Jean-Max Tyburn, James G. Kempf, Francis Taulelle, Johan A. Martens, and Eric Breynaert. Long-Term Generation of Longitudinal Spin Order Controlled by Ammonia Ligation Enables Rapid SABRE Hyperpolarized 2D NMR. *ChemPhysChem*, 22(12):1170–1177, 2021.

[308] Andrey N. Pravdivtsev, Alexandra V. Yurkovskaya, Herbert Zimmermann, Hans-Martin Vieth, and Konstantin L. Ivanov. Transfer of SABRE-Derived Hyperpolarization to Spin-1/2 Heteronuclei. *RSC Advances*, 5(78):63615–63623, 2015.

[309] Maurice Goldman, Haukur Jóhannesson, Oskar Axelsson, and Magnus Karlsson. Design and Implementation of ^{13}C Hyperpolarization from Para-Hydrogen for New MRI Contrast Agents. *Comptes Rendus Chimie*, 9(3):357–363, 2006.

[310] Stephan Knecht and Konstantin L. Ivanov. Quantitative Quantum Mechanical Approach to SABRE Hyperpolarization at High Magnetic Fields. *The Journal of Chemical Physics*, 150(12):124106, 2019.

[311] Stephan Knecht, Sara Hadjiali, Danila A. Barskiy, Alexander Pines, Grit Sauer, Alexey S. Kiryutin, Konstantin L. Ivanov, Alexandra V. Yurkovskaya, and Gerd Buntkowsky. Indirect Detection of Short-Lived Hydride Intermediates of Iridium N-Heterocyclic Carbene Complexes via Chemical Exchange Saturation Transfer Spectroscopy. *The Journal of Physical Chemistry C*, page 6, 2019.

[312] Danil A. Markelov, Vitaly P. Kozinenko, Stephan Knecht, Alexey S. Kiryutin, Alexandra V. Yurkovskaya, and Konstantin L. Ivanov. Singlet to Triplet Conversion in Molecular Hydrogen and its Role in Parahydrogen Induced Polarization. *Physical Chemistry Chemical Physics*, 23(37):20936–20944, 2021.

[313] Stephan Knecht, Alexey S. Kiryutin, Alexandra V. Yurkovskaya, and Konstantin L. Ivanov. Efficient Conversion of Anti-Phase Spin Order of Protons Into ^{15}N Magnetisation Using SLIC-SABRE. *Molecular Physics*, 117(19):2762–2771, 2019.

[314] Thomas Theis, Milton Truong, Aaron M. Coffey, Eduard Y. Chekmenev, and Warren S. Warren. LIGHT-SABRE Enables Efficient In-Magnet Catalytic Hyperpolarization. *Journal of Magnetic Resonance*, 248:23–26, 2014.

[315] J. Natterer, O. Schedletzky, J. Barkemeyer, J. Bargon, and S. J. Glaser. Investigating Catalytic Processes with Parahydrogen: Evolution of Zero-Quantum Coherence in AA'X Spin Systems. *Journal of Magnetic Resonance*, 133(1):92–97, 1998.

[316] I. del Rosal, L. Maron, R. Poteau, and F. Jolibois. DFT Calculations of ^{1}H and ^{13}C NMR Chemical Shifts in Transition Metal Hydrides. *Dalton Transactions*, 30:3959–3970, 2008.

[317] Christian Bengs and Malcolm H. Levitt. SpinDynamica: Symbolic and Numerical Magnetic Resonance in a Mathematica Environment. *Magnetic Resonance in Chemistry*, 56(6):374–414, 2018.

[318] Danila A. Barskiy, Lucia A. Ke, Xingyang Li, Vincent Stevenson, Nevin Widarman, Hao Zhang, Ashley Truxal, and Alexander Pines. Rapid Catalyst Capture Enables Metal-Free Para-Hydrogen-Based Hyperpolarized Contrast Agents. *The Journal of Physical Chemistry Letters*, 9(11):2721–2724, 2018.

[319] Bryce Kidd, Jonathan L. Gesiorski, Max E. Gemeinhardt, Roman V. Shchepin, Kirill V. Kovtunov, Igor V. Koptyug, Eduard Y. Chekmenev, and Boyd M. Goodson. Facile Removal of Homogeneous SABRE Catalysts for Purifying Hyperpolarized Metronidazole, a Potential Hypoxia Sensor. *The Journal of Physical Chemistry C*, 122(29):16848–16852, 2018.